


FACULTEIT WETENSCHAPPEN
VAKGROEP FYSICA EN STERRENKUNDE
ACADEMIEJAAR 2013-2014

Measurement of cosmic ray composition and energy spectrum between 1 PeV and 1 EeV with IceTop and IceCube.

Meting van de samenstelling en het energiespectrum van kosmische straling tussen 1 PeV and 1 EeV met IceTop en IceCube.

Tom Feusels
Promotor: Prof. Dr. Dirk Ryckbosch

Proefschrift ingediend tot het verkrijgen van de graad van
Doctor in de Wetenschappen: Fysica en Sterrenkunde

Contents

Introduction

Since the discovery of cosmic ray radiation more than hundred years ago, many experiments have been studying its properties. The main question which is still not solved today is where this highly penetrating high energy radiation actually comes from and how it is produced. At the surface of the Earth charged cosmic rays up to 10^{20}eV or 16 J have been observed. These energies are much higher than can be produced by man-made accelerators. If we know where these cosmic rays originate from, then we are probing the physics of the most violent and energetic sources in the Universe.

The basic measurement for cosmic rays is their energy spectrum. For a long time scientists were under the impression that the energy spectrum followed a single powerlaw. About fifty years ago a change in the spectral index was seen for the first time at about 3 PeV. This steeping in the spectrum is called the knee. More than ten years later another feature, the ankle, was discovered at a few EeV, where the spectrum becomes less steep again. The energy range between the knee and the ankle is not well understood, but contains the interesting region where the galactic sources are thought to reach their limit for accelerating the cosmic rays, while the extra-galactic might start to dominate the energy spectrum. The apparent single power law between the knee and ankle is very difficult to explain and requires a lot of fine-tuning in theoretical models. Therefore accurate measurements of both the primary energy spectrum as the composition are needed to understand the transition region from galactic to extra-galactic sources. This is the energy range that is studied in this thesis.

The flux of high energy cosmic rays is too low for direct detection by satellite or balloon experiments. When a high energy cosmic ray particle enters the atmosphere, it will interact and generate an extensive air shower. Detectors at ground level operate in coincidence to trigger on multiple secondary particles from the air shower initiated by the same primary cosmic ray. By measuring different components of the extensive air shower in parallel with different detection techniques, the energy and mass the primary cosmic ray can be deduced through dedicated simulations.

The goal of the analysis presented in this thesis, is to measure the composition and the energy spectrum of cosmic rays with high accuracy between the knee and the ankle. For this purpose the IceCube Neutrino Observatory has been built at the geographic South Pole. The surface component, IceTop, is a square kilometer air shower array which detects secondary cosmic ray particles with ice Cherenkov tanks. When air showers further propagate through the South Pole ice, only compact groups of high energy ($>$300 GeV) muons survive. They generate Cherenkov light that is detected by IceCube strings instrumented with optical detector modules. From coincident air showers the electromagnetic component, important for determining the primary cosmic ray energy, is probed by IceTop while the high energy muon bundles from the same shower is seen by IceCube. These type of showers are studied here in order to measure not only the primary energy but also the mass of the primary particle simultaneously.

In Chapter 1 I will start with a thorough overview on cosmic ray physics and extensive air showers and discuss the potential sources, acceleration mechanisms and theoretical models. The IceCube Neutrino Observatory is presented in Chapter 2 with a detailed explanation about both detector components, the detector modules and the DAQ. The environment which the cosmic rays encounter on their way to the actual detector influences the measurement and is also discussed Chapter 2. Detailed simulations are necessary to interpret the data and are introduced in Chapter 3.

To translate signals from Cherenkov photons in IceTop and IceCube to properties of the air shower, like the core position, its direction, the lateral signal distribution and the energy loss profile of the propagating

muon bundle, simple and more advanced reconstructions are used. The existing reconstructions I improved and new reconstructions I developed are explained in Chapter 4. High quality reconstruction are obtained by performing advanced hit cleaning algorithms on the detected signals before reconstructions and by removing low quality events. These methods are described in Chapter 5 and result in a high quality selection of data with reconstructed variables that are sensitive to primary mass and primary energy. The extraction of the primary mass and primary energy is done by a combination of a neural network approach, followed by a template fitting to extract the average mass for each reconstructed energy. The technical details of these analysis tools are explained in Chapter 6. Before the final energy spectrum and composition measurement is discussed in Chapter 8, I will first give an overview about the systematic uncertainties in this analysis in Chapter 7.

Chapter 1

Cosmic Ray Physics

More than 100 years ago cosmic rays were discovered as highly penetrating, extraterrestrial radiation. Since then many experiments have been performed to measure the properties of this strange radiation and essentially to figure out where exactly it comes from. At high energies cosmic rays are rare and are therefore difficult to detect directly. They interact in the atmosphere to generate extensive air showers, a cascade of lower energy, secondary particles. These air showers can be detected with several different experimental techniques that probe different properties of the air showers.

1.1 Cosmic Rays

1.1.1 History

Figure 1.1: Victor Hess in the balloon's basket sometime between 1911 and 1912 [1].

After the discovery of radioactivity and X-rays at the end of the 19^{th} century, scientists started investigating the ionisation of gases in more detail. Julius Elster and Hans Geitel, and Charles Thomson Ress Wilson saw that, even when they closed and isolated their detectors (electrometers), they still detected the production of ions [2]. As there was no active source they concluded this radiation must come from the detector walls, but Wilson also wondered whether this very penetrating radiation could be extraterrestrial.

Between 1900 and 1903 Franz Linke, a German meteorologist, used the same detectors as Elster and Geitler to measure the ionisation of air at different altitudes during twelve balloon flights [3]. He found that the ionisation is roughly the same between altitudes of 1000 m to 3000 m, but at 5500 m the ionisation was four times larger. Even though he was the first to discover cosmic ray radiation, as extraterrestrial penetrating radiation, he has never been recognized.

While the electrometers were being improved, scientists over the whole world studied the ionisation effect with different materials and material thicknesses around their detectors. The general consensus at the beginning of the 20^{th} century was that this ionisation is caused by the natural radioactivity of the Earth.

To investigate where exactly the ionising radiation came from in more detail, Domenico Pacini performed radiation measurements in 1910, 300 m away from the coast on the water's surface and 3 m below the water's surface where he still observed an ionising radiation. As there were no solid materials on the sea, he concluded that the source must be some penetrating radiation in the atmosphere [4].

Wilson developed the first cloud chamber in 1911 to visualize alpha and beta rays, when they create condensed bubbles after ionising the air. On two of his pictures straight tracks from cosmic muons can be seen, which he misidentified as beta rays one year before the discovery of cosmic rays.

Physik. Zeitschr. XIII, 1912. Hess, Durchdringende Strahlung bei sieben Freiballonfahrten. 1089

Tabelle der Mittelwerte.

Mittlere Höhe über dem Erdboden m	Beobachtete Strahlung in Ionen pro ccm und sec.			
	Apparat 1	Apparat 2	Apparat 3	
	q_1	q_2	q_3 (reduziert)	q_3 (nicht reduziert)
0 bis 200	16,3 (18)	11,8 (20)	19,6 (9)	19,7 (9)
200—500	15,4 (13)	11,1 (12)	19,1 (8)	18,5 (8)
500—1000	15,5 (6)	10,4 (6)	18,8 (5)	17,7 (5)
1000—2000	15,6 (3)	10,3 (4)	20,8 (2)	18,5 (2)
2000—3000	15,9 (7)	12,1 (8)	22,2 (4)	18,7 (4)
3000—4000	17,3 (1)	13,3 (1)	31,2 (1)	22,5 (1)
4000—5200	19,8 (1)	16,5 (1)	35,2 (1)	21,8 (1)
	34,4 (2)	27,2 (2)	—	—

Figure 1.2: Mean values of all measurements (in ions per cubic centimeter (ccm) per second) during the seven flights at different altitudes with the number of measurements in brackets.

In April to August 1912, Victor Hess performed seven balloon flights where he measured the ionisation with two or three highly improved and calibrated electrometers. The first six flights were at low altitudes of 150 m and 2750 m, while his last flight reached an altitude of 5350 m. The measurements are summarized in Fig. 1.2. He came to the following conclusions : *"Die Ergebnisse der vorliegenden Beobachtungen scheinen am ehesten durch die Annahme erklärt werden zu können, daß eine Strahlung von sehr hoher Durchdringungskraft* ***von oben her in unsere Atmosphäre eindringt****, und auch noch in deren untersten Schichten einen Teil der in geschlossenen Gefäßen beobachteten Ionisation hervorruft. ...Da ich im Ballon weder bei Nacht noch bei einer Sonnenfinsternis eine Verringerung der Strahlung fand, so kann man* ***wohl kaum die Sonne als Ursache dieser hypothetischen Strahlung ansehen****,..."* [5]:

- There is a highly penetrating radiation that enters the atmosphere from above;
- This radiation also contributes to the radiation seen in closed detectors at lower altitude;
- As the same intensity of radiation was seen during the night and during a solar eclipse, the sun can not be regarded as the source of this extraterrestrial radiation.

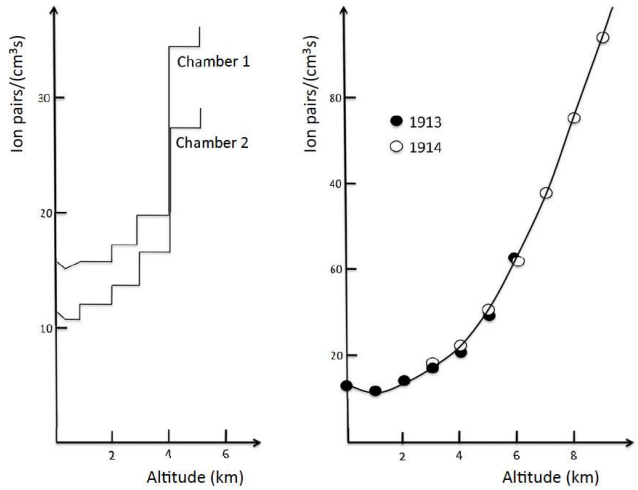

Figure 1.3: The left plot shows the measurement from Hess, while the right plot shows measurements from Kolhörster which are in agreement and extend up to 9300 m.

For this discovery Hess was awarded the Nobel Prize in 1936.

Subsequently, Werner Kolhörster performed three balloon flights up to 6000 m in 1913 and confirmed the results from Victor Hess. At the end of June 1914, he started a record flight, with improved electrometers, reaching an altitude of 9300 m. In Fig. 1.3 both Hess's measurements and Kohlhörster's measurements are shown to agree very well. The measurements confirmed that the high-energy radiation has an extraterrestrial origin [4].

1.1.2 Cosmic Rays

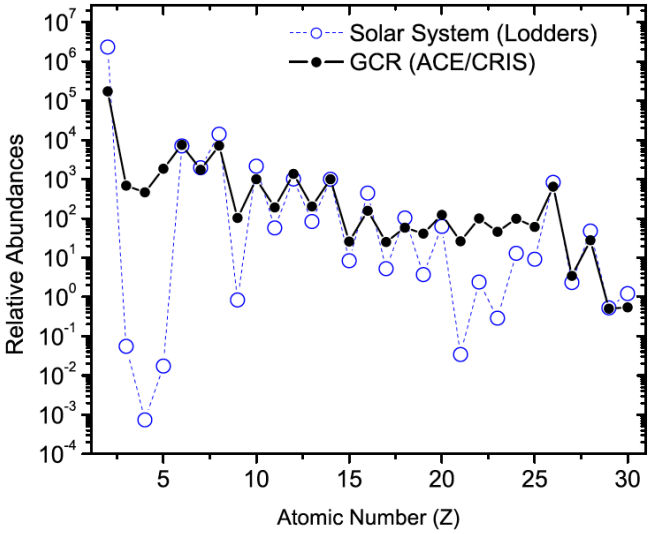

Figure 1.4: Abundances of elements observed in the cosmic rays by CRIS and elements in the proto-sun (Solar system abundances) from [6]. Abundances normalized to 1000 for Si.

Extraterrestrial particles of which some fraction enters the Earth's atmosphere are called cosmic rays or

cosmic ray radiation. Neutral cosmic rays consist of neutrinos and gamma-rays[1] and will not be discussed in detail in this thesis. Here, we will mainly focus on charged cosmic rays.An example of low energy cosmic rays is the Aurora Borealis and the Aurora Australis, which is caused by particles from solar flares sent towards the Earth where they initially get caught by the Earth's magnetic field and are then visible near the magnetic poles.

Cosmic rays consist primarily of hydrogen nuclei ($\sim$89% by number), with $\sim$ 9% helium, about 2% heavier nuclei and less than 1% electrons. The observed cosmic rays are a mixture of primary cosmic rays – nuclei that were accelerated at the source and reach us essentially unchanged – and secondary cosmic rays – the products of cosmic-ray interactions with nuclei of atoms in the interstellar medium. The secondary nature of some of the cosmic rays can be illustrated by comparing the elemental composition of the observed cosmic rays with that of the solar system. The relative abundance for cosmic rays, measured by the Cosmic Ray Spectrometer (CRIS) on the ACE spacecraft between 1997 and 2004 [6], compared to abundances of elements in the solar system [7] is shown in Fig. 1.4. CRIS measured the elemental and isotopic composition over the energy range from 50 to 500 MeV/nucleon. The relative abundances of many of the elements in the cosmic rays generally follow the relative abundances in the Solar System, illustrated by $_6$C, $_8$O, $_{10}$Ne, $_{12}$Mg, $_{14}$Si, $_{26}$Fe, $_{28}$Ni. But elements that are rare in the Solar System compared with heavier elements are relatively more abundant in the cosmic rays, which is illustrated by $_3$Li, $_4$Be, $_5$B, $_{21}$Sc, $_{22}$Ti, $_{23}$V, $_{24}$Cr, $_{25}$Mn. The abundance of the latter group of elements results from the fragmentation of the cosmic-ray nuclei as they propagate through the interstellar medium with a mean path length of 7 g/cm^2.

From the abundance of elements in cosmic rays one could also try to answer the question which nuclei are accelerated to cosmic-ray energies by a supernova remnant: the nuclei that were synthesized in the supernova or the ambient material in the interstellar medium, synthesized in previous supernovae. Nickel-59 (^{59}Ni) is synthesized in supernovae and decays by nuclear capture of an atomic electron. Because the half-life of this process is 0.76·10^5 years ^{59}Ni can be used as a clock. A supernova shock exists for a time shorter than the ^{59}Ni half-life. Therefore if the nuclei were accelerated to cosmic-ray energies by the same supernova in which they were synthesized, ^{59}Ni would survive because at those energies all its atomic electrons have been stripped by collisions with the interstellar gas and it becomes effectively stable. If the supernova does not accelerate its ^{59}Ni-ions, they will decay through electron capture. CRIS observed that there is essentially no ^{59}Ni in the cosmic rays; it has all decayed to ^{59}Co. These data demonstrate that the time between nucleosynthesis and acceleration to cosmic-ray energies is at least of the order 10^5 years. Thus cosmic rays are accelerated from interstellar material [6].

Cosmic Ray Energy Spectrum

The all-particle cosmic ray energy spectrum has been measured extensively over the last 50 years. Up to $\sim$500 TeV the spectrum has been measured by direct experiments, explained in Section 1.2.2 while at higher energies indirect experiments deduced the cosmic ray energy from properties of extensive air showers, created by the interaction of the cosmic ray particles with the air molecules. The differential flux $\mathrm{d}\,\Phi/\,\mathrm{d}\,E$ weighted by the energy E in m^{-2}s^{1}sr^{-1} is shown in Fig. 1.5 between 10 GeV and 100 EeV. At rigidities exceeding 20 GV (20 GeV for H, 10 GeV/nucleon for He) cosmic rays are not affected by the solar wind which carries a magnetic field that modulate the flux of charged cosmic ray nuclei entering the solar system (solar modulation). Additionally there is the geomagnetic field that bends the trajectories of low energy charged particles and prevents the low rigidity particles ($\sim$ 14.9 GV at the magnetic equator and $\sim$ 0.93 GV at a magnetic latitude of $\pm$ 60°) from reaching the atmosphere.

The cosmic ray energy spectrum shows an almost featureless power law spectrum over ten orders of magnitude in energy:

$$\frac{\mathrm{d}\,\Phi}{\mathrm{d}\,E} = \Phi_0 E^{-\gamma}, \tag{1.1}$$

with Φ_0, the flux normalization in m^{-2}s^{1}sr^{-1} and γ, the spectral index. There are two transition regions,

[1] Actually photons in all wavelengths from outer space can be regarded as cosmic rays

discussed more in detail in Section 1.1.5, where the slope γ of the spectrum changes. The first slope changes from about -2.7 to -3 at around 4 PeV is called the *knee*, while the second slope change from -3 to -2.6 at around 3 EeV is called the *ankle*. A faint feature at $\sim$ 400-800 PeV is called the *second knee*, but needs to be confirmed by higher precision experiments. Above about 30 EeV there is a steep decline in flux which could be due to the limit of the cosmic ray accelerators at the source or due to a predicted flux suppression, called the Greisen-Zatsepin-Kuzmin [8, 9] cutoff.

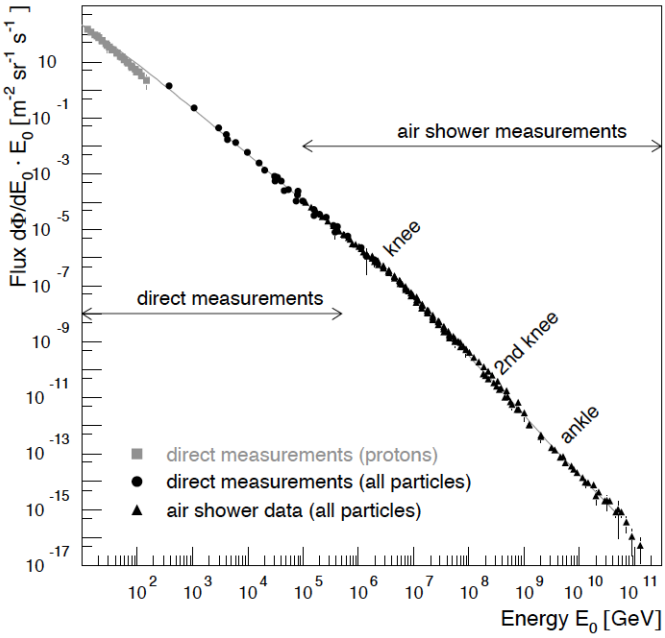

Figure 1.5: Cosmic ray energy spectrum, plotted as differential flux weighted by the cosmic ray energy E_0.

The knee was discovered by Kulikov and Khristiansen in 1959 when they measured the size spectrum with a 20 m by 20 m hodoscope[2] array [10]. The left plot in Fig. 1.6 shows the measured integral size spectrum together with an older measurement at higher energies. The data indicate with a high probability that a change in the character of the spectrum may occur in the investigated region N = $8{\cdot}10^4$ to $1.5{\cdot}10^6$, later called the *knee*. The size range corresponds to the primary range E = 10^{15} to 10^{18} eV. They conclude that *"the observed spectrum is a superposition of the spectra of particles of galatic and metagalactic origin"*.

The other break in the size spectrum was observed in 1963 after three years of data taking by the Volcano Ranch experiment, an array of 19 scintillators in a 16 km^2 grid situated at 1770 m altitude in New Mexico [11]. This flattening of the energy spectrum at about 10^{18}eV is now called the *ankle*.

The number of particles above 100 GeV is higher than that above 10^{11} GeV by sixteen orders of magnitude. At about 10 PeV there are six particles per square kilometer per minute hitting the Earth. At a few 100 PeV only one cosmic ray particle per square kilometer per day crashes into the atmosphere and at a few 10 EeV it is even reduced to three events per square kilometer per century.

Even though the cosmic ray energy spectrum has been measured by many experiments, the systematic uncertainties in the energy assignment are about 20%. At the highest energies the most recent experiments Auger[12] and Telescope Array (TA)[13, 14] observe the same shape in their spectrum, but differ by 15% in absolute energy scale [15]. The energy region between the knee and ankle, and mainly between 100 PeV and 1 EeV is not well measured by a high resolution experiment. In the recent years more and more hints arose that the energy spectrum is not as featureless as originally thought. Hence, accurate high statistics

[2] A hodoscope is a tracking detector which consists of several segments with scintillating material. The sequence of several hit scintillator segments can be connected to reconstruct the track of the particles.

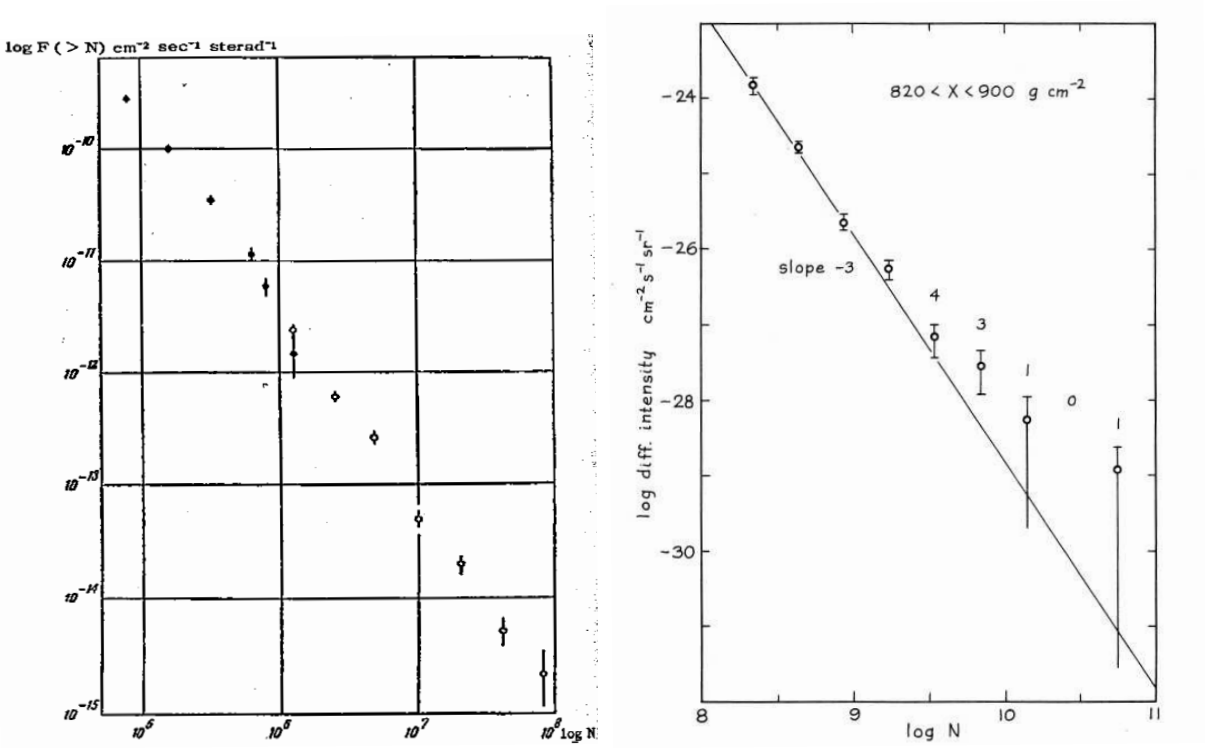

Figure 1.6: The left plot shows the size spectrum measured by Kulikov and Khristiansen in 1959 combined with an earlier measurement at higher energies, which together shows a change in spectral index, later called the *knee* [10]. The right plot shows the size spectrum measured by Linsley *et al.* in 1960-1963, which again shows a change in spectral index, called the *ankle* [11].

measurements in the transition region from the knee to the ankle are needed. This is one of the major objectives of this thesis.

An overview of the measurement of the cosmic ray composition in the energy range between 100 TeV and 100 PeV is shown in Fig. 1.7 [16]. Composition measurements are inherently difficult. The range of measurements shows the large uncertainty, although if the measurements are grouped per type (direct, optical, electron/muon) and per hadronic interaction model used in simulation, the results are very comparable. The general trend is that the composition is getting heavier beyond the knee. At the highest energy there is again a large spread between different measurements which motivates the main objective of this thesis, namely an accurate composition measurement between the knee and the ankle.

1.1.3 Sources - Acceleration - Propagations of Galactic Cosmic Rays

The Life and Death of a Star

In 1934, W. Baade and F. Zwicky first mentioned supernovae as potential sources for cosmic radiation. Supernovae were seen as a class of new stars (*novae*) which are very rare[3] and extremely bright as they emit nearly as much light as the whole galaxy in which they originate [18]. They estimated the amount of continously emitted radiation from supernovae, based on the distribution of galaxies and the observed frequency of supernovae in a given galaxy, and compared with the observations of the intensity of cosmic rays made by E. Regener in 1933 (based on ion counts). They conclude : *"The hypothesis that super-novae emit cosmic rays leads to a very satisfactory agreement with some of the major observations on cosmic*

[3]Baade and Zwicky estimated about one supernova per stellar system per several centuries while the current estimate is about three supernova in the Milky Way per century [17].

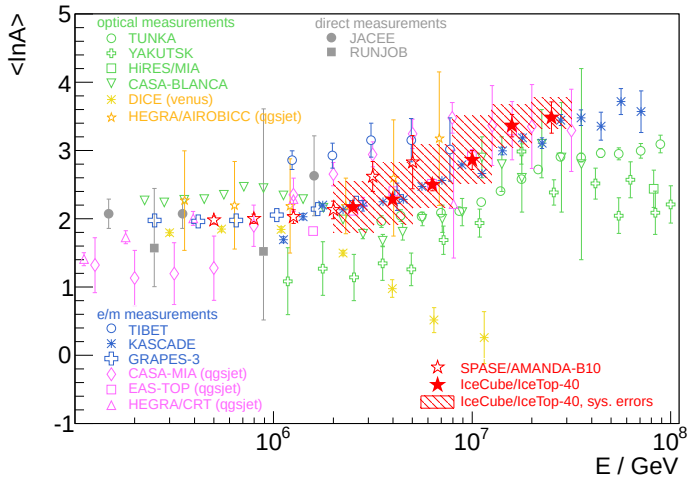

Figure 1.7: The cosmic ray composition spectrum, plotted as mean log mass $< \ln A >$ as a function of cosmic ray energy E, compared between different experiments from [16]. The different colour codes group experiments that use similar techniques and measurements with the same hadronic interaction model.

rays." Based on the fact that no supernova eruption occurred in the Milky Way, during the period of the first observations and measurements, they also concluded that "*... our own Galaxy has emitted no cosmic rays during the years in which these rays have been observed*" [19].

Stars, like our Sun, are huge nuclear fusion factories. Depending on the mass of the star subsequent nuclear fusion of hydrogen, helium, carbon, oxygen and silicon happens in the core of the star. Each stage of this core fusion generates a new shell of material around the core, creating an onion-like structure.

Once a star (with mass $\gtrsim 8$ solar masses $M_\odot$) develops an iron-rich core, its core contracts within a tenth of second, so that the temperature rises to $5{\cdot}10^9$K. The intensely hot core emits gamma-ray photons that are high energetic enough to break the iron nuclei into smaller helium nuclei through photodisintegration. The core becomes so dense that electrons are forced to interact with the protons to form neutrons : $e^- + p \rightarrow n + \nu_e$. This creates a very compact and very dense neutron-rich core ($4{\cdot}10^{17}$ kg/cm^3), which cannot be compressed anymore. The core contraction process stops and the innermost part of the core bounces back. This *core bounce* sends a powerful pressure wave into the outer core. During this critical stage,the cooling of the core has caused the pressure to decrease profoundly in the regions surrounding the core. Without pressure to hold it up against gravity, the material surrounding the core gets pulled into the rigid core at 15% of the speed of light. There it encounters the outward- moving pressure wave, which pushes all the material back out toward the star's surface. The outward- moving wave accelerates as it encounters less and less resistance and reaches a speed greater thatn the sound speed in the star's outer layers. When this happens, the wave becomes a *shock wave* (like the sonci boom created by an airplane flying fast than the speed of sound) [20].

After only a few hours the star's surface is reached by this shock wave, by which time the outer layers of the star have begun to lift away from the core. The energy released is humongous (10^{46}J). When the star's outer layers thin out sufficiently, a portion ot his energy escapes in a torrent of light. The star has become a *supernova*. Before the star ejects a large fraction of its material into space, the material is compressed to much by the passage of the shock wave through the star's outer layers that a new wave of thermonuclear reactions set in. These reactions produce many more chemical elements, including all elements heavier than iron. The energy-rich environment of a supernova shock wave is almost the only place in the universe where such heavy elements as zinc, silver, tin, gold, mercury, lead and uranium can be produced. There are many varieties to similar processes that also lead to a supernova explosion. Here the core-collapse model, typical for type Ib, Ic and type II supernovae (classified depending on the spectral emission lines), was described. During the last decades astronomers have seen even more powerful types of exploding stars. These so-called

hypernovae realse a total energy of 10-50 times that of supernovae.

The material synthesized in the star and ejected prior to the supernova explosion, together with the interstellar matter (ISM) is hit by the expanding supersonic (non-relativistic) shock wave from the final explosion and forms a supernova remnant (SNR). The final explosion can expel up to a large fraction of its matter at speeds of nearly 10% of the speed of light. The shock wave forms ahead of the ejected matter and compresses and heats the upstream plasma up to millions of K due to the conversion of kinetic energy. At this temperature the SNR emits radiation in many wavebands. The SNR expands into space and may extend over tens of parsecs , slowly decelerates and merges with the surrounding ISM after roughly 30,000 years.

The most famous SNRs are shown in Fig. 1.8. The Crab Nebula (6500 light years (ly) away), shown in X-ray (blue-purple), Optical (green) and Infrared (red), is assumed to originate from a Galactic Supernova observed first by Chinese astronomers in 1054 AD. Tycho Brahe observed a galactic supernova in 1572 AD (shown in X-ray, infrared and optical) which is about 13000 light years away. Kepler's supernova remnant (shown in X-ray and optical), from a supernova seen in 1604, is about 13000 to 23000 light years away. One of the youngest galactic SNR is Cassiopeia A (shown in Infrared, Optical and X-ray), is 11000 light years away and about 330 years old. Recently the youngest, galactic SNR was discovered, named G1.9+0.3, and is only 140 years old. SN 1987A is the closest, observed supernova since Kepler's in the Milky Way itself at 168000 light years away in the Large Magellanic Cloud. At that time huge neutrino detectors (Kamiokande II, IMB and Baksan) were in operation and detected together 24 antineutrino's about two hours before the visible light from the SN reached the Earth.

Figure 1.8: Six very famous supernova remnants ordered according to their age. **Top row**: Crab Nebula (1054 AD) [21], Tycho's SNR (1572 AD) [22], Kepler's SNR (1604 AD) [23]. **Bottom row** : Cassiopeia A (330 yr old) [24], G1.9+0.3 (140 yr old) [25], Supernova 1987A [26]

Acceleration

In 1949 Enrico Fermi proposed a mechanism which could accelerate particles in interstellar space. The main process of acceleration, according to this so-called second order Fermi acceleration, is due to the interaction of cosmic particles with moving magnetic fields which are present in the interstellar space. Particles above a certain injection threshold gain energy by collisions against the moving irregularities of the interstellar magnetic field. Although the rate of energy gain is very slow, this mechanism could produce the observed cosmic ray energies and naturally results in a powerlaw energy spectrum with a power γ close to the experimentally observed one [27].

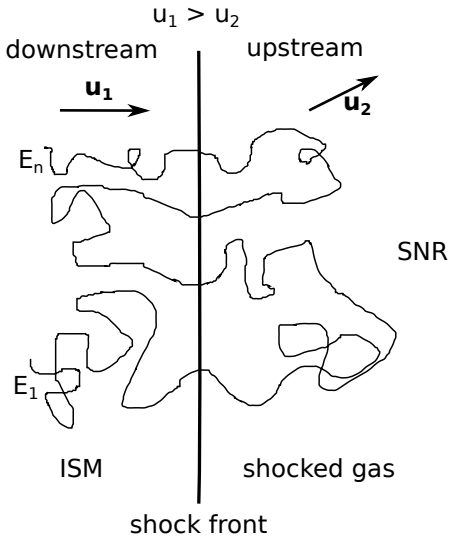

Figure 1.9: Principle of the Fermi or diffusive shock acceleration. The situation near the shock front is shown in the rest frame of the shock front. On the left-hand side the interstellar matter (ISM) in the downstream region moves with velocity $\boldsymbol{u}_1$ to the shock front, while the shocked gas on the right-hand side moves away from the shock front with velocity $\boldsymbol{u}_2$. After crossing the shock front a particle diffuses through the magnetic field in the shocked gas back to face the shock front and cross again.

The Fermi acceleration mechanism could also be applied to the outer edges of SNRs. At the outer edges, there is a very narrow boundary layer where the interstellar gas is rapidly compressed and heated, becoming part of the advancing high-speed SNR gas. The swept-up gas should be compressed to about four times its initial density, due to conservation of mass flux, momentum flux and energy flux (Rankine-Hugoniot conditions[4] [28, 29, 30]). If there are fast-moving particles present in the gas that is being compressed (*unshocked gas downstream*), then they could move through the magnetic fields and cross the shock front where they gain energy. In the *shocked plasma upstream* they could scatter and wander back through the compression zone [31].

Suppose a particle gains energy $\Delta E = \xi E$ during each encounter with the shock front. After n encounters it has an energy $E_n = E(1+\xi)^n$, so $n = \log(E/E_0)/\log(1+\xi)$. The number of particles with energy E or higher is :

$$\begin{aligned} N(\geq E) &= \sum_{m=n}^{\infty} (1-P_{esc})^m = \frac{(1-P_{esc})^n}{P_{esc}} \\ &= \frac{1}{P_{esc}} \left(\frac{E}{E_0}\right)^{-\gamma} \qquad \text{with}\, \gamma = \frac{\log \frac{1}{1-P_{esc}}}{\log(1+\xi)} \sim \frac{P_{esc}}{\xi} \end{aligned} \tag{1.2}$$

[4]The Rankine-Hugoniot conditions describe the relationship between the states on both sides of a shock wave in a one-dimensional flow in fluids.

with P_{esc} the probability at each interaction to escape the acceleration region.

A particle in the downstream region[5] (left-hand side on Fig. 1.9) of an approaching SNR sees the shock front approaching with speed $-\boldsymbol{u}_1$ in the rest frame of the particle. The shocked gas upstream moves with velocity $\boldsymbol{u}_2$ away from the shock front and thus approaches the particle in the downstream region with velocity $\boldsymbol{V} = -\boldsymbol{u}_1 + \boldsymbol{u}_2$. After crossing the shock front, the particle can scatter back and will now see the shock front approaching again. The unshocked gas now approaches with speed $-\boldsymbol{V}$ in the new rest frame of the particle, the rest frame of the upstream region. By Lorentz transformations from the downstream rest frame, where the particle has energy E_1, to the upstream region, and after scattering back to the downstream rest frame, one obtains as relative energy gain :

$$\xi = \frac{\Delta E}{E} = \frac{1 - \beta\cos\theta_1 + \beta\cos\theta_2 - \beta^2\cos\theta_1\cos\theta_2}{1-\beta^2} - 1. \tag{1.3}$$

After averaging over the angles θ_1, θ_2 by which it crosses the shock front (on average head-on collisions) the relative energy gain of this ping-pong mechanism becomes : $\xi = \frac{4}{3}\beta = \frac{4}{3}\frac{u_1-u_2}{c}$. The escape probability P_{esc} can be calculated by dividing the rate of convection upstream away from the shock, $\rho_{cr}u_2$, where ρ_{cr} is the number density of particles undergoing acceleration, by the rate of encounters with the shock. This is given by the projection of an isotropic flux onto the planar shock front (for large, planar shocks) $\int_0^1 \cos\theta \,\mathrm{d}\cos\theta \int_0^{2\pi} d\phi \frac{c\rho_{cr}}{4\pi} = \frac{c\rho_{cr}}{4}$. The escape probability becomes $P_{esc} = \frac{4u_2}{c}$ and gives the cosmic ray spectral index γ :

$$\gamma = \frac{P_{esc}}{\xi} = \frac{3}{u_1/u_2 - 1}. \tag{1.4}$$

Shocks form when the speed of the propagating pressure wave u_1 is larger than the sound speed in the interstellar gas c_1. The Mach number of the flow $M = u_1/c_1$. Using the continuity of the mass flow across the shock, $\rho_1 u_1 = \rho_2 u_2$, the kinetic gas theory [33] and the fact that the ratio of specific heats c_p/c_v for a monoatomic gas is 5/3, we get :

$$\frac{u_1}{u_2} = \frac{\rho_2}{\rho_1} = \frac{(c_p/c_v+1)M^2}{(c_p/c_v-1)M^2+2} = \frac{(5/3+1)M^2}{(5/3-1)M^2+2} \tag{1.5}$$

$$\Rightarrow \gamma \approx 1 + \frac{4}{M^2} \xrightarrow{\text{for strong shock with } M \gg 1} 1.1, \tag{1.6}$$

in Eq. 1.2 which corresponds to a differential spectral index of 2.1 in Eq. 1.1. Implicitly it is assumed that the particles being accelerated do not affect the conditions in the acceleration region, which is called the test particle approximation [32].

This first order[6] Fermi acceleration mechanism or diffuse shock acceleration is very promising to describe the way cosmic rays are accelerated. However, this model does not seem to match observations of cosmic rays at the highest energies. One of the main problems is the maximum energy cosmic ray particles can obtain during the lifetime of a supernova remnant. Lagage and Cesarsky calculated the upper limit to the energy that can be acquired by particles trapped in the vicinity of a supernova shock [34]. The maximum energy per particle that can be achieved with shock acceleration depends on the finite lifetime of the supernova blast wave. The particles in the upstream region of the shocks either cross the shock and gain energy or diffuse away. The time a particle cycles back and forth through the shock, is $\tau_{\text{cycle}} = \frac{4}{c}\left(\frac{D_{upstream}}{u_1} + \frac{D_{downstream}}{u_2}\right)$, with D the diffusion coeffient and u_j the gas velocity in the shock frame. The diffusion length, λ_D cannot be smaller than the Larmor radius of the particle, $r_L = pc/(ZeB)$, with Z the charge of the particle and p its momentum. The idea is that energetic particles cannot respond to irregularities in the magnetic field smaller than the particle gyroradius. This gives a minimum diffusion coefficient $D = \frac{\lambda_D c}{3} \leq \frac{r_L c}{3} = \frac{1}{3}\frac{Ec}{ZeB}$. Because

[5]The upstream region is the region through which the shock front has passed, while the downstream region constitutes of interstellar gas to which the shock front moves in the lab frame. In some references, like [32], the opposite definition is used.

[6]The shock front acceleration is called first order Fermi acceleration because the energy gain ξ is proportional to β, while for the second order Fermi acceleration in interstellar magnetic clouds is proportional to β^2.

the minimum acceleration time $\tau_{\rm cycle} \geq \frac{20}{3}\frac{E}{u_1 ZeB}$ for $D_{upstream} = D_{downstream} = D$ and for a strong shock with $u_2 = u_1/4 = u_1/4$ and because the maximum acceleration time is limited by the lifetime of the shock $\tau_{snr} = \frac{R_{snr}}{u_1}$, we get :

$$\begin{aligned} \frac{R_{snr}}{u_1} &\geq \frac{20}{3}\frac{Ec}{u_1^2 ZeB} \\ \Rightarrow E_{max} &\leq \frac{3}{20}\frac{u_1}{c} ZeBR_{snr} = \frac{3}{20}\frac{u_1^2}{c} ZeB\tau_{snr}. \end{aligned} \tag{1.7}$$

Lagage and Cesarsky show that most acceleration occurs before the SN has swept up its own mass, after which the shock begins to weaken. Therefore we can calculate τ_{snr} from

$$\frac{4}{3}\pi R_{snr}^3 \rho_{ISM} = M_{ejecta}, \tag{1.8}$$

with $M_{ejecta} = 10 M_\odot$ ejected at a velocity of $c/60$ into the nominal ISM with a density ρ_{ISM} of one proton per cm^3, and obtain $\tau_{snr} \sim 1000$ yrs. With an estimate of $B_{ISM} \sim 3\mu$G, the maximum energy E_{max} becomes then :

$$E_{max} \leq Z \cdot 10^{14} eV, \tag{1.9}$$

under favourable assumptions. In this calculation the cosmic rays are treated as test particles such that they do not influence the shock structure itself. Because E_{max} is proportional to Z, this also predicts a break in the cosmic ray spectrum ; beyond the break the cosmic ray flux should be progressively enriched in heavy elements at higher energies [32, 34, 35]. The maximum energy cosmic ray particles can obtain from SNR acceleration of only $Z \cdot 10^{14}$ eV poses a big problem because the experiments show that the energy spectrum continues to higher energies. The very elegant SNR shock acceleration mechanism does not seem to be powerful enough to accelerate cosmic rays up to the knee in the energy spectrum as observed.

Recent development in the theory has shown that the magnetic field can be much larger due to the effect the cosmic ray particles themselves have on the μG magnetic field. In the above *test particle* approximation (linear diffusive shock acceleration), the impact from the particles that are being accelerated on the accelerator have been neglected. However, the non-linear diffusive shock acceleration (NLDSA) from the last decades, accounts for the magnetohydrodynamic (MHD) turbulence generated by cosmic rays ahead of the shock. The cosmic rays scatter on this magnetohydrodynamic turbulence with wavelengths matched to the particle's gyro-radius. The consequence is that the cosmic ray spectrum is distorted and that the magnetic field in the acceleration region is amplified, which increases the maximum energy cosmic rays can obtain. Hence, particles are accelerated because there is a high magnetic field in the acceleration region which makes sure the particles cross the shock front a lot during the lifetime of SNR expansion, but the high magnetic field itself is present because particles are accelerated efficiently. Without this non-linear process, there is no acceleration of cosmic rays possible up to the energies at the knee region and above. There are several ways to amplify the magnetic field by turbulence [36]. Some authors claim the turbulence is already present downstream and is not cosmic ray induced, and will only help with particle acceleration for perpendicular shocks [37]. In [38, 39] they find that the magnetic field can be amplified up to factor of 100, which increases the maximum cosmic ray energy up to $\sim Z \cdot 10^{16}$eV. This creates the possibility that cosmic rays up to the ankle region at 10^{18} eV can be caused by NLDSA in SNR.

Propagation

The spectra of cosmic rays are shaped by two basic processes – the acceleration in the sources as explained above and the subsequent propagation in the interstellar medium. Upon leaving the acceleration site, the charged energetic particles diffuse in random magnetic fields ($\sim 3\mu$G) which account for their high isotropy and relatively long confinement time in the Galaxy.

Ginzburg and Syrovatskii [40] wrote down the transport equation for cosmic rays in the Galaxy as follows :

$$\frac{\partial \mathcal{N}_i(\boldsymbol{r},E,t)}{\partial t} = \overbrace{Q_i(\boldsymbol{r},E,t)}^{\text{source}} + \overbrace{\boldsymbol{\nabla}\cdot(D_i\boldsymbol{\nabla}\mathcal{N}_i)}^{\text{diffusion}} - \overbrace{\boldsymbol{\nabla}\cdot\boldsymbol{w}\,\mathcal{N}_i(E)}^{\text{convection}} - \overbrace{\frac{\partial}{\partial E}\left[b_i(E)\mathcal{N}_i(E)\right]}^{\text{energy loss/gain}} - \overbrace{p_i\mathcal{N}_i(E,t)}^{\text{particle loss}} + \overbrace{\frac{v\rho}{m}\sum_{k\geq i}\int\frac{\mathrm{d}\,\sigma_{i,k}(E,E')}{\mathrm{d}\,E}\mathcal{N}_k(E')\,\mathrm{d}\,E'}^{\text{particle gain}}, \tag{1.10}$$

where $\mathcal{N}_i(\boldsymbol{r},E,t)$ is the density of cosmic rays of a given mass i, with energy E at a given location in the Galaxy $\boldsymbol{r}$ at time t. The source term $Q_i(\boldsymbol{r},E,t)$ is defined as the number of particles of type i produced (accelerated) per cm^3 at time t with energy between E and $E+\delta E$ in a given location in the Galaxy. The cosmic ray diffusion is characterized by the diffusion coefficient $D=\frac{1}{3}\lambda_D v$, with λ_D the diffusion mean free path and v the particle velocity. Galactic winds, present in many galaxies, create convection of cosmic rays with a convection velocity $\boldsymbol{w}$. Convection not only transports cosmic rays, but also produce adiabatic energy loss. The cosmic ray particle could either lose energy while propagating through the Galaxy (eg. mostly ionization for protons and heavy nuclei) or gain energy in *reacceleration* processes in galactic magnetic fields (eg. 2nd order Fermi). This is quantified by $b_i(E)=\frac{\mathrm{d}\,E}{\mathrm{d}\,t}$. Because of interactions or decays, particles of type i could change in particles of type j. This is expressed in $p_i=\frac{v\rho}{\lambda_{i,int}}+\frac{1}{\gamma\tau_i}$, with $\lambda_{i,int}$ the interaction length for particle i and $\gamma\tau_i$ its Lorentz dilated lifetime. Through collisions with interstellar matter new particles could be formed, and particles of type i could be gained in this spallation process. The particle gain or cascade term includes both particles from the same type of nuclei at higher energy, eg. in nucleonic cascades, as particles from heavier nuclei created by nuclear fragmentation processes [32, 41, 42, 43].

The main propagation processes are easy to describe in the *leaky box* approximation. In the leaky box model, the diffusion and convection terms are approximated by the leakage term $\frac{\mathcal{N}_i}{\tau_{esc}}$ with a characteristic escape time τ_{esc} of CR from the Galaxy. No spatial dependence of cosmic ray distribution, source density, escape time, and any other parameters are taken into account. The leaky box model states that cosmic rays propagate through a mean amount of matter in the Galaxy that contains their sources with an average path length λ_{esc} before they escape from it. By definition $\lambda_{esc}=\rho_{ISM}\beta c\tau_{esc}$, with ρ_{ISM} the average matter density. Neglecting the energy loss and gain during propagation, and assuming an equilibrium cosmic ray density the simplified transport equation for stable nuclei becomes :

$$\frac{\mathcal{N}_i(E)}{\tau_{i,esc}(E)} = Q_i(E) - \frac{\beta c\rho_{ISM}}{\lambda_{i,int}(E)}\mathcal{N}_i(E) + \frac{\beta c\rho_{ISM}}{m}\sum_{k\geq i}\sigma_{k\to i}\mathcal{N}_k(E), \tag{1.11}$$

where the last term sums over all higher mass nuclei that produce particle type i in spallation processes. If we then further assume no cosmic ray nuclei are created in propagation, ie. only account for particle loss and diffusion, the leaky box model gives the shape of the energy spectrum of a primary nucleus i after propagation as :

$$\mathcal{N}_i(E) = Q_i(E)\cdot\left(\frac{1}{\tau_{i,esc}(E)}+\frac{\beta c\rho_{ISM}}{\lambda_{i,int}(E)}\right)^{-1} \tag{1.12}$$

$$\sim E^{-2.1}\cdot\left(\left(\frac{R}{3\,\mathrm{GV}}\right)^{0.6}\right)^{-1}. \tag{1.13}$$

From the measured ratio B/C of secondary boron to primary carbon nuclei one could fit[7] the energy depen-

[7] This leaky box calculation comes from [41] and is also illustrated by Eqn. 2 and 4 from [43]. More recent fits of the plain diffusion model to the energy dependence of the B/C ratio in [42] and Section 6 of [43] yield $\lambda_{esc}\sim(R/4.9\,\mathrm{GV})^{-0.54}$ for $R>$4.9 GV.

dence of λ_{esc} and find $\lambda_{esc} \sim (R/3\ \mathrm{GV})^{-0.6}$ for a magnetic rigidity $R = r_{\mathrm{L}}B = pc/Ze > 3$ GV. For protons, λ_{esc} is always smaller than λ_{int} (50.8 g/cm^2 for protons at low energy), hence the second term that will modify the source energy spectrum has a rigidity dependence of $\mathrm{R}^{-0.6}$. From the first order Fermi acceleration a spectral index of 2.1 at the source was obtained. Together with the energy dependence obtained from the leaky box approximation to diffusion through the Galaxy the observed spectral index of 2.7 can be explained [41, 42].

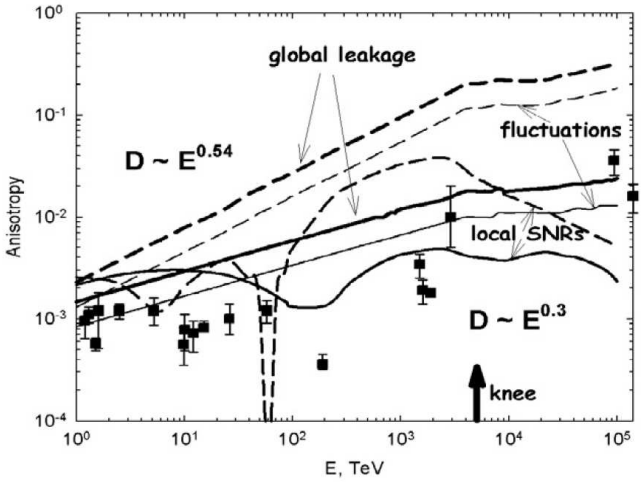

Figure 1.10: The anisotropy of cosmic ray protons and nuclei in the reacceleration (solid curves) and plain diffusion (dashed curve) model for an observer at the Solar System from [43]. Also shown are the contributions from local supernova remnants. The data points show the measurements of the cosmic ray anisotropy.

In contrast to the leaky box approximation based on an average escape length λ_{esc}, more complex diffusion models calculate the energy dependence of the diffusion coefficient D and include processes like convection, reacceleration/wave damping and local sources to explain the energy dependence in the B/C ratio. In the diffusion model with *reacceleration*, the stochastic acceleration due to scattering of CR particles on randomly moving magnetohydrodynamic waves, the B/C energy dependence can be explained with a diffusion coefficient that varies as a single power law of rigidity $D \sim R^{0.3}$ over the whole energy range [42]. This corresponds to particle scattering on MHD turbulences with a Kolmogorov spectrum [44, 45]. The relation between the escape length λ_{esc} from the leaky box model and the diffusion coeffient D in terms of a simple diffusion model is $\lambda_{esc} = \mu v H/(2D)$, with $\mu \approx 2.5$ mg the surface gas density of the Galactic disk, and H the height of the cosmic-ray halo ($H \approx 4$ kpc) [43]. From this we can understand that an $\mathrm{R}^{0.3}$-dependence of the diffusion coefficient D gives an $\mathrm{R}^{-0.3}$ for an equivalent λ_{esc} in Eq. 1.12 and thus a change in the energy spectrum of $\mathrm{E}^{-0.3}$. However, this smaller energy dependence of the diffusion coeffient cannot explain the observed spectral index of 2.7.

There is also a problem with large energy dependences. High isotropy is a distinctive characteristic of galactic cosmic rays observed at Earth. The global leakage of cosmic rays from the Galaxy and the action of individual sources lead to anisotropy but the trajectories of energetic charged particles are very tangled by regular and stochastic interstellar magnetic fields that make the cosmic ray angular distribution isotropic. In Fig. 1.10 the observed anisotropy is compared with the expected anisotropy from the energy dependence of the diffusion coefficient. Large diffusion coefficients result from small escape lengths and escape times in the leaky box interpretation. This means the cosmic rays do not diffuse for a long time in the Galactic halo and the Galactic magnetic fields. More cosmic rays are coming then directly from the source without being deflected too much. Hence, a large diffusion coefficient means a large anisotropy. The energy dependence deduced in the leaky box approximation which would match the spectral CR index, does not fit the observed anisotropy as can be seen in Fig. 1.10, while the diffusion model with reacceleration fits the anisotropy data

better. This is another big problem in the current understanding of acceleration and propagation of galactic cosmic rays [31, 43].

TeV gamma rays from SNR

A third problem that current SNR models face is the lack of sufficient TeV gamma ray emission from SNRs. When a flux of hadrons with an energy spectrum $\mathrm{d}N/\mathrm{d}E \propto E^{-\gamma}$ passes through gas, they will generate a flux of gamma rays with a similar spectrum in the GeV up to a few TeV energy range, by the decay of neutral pions π^0 formed in nuclear collisions. Since 2003 new imaging atmospheric Cherenkov telescopes have been commissioned, namely H.E.S.S. in Namibia, VERITAS in Southern Arizona and MAGIC on the Canary Island of La Palma, with one of the main objectives to find the TeV gamma-ray emission from π^0 decays in SNR. However, disentangling the spectral signature of this process from other sources of gamma-ray emission (ie. leptonic inverse Compton scattering and Bremsstrahlung processes) is difficult [46]. First hints of the pion decay signature have been recently reported by Fermi-LAT [47] and two other recent examples of potential hadronic acceleration are reported by VERITAS [48, 49]. These signatures hint that this third problem for SNR as source for galactic cosmic rays is about to be solved.

1.1.4 Extragalactic Sources

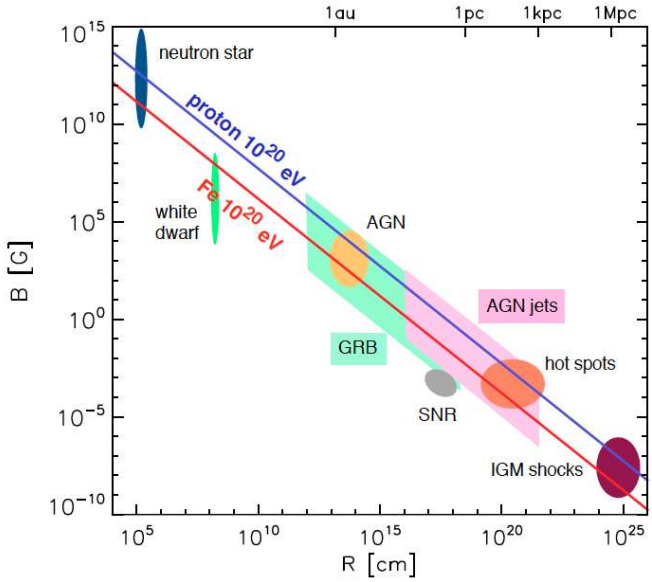

Figure 1.11: Updated Hillas[50] diagram from [51]. On the blue (red) line protons (iron nuclei) can be confined to a maximum energy of E_{max} = 10^{20}eV. The most powerful candidate sources are shown with the typical range of their parameters.

The Larmor radius $r_{\mathrm{L}} \sim 110$ kpc $\mathrm{Z}^{-1}(\mu\mathrm{G/B})(\mathrm{E/100\ EeV})$, of ultra high energy cosmic rays (UHECRs) in Galactic magnetic fields is much larger than the thickness of the Galactic disk. Thus, confinement in the Galaxy is not maintained at the highest energies which motivates the search for extragalactic sources. Requiring that candidate sources are capable of confining particles up to E_{max}, translates into a simple selection criterium for candidate sources with magnetic field strength B and radial extension R : $r_{\mathrm{L}} \leq R$, ie. $E \leq E_{\mathrm{max}} \sim 1$ EeV $Z(B/1\mu\mathrm{G})(R/1\mathrm{kpc})$ [50]. Fig. 1.11 shows the so-called *Hillas-plot* where candidate sources are placed in a $B-R$-space, taking into account the typical range of these parameters. Most astrophysical objects do not even reach the iron confinement line up to 10^{20}eV, leaving the best candidates

for UHECR acceleration to be: neutron stars, Active Galactic Nuclei (AGN), Gamma Ray Bursts (GRB), and accretion shocks in the intergalactic medium. In addition to being able to accelerate up to $E_{\max} > 200$ EeV, candidate UHECRs accelerators should have luminosities that can account for the observed fluxes [51].

Gravitational accretion shocks

The accretion of dark matter and gas could produce shocks around the largest structures of the Universe (eg. clusters of galaxies, filaments, ...), where diffusive shock acceleration can happen. For clusters of galaxies, one can estimate the linear extension of the magnetized shock as $\sim 1-10$Mpc and the magnetic field intensity on both sides of the shock to be around 1 μG, which would allow particles to be confined up to $E \sim 10^{20}$eV. Note however, that the strength of the magnetic field upstream of the shock could actually be much lower tha 1 μG, as it was produced out of the weakly magnetic void; thus shock acceleration can occur only if the magnetic field upstream can be strongly amplified. Recently detailed calculations, including energy losses due to interactions of protons with radiative backgrounds demonstrated that for realistic shock speeds of a few thousand km/s and a background magnetic field close to 1μG, the maximum energy achievable by protons cannot exceed a few times 10^{19}eV, due to radiative losses [51].

Active Galactic Nuclei

An AGN is composed of an accretion disk around a central super-massive black hole and is sometimes associated with jets terminating in lobes (or hot spots) which can be detected by radio astronomy. For a black hole of mass $M_{\rm bh} \sim 10^9 M_\odot$, the magnetic field in the central region yields $B \sim 300$ G. Assuming the central region to be of the order $R \sim$100 A.U., particles could be confined up to $E_{\max} \sim 150$ EeV and accelerated to $E \lesssim 10^{20}$eV by electrostatic acceleration in the black hole magnetosphere [51]. The main problem is the large energy loss in the very dense radiation fields in the central region of AGN. The AGN jets are a different possible site of UHECR acceleration. The advantage of the jet site is that the accelerated protons would be injected with the Lorentz factor of the jet, which may easily be of the order of 10 or higher [41]. AGN are often suggested as continuous emitters of UHECRs. However, transient events such as AGN flares more easily meet the UHECR acceleration requirements.

Gamma-ray Bursts

GRBs are brief outbursts of mostly MeV gamma-rays. Their spectra extend to higher energy (up to 20 GeV). The burst duration varies from a fraction of a second to hundreds of seconds. All contemporary GRB models use Lorentz factors of the GRB jets of order 100 to 1000. The explosion of a GRB leads to the formation of multiple shock regions which are potential acceleration zones for UHECRs. The value of the magnetic field at these shocks is estimated to be of the order $B \sim 10^6$ G at a distance $R \sim 10^{12}$ cm from the center. These values are derived for internal shocks that happen before the ejected plasma reaches the interstellar medium, assuming $B \sim 10^{12}$G near the central engine (of size $R \sim 10$ km) and an evolution $B \propto R^{-1}$. The wide green region presented in Fig. 1.11 stems from this dependence: parameters can take different values at different times of the GRB explosion. The flux of gamma-rays reaching the Earth from GRBs is generally comparable to the observed flux of UHECRs, implying a tight energetic requirement for GRBs to be the sources of UHECRs [41, 51].

Neutron Stars

Young millisecond magnetars are neutron stars with extremely strong surface dipole fields of order 10^{15}G. Therefore they easily fulfill the Hillas criterion and can accelerate UHECRs up to EeVs. One model for example suggests that iron ions from the surface of a young neutron star are accelerated by magnetohydrodynamic winds. Magnetars, as GRBs, are transient sources [41, 51].

Exotic models

Instead of accelerating lower energy cosmic ray particles to ultra high energies by confining them in violent acceleration regions like those mentioned above (*bottom-up models*) the particles could also be decay products of very massive X particles with M_X as high as 10^{25}eV (*top-down models*). All top-down models for UHECRs have two distinct features : flat injection spectrum and a particle composition different form the bottom-up acceleration scenarios. In the top-down models the massive X particles decay into a chain of all known elementary particles with nucleons and mesons, of which most then decay into neutrinos, electrons and γ-rays, as final products. As a result the injection fluxes of γ-rays and neutrinos exceed the nucleon fluxes by a factor of about 30, except at energies close to M_X. Examples of top-down models are : topological defects, like magnetic monopoles and cosmic strings, cold dark matter, Z-burst model [41].

1.1.5 Modeling the Cosmic Ray Energy Spectrum

In Section 1.1.3 the general form of the cosmic ray energy spectrum could be understood from the acceleration at the source and their propagation to the Earth. To be able to explain the full details of the observed energy spectrum up to the highest energies, a detailed modeling of the acceleration, propagation (ie. diffusion and spallation) and source distribution in the Galaxy is necessary. The energy region where the contribution to the observed cosmic rays from the Galaxy decreases and the contribution from extra-galactic sources increases is called the transition region. This region provides important constraints for any models that try to explain the cosmic ray sources. In addition, any features larger than statistical fluctuations must be accounted for by the models.

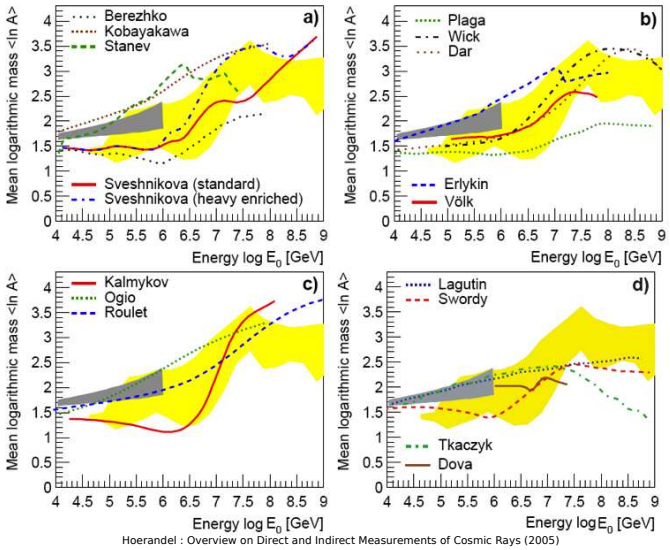

Figure 1.12: The mean logarithmic mass of cosmic rays as a function of their energy for four groups of knee models and data from direct observations (dark grey) and indirect measurements (light grey area). **Top left**: Acceleration in SNRs. **Top right**: Acceleration in GRBs (Wick, Dar and Plaga), the single source model (Erlykin) and reacceleration in the galactic wind (Völk) **Bottom left**: Models where the knee is explained by diffusion in the Galaxy **Bottom right**: Propagation in the Galaxy as well as interaction with background photons (Tkaczyk) and neutrinos (Dova). References to the models can be found in [52, 53].

B. Peters was very surprised about the apparent smoothness of the energy spectrum measured up to 1961. He states : *"One of the most remarkable features of cosmic radiation is presented by the apparently smooth and uniform variation of particle number with energy over a very large energy range. This fact is usually expressed by the statement that a power law with an almost constant exponent represents the energy*

distribution over nine or even ten orders of magnitude. This is not easy to understand." From that observation he concludes that either of the following statements should be true :

1. One single source dominates.
2. Several or many sources contribute comparable amounts. The sources must have **precisely the same energy spectra**.
3. The bulk of particles is contributed by different sets of sources. The strength of the various sets **must be very accurately tuned** to have this smooth power law energy spectrum.

However, it is hard to believe that either condition 2 or 3 could be satisfied over the entire range of observable cosmic ray energies. *"If careful examination of the intensity of the cosmic radiation should reveal no significant localized departures from a power law, it would seem difficult to avoid the conclusion that a single source prevails."* It is important to keep this quote in mind in light of the energy spectrum measurements from the last couple of years and the one that will be presented in this thesis in the last chapter.

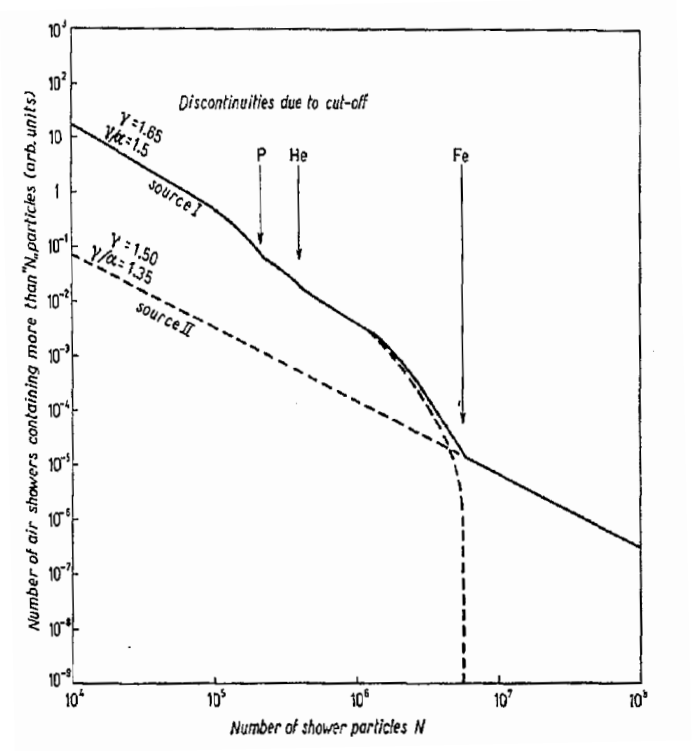

Figure 1.13: The distribution of the number of air showers that contain at least N shower particles (or integral size-frequency distribution which relates to the integral energy spectrum) caused by a dominant source I, which shows discontinuities due to the rigidity dependent cut-off, and which gets dominated by a weaker source II, after the cut-off of Fe from source I [54].

"If such a complex radiation observed at the Earth was subject to a cut-off, and another, much weaker source contributed the bulk of particles above this cut-off, then the differential flux of air showers would not show any gap. The cut-off would occur at a critical magnetic rigidity which means that the energy at which the cut-off takes place will be higher, the higher the charge of the primary nuclei is. Hence, a cut-off in a complex spectrum can never be sharp as long as the quantities observed are functions of primary energy. The energy region in the primary spectrum which is affected by such a cut-off in rigidity will extend over at least a factor of thirty, ie. the energy ratio between iron nuclei and protons which have equal radii of

curvature in interstellar magnetic fields. Another, much weaker source could therefore cut in, in such a way that the differential flux for air showers does not exhibit a break, but only a discontinuity in slope, while the integral energy spectrum remains almost smooth. Nevertheless, one predicts very marked observable effects, when the primary radiation, coming from a source which dominates observations at lower energy, approaches such a critical magnetic rigidity." [54] This is illustrated in Fig. 1.13. Peters was the first to predict a rigidity dependent cut-off as an explanation for breaks in the energy spectrum (the first hints of the knee were observed two years earlier, see Fig. 1.6). This is now referred to as the Peters cycle.

Knee models

Currently, there is still no perfect understanding of what causes the features like the knee, the ankle, and the fine structure in the cosmic ray energy spectrum. There are many models in the literature. Proposed explanations for the knee can be divided into four categories. The first three discuss astrophysical reasons while in the fourth class the knee is attributed to new physics caused by high-energy cosmic ray interactions in the atmosphere. However, this particle physics explanation of the knee is nowadays highly disfavoured, since hadronic interaction models used for the interpretation of cosmic ray data were found to be consistent with particle production measurements from the LHC at 7 TeV center of mass energy, corresponding to a primary cosmic ray energy of $10^{16.4}$ eV [52, 55].

Models in the first category relate the knee to the acceleration process. Differences in the modelling of the injection in the acceleration regime of SNR, the shock physics themselves, accounting for oblique shocks instead of standard parallel shocks all give different explanations for the knee and give rise to different composition predictions. The source distribution could also explain the knee [56]. While in some models a dominant single supernova remnant from a recent and nearby explosion in addition to a background of many undefined sources gives a possible explanation for a sharp knee [57, 58], other models use different types of many supernovae explosions [59], which also predicts a more complicated structure in the energy spectrum, to explain the knee. Reacceleration of cosmic-ray particles in the Galactic wind is another way to extend the maximum energy of galactic cosmic rays up to the ankle, in a rigidity dependent way. The last class of models related to the acceleration process to explain the knee structure are those that propose GRBs as a special case of supernova explosions.

Models of the second category connect the knee with leakage of cosmic rays from the Galaxy. In the leaky box model, as discussed in Section 1.1.3, a diffusive shock acceleration is combined with an energy dependent propagation pathlength. In other models, the knee follows from diffusive propagation through the Galaxy.

Interactions of cosmic rays with background particles in the Galaxy are also considered as the origin of the knee. More detailed discussion and references to these models can be found in [52, 53]. To distinguish between the different models the measurement of the mean logarithmic mass as a function of the cosmic ray energy in the knee region is crucial as illustrated by Fig. 1.12. Currently the experimental accuracy is not good enough to distinguish between the different models and high resolution measurements are needed. This is the main objective of the analysis presented in this thesis.

Most models represent the principal aspects of cosmic-ray acceleration, propagation, or interactions. Most probably, combinations of these basic processes are needed to form a realistic description of the cause of the observed cosmic ray energy spectrum. At present, the experimental results do not allow to select a single approach as the best model. However, within the boundaries given by the experiments, current measurements of energy spectrum and composition are compatible with an interpretation of the knee due to a rigidity dependent leakage of cosmic rays from the Galaxy and/or a rigidity dependent maximum energy of galactic sources [52, 55].

Ankle models

The Universe is observed to be permeated by an isotropic thermal radiation that follows the Planck distribution for black body radiation, with a temperature of 2.7 K. This so-called cosmic microwave back-

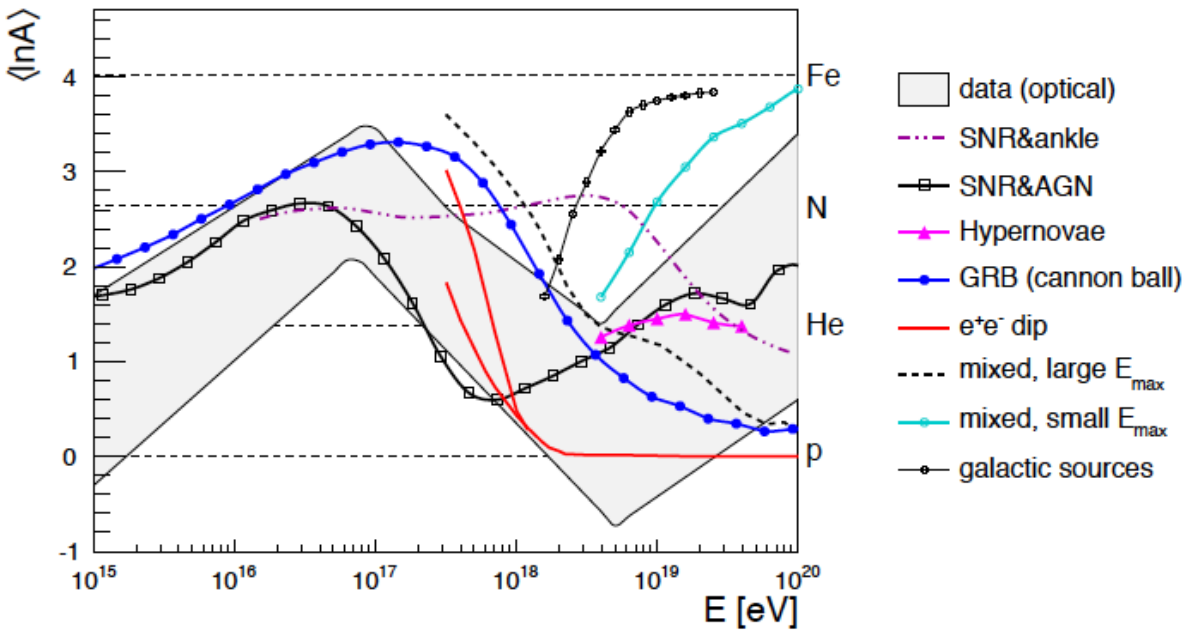

Figure 1.14: Mean logarithmic mass as a function of the cosmic ray energy for different models that try to explain the ankle region from [55] where the references to the different models can be found. The light grey band shows the uncertainty range from a range of experimental data.

ground (CMB) limits the maximum propagation distance for ultra-high energy protons and therefore prevents them from reaching the Earth. Protons interact with the low energy CMB photons and create pions through photohadronic interactions : $p\gamma \rightarrow N + n\pi$ (with N a nucleon and n the number of produced pions). The energy threshold for this interaction for a photon with energy ϵ is $E_{p,\pi}$ ∼200 EeV ($\epsilon_{\rm CMB}/\epsilon$) with $\epsilon_{\rm CMB} \simeq 2.7 k_B T_{\rm CMB} \sim 6 \times 10^{-4}$eV, the mean energy of a CMB photon. At slightly lower energy cosmic rays interact with infrared, optical and ultraviolet background photons through electron- positron pair production, also called Bethe-Heitler process : $p\gamma \rightarrow pe^+e^-$, with an energy threshold of $E_{p,ee}$ ∼0.8 EeV ($\epsilon_{\rm CMB}/\epsilon$) [51]. This could explain the so-called second knee.

There are three main classes of models that try to explain the origin of the ankle. The classic models assume that the transition from galactic to extragalactic cosmic rays occurs at the flat part of the observed spectrum in the energy interval $E^{trans} \sim (3-10)$ EeV. The transition energy is given by the intersection of a flat extragalactic spectrum and a very steep galactic one. In the majority of the classic ankle models the extragalactic component is assumed to be pure proton, while the galactic one should be naturally represented by iron nuclei at energies above the iron knee. These models predict a transition from an iron-dominated composition to a proton-dominated one at the ankle energy.

In the mixed composition model it is assumed that the extragalactic component consists of nuclei of various types. Thus a transition occurs here from iron to lighter nuclei of mixed composition; it can occur at the ankle or near it. One example is the *disappointing model* [60], which assumes a rigidity dependent acceleration ($E_i^{max} = Z_i E_p^{max}$ in the extragalactic sources. This model is called disappointing because of the lack of many signatures predicted in proton-dominated models, such as cosmogenic (GZK) neutrino production and correlation of CR arrival directions with distant sources. It is also disappointing because the end of the spectrum would correspond to the highest energy to which cosmic-ray acceleration is possible, rather than the GZK effect.

In the dip model the transition begins at the second knee and is completed at the beginning of the dip, at $E \approx 1$ EeV. The ankle in this model appears as an intrinsic part of the dip. Like in the classic ankle model, the transition here also occurs as an intersection of the flat extragalactic component with a steep

galactic spectrum. In contrast to the classic ankle and mixed composition models, the dip model predicts an almost pure proton composition above $E \approx 1$ EeV and a pure iron composition below this energy. The extragalactic proton assumption is confirmed by the observation of the pair-production dip, from the energy loss process by e^+e^--pair production due to the interaction of extragalactic protons with the CMB photons $p + \gamma_{CMB} \rightarrow p + e^+ + e^-$, in the energy range (1 - 40 EeV) and the beginning of the GZK cutoff in the energy range (40-100 EeV). Both features are consistent with of a proton dominated spectrum [61].

In Fig. 1.14 the mean log mass for those ankle models are shown [55]. For the classic models, they are combined with a galactic component from SNR. Additionally shown is the GRB cannonball model, discussed in the previous section. Another source plotted in Fig. 1.14 that potentially has enough energy to accelerate intermediate mass or heavy nuclei to ultra-high energies is hypernova remnants [62], like SN1998bw which is associated with GRB980425.

Matching galactic and extragalactic contributions in the transition region

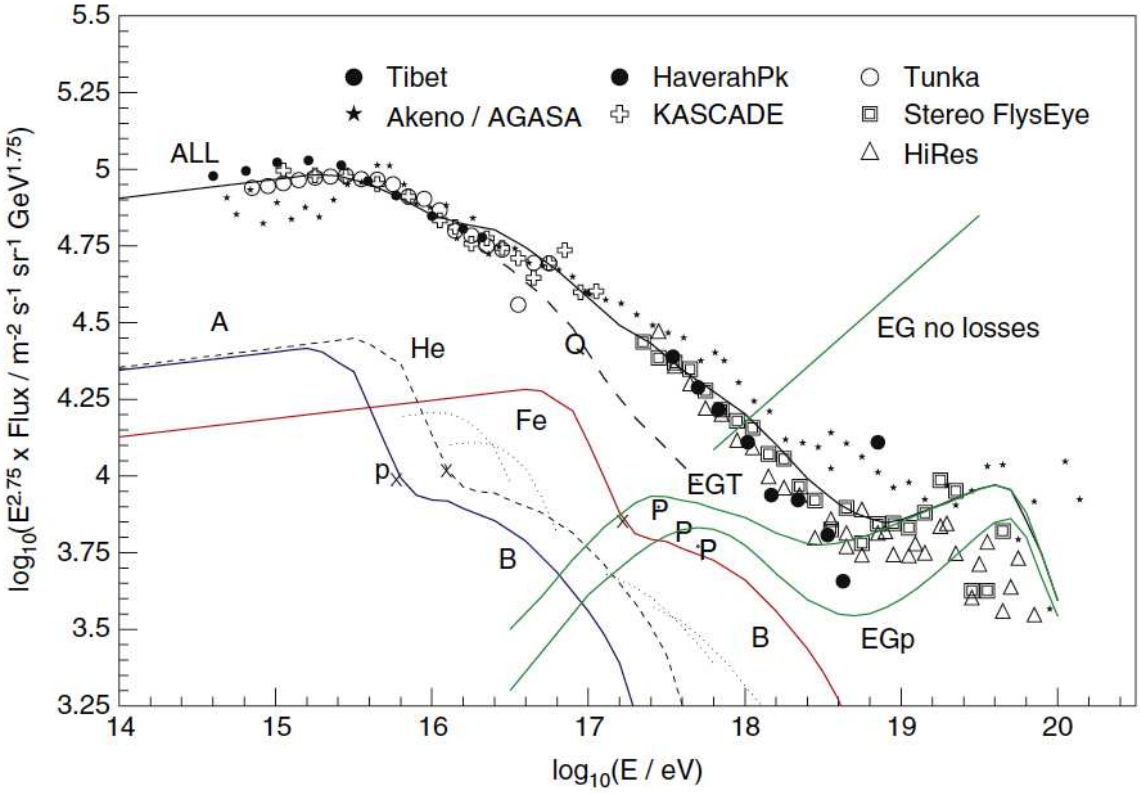

Figure 1.15: The cosmic ray energy spectrum weighted by $E^{2.75}$ for different experiments and compared with the Hillas model from [31], with a SNR component "A" with the same rigidity dependence for five mass groups (H, He, CNO, Ne-S and Fe) and extra-galactic H+He (EGT). The dashed line Q is the total energy spectrum without an extra galactic component "B".

The biggest challenge is to merge the appropriate knee and ankle models to be able to describe the smooth energy spectrum from the knee region through the transition region up to and beyond the ankle, as well as to explain the measured composition. Hillas based his model on the first unfolding results from the KASCADE experiment that hinted a rigidity-dependent cutoff. Fig. 1.15 shows his attempted decomposition of the all-particle spectrum into three parts. Component 'A' is a uniform (same shape for all nuclei) spectrum in rigidity, $R^{-2.69}$, consistent with the expectations of a simple shock acceleration model, where the knee represents the end of the spectrum of cosmic rays accelerated by supernova remnants in the Milky Way. At

the highest energies there is an extragalactic component, for which he used the dip model with a pure proton component (EGp) or proton+Helium (EGT). The galactic 'A' component, combined with the extragalactic component EGT, gives dashed line 'Q', which falls below the observed total flux. Therefore he suggested that an additional component 'B' is needed at several times 10^{17}eV, as the iron from component 'A' cuts off before the extragalactic component kicks in. The lines (B) result from the assumption that the additional galactic component still has the same rigidity dependence and relative numbers of nuclei as component 'A'. The main question is now which sources and galactic acceleration mechanisms can explain this necessary component [31].

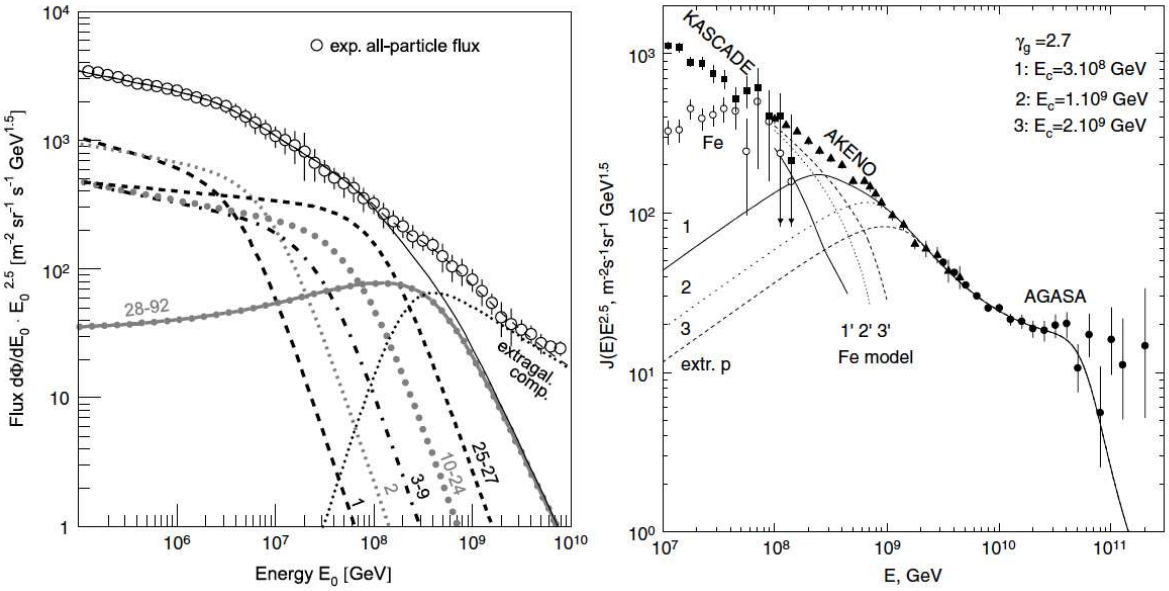

Figure 1.16: **Left**: The poly-gonato model from [63] with the different contributions of the atomic elements shown as dashed lines. **Right**: Berezinsky's model [64] where the extragalactic component is extended to lower energies with different critical energies E_c.

Another possibility to match the all-particle flux is a significant contribution of ultra-heavy elements (26< Z <92) at energies around 4·10^{17}eV as illustrated on the left of Fig. 1.16. The figure shows spectra for elemental groups with nuclear charge numbers as indicated, derived from direct and indirect measurements according to the phenomenological poly-gonato model [63]. In this approach the 'B' component as referred to by Hillas is caused by the fall-off of the heaviest elements with Z up to 92 and hence just the heavy element rigidity dependent cut-off from component 'A'. In this scenario a significant extragalactic contribution is required at energies E$\geq 4 \cdot 10^{17}$ eV. On the right of Fig. 1.16 Berezinsky's model [64] is shown. Instead of extending component 'A' as the poly-gonato model does with ultraheavy elements, Berezinsky extends the extragalactic component to lower energies to match the rigidity dependent galactic spectrum. He uses the dip model for the extra-galactic component as Hillas, but enhanced at lower energies to match the galactic iron. Assuming a power law injection spectrum with a spectral index $\gamma = -2.7$ (without cosmological source evolution) and -2.4 (with cosmological source evolution), the spectrum can be described for $E > 10^{17.5}$eV with a proton-dominated composition. This matches the data from several experiments (AGASA, HiRes, Yakutsk) quite well after energy rescaling. Below a characteristic energy $E_c \approx 1 \cdot 10^{18}$eV the spectrum flattens and the steeper galactic spectrum becomes dominant at $E < E_c$. The transition energy approximately coincides with the position of the observed second knee. The critical energy E_c is determined by the energy where adiabatic and pair-production energy losses are equal [65].

Fig. 1.17 shows an example of a model that finetuned both galactic and extragalactic components to try to match the observed data [66]. For the galactic component they assumed a smoothed distribution of Galactic

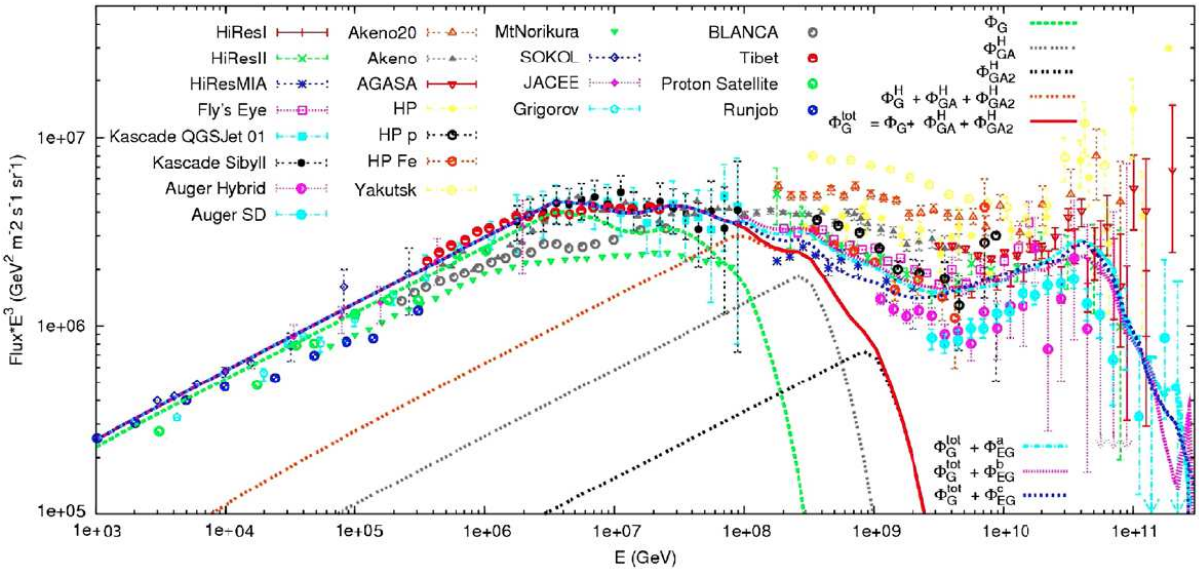

Figure 1.17: The model from [66] that tried to fine-tune both galactic and extra-galactic components to fit the spectrum. Two additional galactic component ϕ_{GA1} and ϕ_{GA2} are needed to prevent discontinuities, which are not observed, to appear in the spectrum. As extra-galactic component the mixed-composition model is used here.

SNRs, in which the acceleration depends on particle rigidity and therefore, that a maximum achievable rigidity ρ_0 exists which is the same for any nucleus. Thus the spectrum injected into the interstellar medium is a single power law up to this maximum rigidity, followed by an exponential cut-off. Propagation in the interstellar medium is treated numerically. The cut-off rigidity is chosen in such a way that the total spectrum of all nuclei combined reproduces the position of the first knee observed by Kascade at ~ 5 PeV. The calculated main Galactic spectrum from SNRs is then combined with a proton or a mixed composition extragalactic model. Difference source evolution scenarios are taken into account (a : strong-evolution, b : SFR model, c : uniform source distribution model). From the Galactic side, the free parameters of the fitting procedure are the normalization of the low energy abundance of the medium and heavy nuclei with respect to protons, somehow reflecting uncertainties in efficiency of low-energy injection of nuclei at the acceleration mechanism, and the scale of the exponential cut-off above ρ_0. When trying to match the galactic and extragalactic spectra, they made the same observation as Hillas, namely that there was a flux deficit above 10^8 GeV which can only be solved by the introduction of an additional Galactic component. For the proton extragalactic they only needed one additional Galactic component, but could not find a smooth match at 10^8GeV. Some discontinuity or wiggle seems unavoidable, due to the fact that the extragalactic spectrum should have a rather abrupt low-energy cut-off. As this discontinuity is not possible, they preferred the mixed composition extragalactic component, as shown in Fig. 1.17 , but they needed two additional Galactic components to match both spectra. These components have the same shape, and possibly conceptually a similar origin, as the main diffuse Galactic spectrum. This means that Galactic accelerators should exists with higher maximum energies [66].

The three-population picture introduced by Hillas is also implemented in the *H3a* and *H4a* model by assuming that each of the three components j contains five groups of nuclei (H, He, CNO, Mg-Si and Fe) and cuts off exponentially at a characteric rigidity $R_{c,j}$. Thus the all-particle spectrum is given by

$$\frac{\mathrm{d}\,N}{\mathrm{d}\log E} = E\frac{\mathrm{d}\,N}{\mathrm{d}\,E} = \phi_i(E) = \sum_{j=1}^{3} a_{i,j} E^{-\gamma_{i,j}} \exp\left[-\frac{E}{Z_i R_{c,j}}\right], \tag{1.14}$$

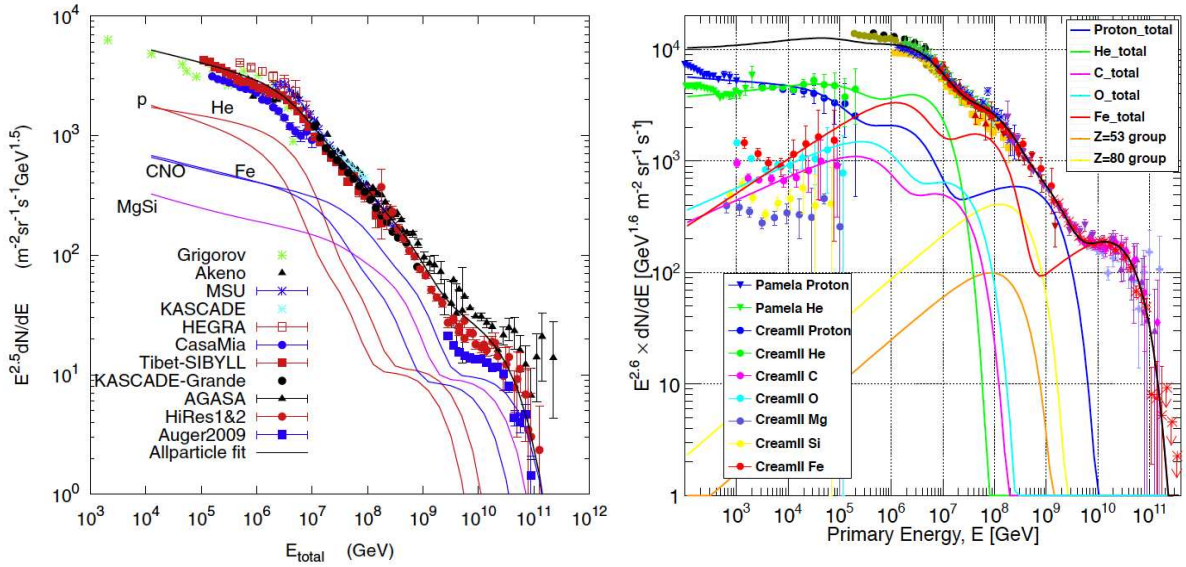

Figure 1.18: **Left**: The H4a model from [67] compared to experimental data plotted as an $E^{2.5}$ weighted energy spectrum. The individual contributions from each of the five mass groups are shown additionally. **Right**: A slightly different fit is done in the GST model from [68]. The individual components are fit to the recent CREAM-II and PAMELA data at low energy.

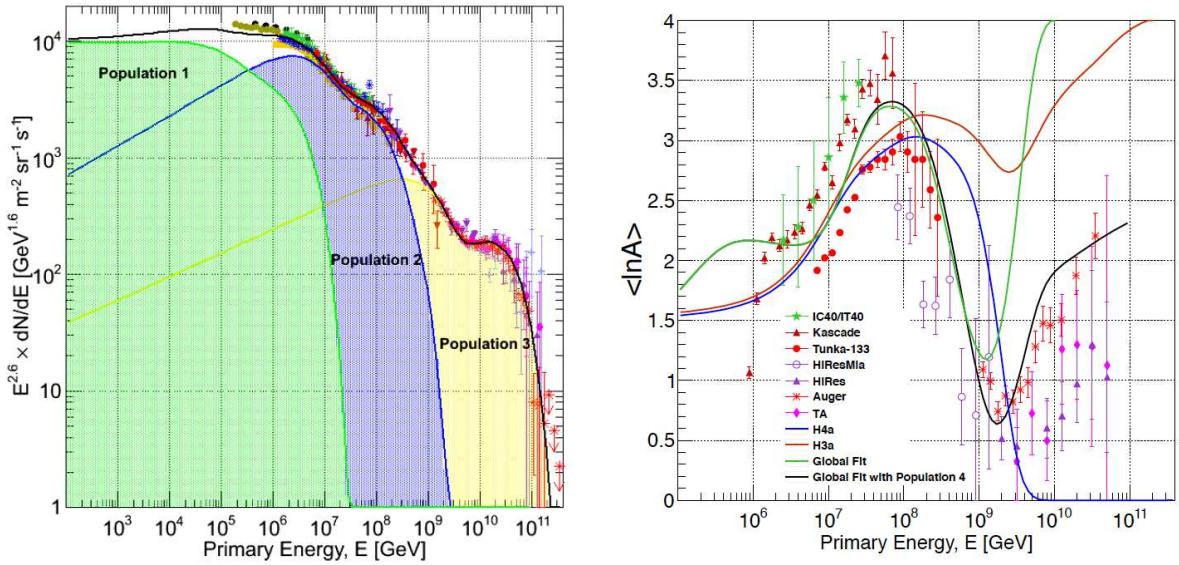

Figure 1.19: **Left**: The contributions of the three populations in the GST model [68] to the total energy spectrum. **Right**: The mean logarithmic mass for a set of recent experimental data compared to the H3a and H4a model from [67] and the GST model [68].

with the spectral indices for each group and normalizations given by Table 1.1. The parameters for Population 1 are from the measurements by the CREAM experiments, which are extrapolated to a rigidity of 4 PV to describe the knee. Another noteworthy feature is the possibility illustrated in this fit of explaining the ankle as a Peters cycle containing only protons and iron, which is an example of the disappointing model, mentioned in Section 1.1.5, of the end fo the cosmic-ray spectrum.

The fitresult for the H4a model (with pure proton for extragalactic component) is shown on the left plot

in Fig. 1.18 [67], while the mean log mass is shown on the right plot of Fig. 1.19.

	p	He	CNO	Mg-Si	Fe
Pop. 1 :	7800	3550	2200	1430	2110
R_c = 4 PV	1.66	1.58	1.63	1.67	1.63
Pop. 2 :	20	20	13.4	13.4	13.4
R_c = 30 PV	1.4	1.4	1.4	1.4	1.4
Pop. 3 (H3a) :	1.7	1.7	1.14	1.14	1.14
R_c = 2 EV	1.4	1.4	1.4	1.4	1.4
Pop. 3 (H4a) :	200				
R_c = 60 EV	1.6				

Table 1.1: Parameters from the H4a fit.

An alternative picture is given by [68], which uses the same three population fit as Eq. 1.14, but with qualitatively different parameters, as given by Table 1.2. In particular, the first population has a much lower cutoff of R_c = 120 TV, related to the significantly harder spectra assumed for the first population. Each component in the first population is fitted only above R_c = 200 GV, after the spectra hardening noted by the CREAM and PAMELA experiment. With these harder spectra, compared to the H3a and H4a fits, the heavy components cannot be extended past the knee region. It is interesting to note that $R_c \approx$100TV is the classical result for the expected maximum energy of SNR expanding into the interstellar medium with an un-amplified magnetic field a few μG, as discussed in Section 1.1.3. The spectra of this *GST* fit are shown on the right plot of Fig. 1.18 from below the knee to the ankle. The contributions of individual elements are shown, as well as the spectra of nuclei from CREAM and PAMELA. The bump in the energy spectrum around 10^{17}eV corresponds with an *iron knee* as reported by KASCADE-Grande and GAMMA. Also interesting to note is the contribution of heavy elements ($26 > Z > 82$) in the second population alone to smoothen the transition with the proton component of the third population. On the left plot of Fig. 1.19 the contributions of each population to the total spectrum are shown. The mean log mass of this model is shown on the right plot of Fig. 1.19, where a version of this global fit with an additional fourth population is also shown, which accomodates for the composition measured by the Auger experiment.

	p	He	C	O	Fe	$50 < Z < 56$	$78 < Z < 82$
Pop. 1 :	7000	3200	100	130	60		
R_c = 120 TV	1.66	1.58	1.4	1.4	1.3		
Pop. 2 :	150	65	6	7	2.3	0.1	0.4
R_c = 4 PV	1.4	1.3	1.3	1.3	1.2	1.2	1.2
Pop. 3 :	14				0.025		
R_c = 1.3 EV	1.4				1.2		
Pop. 2 :	150	65	6	7	2.1	0.1	0.53
R_c = 4 PV	1.4	1.3	1.3	1.3	1.2	1.2	1.2
Pop. 3 :	12				0.011		
R_c = 1.5 EV	1.4				1.2		
Pop. 4 :	1.2						
R_c = 40 EV	1.4						

Table 1.2: Parameters from the GST fit.

Most models mentioned above shown the need for a second Galactic component, the *B component* as introduced by Hillas. In [66], they claim that few or even a single source could be responsible for this component. In [59] numerical simulatations of cosmic ray acceleration for four types of supernova remnants, which constitute 90 percent of all supernovae, are performed. The obtained source spectra are shown in the inlay of Fig. 1.20. It shows that about 1/3 of supernova explosion kinetic energy E goes to cosmic rays, which is in agreement with the empirical model of cosmic rays. After treating the cosmic ray propagation in the leaky-box approximation, they obtained the solid line from Fig. 1.20 for the combined spectrum of protons and ions. It was assumed that the charge composition of accelerated particles was the same in all SNRs except that the highest-energy part of the spectrum produced by Type Ib/c supernovae at pc/Z $> 10^5$

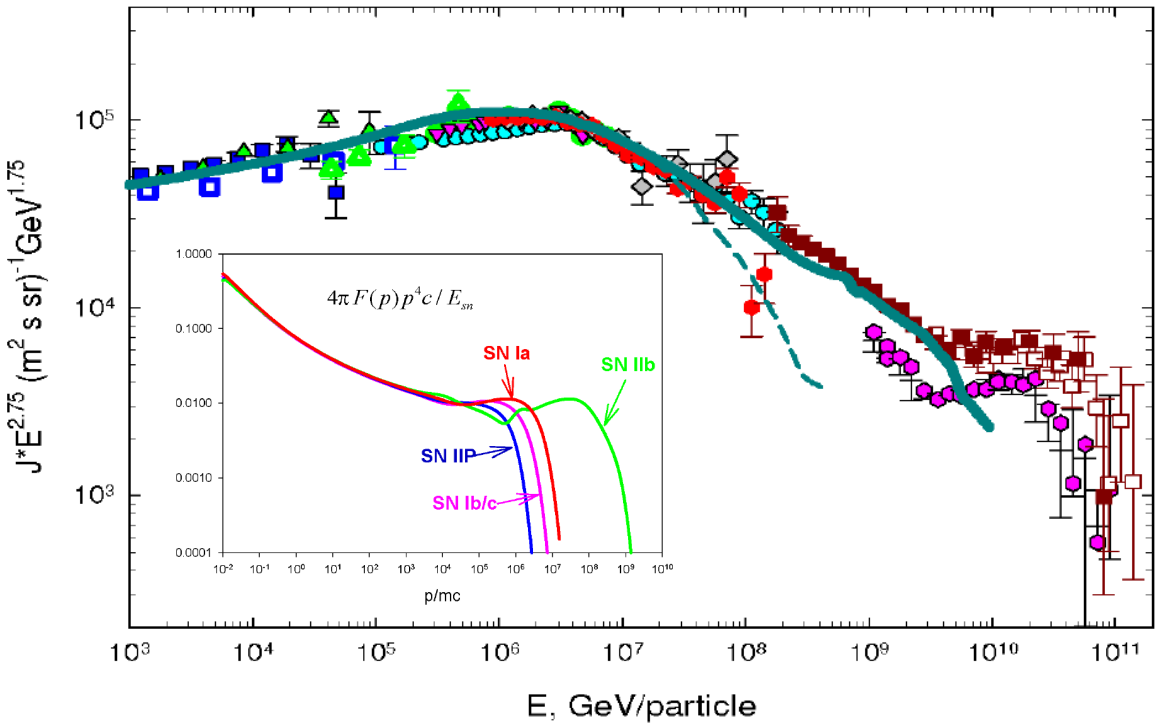

Figure 1.20: The inlay shows the source spectra produced by different types of supernovae in the assumption that the accelerated particles are protons. The resulting energy spectrum based on a combination of different types of SNRs is shown as the thick solid line [59].

GeV had no hydrogen. Only a tiny ratio ($\sim$ 3%) of supernova remnants with a small ejected mass, a large shock velocity, a high kinetic energy of ejecta (as IIb remnants) can provide the region of all particles' spectra around 10^{17-18}eV. In this model both the knee and the transition region are naturally explained by a combination of different types of SNR. The dominant contribution of a few nearby sources to explain the knee and the transition region is discussed in [69], where Vela Junior (also called RX J0852.0-4622 or G266.21.2) is found to be the only single source suited to explain the knee, and Cas A, considered as a Type IIb SNR, as best candidate for the region $10^{17} - 5 \cdot 10^{18}$eV.

Discussion

The energy spectrum predictions of all models mentioned above are very similar for the all particle spectrum, but as shown in Fig. 1.12 the mean log mass spectra are quite different. Even more different are the individual energy spectra for the light, medium and heavy mass groups. Therefore a combined high resolution measurement of these three properties will put the strongest constraints on the models and will be crucial for our understanding of the true nature of cosmic rays. This is the main goal/motivation for the analysis performed in this thesis.

1.2 Extensive Air Showers

The development of the coincidence approach in the late 1920s, early 1930s by Walter Bothe and later by Bruno Rossi was crucial for the discovery and study of extensive air showers. By setting up Geiger-Müller counters in coincidence, one could detect particles passing through both counters. Inspired by previous ex-

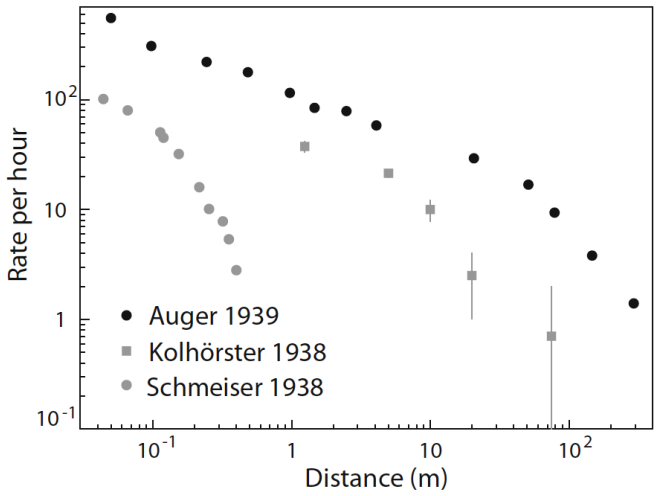

Figure 1.21: Decoherence curves measured with Geiger counters separated up to 300 m distance from [70]. The measurements of Schmeiser were done at sea level with counters with different effective area, while the measurement from Auger was done at the Jungfraujoch at an altitude of 3450 m.

periments by Bothe and Kohlhörster, Rossi observed a rapid increase of triple coincidences in a triangular arrangement of Geiger-Müller counters when an increasing amount of lead (centimeters) was placed above [71]. Only with further increasing absorber thickness, the coincidence rate start to decline ("*Rossi's transition curve*") Rossi concluded that soft secondary particles were produced by cosmic particles entering the material. These secondary particles then suffer increasing absorption with increasing total thickness of the absorber. The same basic observation was made a year later by Regener and Potzer [72] when studying the vertical intensity of cosmic rays in the stratosphere up to a height of 28 km by recording the rate of threefold coincidences. They observed an unexpected clear maximum in the coincidence rate at about 14 km above sea level. Regener interpreted the maximum as being due to the multiplication of electrons in the atmosphere.

Schmeiser and Bothe pointed out that Rossi's transition curve implied the occurrence of showers in air – which they named "*Luftschauer*" – and showed that particles in air showers had separations up to 40 cm [73]. Independently, Kolhörster *et al.* [74] reported data on the rate at which coincidences between a pair of Geiger counters fell as function of separation. The results of these pioneering measurements are shown in Fig. 1.21. Rossi however already made the same discovery in 1934, when he noted that there was a correlated arrival of particles at widely-separated detectors [75]. A couple years later, Auger and his collaborators [76] who were later credited for their discovery of extensive air showers (and the others forgotten) performed measurements at the Jungfraujoch (3500 m) in the Swiss Alps with improved coincidence circuits. They were able to separate their detectors by up to 300 m. Their measurement is also shown in Fig. 1.21. Their major achievement however was that they were able to estimate the primary energy to be around 10^{15} eV for coincidences at 300 m, based on the number of particles in the showers [70]. Auger concluded : "*It seems natural to suppose that they represent the end effects of the showers that they primary particles, probably electrons, which enter the high atmosphere, produced there. If this is the case, we should be able to recognize it by the existence of a "coherence" of these shower particles, the multiple effects of a single initial particle remaining bound in time and space. We have shown the existence of these extensive air showers...*"[76].

1.2.1 Air Shower Physics

The development of an air shower can be illustrated by comparing both plots in Fig. 1.22. On the left, a cloud chamber picture of a shower created in lead plates by a cosmic ray proton of about 10 GeV is shown [77]. The cross-sectional area of the cloud chamber is 0.5×0.3 m^2 and the lead absorbers have a thickness

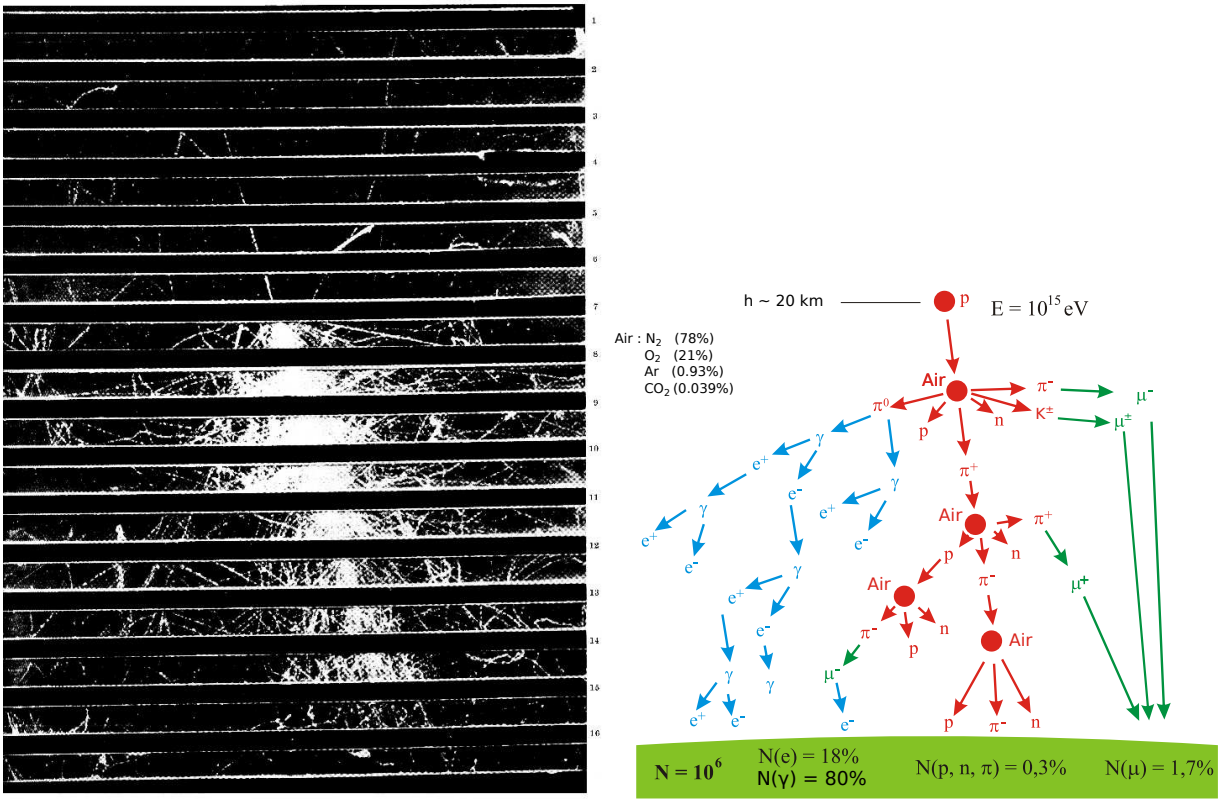

Figure 1.22: **Left** : image of a particle cascade as seen in a cloud chamber at 3027 m altitude. The primary particle is estimated to be a 10 GeV proton. **Right**: Schematic of PeV proton extensive air shower. The proton interacts with an air nucleus at about 20 km and creates an electromagnetic component (blue), a hadronic component (red) and a muonic component (green).

of 13 mm each. Except for the scale, most typical features of an extensive air shower are visible. When a high-energy particle (eg. a PeV proton) enters the atmosphere (which exists of 78% N_2, 21% O_2, 0.93% Ar, 0.039% CO_2, and smaller fractions of other gases) it will interact with an air nucleus. The proton-air cross-section (see Fig. 3.3) for a 1 PeV proton is 380 mb, which gives an average interaction height of 20 km at South Pole (because $\lambda_{\rm int}[{\rm cm}] = \frac{m_{\rm air}}{\sigma_{\rm int}}\rho$). This interaction can be represented as

$$p + A \rightarrow p + X + \pi^{\pm,0} + K^{\pm,0} \cdots , \tag{1.15}$$

with X representing the fragmented nucleus and charge and all other quantum numbers conserved. The proton in the exit channel is called the leading particle, typically carrying about 50% (its inelasticitiy) of the incoming energy. The generated particles from the interaction of the primary cosmic ray will further propagate through the atmosphere and depending on the density of the atmosphere, the type of particle and its cross-sections will either interact again or decay.

High energy electrons will emit Bremsstrahlungs photons and π^0's will decay immediately to 2 photons. The high energy photons will form an e^+e^--pair through pair production, which will again emit lower energy photons. This dominant shower component is called the electromagnetic component and creates a huge amount of low energy electrons, positrons and photons at ground level.

The hadronic component is formed by the chain of interactions of (secondary) protons, neutrons and pions with air nuclei, creating fragmented nuclei and more lower energy protons, neutrons, pions and kaons. If the

pions, kaons (and hyperons) decay, they will form the muonic component through the following processes :

$$\pi^{\pm} \rightarrow \mu^{\pm}\overset{(-)}{\nu_{\mu}} \qquad \text{(BR.: } 99.98770 \pm 0.00004\%\text{)} \tag{1.16}$$

$$K^{\pm} \rightarrow \mu^{\pm}\overset{(-)}{\nu_{\mu}} \qquad \text{(BR.: } 63.55 \pm 0.11\%\text{)} \tag{1.17}$$

The cross-section for the creation of kaons and hyperons in proton-air collisions are down by a factor of around 10, at least at energies up to $\sim 10^{15}$eV [78].

At ground level the secondary particles are dominated by photons ($\sim$80%) and electrons ($\sim$18%) with a small fraction of muons ($\sim$1.7%) and very small fraction of hadrons ($\sim$0.3%). The main challenge is to identify the nature and to determine the energy of the particle that initiated the shower. Assumptions have to made on where the particle the particle had its first interaction and what the features of the hadronic interactions are. Key parameters such as the cross-sections for the interactions of protons (and heavier) nuclei) with nuclei, pion-nucleus cross-sections (see Fig. 1.23), the fraction of energy radiated as pions in each collision and the number of particles produced are needed [70]. This will be done through Monte Carlo simulations, described in Chapter 3.

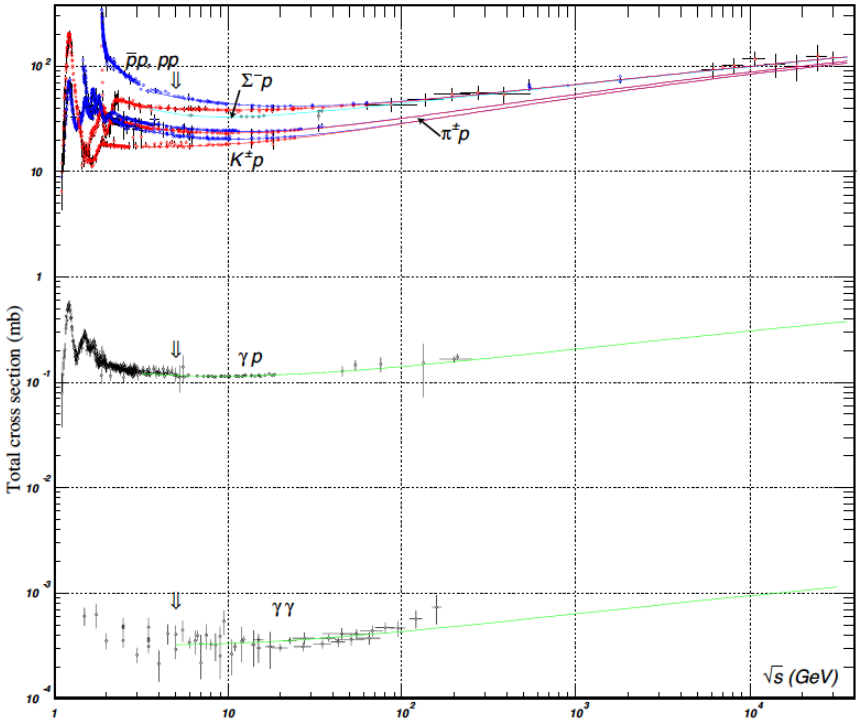

Figure 1.23: Proton-proton cross-section..

Electromagnetic cascades

The idea of cascade development and the most important features of an electromagnetic (EM) shower can be illustrated by the toy model, called the Heitler model [80] but originally introduced by Carlson and Oppenheimer [81]. In this model, only one particle of energy E is considered, which interacts after travelling an interaction length λ_e. Two new particles are created by the interaction, each carrying an energy $E/2$. This could represent $e^{\pm}$ pair production of an initial photon or Bremsstrahlung emission of a photon by an initial electron or positron. A schematic of such a cascade model is shown in the left plot in Fig. 1.24. After one generation or interaction, the cascade consists of 2 particles. After two generations, the cascade consists of 2^2 particles, each with energy $E/2^2$. At depth $X = n\lambda_e$, the cascade consists of $N(X) = 2^n = 2^{X/\lambda_e}$

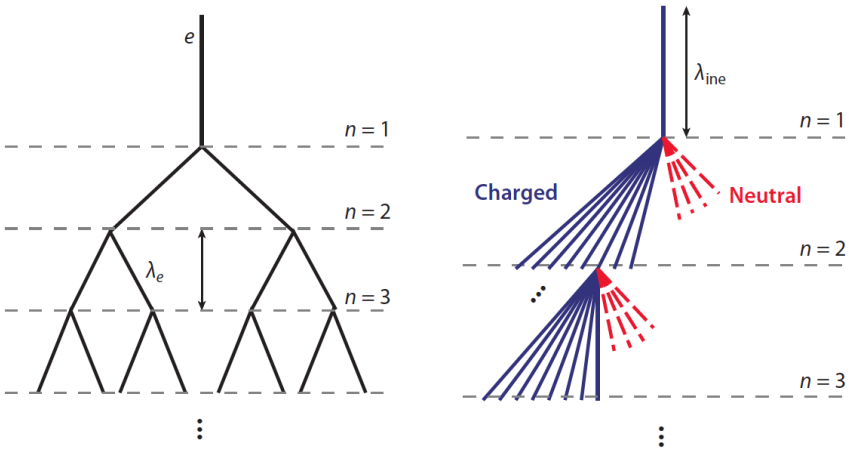

Figure 1.24: Simplified cascade model of an air shower [79]. On the left : an electromagnetic cascade. On the right : the hadronic component of a hadron-induced shower. Onlye one charged hadron interaction is shown for each generation.

particles with energy $E(X) = E_0/N(X) = E_0/2^{X/\lambda_e}$, with E_0 the energy of the initial particle (at generation 0). The particle-multiplication process continues until the ionization energy loss dominates over the radiative losses, and hence the interaction cross-section will be zero. The energy at which ionization energy loss equals Bremsstrahlungs energy loss, is called the critical energy E_c and is 86 MeV for electrons in air. Therefore the number of particles in the shower reaches the maximum at $E = E_c$, which gives :

$$N_{\max} = N(X_{\max}) = \frac{E_0}{E_c} \quad \text{and} \quad X_{\max} = \lambda_e \frac{\log(E_0/E_c)}{\log 2}. \tag{1.18}$$

Although the model is extremely simple, it describes qualitatively correctly the shower development of electromagnetic as well as of hadronic showers up to the maximum of shower development. The number of shower particles at shower maximum $N_{\max}$ is always proportional to the primary energy E_0 and the depth of shower maximum $X_{\max}$ is proportional to the logarithm of the primary energy [32, 41, 79].

The mathematically correct treatment of cascading is the solution of a set of coupled transport equations (similar as for propagation of cosmic rays discussed in Section 1.1.3), which means including particle loss and particle production terms. The basic equation for particle fluxes of type j at atmospheric depth X is:

$$\frac{\mathrm{d}\, F_j(E,X)}{\mathrm{d}\, X} = -\left(\frac{1}{\lambda_j} + \frac{1}{d_j}\right) F_j(E,X) + \sum_i \int \frac{g_{ij}(E_i,E_j)}{E_i} \frac{F_i(E_i)}{\lambda_i}\, \mathrm{d}\, E_i, \tag{1.19}$$

where λ_j is the mean free path for inelastic interactions of a particle of type j and d_j its decay length. The mean free path $\lambda_j = A/(N_A \sigma_j)$, with N_A the number of nuclei with mass A and σ_j the interaction cross-section. The decay length d_j for zenith angles θ below 60° is defined as :

$$\frac{1}{d_j} = \frac{\epsilon_j}{EX\cos\theta}, \tag{1.20}$$

where ϵ_j is the critical energy at which the interaction probability in the atmosphere equals the decay probability. Particle with energies below ϵ_j will more likely decay, while they will more likely interact if their energy is above ϵ_j. The second term in Eq.1.19 is the source term, which sums over the production of secondary particles j with energy E_j by particles i with energy E_i. These coupled are of course valid for both

hadronic and electromagnetic cascades. For electromagnetic cascades these can be written more explicitly to :

$$\begin{cases} \dfrac{\mathrm{d}\,\gamma}{\mathrm{d}\,X} = -\dfrac{\gamma(W,X)}{\lambda_{\mathrm{pair}}} + \displaystyle\int_W^\infty e^{\pm}(E',X)\frac{\mathrm{d}\,n_{e\to\gamma}}{\mathrm{d}\,W\,\mathrm{d}\,X}\,\mathrm{d}\,E' \\ \dfrac{\mathrm{d}\,e^{\pm}}{\mathrm{d}\,X} = -\dfrac{e^{\pm}(E,X)}{\lambda_{\mathrm{Brems}}} + \displaystyle\int_E^\infty e^{\pm}(E',X)\frac{\mathrm{d}\,n_{e\to e}}{\mathrm{d}\,E\,\mathrm{d}\,X}\,\mathrm{d}\,E' + 2\int_E^\infty \gamma(W',X)\frac{\mathrm{d}\,n_{\gamma\to e}}{\mathrm{d}\,E\,\mathrm{d}\,X}\,\mathrm{d}\,W', \end{cases} \tag{1.21}$$

where $\gamma(W,X)\,\mathrm{d}\,W$ is the number of photons in $\mathrm{d}\,W$ at depth X and $e^{\pm}(E,X)\,\mathrm{d}\,E$ is the number of $e^{\pm}$ in $\mathrm{d}\,E$ at depth X [32, 41].

Hadronic cascades

For hadronic showers the Heitler model can be generalized [82] to understand the basic properties. This is illustrated on the right plot of Fig. 1.24. The interaction of a hadron with energy E produces n_{ch} charged particles ($\pi^{\pm}$) and 1/2 n_{ch} neutral particles (π^0), each with energy E/n_{tot}. Neutral particles decay immediately to photons ($\pi^0 \to \gamma\gamma$), initiating electromagnetic showers. The charged particles travel another distance λ_{ine}, the interaction length of strongly interacting particles (for pions in air, $\lambda_{\mathrm{ine}} \approx$120 g/cm^2), and interact again with air nuclei. This process continues until the energy of the charged particles falls below the typical decay energy E_{dec}, where they then are all assumed to decay and produce one muon per hadron.

In each hadronic interaction, one-third of the energy is transferred via π^0 decay to the EM shower component. After n generations, the energies in the hadronic and EM components are :

$$E_{\mathrm{had}} = \left(\frac{2}{3}\right)^n E_0 \qquad \text{and} \qquad E_{\mathrm{EM}} = \left[1 - \left(\frac{2}{3}\right)^n\right] E_0. \tag{1.22}$$

The depth of the shower maximum of a hadronic cascade is determined by the EM particles which outnumber all the other contributions. The first interaction yields $\frac{1}{2}n_{\mathrm{ch}}\pi^0 \to n_{\mathrm{ch}}$ photons. Each photon initiates an EM shower of energy $E_0/(3n_{\mathrm{ch}})$. Considering only the EM subshowers produced in the first hadronic interaction we get :

$$\begin{aligned} X_{\mathrm{max}}^{(\mathrm{had})}(E_0) &\approx \lambda_{\mathrm{ine}} + X_{\mathrm{max}}^{(\mathrm{EM})}[E_0/(3n_{\mathrm{ch}}] \\ &\approx \lambda_{\mathrm{ine}} + \lambda_e \frac{\log[E_0/(3n_{\mathrm{ch}}E_c)]}{\log 2}. \end{aligned} \tag{1.23}$$

Using only the first interaction will certainly underestimate $X_{\mathrm{max}}^{(\mathrm{had})}(E_0)$, but the structure of Eq.1.23 will not change when including higher hadronic interactions.

The number of electrons at shower maximum of a hadronic shower corresponds to that of an EM shower with reduced energy E_{EM}. To calculate the muon multiplicity, the energy at which a hadron decays to a muon needs to be calculated first :

$$E_{\mathrm{had}} = \frac{E_0}{(n_{\mathrm{tot}})^n} = \frac{E_0}{(\frac{3}{2}n_{\mathrm{ch}})^n} \tag{1.24}$$

$$E_{\mathrm{dec}} = \frac{E_0}{(\frac{3}{2}n_{\mathrm{ch}})^{n_c}} \tag{1.25}$$

$$\Rightarrow n_c = \frac{\log(E_0/E_{\mathrm{dec}})}{\log(\frac{3}{2}n_{\mathrm{ch}})} \tag{1.26}$$

The number of muons follows from that of the charged hadrons, $N_\mu = N_\pi = (n_{\rm ch})^n$:

$$\log N_\mu = \log N_\pi = n_c \log n_{\rm ch} = \beta \log(E_0/E_{\rm dec}) \quad \text{with } \beta = \frac{\log n_{\rm ch}}{\log(\frac{3}{2} n_{\rm ch})} \tag{1.27}$$

$$\Rightarrow N_\mu = \left(\frac{E_0}{E_{\rm dec}}\right)^\beta, \tag{1.28}$$

for $n_{\rm ch} \approx 10 - 100$, $\beta = 0.85 - 0.92$. The number of muons produced in an air shower depends on primary energy, the air density (through $E_{\rm dec}$), and the charged and total particle multiplicities of hadronic interactions (through β). However, the parameters $E_{\rm dec}$ and $n_{\rm ch}$ are effective parameters only in this simplified model and must be obtained from detailed simulations [82, 79].

Because the binding energy of ∼5 MeV per nucleon is smaller than the typical interaction energies, one can consider a nucleus of mass A as a superposition of A independent nucleons with an energy E_0/A. Applying this *superposition model* in the Heitler-Matthews model, the shower maximum and muon multiplicity of nucleus-induced showers can be deduced :

$$N^{\rm (A)}_{\rm EM,max}(E_0) = A \cdot N^{\rm (p)}_{\rm EM,max}(E_0/A) \approx N^{\rm (p)}_{\rm EM,max}(E_0) \tag{1.29}$$

$$X^{\rm (A)}_{\rm max}(E_0) = X^{\rm (p)}_{\rm max}(E_0/A) \tag{1.30}$$

$$N^{\rm (A)}_{\mu}(E_0) = A \cdot \left(\frac{E_0/A}{E_{\rm dec}}\right)^\beta = A^{1-\beta} \cdot N^{\rm (p)}_{\mu}(E_0). \tag{1.31}$$

If the fraction of energy transferred to the EM shower component were independent of energy, there would be no mass dependence of the number of charged particles at the shower maximum. In contrast, the number of muons and the depth of shower maximum depend on the mass of the primary particle. The heavier the shower-initiating particle is, the more muons are expected for a given primary energy and the shallower the depth of maximum. Iron showers contain approximately 40% more muons than proton showers [82, 79]. This will be one of the basic ideas for determining the nature of the cosmic ray particle with detectors that detect only the secondary particles of the extensive air shower.

The longitudinal profile for hadronic showers has been parametrized by Gaisser [32] as a function of the point of first interaction X_1, the depth of shower maximum $X_{\rm max}$ and size $N_e^{\rm max}$ at maximum and the mean free path λ :

$$N_e(X) = N_e^{\rm max} \left(\frac{X - X_1}{X_{\rm max} - \lambda}\right)^{\frac{X_{\rm max} - \lambda}{\lambda}} \exp(-\frac{X - X_1}{\lambda}). \tag{1.32}$$

This equation is used as a standard fit for the shower longitudinal development and is usually called the Gaisser-Hillas formula [41].

Muonic component and high energy muon bundles

As mentioned in the previous section, knowledge about the muon component is very important because a good determination of the muon properties of the air shower is necessary in order to deduce the nature of the primary cosmic ray, while for the primary energy the shower size (near shower maximum) is more important. To calculate the muon energy spectrum, we first need to know the fluxes of the particles that decay to muons, the charged pions and kaons. The first step is the calculation of muons and muon neutrinos from charged pion and kaon decays (Eq.1.16). The production spectrum of the decay particles of energy E at depth X is a sum of all atmospheric decays of particles of type i that generate particles of type j :

$$P_j(E, X) = \sum_i \int_{E_{\rm min}}^{E_{\rm max}} \frac{{\rm d}\, g_{ij}(E, E')}{{\rm d}\, E} D_i(E', X)\, {\rm d}\, E', \tag{1.33}$$

where $\mathrm{d}\, g_{ij}(E', E)/\,\mathrm{d}\, E$ is the spectrum of secondaries j from decaying particles of type i with energy E'. D_i is the spectrum of decaying mesons of energy E' at atmospheric depth X, which is the flux of such particles weighted by the decay probability $\epsilon_i/(E' \cos\theta)$ where θ is the zenith angle of the air shower. $E_{\min}$ and $E_{\max}$ are the minimum and maximum energy of the decay particles. Accounting for two-body decays of pions and kaons, and assuming a proton primary cosmic ray spectrum of $1.8E^{-2.7}\mathrm{cm}^{-2}\mathrm{s}^{-1}\mathrm{sr}^{-1}\mathrm{GeV}^{-1}$ Gaisser [32] obtains the muon spectrum after an integration over the muon production in the whole atmosphere :

$$\frac{\mathrm{d}\, N_\mu}{\mathrm{d}\, E_\mu} \simeq 0.14 E_\mu^{-2.7} \left[\frac{1}{1 + \frac{1.1 E_\mu \cos\theta}{115\ \mathrm{GeV}}} + \frac{0.054}{1 + \frac{1.1 E_\mu \cos\theta}{850\ \mathrm{GeV}}} \right], \tag{1.34}$$

where the first term represents the muons from pion decay (with critical energy ϵ_π = 115 GeV) and the second term from kaon decay (with critical energy ϵ_K = 850 GeV). 0.054 is the weight of the kaon contribution to the muon flux coming from the kaon production cross section and the muon branching ratio of kaon decays. Muon energy loss is not accounted for, which means the equation will only be correct at relatively high muon energy.

Eq.1.34 reveals two important features of the muon energy spectrum. At low energy ($E_\mu \ll \epsilon_\pi$) the muon spectrum has the shape of the primary cosmic ray spectrum, while at high energy it steepens by one power of E_μ as the thickness of the atmosphere is not large enough for pions to decay. Because of the $\cos\theta$ factor pions decay more easily in non-vertical showers and muons at large angles thus have a flatter energy spectrum. Also important to note is that the kaon contribution to the muon flux increases with the muon energy because of the higher value of ϵ_K [41].

However, for composition measurements the muon energy spectrum within one shower with energy E_0 and mass A is more important. The calculation is very similar. One starts with the spectrum of decaying pions and kaons with zenith angle θ:

$$\mathcal{D}_\pi = \frac{\mathrm{d}\, N_{\pi,\mathrm{dec}}}{\mathrm{d}\, X\, \mathrm{d}\, E_\pi} = \frac{\epsilon_\pi}{E_\pi X \cos\theta} \frac{\mathcal{F}_\pi(\xi_\pi, X)}{E_\pi} \tag{1.35}$$

$$\mathcal{D}_K = \frac{\mathrm{d}\, N_{K,\mathrm{dec}}}{\mathrm{d}\, X\, \mathrm{d}\, E_K} = \frac{\epsilon_K}{E_K X \cos\theta} \frac{\mathcal{F}_K(\xi_K, X)}{E_K}, \tag{1.36}$$

where the yield function $\mathcal{F}_i = E_i N_i(E_i, E_0, X)$ gives the number of particles of type i per logarithmic interval of fractional energy $\xi_i = E_i/E_0$ and X the atmospheric depth. For two-body decay like pion and kaon decay, the muon energy spectrum is only function of the energy of the parent particle :

$$\left(\frac{\mathrm{d}\, N_\mu}{\mathrm{d}\, E_\mu}\right)_{\pi\to\mu\nu} = \frac{\mathrm{BR}}{1 - r_\pi} \frac{1}{E_\pi} = \frac{1}{1 - r_\pi} \frac{1}{E_\pi} \tag{1.37}$$

$$\left(\frac{\mathrm{d}\, N_\mu}{\mathrm{d}\, E_\mu}\right)_{K\to\mu\nu} = \frac{\mathrm{BR}}{1 - r_K} \frac{1}{E_K} = \frac{0.635}{1 - r_K} \frac{1}{E_K}, \tag{1.38}$$

with $r_M = m_\mu^2/m_M^2$ the squared mass ratio, BR the branching ratio for the decay and $r_M E_M \leq E_\mu \leq E_M$. The muon production spectrum (for high energy muons) is then given by integrating the product of the muon energy spectrum of the decaying mesons with the energy spectrum of the decaying mesons over all meson

energies :

$$\frac{\mathrm{d}\,N_\mu}{\mathrm{d}\,E_\mu\,\mathrm{d}\,X} = \int_{E_\mu}^{E_\mu/r_\pi} \left(\frac{\mathrm{d}\,N_\mu}{\mathrm{d}\,E_\mu}\right)_{\pi\to\mu\nu} \mathcal{D}_\pi\,\mathrm{d}\,E_\pi + \int_{E_\mu}^{E_\mu/r_K} \left(\frac{\mathrm{d}\,N_\mu}{\mathrm{d}\,E_\mu}\right)_{K\to\mu\nu} \mathcal{D}_K\,\mathrm{d}\,E_K \tag{1.39}$$

$$= \int_{E_\mu}^{E_\mu/r_\pi} \frac{1}{1-r_\pi}\frac{1}{E_\pi}\frac{\epsilon_\pi}{E_\pi X\cos\theta}\frac{\mathcal{F}_\pi(\xi_\pi, X)}{E_\pi}\,\mathrm{d}\,E_\pi \tag{1.40}$$

$$+ \int_{E_\mu}^{E_\mu/r_K} \frac{0.635}{1-r_K}\frac{1}{E_K}\frac{\epsilon_K}{E_K X\cos\theta}\frac{\mathcal{F}_K(\xi_K, X)}{E_K}\,\mathrm{d}\,E_K \tag{1.41}$$

$$= \frac{\epsilon_\pi}{E_0\cos\theta}\frac{1}{E_0}\int_{\xi_\mu}^{\xi_\mu/r_\pi} \frac{\mathcal{F}_\pi(\xi_\pi, X)}{X(1-r_\pi)}\frac{\mathrm{d}\,\xi_\pi}{\xi_\pi^3} \tag{1.42}$$

$$+ \frac{0.635\epsilon_K}{E_0\cos\theta}\frac{1}{E_0}\int_{\xi_\mu}^{\xi_\mu/r_K} \frac{\mathcal{F}_K(\xi_K, X)}{X(1-r_K)}\frac{\mathrm{d}\,\xi_K}{\xi_K^3}, \tag{1.43}$$

with $\xi_\mu = E_\mu/E_0$.

To get the total number of muons, we integrate the muon production spectrum over the whole atmosphere X. Since production of high energy muons takes place high in the atmosphere, it is safe to extend the integration to ∞ :

$$\frac{\mathrm{d}\,N_\mu}{\mathrm{d}\,E_\mu} = \int_0^\infty \frac{\mathrm{d}\,N_\mu}{\mathrm{d}\,E_\mu\,\mathrm{d}\,X} = \frac{\epsilon_\pi}{E_0\cos\theta}\frac{1}{E_0}F_\pi(\xi_\mu) + \frac{0.635\epsilon_K}{E_0\cos\theta}\frac{1}{E_0}F_K(\xi_\mu), \tag{1.44}$$

with $F_i(\xi_\mu)$ the integral over X. For the IceCube detector the muons need to have a minimum energy to be able to penetrate at least 1500 m of ice, so we get:

$$N_\mu(>E_{\mu,\mathrm{thr}}) = \int_{E_{\mu,\mathrm{thr}}}^{E_0/A} \frac{\mathrm{d}\,N_\mu}{\mathrm{d}\,E_\mu}\,\mathrm{d}\,E_\mu \tag{1.45}$$

$$= \frac{\epsilon_\pi}{E_0\cos\theta}\frac{1}{E_0}\int_{E_{\mu,\mathrm{thr}}}^{E_0/A} F_\pi(\xi_\mu)\,\mathrm{d}\,E_\mu + \frac{0.635\epsilon_K}{E_0\cos\theta}\frac{1}{E_0}\int_{E_{\mu,\mathrm{thr}}}^{E_0/A} F_K(\xi_\mu)\,\mathrm{d}\,E_\mu \tag{1.46}$$

$$= \frac{\epsilon_\pi}{E_\mu\cos\theta}\xi_\mu\int_{\xi_{\mu,\mathrm{thr}}}^{1/A} F_\pi(\xi'_\mu)\,\mathrm{d}\,\xi'_\mu + \frac{0.635\epsilon_K}{E_\mu\cos\theta}\xi_\mu\int_{\xi_{\mu,\mathrm{thr}}}^{1/A} F_K(\xi'_\mu)\,\mathrm{d}\,\xi'_\mu. \tag{1.47}$$

The above equation is difficult to solve analytically, therefore Elbert [83] suggested the following parametrization :

$$N_\mu(>E_{\mu,\mathrm{thr}}) \approx \frac{14.5\ \mathrm{GeV}\cdot A}{E_\mu\cos(\theta)}\left(\frac{E_0}{A\cdot E_\mu}\right)^{0.757}\left(1-\frac{A\cdot E_\mu}{E_0}\right)^{5.25}, \tag{1.48}$$

where the superposition model is used for nuclear primaries and the parameters were obtained from Monte Carlo simulations. Similar results were obtained from Monte Carlo simulations by Gaisser and Stanev [84] and Forti *et al.* [85]. A more analytical approach with comparable results is discussed by Lipari in [86].

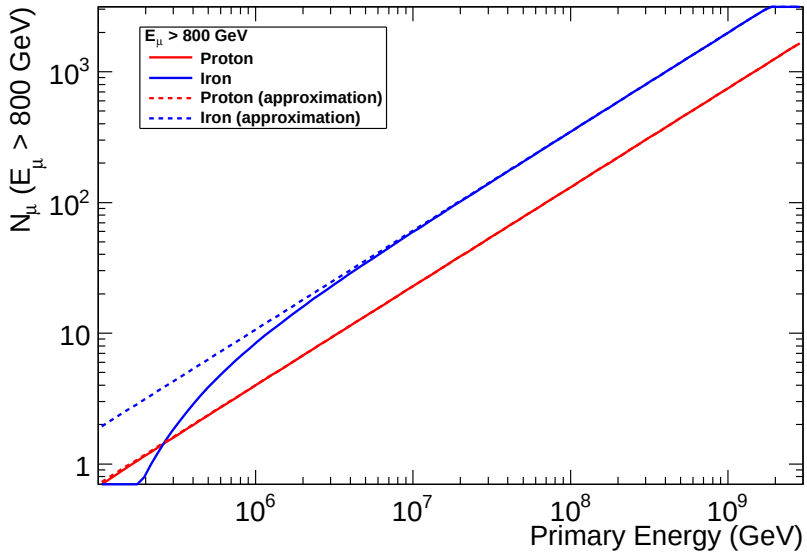

Figure 1.25: The muon multiplicity above a threshold energy of 800 GeV (the average energy to reach the bottom of the IceCube detector) as function of the primary energy for proton (red) and iron (blue) from the Elbert formula, Eq. 1.48. The approximation shows the Elbert formula without the $(1 - AE_\mu/E_0)^{5.25}$ term.

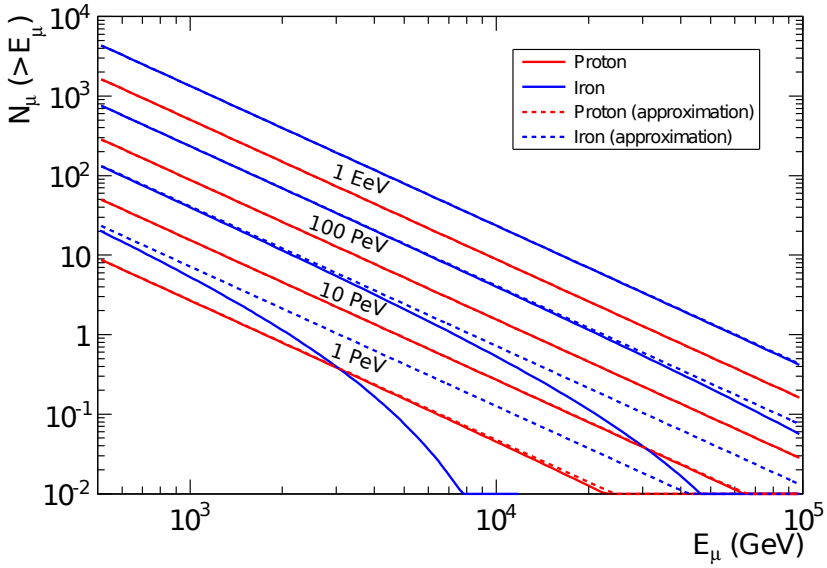

Figure 1.26: The muon multiplicity from the Elbert formula, Eq.1.48, with and without (dotted line) the $(1 - AE_\mu/E_0)^{5.25}$ term for proton (red) and iron (blue) primaries and for four different primary energies.

In comparison with the muon multiplicity from the simple Heitler-Matthews model Eq. 1.31 ($N_\mu \sim E_0^{0.85}$), the number of muons increases less quickly with energy ($N_\mu \sim E_0^{0.757}$). The reason is that, as the primary energy increases, the cascade penetrates deeper into the atmosphere before reaching the energy $\sim E_\mu$. But then the atmosphere becomes denser and pion decay probability smaller. The factor $(1 - AE_\mu/E_0)^{5.25}$ reflects the inclusive cross section for pion production, which vanishes near the kinematic limit [32]. The importance of this term can be seen in Figs.1.25 and 1.26. In Fig. 1.25 the muon multiplicity for muons

above 800 GeV is plotted as a function of primary energy E_0. Only for proton showers below 1 PeV, this term gives rise to a faster decrease in the number of muons and and in a much smaller difference between proton-induced and iron-induced showers. In Fig. 1.26 the muon multiplicity for different primary energies is plotted as function of the muon energy for both proton and iron showers. It can be seen that the probability to create a very high energy muon that carries a large fraction of the initial primary energy is higher for proton showers than for iron shower due to this term, but that this difference becomes small at large primary energies.

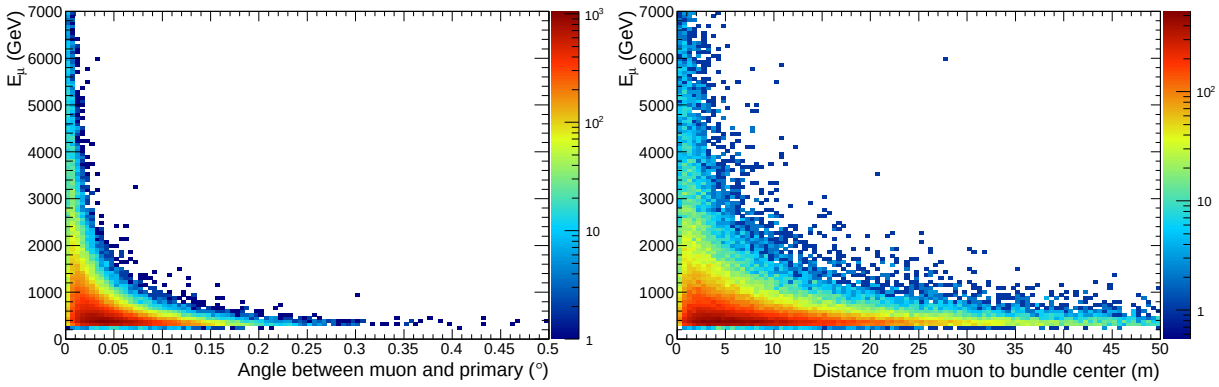

Figure 1.27: **Left**: Muon energy as a function of the angle between the muon and the primary cosmic ray for simulated iron-induced air showers between a few PeV and 100 PeV. Right: Muon energy as function of the distance of the muon to the shower axis on the IceTop surface at an altitude of 2835 m for the same events as the left figure.

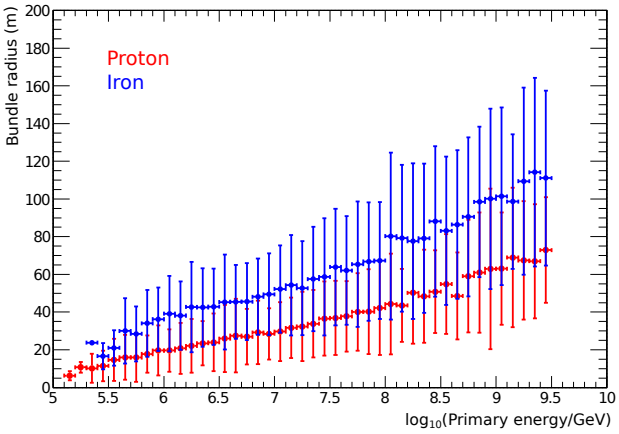

Figure 1.28: The muon bundle radius, defined as distance between the shower axis and the outer muon for muons that reach the center of the IceCube detector (1950 m deep in the South Pole ice), as a function of the primary cosmic ray energy. Both proton (red) and iron (blue) bundles are plotted. The error bars show the spread of the distributions. The

The muon particle density distribution as function of distance to the central axis of the air shower, or muon *lateral distribution*, is flatter than the electromagnetic lateral distribution. High energy muons originate from the high energy pions and kaons generated in the first interactions high in the atmosphere. Therefore they will have a small transverse momentum p_{T}. Muon bundles are groups of one to thousands of high energy muons

(as shown in Fig. 1.26) which are collimated and concentrated near the central axis of the muon bundle. In Fig. 1.27 the angle between the muons of the several iron-induced muon bundles in the PeV-100 PeV primary energy is shown on the left. It shows clearly that muon bundles consist of groups of almost parallel muons with the highest energy muons situated closest to the central axis (shown on the right plot). The muon bundle radius, defined as the distance to the outermost muon, is 10 – 100 m as shown in Fig. 1.28. The large spread in radii is clearly visible. Iron bundles are also much larger, due to the larger muon multiplicity for the same primary energy where those extra lower energy muons are situated at larger radii.

1.2.2 Experimental techniques

Cosmic rays can be detected in several different ways. The flux of low energy cosmic rays is sufficiently high that the primary radiation can be measured with dedicated magnetic spectrometers attached to high altitude balloons or satellites. Those spectrometers can directly measure the nuclear and isotopic composition in the GeV energy range and spectra of individual elements up to TeV/nucleon. Particle calorimeters with a combination of magnetic spectrometers for the charge and momentum measurements, tracking detectors (wire chambers or scintillators), calorimeters for energy measurement; and transition radiation detectors, Cherenkov detectors or time-of- flight detectors for dedicated particle identification – detectors also used in accelerators – extend the energy measurements to 100 TeV per nucleus. The main disadvantage of large particle calorimeters is that they are much heavier than magnetic spectrometers and high altitude balloons can only lift payloads up to 4 tons. The satellite experiments are listed in Table 1.3 and the balloon experiments in Table 1.4. Only those that measured proton/Helium energy spectra and/or spectra for heavier nuclei are mentioned. Experiments which focussed on cosmic ray muons, electrons, positrons, isotopes and antimatter are not listed. Recent nuclei spectra measurements are made by the space-based detectors CRN, HEAO-3 and ACE (at solar minimum) and for a larger energy range by balloon-borne experiments, such as CREAM, ATIC, TRACER and TIGER. These measurements have been performed over the years using different techniques: energy loss detectors (ISEE-3, ACE-CRISS), Cherenkov detectors (HEAO-3), Transition Radiation Detector (CRN [124]), and magnetic spectrometers (AMS-01, AMS-02 and PAMELA). A good overview for spaceborne experiments can be found in [87] and for high-altitude balloon experiments in [88].

Experiment	Type	Energy range	Period
AMS-01	Spectrometer on space shuttle STS-91	1 - 200 GeV	1998
AMS-02	Spectrometer on ISS	1 - 200 GeV	2011 -
CRIS	Spectrometer on ACE	1 - 200 GeV	1997 -
ISEE-3	Energy loss detector	1 - 200 GeV(?)	1978-1982
CRN	Transition Radiation Detector (Spacelab2 misson aboard the Challenger space shuttle)	10 - 1 TeV/n	1985
HEAO-3	Cherenkov detector	? - 35 GeV/n	1979-1981
PAMELA	Spectrometer	0.1 - 1 TeV/n	2006 -
Proton (1-2-3-4)		50 GeV - 1 PeV	1965-1968
SOKOL (1-2)	Cherenkov/Calorimeter on Zenit/ Vostok type spacecraft	2 - 100 TeV	1984 (Kosmo-1543 with Sokol)/ 1985 (Kosmo-1713 with Sokol-2)

Table 1.3: Overview of satellite experiments.

From a few hundred TeV onwards the flux becomes so low that a detection area is needed that cannot be carried by balloons or satellites anymore (need an area number). Indirect experiments are needed with large arrays that measure the secondary particle radiation from the extensive air showers created by the primary cosmic rays. From the properties of these secondary particles these indirect experiments can deduce the primary type and energy of the incident cosmic ray particles. However, due to strong fluctuations in the shower development this is not possbile anymore on event-by-event basis.

For indirect experiments, which are situated on the surface of the Earth, it is important to be situated close

Experiment	Type	Energy range	Period
BESS/BESS-Polar	Spectrometer (p, He)	1 - 200 GeV	1993-2004 (9 flights)
CAPRICE	Spectrometer/Calorimeter/RICH	0.4-300 GeV	1994-1998 (3 flights)
ATIC	Calorimeter	30 GeV - 500 TeV	2001-2008 (4 flights)
CREAM	Calorimeter + TRD	30 GeV - 500 TeV	2004-2010 (5 flights)
JACEE	Emulsion chambers	2 - 800 TeV	1979-1996 (15 flights)
RUNJOB	Emulsion chambers	10 - 500 TeV	1995-1999 (10 flights)
TRACER	Transition Radiation Detector	10 - 300 TeV	2003/2006 (2 flights)
TIGER	Cherenkov/Hodoscope/Scintillator ($26 < Z < 40$)		1997/2001/2003 (3 flights)
Super-TIGER	Cherenkov/Hodoscope/Scintillator ($26 < Z < 40$)		2012-2013 (1 flight)
MASS	Spectrometer/Scintillator/ Cherenkov/ Calorimeter	0.1 - 40 GeV/n	1989/1991 (2 flights)
IMAX	Spectrometer	0.2 - 3.2 GeV/n	1992 (1 flight)

Table 1.4: Overview of high altitude balloon experiments which measured the energy spectrum of proton and helium and/or heavier nuclei.

to shower maximum for the pursued energy range. Because the shower size is maximum at shower maximum, the shower-to-shower fluctuations will be minimal, and hence the detector response and the energy resolution. For cosmic rays in the PeV-EeV range, this means high-altitude locations ($\sim$ 3000 m) are desirable, while for ultrahigh energy cosmic ray experiments, sea level is more suitable.

Intrinsic shower fluctuations make each shower from the same primary energy, type and direction look slightly different. At high energies there is also no real calibration source or measurements from acceleration data available from which individual detectors can be optimized to deduce their primary type and energy. Therefore hybrid detectors which combine several techniques to measure several different properties of the same extensive air shower are crucial for solid measurements. In Fig. 1.29 different detection techniques for indirect detection of cosmic rays by measuring the properties of extensive air showers are shown. During the development of air showers through the atmosphere, the high energy charged particles (mainly the shower electrons and positrons) will generated Cherenkov light which propagates through the atmosphere and can be detected by large air Cherenkov telescopes. Because of the small refraction index of the atmosphere the Cherenkov cone is narrow and most of the light is emitted along the shower axis and is quite intense. Even 1 TeV showers, that are fully absorbed before they reach observation level, produced observable Cherenkov signals. Wide-angle Cherenkov detector arrays, typical for detection of charged cosmic rays, cover simultaneously a large fraction of the sky and detect any event in their field of view. Example of detector arrays that use atmospheric Cherenkov telescopes are Tunka (near Lake Baikal), Yakutsk and HEGRA. The main problem with this technique is that suitable climatic, meteorological and environmental site conditions are needed, such as low optical background, a mostly cloudless sky (no moon), little precipitation and a dust-free atmosphere with low aerosol contamination, to operate the detectors with a reasonable duty cycle (typically $\leq$10%).

Another way of measuring the longitudinal development of the air showers is through the detection of the fluorescent light emitted by the atmospheric nitrogen atoms excited by the passage of the shower. This light emission is isotropic and much less intense than air Cherenkov. Only very high energy showers generate enough light to generate a signal above the night sky background. Due to the isotropic emission huge volumes of the atmosphere can be monitored and rare ultrahigh energy events that even miss a huge ground array can still be detected. Examples of detectors that use this technique alone is Fly's Eye or in hybrid mode with a particle detector array, Auger.

Charged particles propagating through the atmosphere can also give rise to radio emission. The difference in interaction of electrons, positrons and photons with the atmospheric molecules leads to a charge asymmetry, which will give rise to an increasing negative charge excess as the shower develops through the

atmosphere, that results in the emission of coherent radio frequency Cherenkov emission. The interaction of charged secondary particles with the geomagnetic or geoelectric field can also cause a Cherenkov-like radio emission, which even occurs if there is no net charge excess. The exploitation of the properties of radio emission of extensive air showers is still being studied by test setups like LOFAR, LOPES and RASTA. A very new technique currently being investigated by the Pierre Auger Observatory is detection of cosmic rays using radio detection in the microwave band, which is thought to be caused by molecular Bremsstrahlung radiation.

The most common method of shower detection is based on the arrival of the particle disk at ground level with some more or less loosely packed particle detector array. This impllies that the particle disk is being sampled on arrival at ground level. Based on the particle arrival times in different individual detectors of the array, the arrival direction (or also inclination of the central shower axis) is obtained. The point where the shower axis, which is also roughly the symmetry axis for the air shower and can be seen as the extension of the track of the primary particle if it did not interact, crosses ground level is the shower core. The shower core is characterized by the largest particle density, hence from the particle density in the different detectors the shower core is determined. There are several types of particle detectors possible for the detections of the multiple air shower components. Most surface arrays use scintillator counters (or hodoscopes for tracking) for determining the charged particle density (Geiger counters for older experiments), which will be dominated by the electromagnetic particles. Other detection types like emulsion chambers (eg. Pamir) , cloud chambers (eg. Mount Norikura in Japan), spark chambers and even resistive plate chambers are also used (ARGO-YBJ in Tibet). Instead of measuring the particle density, which is not sensitive to the energy of the particles, one can also use calorimeters to measure the energy deposit. Examples are water (Haverah Park, Auger) and ice (IceTop) Cherenkov detectors, where the charged particles create Cherenkov light in the water or ice, which is detected by photomultipliers. Through shielding of the electromagnetic component with a few meters of rock, the muon component is probed, which is important for composition measurements. Some arrays have denser spaced detectors for studying the cores (eg. Tibet Asγ) or have dedicated hadron calorimeters (Tien Shan in Kazakhstan, EAS-TOP in Italy and KASCADE in Germany). The high energy muon component, of muons which are formed in pion and kaon decays from the first few interactions high in the atmosphere, is measured by deep underground detectors, such as MACRO (under a few km of rock in the mountains at Gran Sasso) and IceCube (under 1450 m of ice, see next chapter) [41, 89]. The main advantage of this kind of coincident detectors is that the TeV energy muons measured deep underground probe the energy per nucleon while the surface array probes the energy per particle of the cosmic ray primary. The disadvantage is the reduced statistical accuracy of the muon measurements and the limited solid angle available for coincident cosmic ray observations [55].

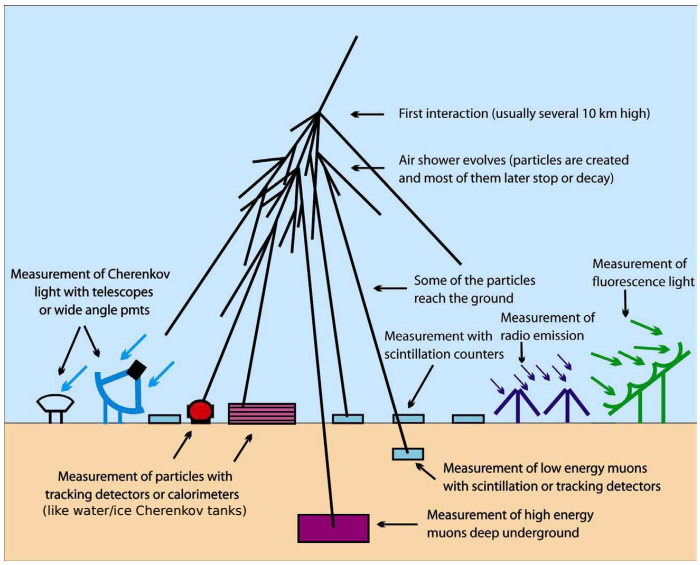

Figure 1.29: Different detection techniques to measure properties of extensive air showers.

Chapter 2

The IceCube Neutrino Observatory

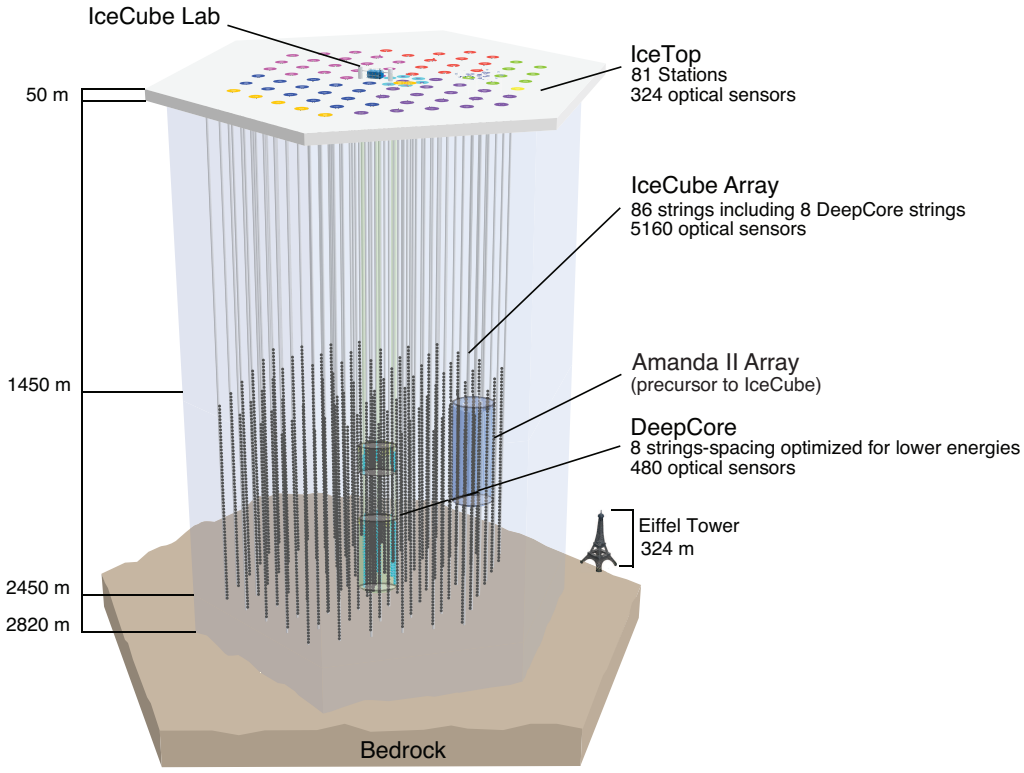

Figure 2.1: The IceCube Observatory with the IceTop air shower array at the surface and the IceCube array in the deep ice. The precursor to IceCube, Amanda II, is also shown. DeepCore is the denser instrumented part of IceCube in the center of the array. The colors on the surface denote the construction periods for the IceCube strings: 2004-2005 (yellow), 2005-2006 (green), 2006-2007(red), 2007-2008(magenta), 2008-2009(purple), 2009-2010(blue), 2010-2011(orange).

2.1 IceTop : the surface air shower array

The surface of the IceCube Neutrino Observatory (Fig. 2.1), at the geographic South Pole (2835 m, 692 g/cm^2), is instrumented by the IceTop air shower array with 81 stations [90]. Each station consists of two ice

Cherenkov tanks which each have two optical detector modules. One module is operating at high gain (5e6, or a PMT voltage of ∼1250 V) and the other module at low gain (1e5, of a PMT voltage of ∼750 V) to extend the dynamic range. IceTop is based on detectors like Auger [12] and Haverah Park [91] which use water tanks with reflective inner walls to detect Cherenkov light generated by charged particles passing through the tank. By triggering on the coincidence between signals in distant stations, low energy noise signals are heavily suppressed. IceTop is built for three main reasons : the first is to veto downgoing muons from air showers for high energy neutrino detections, the second goal of the IceTop array is to calibrate the track and energy reconstruction of the IceCube detector. The difference between independent track reconstructions of IceTop and IceCube can hint toward systematic offsets in IceCube track reconstruction which needs to be calibrated out. With a known primary composition the IceCube absolute energy scale can also be calibrated with IceTop. For coincident events, which pass through both IceTop and IceCube, two independent measures of the energy can be made and the IceTop energy scale measurement can be used to calibrate IceCube.

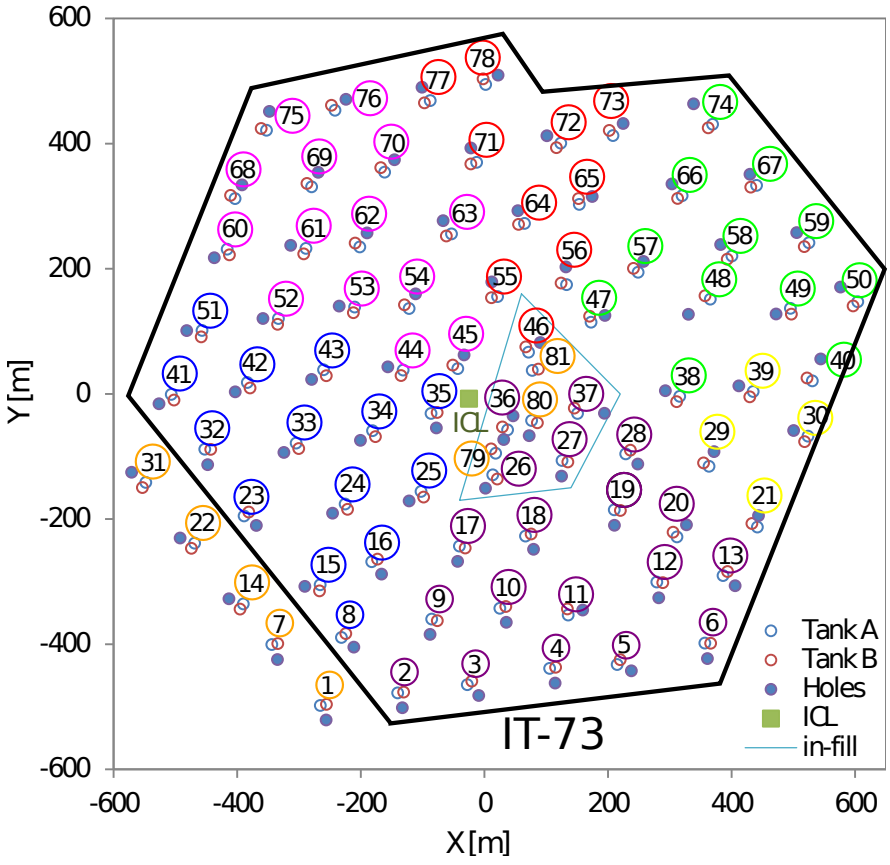

Figure 2.2: The IceTop surface array. The IceCube Laboratory (ICL) where signals are processed for trigger and filter decisions is situated in the center of the array. The InFill array is the denser instrumented part of IceTop in the center. The holes are the IceCube holes where the instrumented string of IceCube are deployed. The colors (same color code as Fig. 2.1 denote the construction periods for the IceTop tanks. IceTop-73 (IT-73) shows the surface area, surrounding the 73 stations used in the analysis presented in this thesis.

The most important goal is to determine the primary cosmic ray energy spectrum and composition in the energy range between the knee and the ankle where the transition from galactic to extragalactic cosmic rays is expected. The threshold of the energy range is determined by the distance between IceTop stations, which is determined by the IceCube string spacing. The IceCube holes have an average grid spacing of 125 m and the IceTop stations are 25 m from the IceCube hole. The distance between two tanks of a station is on average 10 m and is used to form a first local coincidence trigger, explained in Section 2.5.1, to reduce the noise

from single muons ($\sim$ 2 kHz). Additional advantages of using two tanks are that shower fluctuations (both in timing and charge) can be measured by comparing the signals in tank A with signals in tank B on event-by-event basis and that the array can be divided in subarrays (subarray A and subarray B) for reconstruction quality studies.

The primary energy to hit three IceTop stations with a 125 m spacing is about 300 TeV. In the last construction year 2010-2011 three extra stations (79-80-81) were deployed in the center of the array to form the so-called "in-fill array" and decrease the low energy threshold to 100 TeV [92]. The end of the energy range is determined by the amount of statistics needed for an accurate measurement. That is given by the total effective detection area and the expected flux of cosmic rays. IceTop is a one square kilometer array which can detect a few air showers at a few EeV. Therefore the energy range is 100 TeV - $\mathcal{O}(1)$ EeV. The full geometry of the surface array is shown in Fig. 2.2, with the different colors for the different deployment years. The low energy in-fill array is the tetragon in the center. The hexagon-like shape in solid black is the IT-73 geometry which was installed by Feb. 2010 and used in this thesis for the data analysis of 2010-2011 data.

The South Pole provides the ideal location for a surface air shower array because of its altitude. The altitude of 2835 m or 692$\pm$20 g/cm^2, due to surface pressure variation, is very close to the shower maximum $X_{\max}$ between 10 PeV and a few 100 PeV for proton, while it reaches $X_{\max}$ for iron at the highest observable energies (Fig. 2.3). This will result in minimal intrinsic shower fluctuations and hence an optimal detector response and energy resolution in the desired energy range. Also the differences in shower size between proton and iron showers will be minimal above 100 PeV because of the optimal location of IceTop and that will prove to be convenient for energy reconstruction.

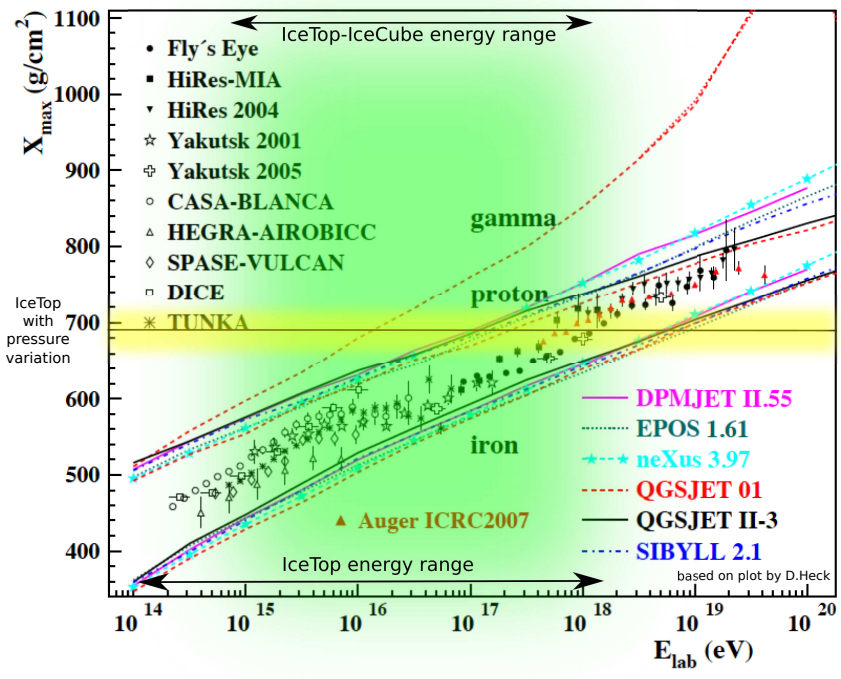

Figure 2.3: Shower maximum as function of primary energy for proton, iron and gamma induced showers from CORSIKA simulations with different hadronic interaction models. The green shaded region is the optimal IceTop-IceCube energy range. The yellow shaded region marks the location of IceTop with pressure variation.

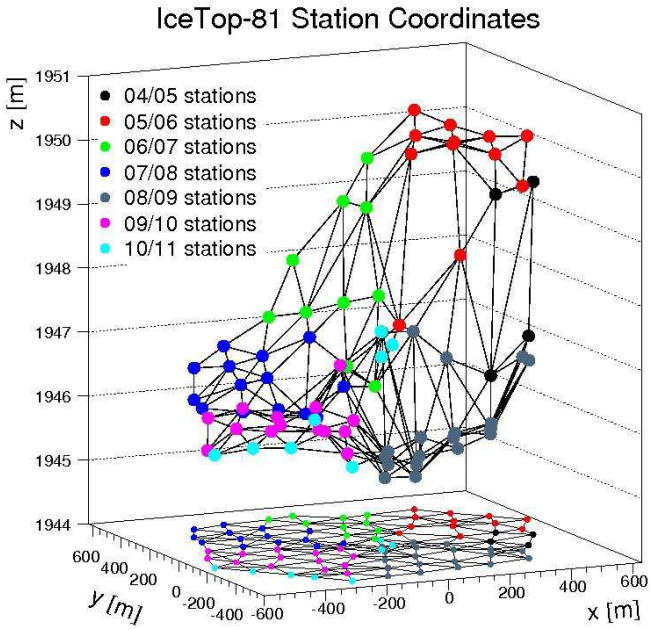

Figure 2.4: The 3D map of the IceTop stations with different colors for different deployment seasons. Over the whole km^2 IceTop area there is a slope of 5 m.

2.1.1 The IceTop Tank

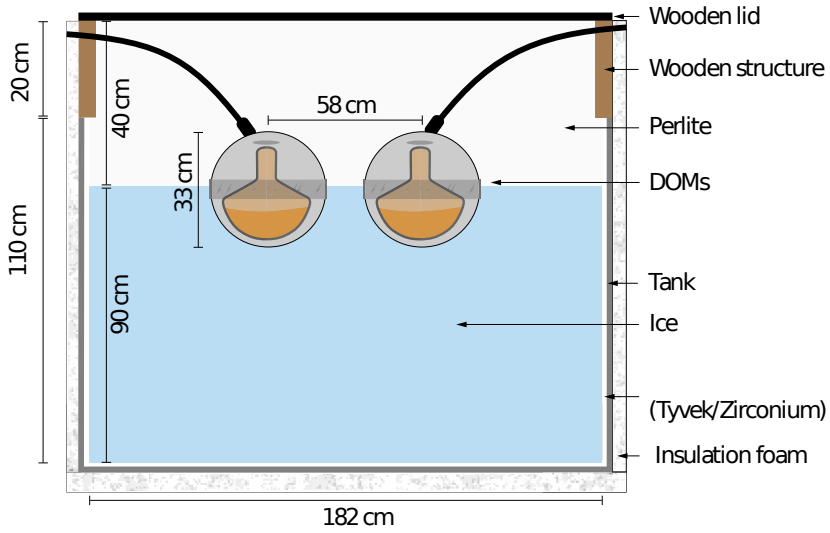

Figure 2.5: Cross section of an IceTop tank.

The IceTop tank (Fig. 2.5) is a black, polyethylene cylinder, 6 mm thick, 1.1 m high and an inner diameter of 1.82 m. It is filled with ice to a height of 90 cm in which the sensitive area of the optical modules are submerged, while the other half is not. The tanks have a diffusively reflective liner (Tyvek bags for eight 2005 tanks and four 2011 tanks, Zirconium for all others). In between the ice surface and the wooden lid is a 40 cm layer filled with expanded perlite (a volcanic glass) for thermal insulation and light protection. The

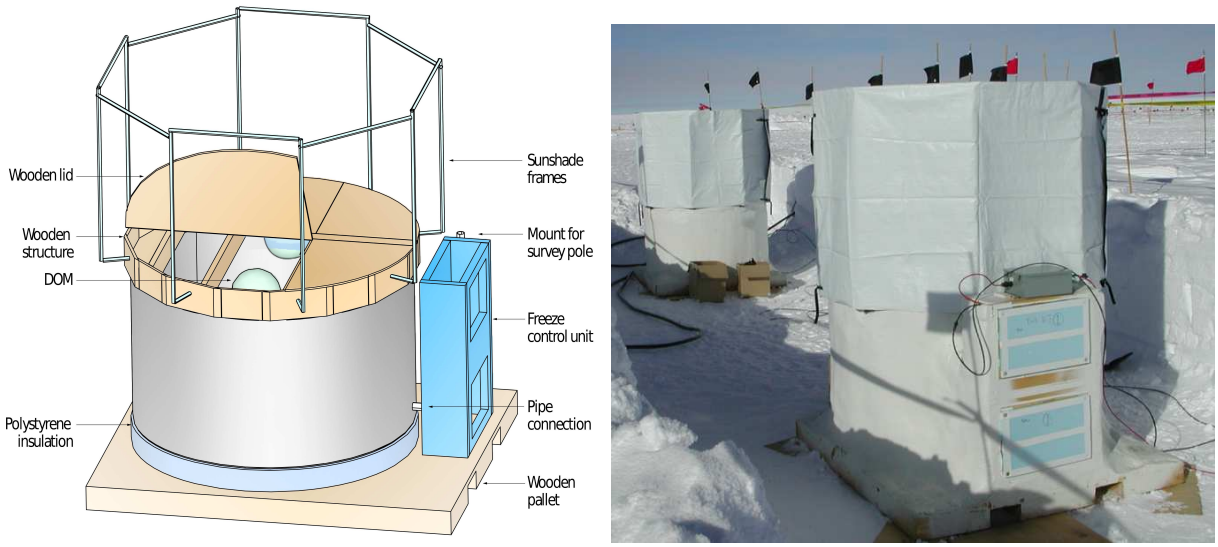

Figure 2.6: **Left**: IceTop tank as it is deployed at South Pole with sunshade frames and freeze control unit.

two optical modules are placed symmetrically about the center of the tank and 58 cm from each other. When deployed the tank rests on a wooden pallet with a layer of 10 cm polysterene in between the bottom of the tank and the pallet. Attached to the tank is a enclosure the freeze control unit. From the pallet to the lid the tank is surrounded by polyurethane foam. On top of the tank is a sunshade frame to prevent direct sunlight from slowing down the freezing process.

2.1.2 Deployment

The first step in the deployment of IceTop at the beginning of a Polar season is to locate the position of the tanks. There bulldozers dig trenches to assure that the top of the tanks is level with the snow surface to minimize drifting. Next, the tanks are prepared for deployment by attaching the framework to hold the sunshades, the optical modules and the top liner in position. The tanks are then transported to their designated trench where they are placed on a wooden pallet and the optical modules are mounted in hangers in a such a way that their PMTs are facing downwards. Then the tanks are filled to a depth of 90 cm so that the optical modules are half-submerged with water from the station in 2005 and in later seasons with filtered water from the IceCube hot water drilling system. The water had to be filtered to reduce the glycol content used by IceCube for the system protection during winter. The Freeze Control Units, explained in the next paragraph, are turned on and the water-filled tanks are cooled and degassed with the lids closed for the first couple of days to prevent drifting snow and other dust to pollute the filtered water. Meanwhile the sunshade frames, which keeps direct sunlight away from the ice surface and could slow down or stop the freezing process, are mounted on the tanks. When a surface layer of ice has been formed after the first couple of the days, the lids are opened again for faster freezing. The full freezing period lasts about 30 to 40 days and depends on the temperature during the season. During that period the freezing process is closely monitored by several temperature sensors in the tank and the ice surface is kept clear from drifting snow, which again insulates and slows down the freezing process. When the water in the tanks is fully frozen, DOM hangers and sunshade frames are removed, the tanks are filled with perlite and the lids are closed. Ideally the trenches are then backfilled after the freeze control units are removed but during seasons where the freezing was slower, the trenches were backfilled earlier and the freeze control units were removed by the winter crew. Finally the optical modules are turned on and commissioning of the newly deployed tanks can start.

The freezing of water in tanks can be done in two approaches: either the water freezes from top to bottom, or it freezes from bottom to top. The main objective is create a cylinder of clear, crack-free ice in which the

Figure 2.7: The deployment of IceTop tanks in 6 steps: Top left: The bulldozer is digging a trench for placing an IceTop station, Top center: Two tanks are placed in a trench, with their top level with the snow surface and filled with filtered water, Top right: Sunshade are installed and the water in the tanks is freezing. Bottom left: View of 2 DOMs in a tank during freezing. A thin layer of drifted snow is visible (before it was removed) and the pipe used to fill the tanks is also visible. The tanks freeze with the lid open to limit insulation from the cold. Bottom center: Trenches are backfilled and several stations are still freezing. Bottom right: On the left the lids of two tanks are visible. The sunshades have been removed, the tanks filled with perlite and the lids closed.

optical modules are half frozen in. This requires a slow process, to prevent cracks, together with a method to remove the air bubbles which are resolved in the water. Also due to the smaller density of ice (0.9167 g/cm^3 at 0°C) with respect to water (0.9998 g/cm^3), the volume will expand and a pressure will build up if the volume is kept fixed. The bottom-up approach for grooming clear ice has the advantage that there is no need to relieve the pressure and that the air bubbles can easily escape. However, the main concern is that a good optical coupling between the surface of the optical module and the surrounding ice to limit the loss of light. Therefore the top-down approach is chosen. As mentioned earlier a Freeze Control Unit (FCU) is used to monitor and control the freezing process. The FCU steers a degasser unit at the bottom of the tank which pumps water through a permeable membrane through which the dissolved gases can diffuse. A vacuum pump then removes these gases. To deal with the expanding pressure as the water freezes from top to bottom water can escape through a pressure relief pipe at the bottom of the tank. This water is collected initially collected in a sump and when full pumped out through an exhaust pipe by the sump pump. To ensure a uniform growth of the top-down expanding ice and limit impurities, the tanks are insulated on the bottom and sides which creates a controlled environment. There is no need for a large mixing pump to make sure not only the water at the bottom is processed by the degasser. The temperature dependence of the water density – water is densest at 4°C – creates a thermal instability. Colder water is heavier and will drop, hence a natural mixing circulation process occurs. During freezing the duty cycle of the pumps is decreased as the more dissolved gases are removed from the water and as less water escapes due to expanding pressure. This is to limit the extra heat needed for the pump, which would again slow down the freezing process [90].

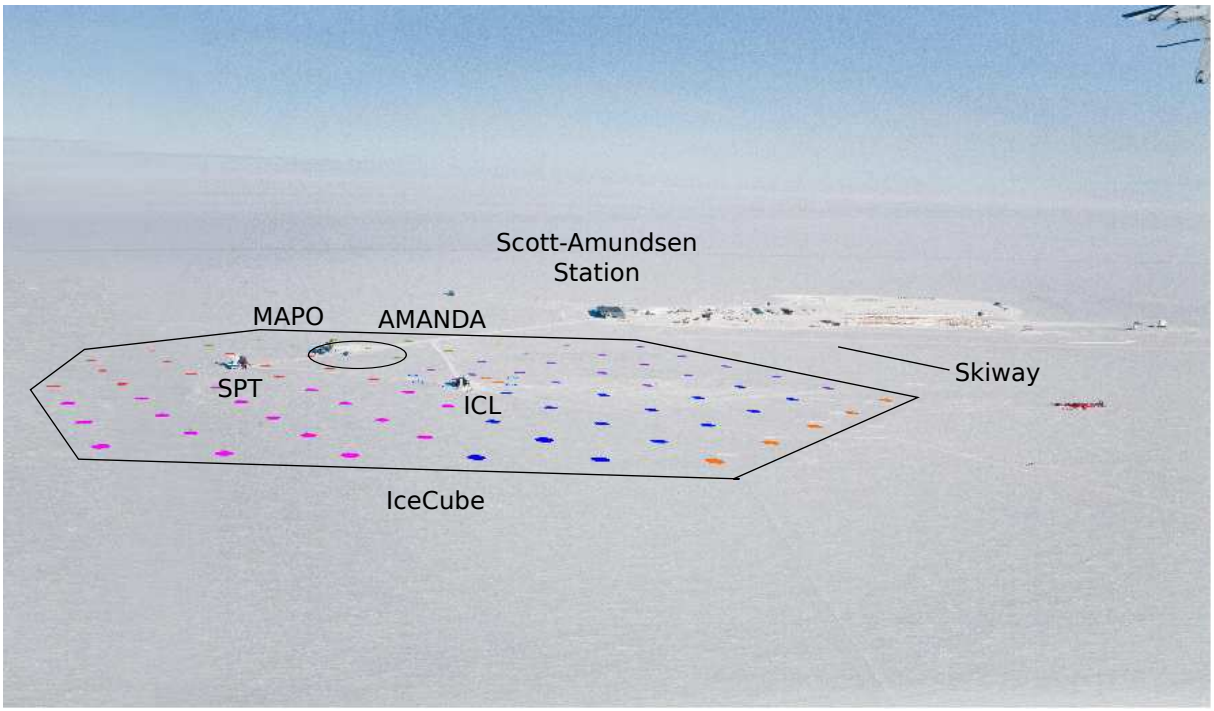

Figure 2.8: Martin A. Pomerantz Observatory (MAPO) which housed the AMANDA electronics.

2.2 IceCube : the 3D in-ice detector

In 1930 Wolfgang Pauli tried to explain the continuous energy spectrum of beta decay, which seemed to violate energy conservation for individual decays, by the prediction of a new particle that is emitted along with the electron, later called the neutrino. However, he feared the particle would be impossible to detect: "I have done something very bad today by proposing a particle that cannot be detected; it is something no theorist should ever do." In 1956, Clyde Cowan and Frederick Reines discovered the neutrino by detecting the decay products caused by inverse beta-decay. As predicted the neutrino is very hard to detect as it only interacts through the weak interaction, is neutral and almost massless (with a mass that is still unknown). Several experiments, like Homestake and Kamiokande, were built to study the low energy neutrino's from the sun.

For the study of neutrino's from more distant and violent sources, for which the predicted flux is much lower than for solar neutrinos, huge detector volumes are needed. The downside of huge detector volumes is that a dense instrumentation to detect all details of the neutrino-nucleus interaction becomes very expensive. Besides, cosmic rays can easily mimic neutrino-like signals and thus provide a huge background. This implies large shielding is necessary for neutrino detectors. The first generation neutrino telescopes, DUMAND (Deep Underwater Muon And Neutrino Detector) and Lake Baikal, used large volumes of water with instrumented cables to detect the Cherenkov light emitted by the muons, electrons or taus from charged current neutrino-nucleus interactions. AMANDA (Antarctic Muon And Neutrino Detector Array) [93, 94, 95], the first generation predecessor of IceCube, used the Antarctic ice sheet as medium to detect high energy neutrino's [96]. AMANDA-II had 19 cables or strings instrumented with 677 optical modules in total at depths between 1500 m and 2000 m. AMANDA-II has been superceded by the IceCube detector which instruments a km^3 compared to the 10^7 m^3 volume of AMANDA-II. In addition to the larger volume, IceCube also learned from the experiences with AMANDA optical modules and designed optical modules that digitized the signals before sending them to the surface for limiting electronic cross-talk which degraded the signals.

The IceCube Neutrino Observatory [97, 98]is a neutrino telescope shown in Fig. 2.1 with two compo-

nents. The surface component, IceTop, is a cosmic ray detector which can reduce the background for neutrino detection and is explained in detail in Section 2.1. The deep underground detector, called IceCube or also "InIce", instruments 1 km^3 in a hexagonal grid of Antarctic ice with 78 strings with an average string spacing of 125 m. On each of those strings 60 Digital Optical Modules (DOMs) are installed between depth of 1450 m and 2450 m and with an average DOM spacing of 17 m. In the last three deployment seasons (2008-2009, 2009-2010 and 2010-2011) additional strings with a smaller string and DOM spacing were installed to form a denser subarray, called DeepCore (DC) [99] as shown on Fig. 2.1, with seven IceCube strings. 13 of the 15 DeepCore strings have a string spacing of 72 m, while six strings have a string spacing of 42 m. The hexagonal shape of the IceCube detector is not perfect – there seems to be two strings missing in the corner – because drilling for string deployment at the planned location for strings 79 and 80 was impossible due to the presence of the remainder of the original South Pole station (19571975). Due to the presence of a big dust layer 2000 and 2100 m depth, this region is not instrumented with DC DOMs. 50 DOMs are placed with a 7 m spacing at depths between 2100 m and 2450 m and the other 10 DOMs are placed directly above the dust layer with a 10 m spacing.

The IceCube detector is designed to detect high energy astrophysical neutrinos above 50-100 GeV and optimally above 1 TeV. These neutrinos can be created by the interaction of ultrahigh energy cosmic rays in the sources (like SNR, GRB and AGN), creating high energy charged pions. The volume of the IceCube detector is chosen based on theoreticl flux predictions from those astrophysical sources and the observed fluxes of high energy gamma rays and ultrahigh energy cosmic rays. Extreme high energy neutrinos ($>$1 PeV) can be a result of the GZK effect where also very high energy pions are formed. These neutrino candidates are called cosmogenic neutrinos. High energy neutrinos can also originate from the annihilation of dark matter particles, Weakly Interacting Massive Particles (WIMPs), in heavy objects (like the center of the Earth, the Sun or the Galactic Halo); or from the decay of exotic processes. An increase in overall noise rate would be signal caused by a huge flux of low energy (MeV) neutrinos from supernova explosions. In addition, the energy spectrum of neutrinos from secondary cosmic rays in extensive air showers can be measured in detail [98]. Typical neutrino searches therefore look for excesses of neutrinos over the downgoing muon and upgoing atmospheric neutrino background, at very high energy (diffuse searches) where a differen shape of the astrophysical flux would be distinguishable from the known atmospheric flux. Other searches look for clustering of neutrinos in direction and/or in time, either blind or near known sources (such as the Sun for WIMP searches). The denser instrumentation in the center that forms the DC subarray, effectively lowers the energy threshold and creates the possibility to use some parts of the detector as veto layer. WIMP searches at lower energies become possible and even the neutrino oscillation measurements can be performed [99].

The 1.5 km ice sheet which shields the IceCube detector from low energy cosmic rays and most secondary particles from high energies creates a unique opportunity for cosmic ray measurements. The only secondaries that are able to propagate to those depths and create signals in the deep detector are high energy muons (typically above 500 GeV). For coincident events which pass through both IceTop and IceCube, the electromagnetic component essential for primary energy measurement and the high energy muons which probe the composition is detectable at the same time.

2.2.1 Ice as medium for muon detection

Charged particles lose energy while they propagate through matter. Depending on the particle type and its energy this happens through several processes. Secondary cosmic ray particles, which IceTop aims to detect, are dominated by high energy (GeV) photons, electrons and muons. IceCube is designed for the detection of neutrino's from all flavours, that interact in the ice (or bedrock) and create electrons, muons and tau's. For cosmic ray studies only the detection of high energy muon bundles matters.

The secondary electromagnetic particles generate electromagnetic cascades according to the same principle as in extensive air showers discussed in Section 1.2.1, but in snow above the tank and in the ice in the tank instead of in air. The charged particles in the electromagnetic cascades have sufficiently high energy that they emit Cherenkov light, which propagates through the tank and gets reflected a few times against the

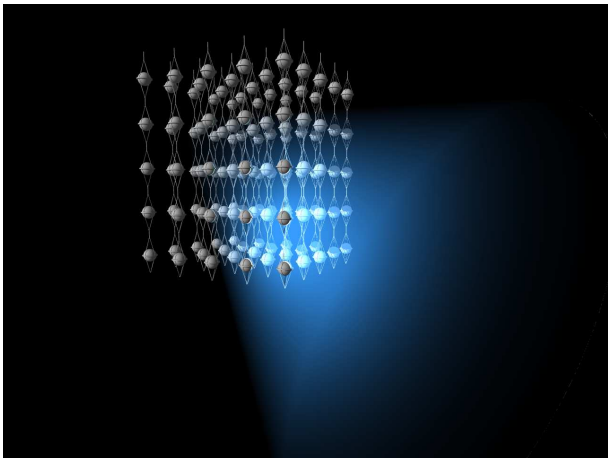

Figure 2.9: The detection principle in IceCube, represented by the cube with instrumented strings, where a muon that passes from the right bottom corner to the top left corner through the detector creates a Cherenkov cone with dominantly blueish light.

bottom and walls of the tank until it gets detected by the downward facing DOMs or absorbed. The secondary muons detected by IceTop are dominated by 2-5 GeV muons that directly emit Cherenkov light, proportional with the tracklength of the muon in the tank.

High energy muons lose energy through ionisation and are above 800 GeV dominated by radiate energy losses, which again create electromagnetic but also hadronic cascades in the ice. The light IceCube detects from high energy muon bundles is therefore a combination of bare Cherenkov emitted by the muon itself and Cherenkov light created by the cascades from the energy losses in the ice (see Fig. 2.9) Below we will discuss the Cherenkov light mechanism more in detail for muons and focus on the energy loss of high energy muons in South Pole ice.

Cherenkov light

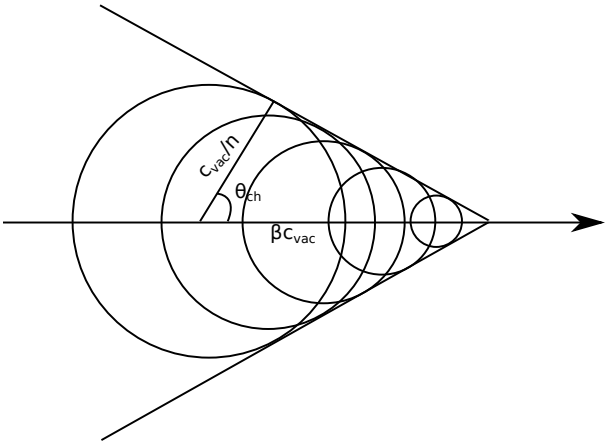

Figure 2.10: Huygens construction that illustrates the creates of a coherent electromagnetic wavefront for charged particles travelling faster than the speed of light in a medium.

Charged particles with a speed $v = \beta c$ that exceeds the phase speed of light in a medium with index of refraction $n_p(\omega)$, $\beta c \geq c/n_p$ or $\beta \geq 1/n_p$, polarize the surrounding medium where along each track

element of the propagating particle brief electromagnetic pulses are emitted such that they create a coherent electromagnetic wavefront. This can be illustrated by a simple approximation using the Huygens construction in Fig. 2.10 where the electromagnetic waves are emitted such that a coherent wavefront only exists if $\cos\theta_c = (c/n_p)/(c\beta) \leq 1$ or $\beta \geq 1/n_p$. The result is particle which drags a cone of Cherenkov light, named after Pavel Cherenkov who discovered it in 1934 [100, 101], behind it. The energy radiated per track length by the particle, derived first by Frank and Tamm in the classical theory from the Maxwell equations [102, 103], is:

$$-\left(\frac{\mathrm{d}\,E}{\mathrm{d}\,x}\right)_{\text{Cherenkov}} = \frac{\alpha Z^2}{c}\int_{\beta n_p(\omega)\geq 1}(1-\frac{1}{\beta^2 n_p^2(\omega)})\omega\,\mathrm{d}\,\omega, \tag{2.1}$$

with c the light speed in vacuum, α the fine structure constant, Z the charge of the particle and $n_p(\omega)$ the frequency dependent refractive index of the medium. Later quantum treatments have been derived as well, but resulted in forms which only differ slightly from the classical theory and mainly in the form of higher order terms [103]. The emitted radiation can also be expressed in an emitted number of photons, with the help of the Planck relation $E = Nh\nu = N\hbar\omega$:

$$\left(\frac{dN}{\mathrm{d}\,x\,\mathrm{d}\,\omega}\right) = \frac{\alpha Z^2}{c}\left(1-\frac{1}{\beta^2 n_p^2(\omega)}\right)$$

$$\left(\frac{dN}{\mathrm{d}\,x\,\mathrm{d}\,\lambda}\right) = \frac{2\pi\alpha Z^2}{\lambda^2}\left(1-\frac{1}{\beta^2 n_p^2(\lambda)}\right) \tag{2.2}$$

$$\tag{2.3}$$

The Eq. 2.1 and 2.2 are called the Frank-Tamm formula. In IceCube, the refractive index $n_p \approx 1.31 - 1.33$ [104], which results in Cherenkov cone with an angle of about 41°, an energy loss of about 400 eV/cm for photons with wavelengths between 400 nm and 700 nm, or roughly 220 emitted photons per cm all for highly relativistic particles with $\beta \approx 1$. For smaller β, the Cherenkov angle narrows and less photons are emitted until $\beta < 1/n_p$ where there will be no more coherent electromagnetic wavefront. The kinetic energy Cherenkov threshold for muons in South Pole ice is ≈ 55 MeV, and for electrons ≈ 0.26 MeV.

While the emission of the Cherenkov photons at an angle θ_{ch} that depends on the phase refractive index, the photon propagate through matter at group velocity $v_g = c/n_g(\omega)$. Also the approximation made in the Huygens construction that the ray direction is normal to the wavefront is only valid for a frequency-independent refractive index [104, 105]. However, the approximation is still very useful for pedagogical purpose.

Minimum ionizing muons with an energy above the Cherenkov threshold produce Cherenkov light according to the Frank-Tamm formula and emitted along the Cherenkov angle θ_c. At higher energies, the energy loss processes (discussed in next section) create electrons, either direct or through pair-production from emitted γ-rays, and other charged particles (photo-nuclear?) with energies above the Cherenkov threshold. Those electromagnetic or hadronic cascades therefore also emit Cherenkov light and contribute to the light detected by the detector modules. The energy loss processes with small energy transfer are very frequent and can be approximated as quasi continuous. In [106], this process has been parametrized as additional Cherenkov emitting track segment dl_{add}:

$$dl_{\text{tot}} = dl_0 + dl_{\text{add}} = dl_0 \cdot (1.172 + 0.0324 \cdot \log(E_\mu/\text{GeV})), \tag{2.4}$$

which describes additional Cherenkov light well for secondary $e^{\pm}$ with energies below 500 MeV and γ's up to 1 GeV. Above those secondary energies the energy transfer becomes larger and the stochastic nature of the secondaries more apparent. Localized electro-magnetic cascades, induced by Bremsstrahlung, pair-production, δ-rays, and hadronic cascades, induced by photo-nuclear interactions, appear and for TeV muons and above will dominate the Cherenkov light production. In [107], the Cherenkov emitting track length

parametrization from [106] has been revisited and updated as follows:

$$dl_{\mathrm{EM}} = 5.21\mathrm{m/GeV} \cdot 0.924/\rho \cdot E_{\mathrm{casc}}/\mathrm{GeV} \tag{2.5}$$
$$dl_{\mathrm{had}} = F \cdot 5.21\mathrm{m/GeV} \cdot 0.924/\rho \cdot E_{\mathrm{casc}}/\mathrm{GeV} \tag{2.6}$$
$$\tag{2.7}$$

where $\rho = 0.9216$ is the ratio of the density of ice (at the center of IceCube (1950 m, T=-30.4°C) and water; and F the ratio of the total tracklength of a hadronic cascade and an electromagnetic cascade. Hadronic cascades are initiated by a hadronic interaction, which then also creates electrons and photons that start an electromagnetic component of the total hadronic cascade. The energy dependent scaling factor F can be parametrized as

$$\bar{F} = 1 - (E_{\mathrm{casc}}/E_s\mathrm{GeV})^{-m} \cdot (1 - f_0), \tag{2.8}$$

with $\bar{F}$, the average of a Gaussian from simulation, $f_0 = 0.467$ the ratio of hadronic and electromagnetic light yield, $m = 0.13$ an arbitrary parameter and $E_s = 0.399$ GeV the extrapolated energy at which the cascade is totally hadronic. For electromagnetic cascades this comes down to $\sim 1.15 \cdot 10^5$ Cherenkov photons per GeV and $\sim 0.61 \cdot 10^5$ photons per GeV for hadronic cascades (using 220 photons per cm). Most of these additional Cherenkov emitting track segments are close to the track and the angle with the track is small because the energy loss photons and electrons are predominantly emitted in the forward direction. As a consequence the Cherenkov light from the energy loss cascades is mainly emitted with the same angle as the Cherenkov light of the naked muon. The difference is however that a more diffuse Cherenkov cone of light is created instead of a bright, sharp one from single particles (Fig. 7.44 in [106]). The parametrizations stated in Eq. 2.4 and 2.5 are the ones used for the simulation in this analysis. The study of Cherenkov light from high energy muons and cascades has been updated since in [108].

High energy muon energy loss

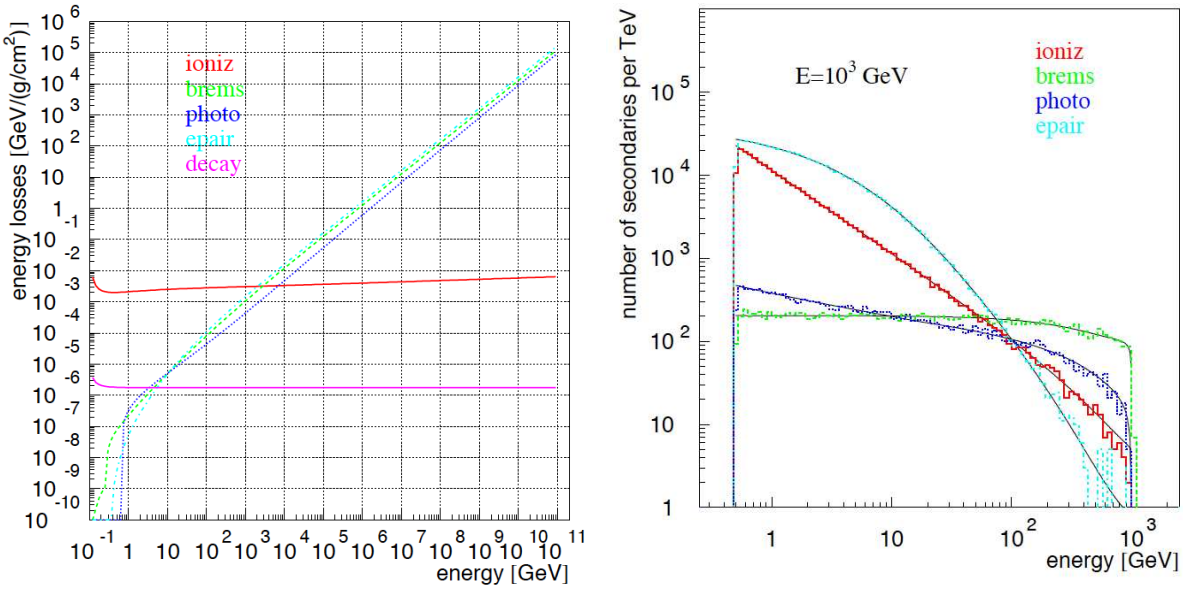

Figure 2.11: **Left**: All muon energy loss processes as function of the muon energy: Ionization (dominant below 1 TeV), Bremsstrahlung, photonuclear interaction, e^+e^- pair production (dominant above 1 TeV) and muon decay. **Right**: The energy distribution of the electron-or photon-induced electromagnetic (hadronic for photonuclear interaction) cascades for a 1 TeV muon [109]

.

When particles propagate through matter they lose energy by interacting with the atoms of the material. The type of interaction and also the type of energy lose depends on the energy of the particle. The Cherenkov light produced by high energy muons depends both on the muon energy and the energy of the energy processes as discussed in the previous section. Therefore a good understanding of the muon energy loss in Antarctic Ice over a broad energy range is important to be able to correctly interpret the detected light signal in function of the muon bundle energy loss behaviour.

At very low energies ($\beta \approx 0.001 - 0.01$) the muon interacts mainly with the nucleus as a whole and loses kinetic energy through nuclear recoil. As the muon energy increases ($\beta\Gamma > 0.1$), the muon interacts with the atomic electrons. With sufficiently high energy the muon will excite the atom and for even higher energy ionizes the atom, with a threshold around $\beta\Gamma = 3. - 3.5$. These electronic energy losses dominate the muon energy loss up to the muon critical $E_{\mu,c}$ when radiative energy losses become more dominant; and are well described by the Bethe's equation in the region $0.1 \lesssim \beta\Gamma \lesssim 1000$ up to a few % [105]. The energy loss through Cherenkov radiation ($\beta\Gamma \gtrsim 1.14$) is included in Bethe's formula, but only gives a small contribution of maximum 40 keV/m.

For high energy muons ($\beta\Gamma > 200$ or $E_\mu > 20$ GeV) the mean energy loss (also called stopping power) can be described by:

$$\begin{aligned}\frac{\mathrm{d}\,E_\mu}{\mathrm{d}\,x} &= \left(\frac{\mathrm{d}\,E_\mu}{\mathrm{d}\,x}\right)_{\mathrm{ion}} + \left(\frac{\mathrm{d}\,E_\mu}{\mathrm{d}\,x}\right)_{\mathrm{pair}} + \left(\frac{\mathrm{d}\,E_\mu}{\mathrm{d}\,x}\right)_{\mathrm{nucl}} + \left(\frac{\mathrm{d}\,E_\mu}{\mathrm{d}\,x}\right)_{\mathrm{Brems}} + \left(\frac{\mathrm{d}\,E_\mu}{\mathrm{d}\,x}\right)_{\mathrm{delta}} \\ &= a(E_\mu) + b(E_\mu)E_\mu \\ &\approx a + bE_\mu. \end{aligned} \tag{2.9}$$

The first term is the electronic or also ionization energy loss and is approximately energy-independent, described the constant $a = 0.259$ GeV/mwe. For very high energies the electron from the ionized muon has sufficient kinetic energy to ionize other atoms and trigger an electromagnetic cascade. The energyloss from these δ-electrons or knock-on electrons is included partially in the ionization term and partially taken into account by the inelastic Bremsstrahlung term. When high energy muons decelerate due to the interaction with the surrounding medium the will emit Bremsstrahlung photons. The Bremsstrahlung cross-section has two main contributions, one from the elastic interaction with the nucleus which the nucleus intact, and an inelastic component that changes the final state of the nucleus. The elastic component of the Bremsstrahlung energy loss is typically added to Bethe's formula and regarding as part of the ionization term. The most dominant process for muon energy loss above 1 TeV is e^+e^- pair production (see Fig. 2.11) through small energy transfer between the muon and the nucleus or an atomic electron. The muon can also exchange virtual photons with the quarks inside the nucleons of the matter it traverses, which will result in new hadronic particles and hence create a hadronic cascade. This inelastic interaction is called photonuclear interaction. Compared to the continuous, energy independent ionization energy loss, the other processes are more stochastic in nature due to the quantum mechanical probability in emitting an electron or photon, expressed by the individual cross sections. Above the critical energy $E_{\mu,c} = a/b$ radiative energy losses dominate but are all together well described by a linear energy dependence, $(\mathrm{d}\,E_\mu/\,\mathrm{d}\,x)_{\mathrm{rad}} = bE_\mu$ [110, 109, 111]. In Antarctic ice the stochastic or radiative energy loss constant $b = 0.363 \cdot 10^{-3}\mathrm{mwe}^-1$. The fitparameters for a and b from [109] have a 3.7% accuracy. The largest uncertainties are in the photonuclear cross-section at the highest energies, because this is calculated by non-perturbative QCD and therefore hard. The muon energy loss is expressed in GeV/(g/cm^2), which is material indepedent. To calculate the energy loss in Antarctic Ice, the correct ice density ρ_{ice}, which is a function of the ice temperature, should be used.

On Fig. 2.11 the separate contributions of all the energy loss processes as function of the muon energy, with muon decay added. Below 1 TeV ionization energy loss ionization loss is dominant, while above 1 TeV pair production is most pronounced, followed by Bremsstrahlung and then photonuclear interaction. On the right, the energy distribution of the secondaries shows that pair production creates lots of low energy stochastics and can therefore later be modelled as quasi-continuous. Photonuclear and even more, Bremsstrahlung are less frequent but are more likely to create large energy losses and are thus much more stochastic. The high energy tail of ionization comes from the knock-on electrons.

The medium : South Pole Ice

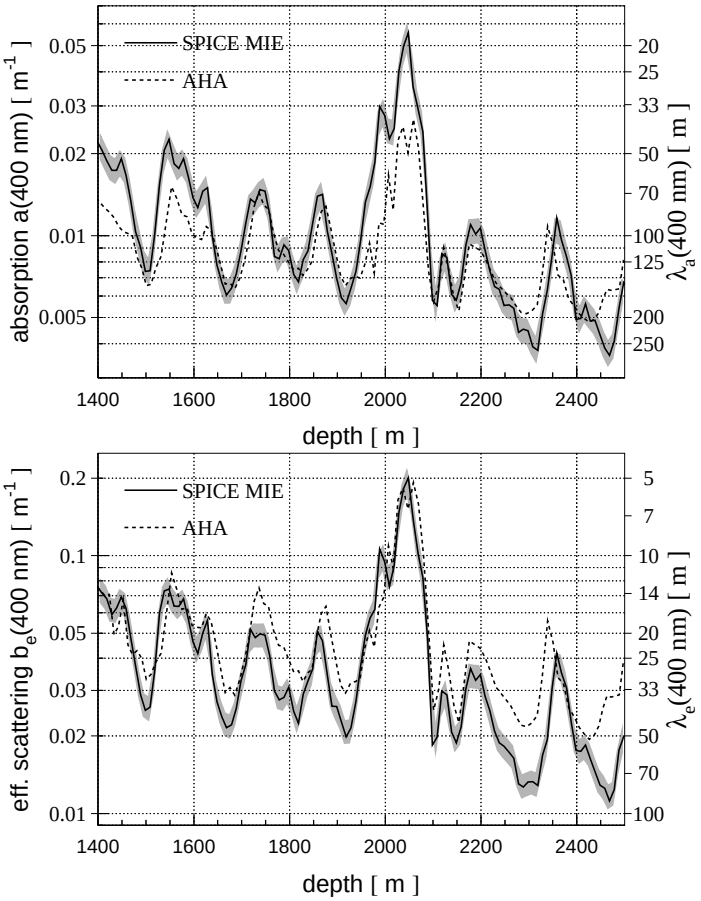

Figure 2.12: Absorption (top) and scattering (bottom) coefficient (left axis) or length (right axis) for a wavelength of 400 nm based on *in situ* LED measurments as a function of the depth in IceCube's depth range. AHA is an older IceModel based on AMANDA measurements, while SPICE Mie is the latest IceModel using IceCube LED flasher measurements. The grey band is a 10% global uncertainty (statistic + systematic).

As the atmosphere and the snow, which will be discussed in Section 2.3, the Antarctic ice forms an important part of the IceCube detector because IceCube is actually a large ice calorimeter. The South Pole is actually a huge glacier situated 2835 m above the bedrock and the top 2000 m is flowing at roughly 10 m/yr along the 40 degree west meridian. In the two previous sections the importances of both the wavelength dependennt refractive index, for Cherenkov light emission and the velocity of light propagation (group refractive index), and the density of the ice, for muon propagation, became clear. From the Frank-Tamm formula and the energy loss behaviour we know how many photons are created, but to know how many photons the detectors will actually see depends on the optical properties of the ice, namely the scattering and absorption length. Scattering delays the photons and gives longer waveforms. Absorption reduces the amount of photons that will hit the DOM.

The temperature profile from the ice surface to the bedrock has been measured by deploying thermistors at several depths on AMANDA strings and reading them out in 2001 after all holes were refrozen and stable. The temperature of the South Pole ice is $\approx$-45° at the top of IceCube at 1450 m and $\approx$-20° at the bottom of IceCube at 2450 m [112].

The Antarctic ice does not have a uniform bulk structure. The first 1000 m the ice contains large concentrations of air bubbles that result in very short scattering lengths. At intermediate depths between 1000 m and 1500 m the air bubbles are more and more compressed due to the increasing pressure and form solid

air-hydrates. Light passes through these air hydrates with almost no scattering. At $\sim$ all air bubbles transformed in this solid phase and scattering and optical properties of the ice below 1500 m only depend on the dust concentration in the ice. This was learned from measurements during the AMANDA construction summarized in [113]. Based on this conclusion, IceCube deployed its detector modules all below 1450 m in the clearer, bubbly free ice. Using pulsed and steady light sources (lasers and LEDs on AMANDA OMs) the first detailed measurement of the optical properties of the ice were made [113].

The measured optical properties show a strong layered structure of the ice between 1400 m and 2500 m (see Fig. 2.12). Four large peaks are visible, at 1550 m (peak A), at 1725 m (peak B), 1875 m (peak C) and 2050 m (peak D or "the dust layer"). These correspond to four stadials[1] in the last glacial period. Peak A is 39000 yr old, peak B is 46200 yr, peak C is 55300 yr and peak D is 66000 yr old [114]. Below the big dust layer (peak D) the layered structure is still present but the ice is overall much clearer than above the dust layer, which motivated the deployment mode for DeepCore. As expected this big dust layer (and the whole layered ice structure too) will highly impact the depth dependence of the observed number of photo-electrons. To observe photo-electrons in the dust layer the track should either pass very close to the DOM, or the energy loss at that depth should be very large (big Bremsstrahlung-induced cascade and/or large muon multiplicity).

Because the data did not agree well with the optical properties from [113], the measurement has been improved by using the LED flashers on IceCube DOMs and an improved fit procedure [115]. Using the LEDs from string 63 at maximum brightness and pulse width several specialized flasher runs were taken in 2008 to create a symmetric light pattern around string 63. With a maximum likelihood procedure the scattering and absorption coefficients (at 405 nm) iteratively change from unbiased bulk ice values to the values that fitted all emitter-receiver pairs both in total charge and in charge per 25 ns time bin, to disentangle absorption and scattering, best. The predicted charges used by the (Poisson-based) likelihood come from a fast simulation with direct photon propagation through the ice with the properties of each iteration. The resulting ice model, called SPICE-Mie because a combination of Henyey-Greenstein and a simplified Mie scattering function were used, describes the data much better. The absorption and scattering coefficients at 405 nm with their overall 10% uncertainty are shown in Fig. 2.12, compared to the initial AHA measurement from [113]. In the same reference the wavelength of both coefficients and temperature dependence of the absorption coefficient is parametrized by a six-parameter ice model, which is also used by the SPICE-Mie model.

In each of the consecutive polar seasons between 2004 and 2011, detailed dust measurements with dust loggers [116, 117] were performed in eight IceCube holes (21, 50, 66, 52, 10, 2, 86 and 14 in order of deployment). These measurements reveal the structure of the dust layers in extreme detail down to a millimeter and demonstrated the existence of the tilt in the ice layers. The depth dependence of the optical properties is not uniform over the array but has xy-dependence. Data from the dust logging of the first seven holes showed great consistency with the properties derived from flashers in the SPICE-Mie ice model and the ice model was additionally improved based on the dust logger data and including the tilt. Recently evidence of an anisotropy in light propagation due to a slight azimuthal dependence of the optical properties of the Antarctic Ice was reported in [118] and taken into account in an updated version of the SPICE-Mie ice model. Both the tilt and anisotropy prove great challenges for using the ice properties in simulation and reconstruction.

2.2.2 Deployment

To put DOMs into the ice one first has to drill holes to a depth of 2450 m. This is accomplished by the use of hot water under high pressure to melt away the ice. Underneath the top layer of accumulated natural snow is a 50 m layer of compacted snow ("firn"). This layer cannot be melted away using a stream of hot water as the water would just run through the snow without melting it away. Therefore a so-called firn drill, consisting of heated copper tubes (see Fig. 2.13), to dig through the firn layer. Afterwards the firn drill is removed and drilling with an enhanced hot water drill (EHWD) commences (top left in Fig. 2.13). The EHWD pushes hot water (90°C) under high pressure through a nozzle to melt away the ice. The water cools down, gets pumped upwards, heated and circulated. A water-filled hole which protects the hole against

[1] A stadial is a period which are too short or not intense enough to be considered glacial periods.

Figure 2.13: Top left: The two drills needed for drilling through the Antarctic ice with the firn drill on the left and the enhanced hot water drill (EHWD) on the right. Top center: Firn drilling drilling through the 50 m layer of compacted snow. Top right: The EHWD drilling a 2450 m hole with hot water. Bottom left: The resulting IceCube hole. Bottom center: Attaching the DOMs to the IceCube cable. Bottom right: Dropping the cable DOM by DOM until they are at their designated locations.

collapse and suited for optimal coupling of the detector modules during refreezing is created. In the last couple of deployment seasons two drills were used and the whole procedure took on average 48 h. Next, a huge cable which carries power and signals between the DOM and the DAQ is deployed and the detector modules are attached with DOM spacing that depends on the type of string (IceCube or DC configuration) (bottom center in Fig. 2.13). When all DOMs are deployed, the cable is lowered into hole until the DOMs are situated at the desired positions. During deployment the inter-DOM spacing is measured and pressure sensors are used to monitor the depth of the string. Finally, after the hole is completely refrozen the DOMs are switched on and commissioning of the string starts. The LEDs on the DOMs (called “flashers”) are used for a more accurate determination of the exact, relative position of the DOMs.

The whole deployment of the IceCube detector took 7 seasons and was completed on December 18, 2010 when the last string was successfully deployed. The deployment scheme of strings and IceTop stations per season can be seen in Table 2.1.

Season	Number of IceCube (DeepCore) strings	Number of IceTop stations	Configuration Name
2004-2005	1	4	IT-4/IC-1
2005-2006	8	12	IT-16/IC-9
2006-2007	13	10	IT-26/IC-22
2007-2008	18	14	IT-40/IC-40
2008-2009	18 (1)	19	IT-59/IC-59
2009-2010	15 (5)	14	IT-73/IC-79
2010-2011	5 (2)	8	IT-81/IC-86

Table 2.1: Construction of IceTop stations and IceCube strings with DeepCore strings between brackets.

2.3 Environment

The environment surrounding the detector is also part of our detection volume. It influences the detector response by changing the energy and amount of detected secondary particles. At South Pole the environment is not fixed but constantly changes. There are short-term variations, like pressure variations, wind (oa. causing snow drifting) and longer term variations, like seasonal variational in the upper atmosphere and snow buildup.

The main goal of the experiment is to measure the properties of cosmic rays before they interact in the atmosphere, hence the detection volume starts at the point where the primary particle interacts. Hence the knowledge and detailed measurement of the part of the detector which we do not control is crucial in performing a good, detector independent measurement about the cosmic ray flux and composition.

2.3.1 Snow

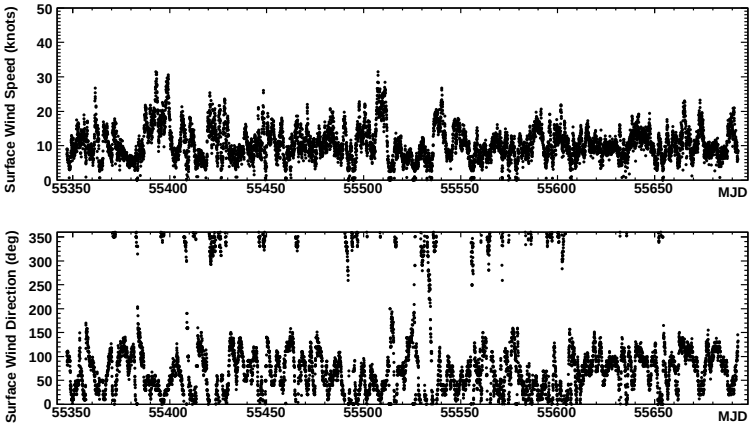

Figure 2.14: Top: Wind speed at South Pole during the IT-73/IC-79 data taking period (June 1, 2010 – May 12, 2011) Bottom: Wind direction at South Pole during the same period, both using data obtained from AMRC [119]

Precipitation at the geographic South Pole is very light (average of 8.6 cm water equivalent) and comes in the form of very light snow or predominantly ice crystals. These ice crystals fall on clear days and create effects like halos and sundogs. The light snow is moved around on the surface by the prevailing winds, which is coming from 020 degrees grid northeast, and which blows with average speeds of 11 knots ($\sim$ 20 km/h) with average maxima up to 30 knots (see Fig. 2.14) [120]. Yearly this gives rise to an average snow accumulation of 22 cm with a spread of 12 cm. On Fig. 2.16 the snow accumulation distribution for the 146 tanks is plotted. The snow accumulation goes even up to 60 cm as shown on the Figure.

In addition to the average snow accumulation, the snow is not distributed uniformly over the square kilometer array. The prevailing wind blows the snow against slopes in the terrain as shown in Fig. 2.4 and against buildings, present in the IceTop array, like the IceCube Laboratory (ICL). Moreover, tanks deployed in earlier seasons have endured less snow accumulation then freshly deployed tanks which have zero snow height at the beginning of the season because they are deployed with their lids level to the snow surface. The result (Fig. 2.15) is an uneven distribution of snow with areas that have no snow to areas with almost 2 m of snow. Snow is therefore an uncontrolled part of the IceTop detector.

Snow has two large effects on the detection of air showers with IceTop. The threshold of the detector, caused by low energy showers which just have enough secondary particles to hit 3 stations and pass the filter condition. With an extra layer of snow on top of the detector, the particles of those low energy showers get seriously attenuated and do not trigger the tanks anymore. Higher energy showers are necessary to pass the

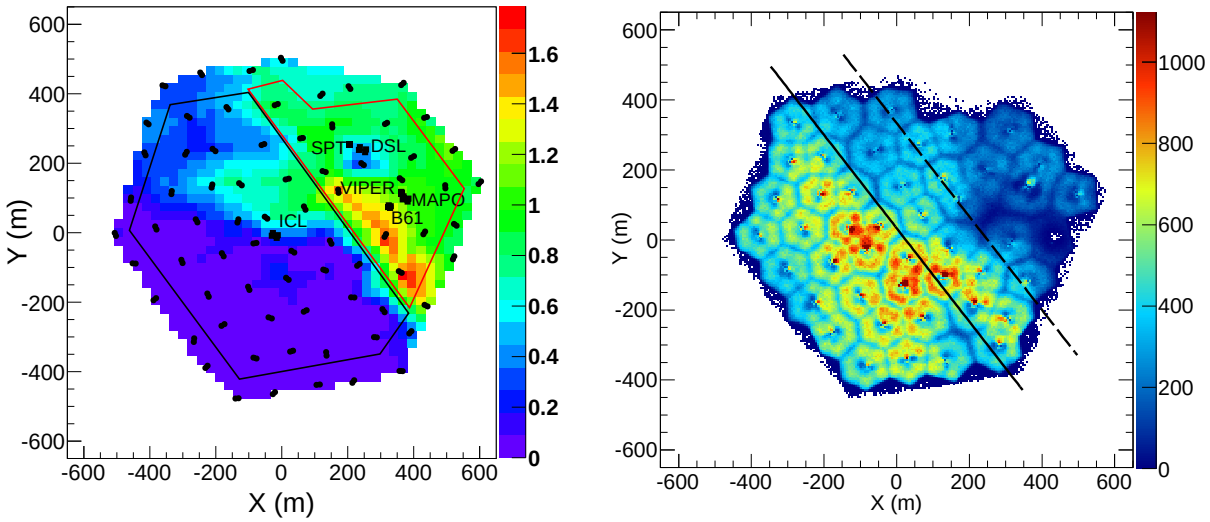

Figure 2.15: **Left**: Snow cover in meters in February 2010. The black dots are IceTop tanks, the acronyms are buildings (IceCube Laboratory, South Pole Telescope, Martin Pomerantz Observatory, VIPER: a telescope for CMB observations, Dark Sector Laboratory and Building 61: an electrical substation with backup generator. **Right**: Distribution of shower core positions at final event selection for the full 2010-2011 data. Parts of the array with less snow see more events as well regions furthest from the stations.

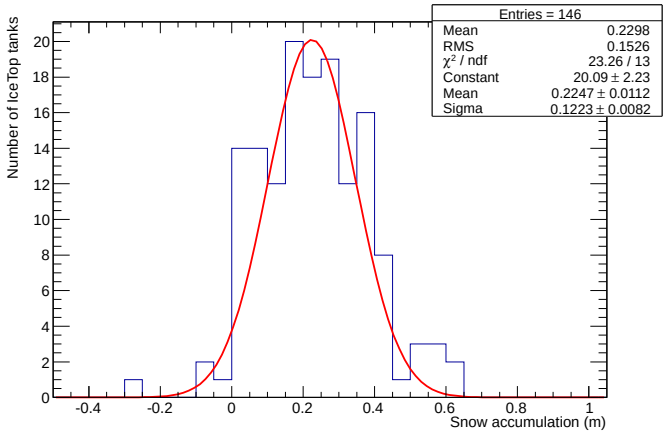

Figure 2.16: Snow accumulation between February 2010 and February 2011 for the 146 IceTop tanks present during the IT-73 data taking.

initial snow layer and then still have enough particles to trigger the tanks. Hence the uneven distribution of snow creates a location-dependent threshold which has to be correctly simulated to treat in efficiency calculations. Figure 2.15 illustrates on the right the different thresholds of the detector. In the new part of the detector, more showers are detected, because the threshold is lower and the flux of lower energy showers is higher. The second effect is the different relation between the detector response and the primary energy, which is derived from simulations. The particle density, which results in a measured signal, from an air shower with some primary energy is attenuated by the amount of snow on top of the tanks. Muons are highly penetrating particles and propagate through the snow almost unharmed. Because the snow coverage

is different for every tank, the electromagnetic particle density is attenuated differently for each tank and the lateral distribution changes. Showers that fall in a part of the array with a low snow coverage, create larger signals than if it would have fallen in a part of the array with more snow. This has to be treated properly in reconstruction which will be discussed in Section .

To properly treat the snow coverage of the array, which is an important part of the detector, in simulation and reconstruction the snow properties at South Pole are measured in detail. On top of each tank is surface marker attached to signal which tanks are deployed where. The height of these markers is well measured. Therefore the snow height can be easily measured manually every season by measuring the part of the marker that sticks out of the snow. In case the markers were buried by the snow, well measured marker extensions were added. Unfortunately these measurements are only feasibly during the Polar summer. Because snow is building up unevenly throughout the intermediate 10 months, more regular measurements are needed.

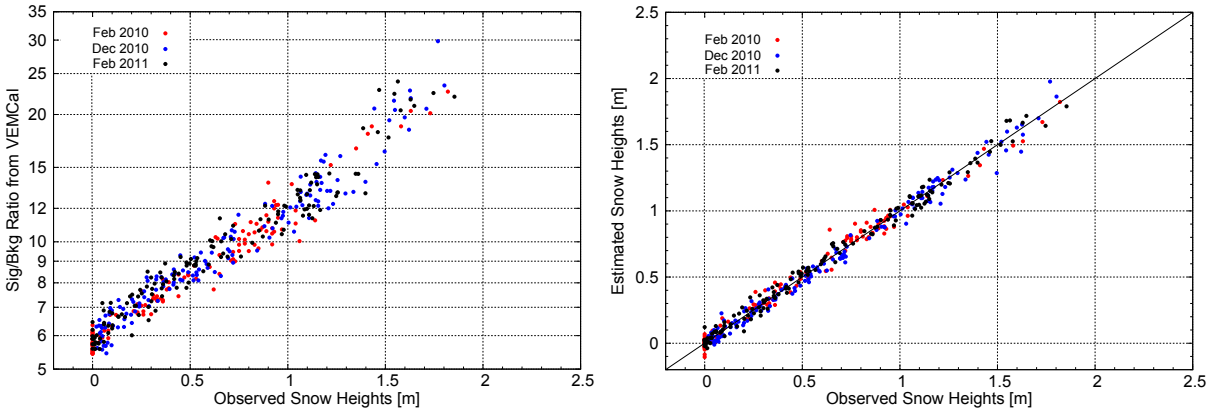

Figure 2.17:

For the charge calibration of the IceTop tanks (see Section 2.6.2), the muon spectrum caused by low energy events which trigger only one tank gives rise to a exponential electromagnetic background with a gaussian-like muon peak. Snow only affects the electromagnetic contribution and will leave the muon component unharmed. Therefore the change of the ratio in muon signal f_μ over electromagnetic background f_{EM} gives us a measure of the snow height:

$$S_\mu/B_{\mathrm{EM}} = \frac{\int_{0.3\mathrm{VEM}}^{2.0\mathrm{VEM}} f_\mu \,\mathrm{d}\, S}{\int_{0.3\mathrm{VEM}}^{2.0\mathrm{VEM}} f_{EM} \,\mathrm{d}\, S}. \tag{2.10}$$

The relation between the S_μ/B_{EM} and the snow height is calibrated with respect to the yearly manual snow height measurements and is fit by the following model :

$$h^{est}_{snow}(t, tank) = A \cdot \log(S_\mu/B_{EM}) + C_{i,tank}, \tag{2.11}$$

with t : three measurements (Feb 2010, Dec 2010 and Feb 2011), $A = 1.19$ a common fit parameter for all tanks, and $C_{i,tank}$ a tank dependent fitparameter. The fitresult is illustrated by Fig. 2.17. The left plot shows the correlation between the ratio of muon signal over EM background and the snow heights. The estimated snow heights obtained from the fitresult compared to the measured snow heights can be observed in the right plot. Fig. 2.18 shows that the snow heights from the calibration data nicely overlap with the yearly measurements over four years. The two stations (19 and 21) are very close to each other but have a very different snow accumulation profile. While station 19 hardly had any snow and also did not gain a lot of snow in the IT-73 data taking period, while tank 21A received an extra 60 cm of snow to reach a snow

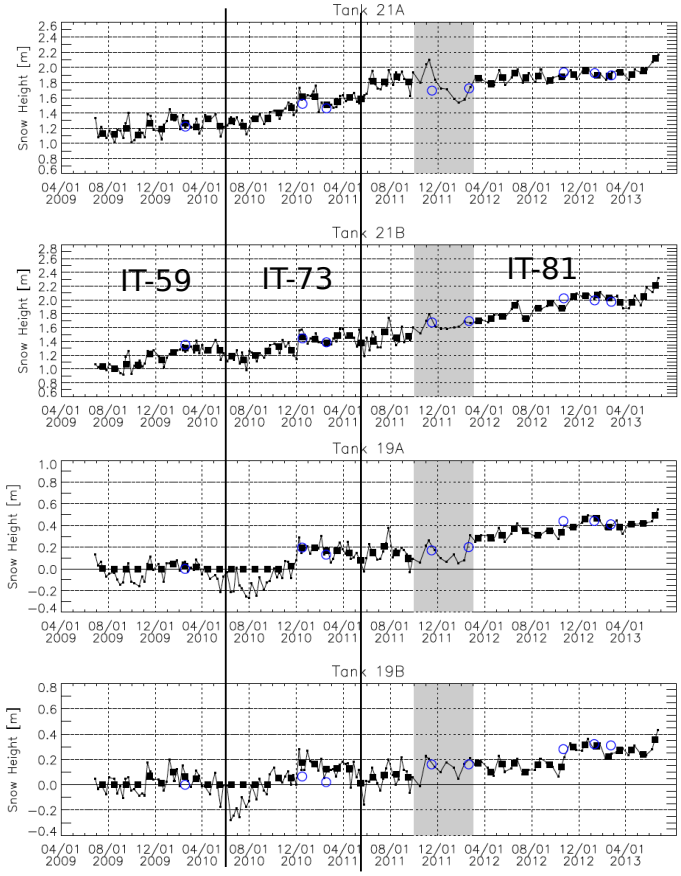

Figure 2.18:

height of almost 2 m at the end of the data taking period. Correct snow height measurements for each tank are therefore crucial for acquiring a good energy resolution.

To correctly account for the location dependent energy threshold and to study correction techniques for snow in reconstruction, snow needs to be simulated. Apart from the individual snow heights above each tank, explained above, the density of snow is an important parameter in the simulation. In Jan 2010, detailed snow density measurements were performed [121] at several locations on and near the IceTop site and at different depths. This was done by determing the mass of fixed volumes (cylinders) of snow samples. Near the trenches where the tanks are deployed, the snow density is quite large (0.42 g/cm^3) and decreasing for larger depths (to 0.34 g/cm^3). This is caused by the compactification of the top snow layers by heavy machines running over the snow during the construction phase. In naturally accumulated snow, measured outside the IceTop array, the density is hardly depth dependent and has a constant value of 0.36 g/cm^3. Detailed simulation of this location and depth-dependence snow density is however very difficult and a value of 0.38g/cm^3 is used as an average.

2.3.2 Atmosphere

The South Pole atmosphere forms an important part of the IceCube Neutrino Observatory. Variations in the lower altitudes impact air shower measurements by IceTop while the variations in the stratosphere affect atmospheric muon and neutrino fluxes detected by IceCube. The average pressure at the IceTop surface is 680 hPa (cfr. 1013.25 hPa at sea level) or an atmospheric depth of 692 g/cm^2. The pressure variation of up to 30 g/cm^2 during the data taking period for the analysis presented in this thesis can be seen in Fig. 2.19. The tilted position of the Earth's axis of 23° with respect to the ecliptic plane gives rise to winters of complete

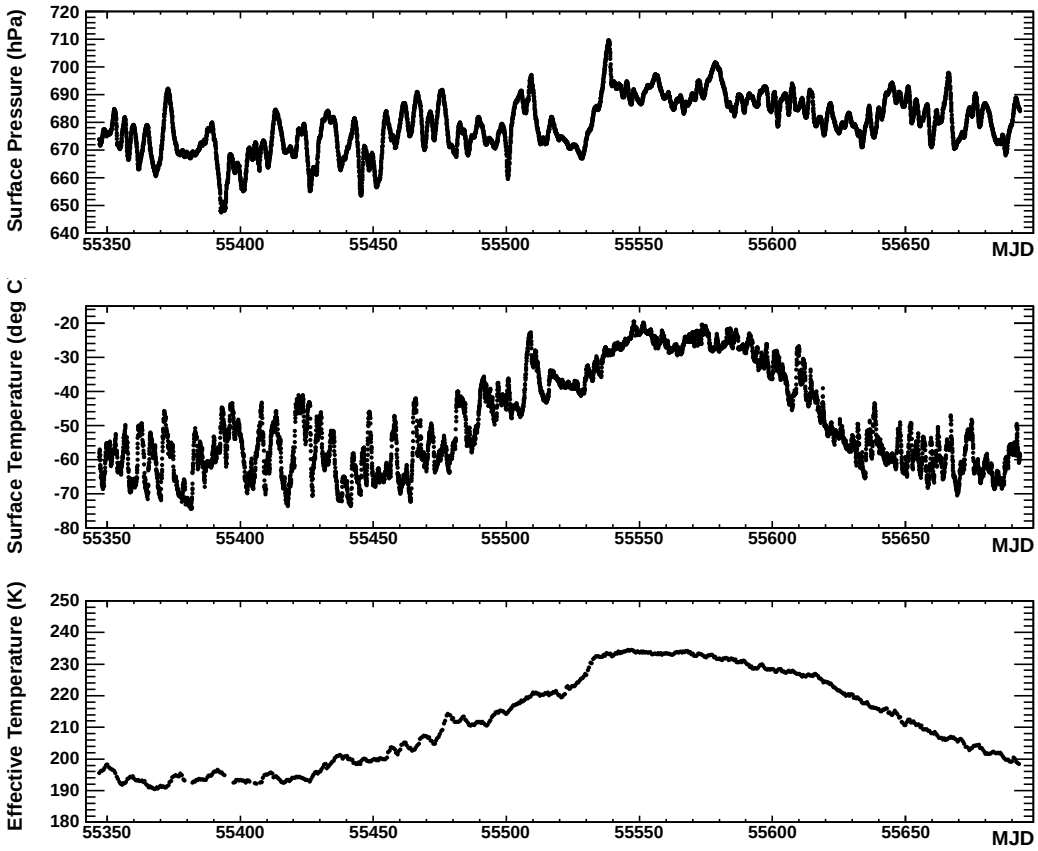

Figure 2.19: The variation of the atmosphere at South Pole during the IT-73/IC-79 data taking period (June 1, 2010 - May 12, 2011) with data from [119]. Top: The surface pressure in hPa. Middle: The surface temperature in °C. Bottom: The effective temperature in K.

darkness and summers with 24h of daylight at South Pole. As a consequence of the long lack of sunlight at high altitudes during the austral winter and the days with 24h of daylight in austral summer, the temperature variation is one of the highest in the world and changes between -25°C and -75°C with an annual average of -50°C. On top of the large daily pressure and temperature variations there are also large seasonal variations, visible in Fig. 2.19.

The sun heats the Earth so typically the temperature decreases for increasing altitude. At South Pole there is an inversion layer of about 500 m where the temperature first increases before decreasing with increasing altitude because the snow and ice cools down the air. In winter there is no solar radiation to compensate for the cooling hence the inversion layer in winter has a stronger temperature gradient (see Fig. 2.20) while in austral summer it is very small to non-existant. Furthermore, large seasonal variations also exist in the lower stratosphere because variation in UV absorption of solar radiation by ozone which increases or decreases heat release in the atmosphere and thus creates large temperature variations. Large surface and upper air temperature variations give rise to large seasonal density and pressure variations [122, 123]. These are caused by a matter transport during spring to South Pole and during autumn away from South Pole caused by the variation in katabatic winds from the South Pole to subpolar regions created by a pressure gradient combined with the high altitude of the Antarctic plateau [124].

The effects of the atmosphere on air shower measurements are similar as the effects of the snow, which is discussed above. The difference is that the whole atmosphere contributes and effects the formation of extensive air showers while snow only alters the secondary particles just before they enter the IceTop tanks.

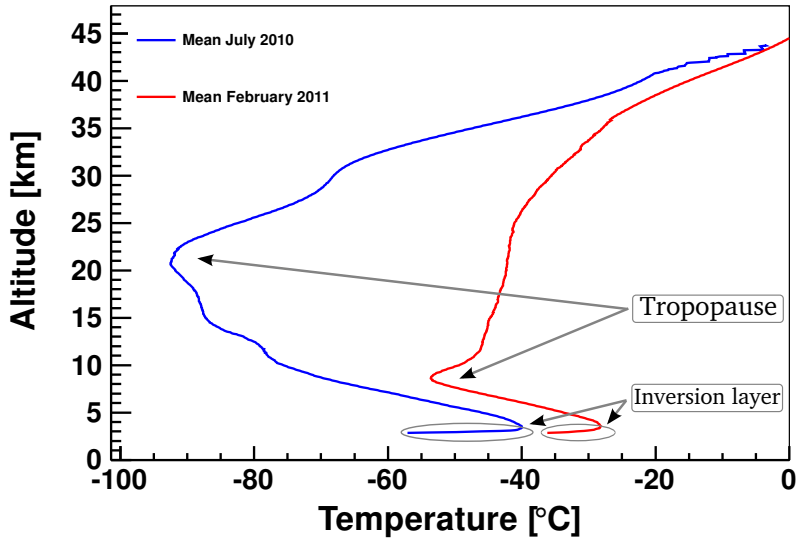

Figure 2.20: The mean temperature profile at South Pole of July 2010 compared to the mean profile of February 2011 from [122]

IceTop rates are anti-correlated with the ±17% surface pressure variation [125], because a high pressure means a larger amount of matter that the showers have to cross, or also a larger atmospheric depth. To survive a larger atmospheric depth showers need a larger primary energy. The flux of higher energy showers is lower, hence the anti-correlation of the surface pressure with the rates. The IceCube muon rate variation is correlated with the ±10% seasonal variation, typically quantified by an effective temperature, defined as a temperature integrated over the whole atmospheric profile weighted with the probability for pion and kaon decay [126, 32]. Also the ±5% variation in atmospheric neutrino flux is correlated with the variation in effective temperature [127]. Both the muon and the neutrino flux are caused by the decay of high energy pions and kaons high in the atmosphere. A higher upper air temperature means a lower local air density which decreases the interaction probability and increases the decay probability, hence more muons and neutrinos. The variation in effective temperature from June 1, 2010 to May 12, 2011 is shown on the bottom of Fig. 2.19 and clearly illustrates the seasonal variations.

Similar to the second effect of snow, the atmospheric changes also affect the distributions of the secondary particles at ground level and the relation between shower size and primary energy will thus depend on the atmospheric conditions. The secondary particles which create signals in the IceTop tanks mainly come from interactions and decays in the last layer of atmosphere above the detector. Changes in the pressure and density of this layer, which can be quite large on daily basis as visible in Fig. 2.19, affect the interactions and influence fluctuations, lateral distributions. However, in [122] and other studies the effects have been shown to be much smaller than the influence of snow. A large effect, which will be accounted for in this analysis in Section 4.2.2, is the change in muon multiplicity due to seasonal variation. The reason is the same as for the change in muon rate, but the muon rate originates from cosmic ray flux, while the muon multiplicity changes from shower to shower depending on its primary energy and primary mass.

2.4 The Digital Optical Module (DOM)

The most important detector element of both the IceCube in-ice detector and the IceTop surface array is the Digital Optical Module (DOM) [128]. A schematic of the DOM is shown in Fig. 2.21, with a picture of a DOM with its upper glass hemisphere on the right. The DOM consists of 25 cm diameter photomultiplier

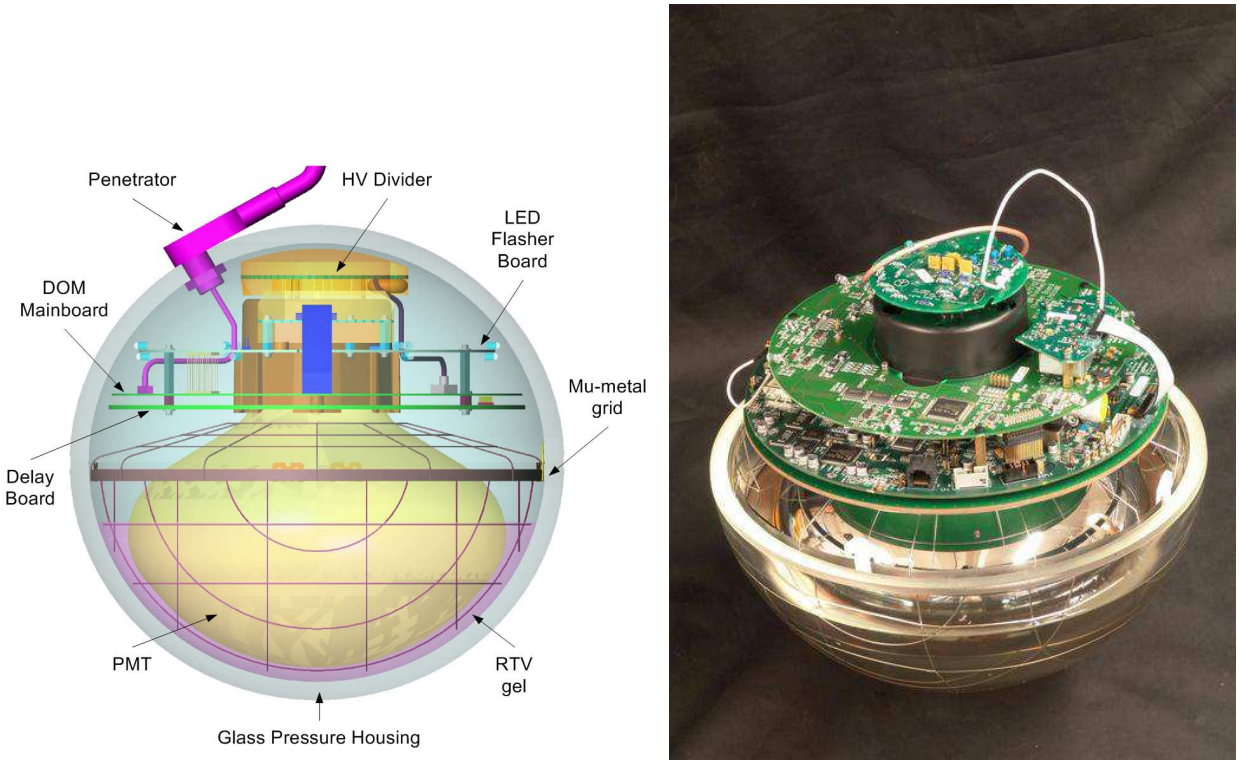

Figure 2.21: **Left**: Schematic of the DOM. **Right**: Picture of a semi dismantled DOM without the upper glass hemisphere.

tube (PMT) (Hamamatsu R7081-02), a modular 2 kV high voltage (HV) power supply for the PMT, the DOM Main Board (MB), a signal delay board and an LED flasher board. These are housed in 13 mm thick glass sphere to withstand the pressure at large depths. The whole assembled DOM is filled with nitrogen to a pressure of half an atmosphere.

Most DC strings use DOMs with a PMT (Hamamatsu R7081MOD) with a higher quantum efficiency to more sensitive to low energy events. The standard PMTs have a quantum efficiency of $\sim$25% at 390 nm, while the DC DOM PMTs have a 40% higher quantum efficiency [99]. The PMT [129] is shielded from the Earth magnetic field by a mu-metal grid that serves as Faraday cage and thus improves the PMT performance. To reduce the loss of photons it is optically coupled to the glass sphere through a flexible gel. The glass and gel set the short wavelength of the DOM at about 350 nm.

When Cherenkov photons arrive on the glass surface near the photocathode of the PMT and dependent on their wavelength and where the enter the glass sphere because the angular acceptance is not isotropic they have a probability of passing through the glass and optical gel and create a photo-electron on the photocathode through the photo-electric effect. From a single photo-electron (PE) up to hundreds of PEs for IceCube or even hundreds of thousands of PE for IceTop then get accelerated in the PMT and create 10^5 to 10^7 times more electrons on a sequence of dynodes at different voltages until they finally hit the anode. For IceCube DOMs, which need to be sensitive to a single photo-electron (SPE), the gain is at 10^7 (HV$\approx$1.5 kV), while IceTop uses 2 DOMs per tank set at high gain (HG) of 10^6 and a low gain (LG) DOM at $5{\cdot}10^5$. At the anode we then have a measurable analog pulse of a -8 mV for an SPE (at $1{\times}10^7$ gain) [129] up to a few volts. The DOM MB decides then whether the pulse is interesting enough to be digitized and buffered until it gets a request from the DAQ in the ICL to transfer some buffered data.

The block diagram of the DOM MB in Fig. 2.22 illustrates the signal capture and digitization. The high voltage PMT anode is AC coupled to the front-end amplifiers on the DOM MB with toroidal transformer (Top left in Fig. 2.22). This will create an undershoot of the signals below baseline and a recovery with a time

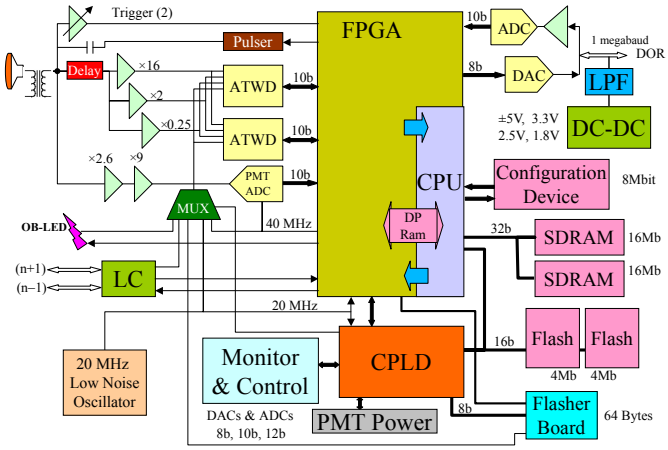

Figure 2.22: Block diagram of the DOM Mainboard with the PMT AC coupled by a toroid transformed to the MB in the top left corner and the ATWD digitizers in the center.

constant that depends on the toroid and the temperature. During calibration this so-called droop is corrected. The signal is then split to 75 ns delay line and the PMT discriminator trigger. When the signal passes a certain discriminator threshold (0.25 times the SPE amplitude for InIce DOMs, $\sim$20 mV for IceTop HG DOMs and $\sim$4 mV for IceTop LG DOMs) the FPGA orders the DOM to start the signal capture and digitization for up to 6.4μs. After the 75 ns delay line, the signal is split and amplified with different gain ($\times$16, $\times$2, $\times$0.25) for optimal digitization for small, medium and large pulses and are called channel 0, channel 1 and channel 2. Then the Analog Transient Waveform Digitizer (ATWD) captures the three signals in 128 analog samples at a rate of 300 Mega Samples Per Second, roughly in 3.3 ns time bins. When the ATWD gets triggered (by the PMT discriminator) to digitize, the 128 samples stored on a set of 128 capacitors are digitized with 128 independent 10 bit (or 1024 channels) ADC converters. If there are samples in channel 0 with more than 768 counts, then channel 1 is digitized as well and the same goes for channel 2. After conversion, the digital signals are transferred to the FPGA. The whole digitization process requires 29μs per ATWD channel. To reduce deadtime there are two ATWDs (ATWDa and ATWDb) that work in a ping-pong fashion. When a DOM retriggers after 6.4μs one ATWD is still digitizing so the other one can start a new hit capture sequence. The PMT signal also gets continuously sampled at 40 Mega Samples Per Second, 256 samples in 25 ns bins, up to 6.4 μs by a fast ADC (FADC) after the signal went through a 180 ns shaping amplifier.

To time stamp the hits, the DOM uses a local clock within the FPGA driven by a 20 MHz oscillator doubled to 40 MHz inside the FPGA. These clocks are calibrated with respect to a Master Clock in the ICL that is synchronized to UTC time through GPS by a producedure, called RAPCal and is described in detail in [128]. In addition to signal capture and digitization the DOM can also calibrate itself by using on-board electronic and LED pulsers.

The Flasher Board hosts 12 LEDs, 6 horizontal and 6 tilted with an angle of $\sim$45° with respect to the flasher board, that produce UV optical (405 nm) pulses which can be set in brightness and are used for simulating event topologies, determining the exact position of the DOMs, and investigate the optical properties of the ice.

2.5 Triggering and Filtering

2.5.1 The trigger

The event-wise trigger forms the decision on whether all DOMs from the IceTop and IceCube detector should be read out. As the readout process creates dead time, the trigger condition cannot be cannot be too loose. On the other hand too strict trigger conditions creates the loss of potentially interesting events. The trigger condition for all different triggers are based on a number of hit detectors from some subdetector in a certain time window according to some logic depending on the type of trigger.

Local Coincidence

The event starts with one to thousands of Cherenkov photons arriving on the photocathode of the PMT. The PMT transforms this into an analog pulse on its anode. If the pulse passes the PMT discriminator ("Trigger" in Fig. 2.22) threshold, the FPGA orders the ATWDs to start the full waveform capture and digitization of the analog signal. For IceTop the MPE PMT discrimator threshold is set to a nominal 7 PE threshold (which means an effective 20 PE threshold if the DOMs in both tanks of a station have to pass the 7 PE threshold). As the PMT does not measure a charge, but an amplitude, the threshold for HG DOMs is set (with the DAC) to about 20 mV. For LG DOMs, the SPE discriminator threshold is used instead and set at 270 PE or about 4 mV. The SPE discriminator threshold for the PMT of InIce DOMs is set at 0.25 PE and tuned on DOM-by-DOM basis.

While the ATWD is processing and digitizing the waveforms, which takes 29μs, the DOM sends out a local coincidence (LC) message to its neighbours. For InIce DOMs the LC tag is sent to its neighbours above and below, which send the LC tag message one DOM further. If there is no confirmation of this local coincidence message, meaning that one of the DOMs that received the message also receives a signal that passed the PMT discriminator threshold, within a time window of 1μs then the FPGA aborts the digitization procedure of the ATWD. Hence the hard local coincidence requirement (HLC) is that two neighbour or next-to-nearest neighbour DOMs are hit with a signal above the PMT discriminator threshold, in a 1μs sliding time window. When the InIce DOM fulfills this HLC requirement, it will send its full digital waveform to the surface (ICL), where it will be further processed for an event-wise trigger. As IceTop is a surface air shower array, the HLC requirement is slightly different. If a HG DOM is hit (sees a signal passed the discriminator threshold), it will send its LC tag to the HG and LG DOM in the neighbouring tank of the same station. When both HG DOMs of the same station, or one HG and one LG DOM, are hit, within a 1μs time window, the station fullfills the HLC requirement for that station and the full waveform information of all DOMs in the tanks is sent to the DOMHub in the ICL. As the HLC requirement reduces the noise from single tank hits, mainly caused by single muons, for IceTop and from PMT dark noise or isolated signal photons in IceCube, the deadtime of the DOM is significantly reduced.

Since the 2009-2010 season IceCube is running in soft local coicidence (SLC) mode. This means that hit information from DOMs which did not fulfill the HLC requirement is also kept and send to the surface. As opposed to the full, highly compressed ($\sim$ 150 bytes/record), waveform information from all channels and the FADC for HLC DOMs, only the time stamp and the three largest FADC samples are transmitted for SLC IceCube DOMs. For IceTop SLCs, the sum of the all 128 samples of the first non-saturated ATWD channel, or chargestamp is transmitted. The advantage of the SLC hits is that they can still be related to the event formed by the HLC DOMs, but because there is also a much higher probability that these are isolated noise this, the SLC mode keeps the dead time still small.

Different triggers

HLC hits from IceCube and IceTop are send to computers, called DOMHubs, which each control either a complete IceCube string or 8 IceTop stations, in the IceCube Laboratory (ICL) at the surface. The program Stringhub converts the coarse time stamps of hits to UTC time and time ordens them. The time ordened hit

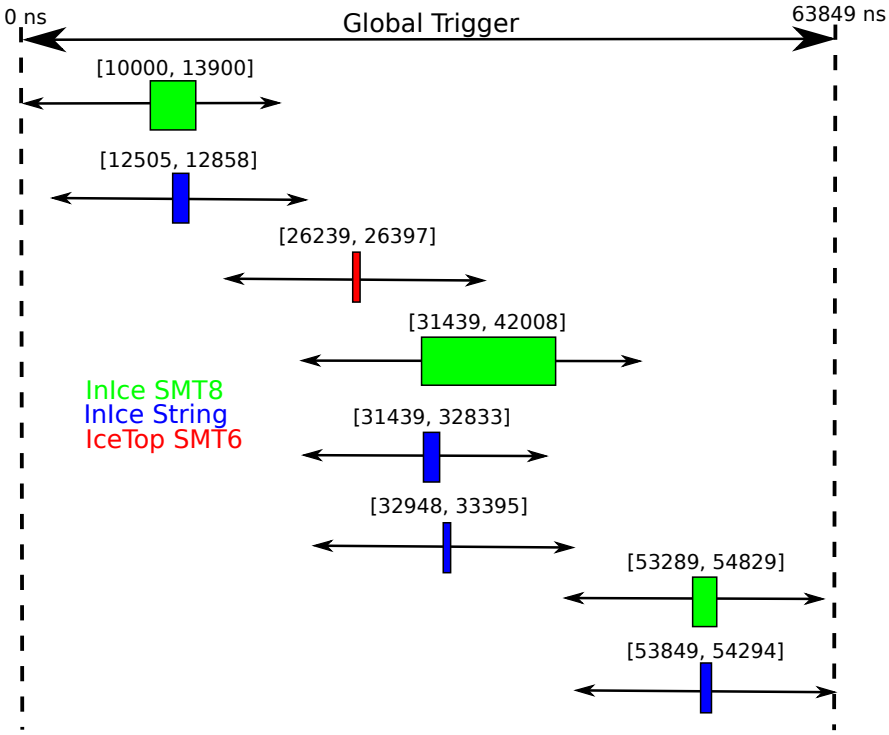

Figure 2.23: The trigger scheme for one long event. The times show the start time and end time of different trigger types, while the arrows illustrate the readout time. The global trigger merges all individual readout windows.

summaries, basically the DOM information and its time stamps, are then evaluated by the trigger system. The full hit information is cached by the Stringhub, pending the trigger and readout decision.

The different trigger types are summarized in Table 2.2. The Simple Majority or Simple Multiplicity Trigger (SMT) looks for M hits within a certain sliding time window. The difference between the three SMT triggers is that they work on different DOM sets. For example the DeepCore SMT works on the bottom 50 DOMs from strings 81-86 and the bottom 22 DOMs on strings 26, 27, 35, 36, 45 and 46. The StringTrigger looks for M DOMs out of N adjacent DOMs on the same string, while the MinBias trigger just triggers every 2^{10}th (or 1024^{th}) hit. The IceTop Calibration trigger, triggers on hits used for VEMCal, explained in Section 2.6.2

The SMT trigger for IceTop and IceCube are crucial for the coincident IceTop-IceCube analysis presented in this thesis, so we will discuss these in more detail , although the description is applicable to most other triggers too. The SMT triggers scans all time ordened hits and looks for M HLC hits (6 for IceTop, 8 for IceCube) in a 5μs time window. The hit time of the first DOM (also called DOM launch start time) of those M defines the start time of the trigger. As long as there are more HLC hits in the 5μs window, the time window keeps sliding and the trigger length increases. This means that the last HLC hit of the SMT can be up to 4.9μs later than the previous last HLC hit. The hit time of the last hit defines the end of the trigger and hence defines the trigger length. All found individual trigger are sent to the global trigger system, which first for each trigger creates a global trigger that defines the time window in which IceTop and IceCube hits should be readout up from the buffer on the DOMHub, also called readout window. The readout window for the subdetector in which the trigger happened is defined as some value (eg. 4μs for InIce SMT) before the starting time of trigger and some value (eg. 6μs for InIce SMT) after the end of the trigger. For the hits in the other subdetector, the readout window is defined around the starting time of the trigger alone [130]. The values for the readout windows of all triggers from the 2010-2011 season are in Table 2.2. Multiple different triggers can have overlapping trigger windows, but SMT triggers of the same type can not overlap. Of course

with multiple triggers, the readout windows also overlap. Therefore the global trigger system merges all readoutwindows. An example from an event from a real data event is shown in Fig. 2.23. The global trigger result and readout windows, separate for IceTop and IceCube, are sent back to the Stringhub and the full event is created by the "Event builder" from the buffered hits.

Trigger name	Parameters	Readout	Rate (Hz)
In-Ice Simple Multiplicity	TriggerWindow = 5μs NHit $\geq$ 8	IceTop : $\pm$10 μs InIce : -4, +6 μs	1952
IceTop Simple Multiplicity	TriggerWindow = 5μs NHit $\geq$ 6	All : $\pm$10 μs	29.2
DeepCore Simple Multiplicity	TriggerWindow = 2.5μs NHit (DC DOMs) $\geq$ 3	IceTop : $\pm$10 μs InIce : -4, +6 μs	179
In-Ice StringTrigger	TriggerWindow = 1.5μs NHit $\geq$ 5 out of 7 adjacent	IceTop : $\pm$10 μs InIce : -4, +6 μs	2062
IceTop Calibration	Hit Type = 4	All : $\pm$1 μs	29.0
IceTop MinBias	Prescale = 10000	All : $\pm$10 μs	0.31
In-Ice MinBias	Prescale = 200 Deadtime = 5 μs	IceTop : $\pm$10 μs InIce : -4, +6 μs	53.6

Table 2.2: The triggers with those used for this thesis in bold. The rates are from run 118134 on May 1, 2011.

2.5.2 Online filtering

The triggered event stream, collected by the DAQ, is too large to be transmitted to the North for analysis. The satellite (Tracking and Data Relay Satellite System (TDRSS [131])) bandwidth allocation for IceCube is 105 GB/day while the triggered data with raw waveforms constitutes almost 1 TB/day. A solution could be to store the data on tape and bring the tapes over yearly during the following Polar summer. However, this limits the data quality and data monitoring possibilities as well as online analyses (like SuperNova, GRB, flare analyses, triggered by satellites like SWIFT and ROTSE or triggering other detectors). An "online filtering system", which performs some more advanced and cpu intensive selections in realtime, is used instead. This "online filtering" reduces the bandwidth allocation to 70-80 GB/day, varying due to atmospheric variations and the position of the sun and the moon which is used for some dedicated filters.

Those filters run on an online filtering system, called PnF ("Processing & Filtering", shown in Fig. 2.24). Triggered events are send to the PnF server from the DAQ and are spread over several filtering clients. The filter clients run online waveform calibrations, feature extractions and reconstructions and perform some analysis specific selections. If the filter condition is passed, the prescale condition is checked. For some filters (like IceTopSTA3_10 and IceTopSTA3_InIceSMT_10) only prescaled, which means every n^{th} event is selected, are sent over TDRSS. All events from PnF, even those that did not pass any filter, are stored on tape at South Pole [132]. The filter selected events are moved by the South Pole Archival and Data Exchange system (SPADE) to a location where they are picked up by TDRSS every day.

The online filters are reviewed and potentially adjusted every new data taking season, which typically runs from May to May. The online filters implemented during the 2010-2011, relevant for the analysis in this thesis are described in Table 2.3. The filter requirements are very easy and only require a minimum number of hit IceTop stations and for some filters the additional presence of an InIce SMT trigger.

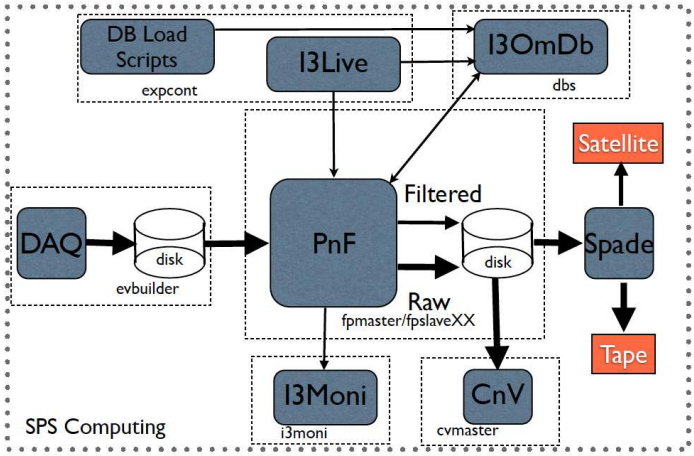

Figure 2.24: The "Processing and Filtering" system which gets triggered events from the DAQ, is controllable through i3live, has access to an online database with all detector and run information, performs the online filtering and sends all events and the filter selected events to SPADE, which either stores them on tape or sends them to the TDRSS satellite system for transmission up North. Figure from [132].

Filter name	Condition	Prescale	Rate (Hz)
IceTopSTA3_10	IceTopSMT & # stations ≥ 3	3	19.9 (6.6)
IceTopSTA8_10	IceTopSMT & # stations ≥ 8	1	1.3 (1.3)
IceTopSTA3_InIceSMT_10	IceTopSTA3_10 & InIceSMT	2	6.0 (3.0)
IceTopSTA8_InIceSMT_10	IceTopSTA8_10 & InIceSMT	1	0.4 (0.4)
InIceSMT_IceTopCoincidence_10	InIceSMT & # IceTop DOMs ≥ 1	100	92.1 (0.92)

Table 2.3: The cosmic ray filters with the filters used for this thesis in bold. The rates and bandwidth depend on atmospheric conditions and are from run 118134 on May 1, 2011. The numbers in between brackets are the prescaled rates.

2.5.3 Offline processing

After the filtered data is sent North over the satellite, the raw data is stored on disk in the data warehouse. A general offline processing is applied next. The level-1 (L1) processing performs the decoding of the compressed data. The geometry, calibration and detector status (GCD) information is retrieved from a general database and common for all events of the same run. With the help of the calibration constants stored in the GCD file, the calibration of the raw, digitized (in counts per time bins) IceTop and IceCube data is executed by the L1 processing. The essential information from the calibrated waveforms that will be used for reconstruction are the charge and time of the individual pulses. This is called feature extraction and is performed as last step of L1-processing. More details about how the calibration and feature extraction for IceTop and IceCube waveforms works will be explained in Section 2.6.

The main goal of level-2 (L2) processing is track reconstruction common for most analyses. For IceTop this means the reconstruction of the shower core and shower direction seeds with first guess algorithms, followed by a full maximum likelihood approach for determing the core, direction and lateral distribution at once. For IceCube the direction and energy estimates of the muon(s) detected by the IceCube DOMs is reconstructed. Essential for the reconstructions are hit cleanings of bad DOMs, broken or malfunctioning during that run, and unrelated hits to the event hit pattern. This is applied at L2 before the actual common reconstructions are performed. Details about the hit cleaning are in Chapter 5, while the reconstructions relevant for this analysis are described in detail in Chapter 4. After initial L2 processing of the IC79 (2010-

2011) data, serious problems with calibration and feature extraction of about 20% of the IceCube waveforms were found. A level-2a (L2a) processing was performed to fix these issues.

No events are cut away at L1 or L2 as these constitute the general offline processing common for all IceCube analyses. Event selections, quality cuts and more analysis specific (and cpu intensive) reconstructions are performed at higher level processing and are referred to as L3, L4, ...

2.6 Calibration and Feature Extraction

The raw data sent to the ICL and then over the satellite to the North contains digitized ATWD and FADC waveforms. The first step towards obtaining the real physics that caused a certain event and its detected group of waveforms is to "undo" the digitization by the DOMs (through which electronic cross-talk could be avoided, data compression increased and hence more events sent over satellite). The calibration of raw data tries to recreate as accurately as possible the actual analog pulse seen by the PMT in the DOMs. To be able to reconstruct the basic properties of the event like the track direction and also more detailed properties useful for identifying the type of event, the analog waveforms have to be interpreted first. The so-called feature extraction extracts the time and charge of either the whole pulse, or for large multi-photo-electron pulses the time and charge of each individual pulse of the whole waveform. That information is then used by reconstruction algorithms, described in Chapter 4, for calculating as many event properties as possible.

2.6.1 Calibration

The raw ATWD waveform consists of readouts from 128 independent digitizers. To convert the raw readout in ADC counts to a voltage, the pedestal and gain for each bin of each ATWD channel are needed. The pedestal is the value the digitizer reads when there is no input voltage. The software on the DOM itself corrects for this pedestal pattern. After this pedestal subtraction an overal baseline remains. An accurate knowledge of the remaining baseline better than one ADC count is crucial for a good calibration because an offset of one or more counts creates serious artefacts after droop correction. The best way to know the overall digitizer offset or baseline is given by beacon hits. These are random cpu-triggered hits at roughly 1 Hz and show the baseline when there was (in most cases) no PMT signal. Baselines for each ATWD chip, channel and the FADC are averaged over 3 runs from a single day each month (to prevent light contamination that happens in some IceTop beacons), stored in a database for usage by the calibration.The FADC is sampled and digitized continuously by a single digitizer and therefore has no bin-to-bin pedestal pattern, but only an overal baseline offset.

After baseline subtraction, the ADC counts are converted back to voltages by multiplying them by their gains (mV/count). The resulting waveform is in millivolt per sample. The length of each sample depends on the effective sampling frequency of the ATWD of roughly 300 MSPS, while for the FADC it is set at 40MSPS giving 25 ns samples. The real pulse information we want to use for reconstruction is the arrival time of each set of photo-electrons arrived at the photocathode. Therefore, a correction for the PMT transit time, time difference between the PMT pulse and the arrival time of the photo-electrons, and the delay for waiting for the trigger decision by the PMT discriminator trigger has to be applied as well by the calibration.

The AC coupling of the PMT to the DOM MB through a toroidal transformer also creates some shaping of the analog pulse measured by the PMT. Because of self-inductance the toroid creates an negative voltage when the PMT pulse is back at its baseline. This results in an undershoot which depends on the magnitude of the PMT pulse, which returns slowly back to its baseline. The characteristics of this droop effect depend on the toroid (toroid with impedances of 43 or 50 Ohm were used in IceCube DOMs) and the DOM temperature. These characteristics are expressed in time constants. The calibration applies a droop correction based on these DOM specific time constants, which were measured for some DOMs in the lab. During the analysis some DOMs did not seem to have correct time constants for the droop correction and mainly IceTop is effected. 10-15% of IceTop DOMs are affected. Although a lot of work was done to try to fix the droop

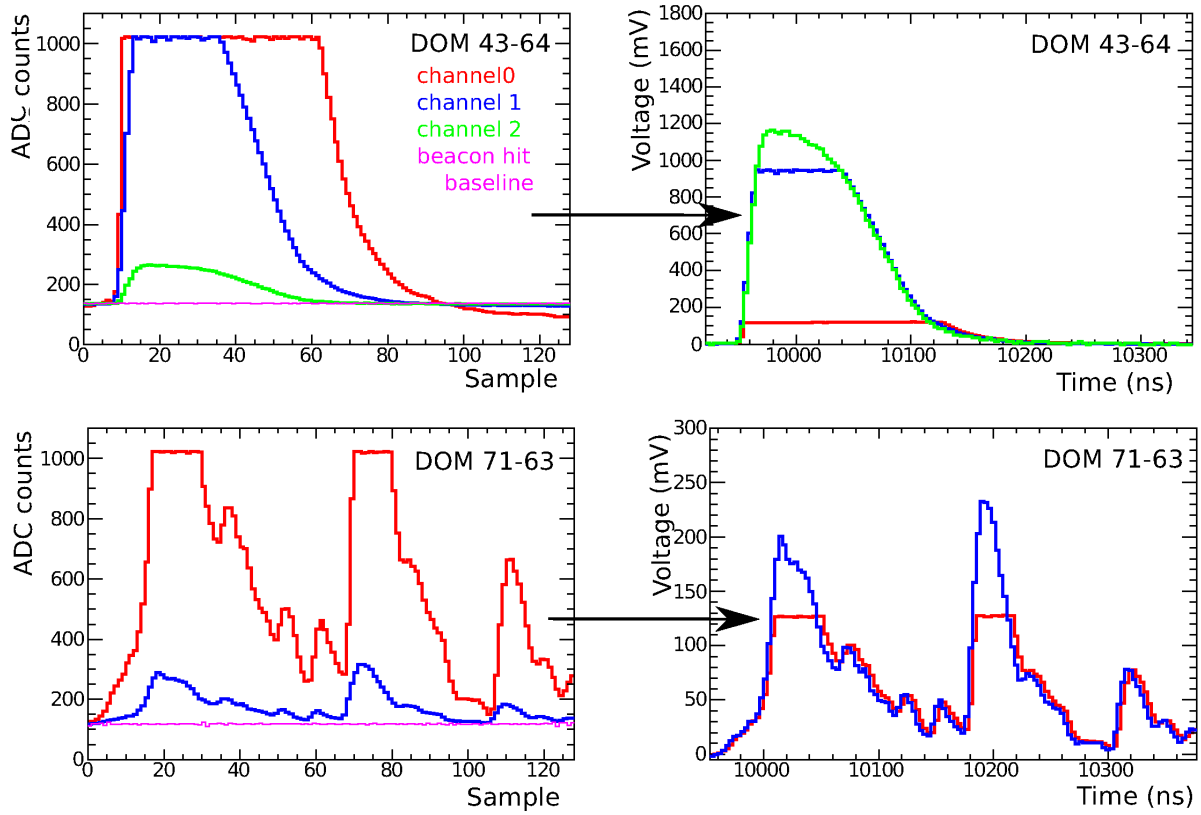

Figure 2.25: Two examples of raw, digital IceTop waveforms, one from DOM(43-64) which was very close to the core of an air shower on Dec 22, 2010, of a few hundred PeV and the other one from DOM(71-63) at hundreds of meters from the core of the same event. On the left side, the digitized waveform readout in all ATWD channels are seen, with the beacon hit baseline of the largest non-saturated waveform. On the right, the result of the calibration. IceTop does not use the FADC as air shower waveforms are typically short pulses, hence it is not shown here.

constants, there were still several unresolved problems. The effect of slightly wrong droop constants is not that bad as only the integrated charge above the baseline is used further in analysis as will be explained further. However, fixing the droop constants for those DOMs will be important for more advanced charge extractions. This has not yet been done up to date.

To determine the calibration constants mentioned above and some additional constants for measuring the PMT gain and other DOM-related quantities, IceCube runs monthly so-called DOMCal runs. DOMCal calibrates the ATWD voltage and sampling frequency, ATWD channel gains and FADC gains, PMT gains and transit times by using onboard electronic pulser and the onboard LED pulser. The calibration results are vetted and stored in a database which the calibration software can access.

On Fig. 2.25 the calibration procedure is illustrated by two characteristic IceTop waveforms, one DOM close to the core position of an air shower with PMT saturation (visible in the green waveform from ATWD channel2) and the other at a few hundred meters from the core with a more complex triple peak structure. Only if the previous ATWD channel has samples above 768 counts, the channel is digitized. Therefore there is no ATWD channel2 for DOM 71-63. Both beacon hit baselines are from the highest non saturated gain and perfectly describe the real pedestal offset (without pedestal pattern subtracted in the DOM itself). The calibrated result for both DOMs is shown on the right. The ATWD saturation, because there are only 10 bits available (or 1024 counts), illustrated clearly for both DOMs, propagates to different saturation values in mV due to the different gains of the channels. There is no baseline left, and the time conversion accounted for the

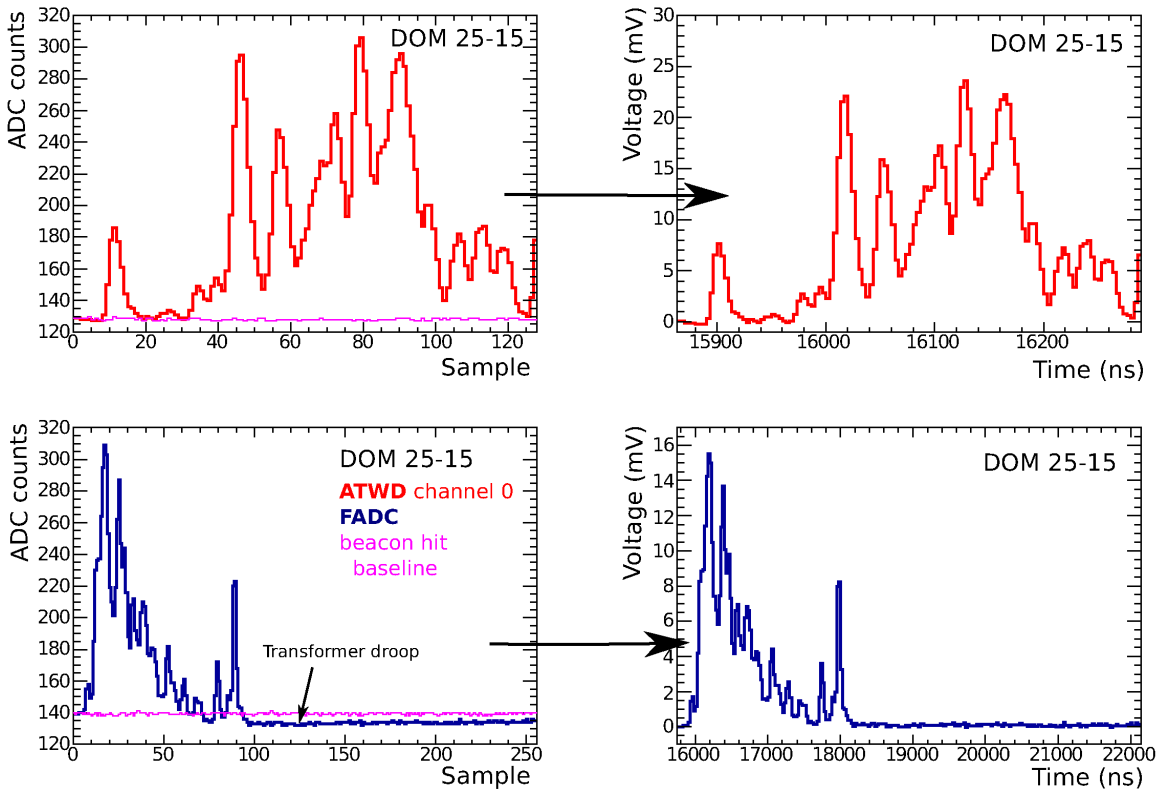

Figure 2.26: An example of an rather complex IceCube waveform in ATWD and FADC, both in digital format (left) and after calibration (right), with the corresponding beacon hit baseline shown.

sampling rate and is the arrival time, relative to the start of the readout of the whole event, of photolectrons at the PMT cathode. Also clear is the different sampling rate for the different gains which creates this apparent one bit offset between the calibrated waveforms.

A rather complex IceCube waveform from DOM 25-15, taken from a large muon bundle that accompanied the same air shower that generated both IceTop waveforms, is plotted in Fig. 2.26. Both ATWD channel0 with its 128 samples and the FADC with its 256 samples can be seen together with their respective beacon hit baselines that again very well describe the real pedestal offset. The transformer droop creates a clear undershoot under the baseline and for this DOM it only recovers very slowly, but that typically depends on the time constants of the toroid in the DOM. After calibration that corrects for this droop, there is no more baseline offset in the tail. Also clear is the advantage of both ATWD and FADC. The ATWD has a better resolution, sees for example an SPE in the very beginning of the waveform, but only over a short time window of about 422 ns, while the FADC has a coarser resolution but captures more delayed, scattered photons from longer and more complex events like this one and over a larger time window of 6.4 μs.

[**?**, 90]

2.6.2 Feature Extraction

IceTop

After calibration of the IceTop waveforms a simple feature extraction is performed. The waveform charge Q is obtained by integrating the whole waveform and calibrating it in units of single photo-electrons (PE) :

$$Q[C] = \frac{1}{R}\int U \,\mathrm{d}\, t = \frac{1}{R}\sum_t U \cdot \Delta t \tag{2.12}$$

$$Q[PE] = \frac{Q[C]}{\mathrm{SPE}[C]} \qquad \text{with} \quad \mathrm{SPE}[C] = G \cdot e \tag{2.13}$$

and where R the front-end impedance, which depends on the toroid type (old toroid : 43 Ohm, new toroid : 50 Ohm), U, and G the PMT gain, which can be HG or LG. The leading edge time of the waveform is defined as the arrival time of the whole waveform. It is calculated as the intersect between the baseline and a line connecting the bin where the waveform is at 10% of the amplitude of the first peak with the 90% bin. Hence each hit DOM yields a time and a integrated charge, that can be used by the reconstructions for core, direction and lateral distribution fits. However, several IceTop waveforms, typically those not too close to the core, exhibit a much more complex multipeak structure. Currently unfolding IceTop waveforms in multiple pulses is not yet been done but could provide a wealth of extra information for analyzing extensive air showers. An example of the IceTop feature extraction for the waveforms from Fig. 2.25 is visible in Fig. 2.28. The shaded area is the integral under the highest non saturated waveform. The leading edge calculation is illustrated by the fitted solid line. While the pulse structure of DOM 43-64 is rather simple and typical for signals close to the core location, DOM 71-63 shows the limits of the limits of the simple leading edge and total charge calculation. A multi-peak unfolding would clearly give a more accurate timing determination and would extract more information potentially useful for more advanced analyses. For this analysis using only total charge and leading edge time proved to be good enough.

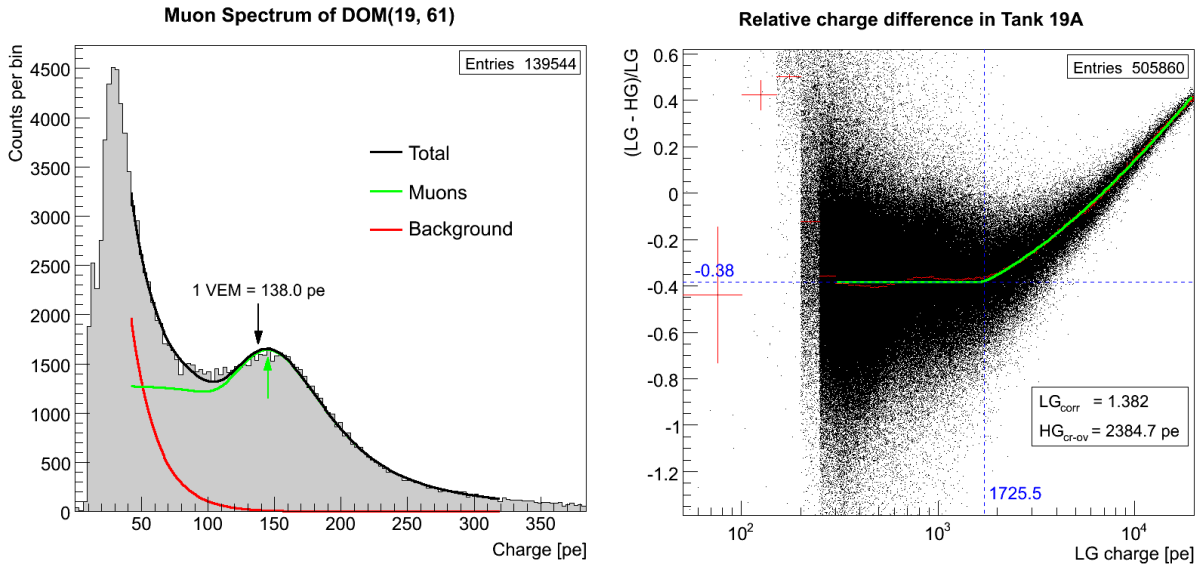

Figure 2.27: **Left**: The charge spectrum for tank 19A in PE from one week (the week of May 1, 2011) of MinBias data with the muon and electromagnetic fitted together and shown separately. The VEM for this tank is 138 PE. **Right**: The cross-calibration of HG and LG with the offset and cross-over value fitted.

There are two types of IceTop tanks: the older tanks and some IT-81 tanks have Tyvek liners while the other tanks have zirconium liners. Also the freezing processing in each tank is slightly different and the

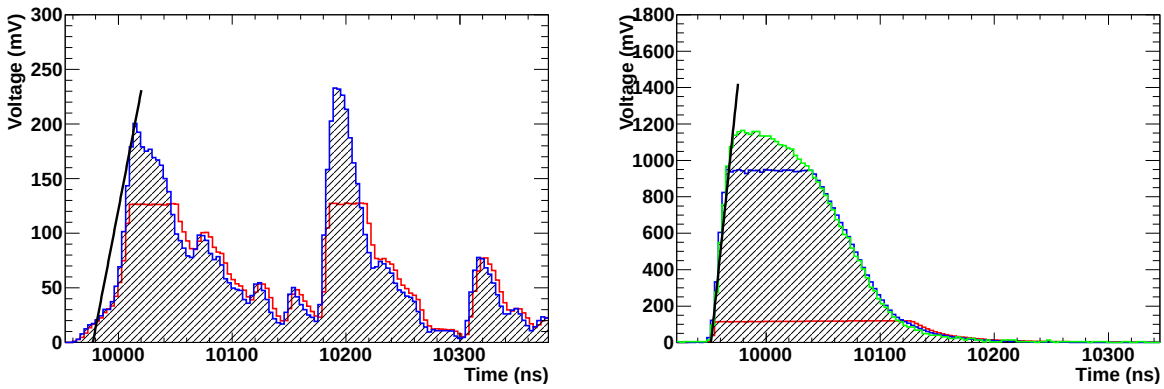

Figure 2.28: Determination of the charge and time of the waveforms from Fig. 2.25. For the charge the integral of the highest not saturated waveform is used, 678 PE (5.34 VEM) for DOM 71-63 and 143 838 PE (1317.2 VEM) for DOM 43-64. The fitted leading edge time is the intersection of the solid line and the x axis.

DOMs have slightly different quantum efficiencies. This means that the same secondary particles give a different signal in different tanks. To calibrate the tank-dependent signal in PE to a common unit for all tanks, low energy cosmic rays are used. Cosmic rays in the GeV-TeV energy range consist of low energy electro-magnetic particles and single muons. Muons propagate straight through the tank and generate of constant amount of light, proportional with their tracklength. Therefore we will express the charge in a tank-independent unit, namely the vertical equivalent muon (VEM).

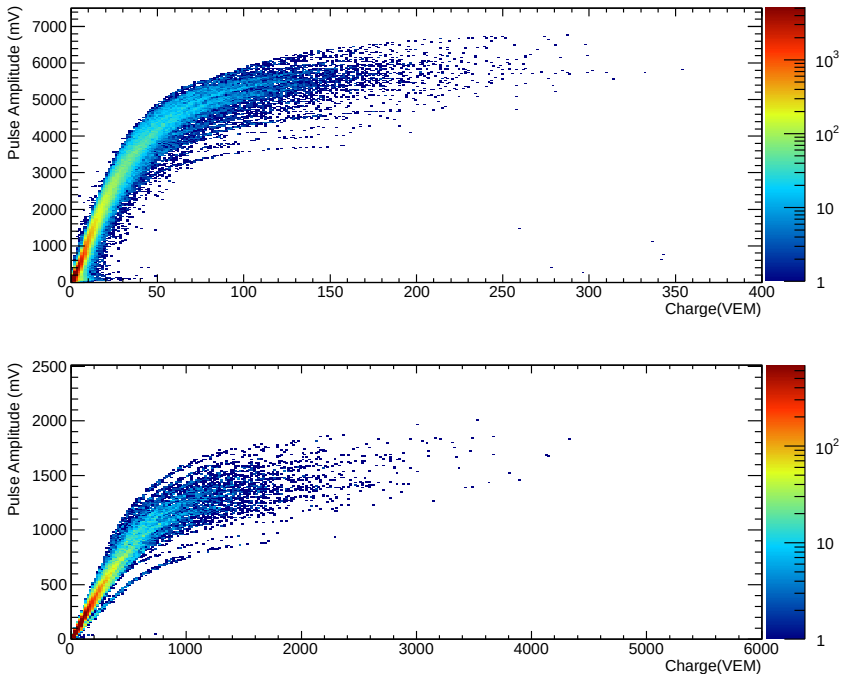

Figure 2.29: Pulse amplitude as function of integrated charge for HG DOMs (top) and LG DOMs (bottom) using two months of IT-73 data.

The charge in PE of a vertical equivalent muon is calibrated by using minimum bias hits. Every 2^{13}th

($8192\mathrm{th}$) hit in a HG DOM, which means the PMT discriminator threshold has been crossed, the full waveform readout is sent through if the hit does not satisfy the HLC condition, otherwise the next non-HLC hit is taken. These minimum bias hits generate a calibration trigger and are then calibrated and their charges calibrated by PnF online. The extracted min bias hits are then sent over the satellite and analyzed in the North. Charge histograms are made such as the left plot of Fig. 2.27 and fitted with an exponential electromagnetic component and a muon component. It has been verified with muon taggers – scintillators triggered when muons pass through – that the peak position at a charge 5% lower is actually formed by muons. Hence a vertical equivalent muon is 95% of the peak position fitted to the charge spectrum of MinBias hits. The value will be different in PE for each HG DOM, but common in VEM of course. To calibrate the LG DOMs with respect to the HG DOMs, signals which are seen by both HG and LG DOMs in the same tank are used. The cross-calibration as shown on the right plot of Fig. 2.27 gives an offset and a HG-LG cross-over value. The offset is due to the different quantum efficiencies of the two DOMs and/or asymmetries in the optical properties of the ice in the tank. At high HG pulse charges the PMT of the HG DOMs are starting to become saturated. This is visible on the right plot of Fig. 2.27 where the relative difference between HG and LG charge becomes increases as function of the unsaturated LG pulse charge. Therefore, as later will be discussed in Chapter 5, the LG pulse charge is used for reconstruction when the HG charge is above the HG-LG cross-over value. Using the offset the LG charge is cross-calibrated with the HG charge through : $(Q_{LG}[VEM] - Q_{HG}[VEM])/Q_{LG} =$offset $y_{off} \Rightarrow Q_{LG}[VEM] = \frac{Q_{HG}[VEM]}{1-y_{off}}$ [**?**].

As illustrated by Fig. 2.17, the ratio of the electromagnetic signal of the VEM spectrum to the muon signal is also used to measure monthly snow heights when no manual measurements are feasible.

The saturation of the PMT in HG and LG DOMs is shown in Fig. 2.29 where the amplitude of the waveform (peak voltage) is plotted as function of the integrated charge. For saturated pulses the amplitude is not increasing linearly anymore while the width of the pulse and hence the integrated charge is. Therefore the deviation from linearity in Fig. 2.29 signals PMT saturation. As mentioned before, from about 10-20 VEM (after the HG-LG cross-over in VEMCal) the LG DOM charge is used for reconstruction instead of the HG DOM thereby evading HG PMT saturation. Large air showers can however even saturate the LG DOMs (Fig. 2.25) and this will be important to simulate correctly and account for in charge based reconstruction, because of course integrated charge becomes an underlimit for the real signal.

IceCube

SPE pulses from the PMT are additonally shaped by the amplifiers before the ATWD. The resulting waveform is therefore a linear combination of these shaped SPE pulses, after calibration with timing and amplitude related to the collection of PEs on the photocathode. Instead of just calculating the total collected charge in units of PE, we want to know the number and arrival of each photo-electron and use that information for reconstructing the detailed properties of the event. On average one photo-electron is detected by IceCube DOMs with a long tail up to $\mathcal{O}(10^4)$ PE from large muon bundles with thousands of muons. The number of photo-electrons can be deconvolved by inverting the following linear system [133] :

$$y_i = y(t_i) = \alpha_1 B_1(t_i) + \alpha_2 B_2(t_i) + \cdots + \alpha_n B_n(t_i) \tag{2.14}$$

$$\Rightarrow \begin{pmatrix} B_1(t_1) & B_2(t_1) & \cdots & B_n(t_1) \\ B_1(t_2) & B_2(t_2) & \cdots & B_n(t_2) \\ \vdots & \vdots & \ddots & \vdots \\ B_1(t_m) & B_2(t_m) & \cdots & B_n(t_m) \end{pmatrix} \begin{pmatrix} \alpha_1 \\ \alpha_2 \\ \vdots \\ \alpha_n \end{pmatrix} = \begin{pmatrix} y_1 \\ y_2 \\ \vdots \\ y_m \end{pmatrix} \tag{2.15}$$

$$\tag{2.16}$$

$y(t_i)$ is the voltage measured in sample i at time t_i by a certain digitizer that goes to m , the total number of samples in all channels and both ATWD and FADC; $\alpha_j = \alpha(t_j)$ the number of photo-electrons that hit the photocathode at time t_j which goes to n, the number of PE pulses. $B_j(t_i)$ quantifies the corresponding SPE pulse shape template with the digitizer and channel that measured y_i, and means the voltage caused by one

photo-electron at time t_j in the sample at time t_i due to the shaping by the amplifier. The times t_j for the PE pulses by dividing 4 SPE pulses over an ATWD sample and the algorithm solves then only the scaling factors α_j.

The SPE shaping pulse templates for all ATWD chips and channels and for the FADC are measured in the lab. Hence the full waveform can be extracted through an unfolding of all present ATWD channels and FADC simultaneously. The condition that the solution must be non-negative – there is not negative number of PE arriving at the photocathode – also accounts for the smoothness of the solution as a kind of regularization. The Non-Negative Least Square (NNLS) algorithm [134] is therefore applied for inverting the matrices. This results in a timing accuracy of ≈ 4 ns in FADC alone and $\lesssim 1$ ns in FADC + ATWD.

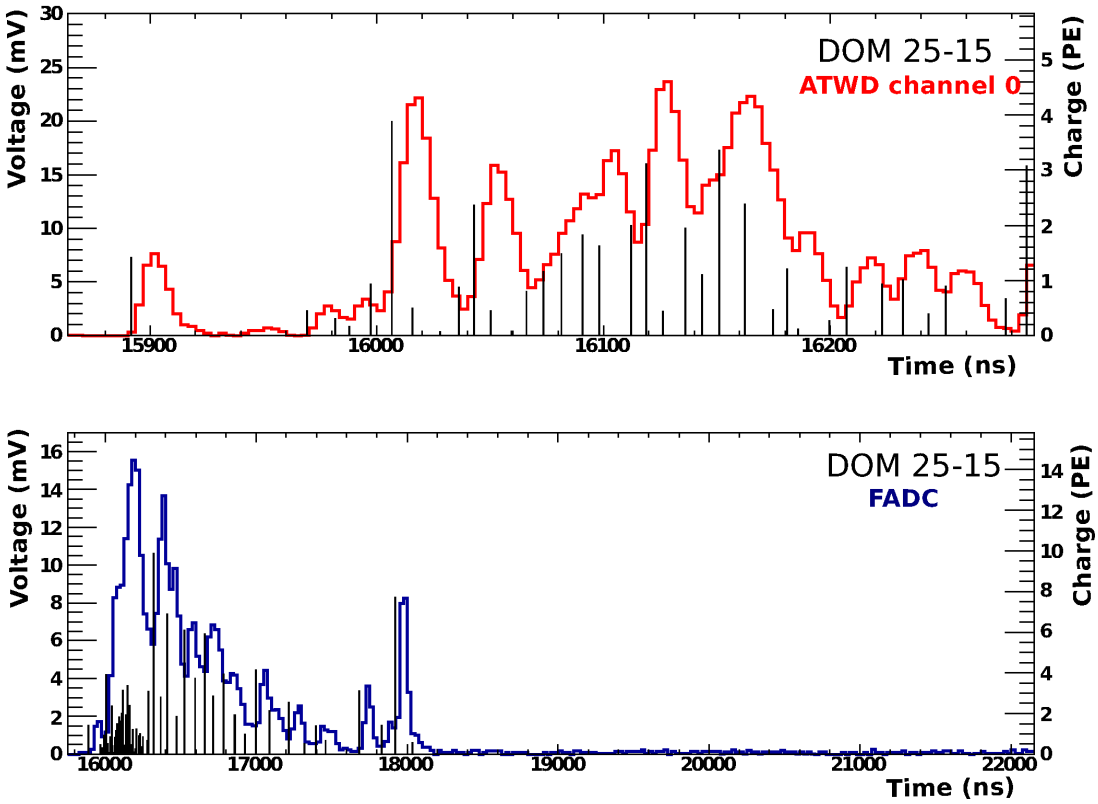

Figure 2.30: Feature extraction of the calibrated ATWD (top) and FADC (bottom) waveforms.

The unfolding result for the complex IceCube waveform is visible in Fig. 2.30 with the calibrated waveform and the charge distribution on the same scale for both ATWD and FADC. As expected the first pulse is an SPE pulse, shaped by the ATWD channel0 amplifier. The time of that SPE nicely matches the leading edge time of the SPE pulse. This is also the case for the rest of the more complex combination of SPEs. The first 422 ns of the ATWD only show up in the very beginning of the FADC, where the more accurate feature extraction in that time window is visible as a lot of PE pulses close together while for the rest of the FADC they are further apart. This particular waveform has a total charge of 105 PE. The unfolded result will be used further by advanced algorithms for extracting the real physics that created this particular waveform (see Chapter 4).

Chapter 3

Simulation

To deduce the composition and energy of the primary cosmic ray particles from the properties of its induced extensive air showers and secondary particles at ground level, a known calibration source is needed. However, on Earth there are no PeV source and cosmic rays do not give known mono-energetic single particle beams. Experiments that measure the longitudinal development, can directly extract the primary energy with the Gaisser-Hillas formula. Experiments that measure the secondary particles at ground level, like IceTop, can only determine the total energy when all secondary particles are detected. As this is highly unpractical at large energies where the shower print is huge, the relation between the observed quantities and the primary energy and mass need to be determined from Monte Carlo (MC) simulations.

Not only the average behaviour of the properties of extensive air showers for different primary energies and composition is important, but also the intrinsic shower-to-shower fluctuations and the shape of the whole distribution because these can all contribute to an accurate determination of direction, core location, primary energy and primary mass.

In addition to extraction the relation between ground level observations and properties of the primary particle, simulations are needed to understand the detector response and develop methods to extract the properties of the secondary particles from the signals in the detector. To learn about the source of cosmic rays, that produce air showers in the atmosphere, which hit the IceCube detector and create some typical signal pattern, we need to go backwards and get the detector out of the data first, use the air shower properties to measure the primary particle properties and from that learn about the sources. Hence the goal of simulation is to mimic the signal and detector response in order to extract the unknowns from comparing simulation to data. A thorough understanding of the detector resulting in accurate simulations is therefore crucial for a good measurement and correct interpretation of the final result.

3.1 CORSIKA

The common need for all cosmic ray experiments over the world is the extensive air shower simulation. To make comparisons easier between experiments they use the same common software, named CORSIKA (COsmic Ray SImulation for KAscade, because it was initially developed for Kascade) [135]. CORSIKA can track protons and nuclei up to iron through a specific atmosphere up to energies of 10^{20} eV. The result is a collection of secondary particles with their type, energy, location, direction and arrival time relative to the first interaction, at a given observation level. Based on user defined settings an initial particle is traced until it interacts with an air molecule according to the nucleus-air cross-sections from a chosen hadronic interaction model. Then all reaction products are propagated further through the atmosphere according to their corresponding decay probabilities and interaction probabilities with other air molecules. Secondary particles below a user-defined energy threshold are not tracked any further as they will anyway not cause any detectable signal in the detector.

The atmosphere in CORSIKA consists of 78.1% N_2, 21.0% O_2 and 0.9% Ar. Several atmospheres are modelled by five layers with an exponential form for the atmospheric depth $X(h)$ as function of the height h

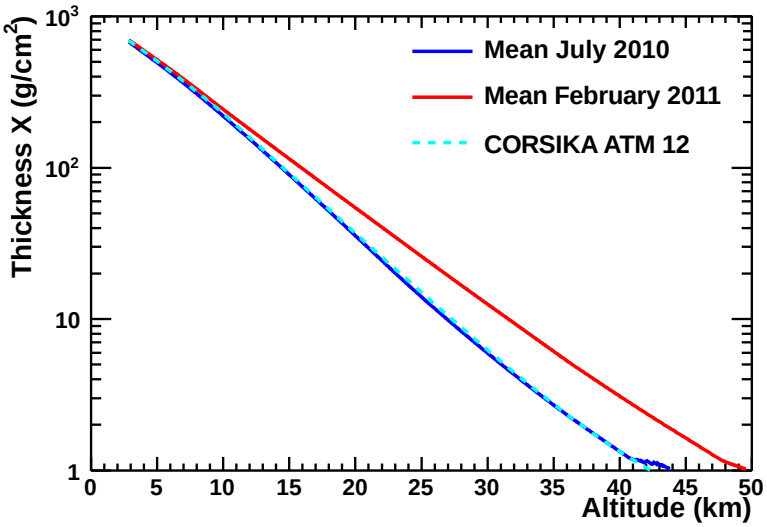

Figure 3.1: Comparison of the atmospheric depth X as a function of the altitude in the atmosphere h between the mean February 2011 atmosphere (red), the mean July 2010 atmosphere (blue) and the CORSIKA July atmosphere, or ATM12 (dashed cyan) from [122].

in the lower four layers and a linear function in the fifth layer up to a height h of 112.8 km:

$$X(h) = a_i + b_i \cdot e^{-h/c_i} \qquad i = 1, \ldots, 4 \tag{3.1}$$

$$X(h) = a_i - b_i \cdot h/c_i \qquad i = 5, \tag{3.2}$$

where a_i, b_i and c_i are the parameters that depend on the model choice and are chosen such that $X(h)$ is continuous over the whole atmosphere and can be differentiated continuously. Four South Pole atmospheres (April, July, October and January) are parametrized according to the MSIS-90-E model [136] by D.Chirkin, two other South Pole atmosphere (January and August) are parametrized by P.Lipari [135].

3.1.1 Hadronic Interaction Models

High energy (typically above 80 GeV) hadronic interactions at very forward directions are not well known because the highest energy collider (Large Hadron Collider at CERN) at Earth reach only an energy of $5{\cdot}10^{16}$eV since 2010 in the lab frame, and will in 2015 reach $2{\cdot}10^{17}$eV when LHC hopefully runs at a center of mass energy of 14 TeV. Additionally, experiments at LHC mainly focus on the kinematic region with large momentum transfer (high p_T), also called hard interactions where perturbative quantum chromodynamics (QCD), the quantum field theory that describes strong interactions, is applicable. Cosmic ray experiments on the other hand detect particles produced in soft interactions, ie. with low momentum transfer, in the extreme forward directions as they can be regarded as very high energy fixed targed experiments. Therefore phenomenological hadronic models that extrapolate from lower energies are needed. Also most collider experiments perform proton-proton collisions whereas high-energy nucleus-nucleus collisions only exist at lower energies (performed at RHIC [138, 139] that reaches up to 200 GeV per nucleon pair for Au-Au collisions and Alice [140] at the Large Hadron Collider (LHC), performing Pb-Pb collisions at a center of mass energy of 2.76 TeV per nucleon pair).

CORSIKA uses a set of user-defined hadronic interactions for the highest energies, of which the most recent models relevant for this thesis are QGSJET II-03 [141, 142, 143], EPOS [144, 145] and SIBYLL 2.1 [146, 147, 148]. All these models treat hadrons as a collection of valence quarks and diquarks, sea quarks and

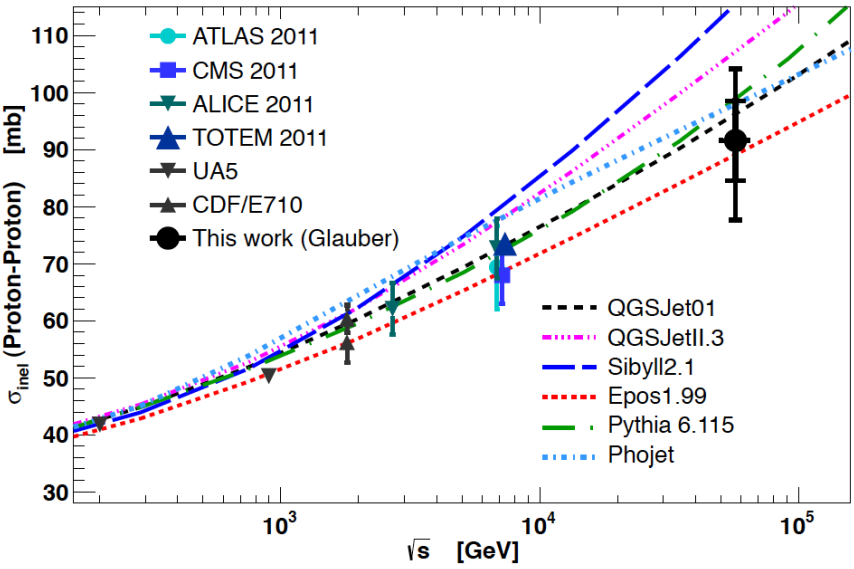

Figure 3.2: The inelastic proton-proton cross-section measured by several recent collider based experiments and the Pierre Auger experiment (labeled as “this work” from [137]) compared to predictions from a set of hadronic interaction models.

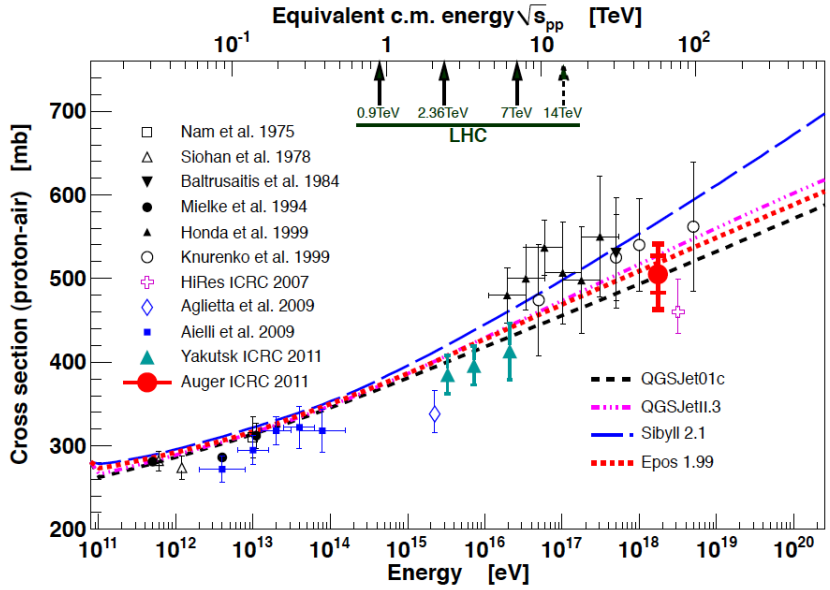

Figure 3.3: The proton-air cross-section measured by several air shower experiment from [137] compared to hadronic interaction model predictions.

gluons. A hadronic interaction is phenomenologically described as exchange of color charge through strings stretched between the partons of the hadrons. The kinetic energy of the partons is transferred to the color field of the string, which subsequently break (string fragmentation) and creates hadrons (hadronization). The models all somehow employ Gribov’s Reggeon field theory (GRT [149]) that treats soft interactions by the exchange of one or several pomerons, a class of multigluon diagrams [79, 89].

QGSJet II is an implementation of the Quark-Gluon-String Model [150, 151], that is based on GRT, and

has a complete microscopic treatment of multipomeron interactions and exchanges. It is the model with the least number of tunable parameters. Recently it has been updated to account for the latest LHC results [152]. This QGSJet II-04 was not yet available for the simulation in this thesis.

SIBYLL 2.1 is based on the dual parton model (DPM), the Lund Monte Carlo algorithms for string fragmentation, and the minijet model for the hard interaction cross section (reference can be found in [148]). SIBYLL contains a minimum number of assumptions and is optimized to describe the air shower observations.

EPOS on the other hand is a model optimized maximally to accelerator data (mainly RHIC data). It is based on a microscopic pomeron model. Several parametrizations, tuned to accelerator data, are used to modify the pomeron model prediction where needed [79]. In [153] EPOS has been tuned additionally to the latest LHC data, however this version was not yet avaiable in the CORSIKA version used for the simulations in this thesis.

To illustrate the present status of how well the hadronic interaction models describe our current knowledge, the proton-proton and proton-air cross sections for several models are compared with the experimental data in Fig. 3.2 and 3.3. The inelastic proton-proton cross sections from the first Figure are measured directly by accelerator based experiments, while the air shower experiment need to apply some assumptions to convert the proton-air cross-sections from Fig. 3.3 to the inelastic proton-proton cross-section. Glauber's multiple scattering theory [154, 155] is typically used to transform hadron-hadron interactions to nucleus-nucleus interactions. Glauber's theory is also used in CORSIKA to calculate the cross-sections from heavier nuclei up to iron with air nuclei. At the highest energies relevant for measurements at the ankle and beyond, the models start to diverge and even though the first cross section from the Pierre Auger experiments does not agree with some models the uncertainties are still large. This clearly shows the uncertainties we have about hadronic interaction at the highest energies and therefore several hadronic interaction models need to be simulated to account for this uncertainty. It should be noted that the cross section is only one property and that some models describe some distributions better than others.

Low energy (below 80 GeV) hadronic interactions are better understood and modelled by FLUKA [156, 157]. The hadronic interaction models are based on resonance production and decay below a few GeV and on the DPM model above.

The electromagnetic interactions are treated by EGS4 [158] which follows each particle and its reactions explicitly according the appropriate scattering and energy loss cross sections, including annihilation, Bhabha scattering, Bremsstrahlung, Møller scattering and multiple scattering for electrons; and Compton scattering, e^+e^--pair production and photoelectric reaction for gamma rays. Direct $\mu^+\mu^-$-pair production and photonuclear reactions have been added in CORSIKA to the existing EGS4 code [135].

3.1.2 Thinning

When the lower energy threshold to keep secondary particles is kept fixed, the number of particles that need to be tracked and stored increases rapidly with the primary energy. As a consequence both the cpu time and file size for one simulated shower grows linearly with primary energy. Enough statistics are needed over the whole energy range to study the mean values and fluctuations over the whole phase space, hence even with large computer clusters resources are limited with storage as main bottleneck. On Fig. 3.4 the average cpu time and file size for one proton-induced air shower simulated with CORSIKA (SYBILL-FLUKA) on a computer cluster in 2010 at University of Wisconsin, Madison (1.8 GHz - 3.0 GHz Opteron and Xeon processors).Almost a day is needed to simulate one 100 PeV air shower and it occupies 7 GB of disk space. For EeV showers one week per shower that will occupy almost 100 GB each is necessary. Large statistics at high energies is therefore impossible.

The solution to the high computer resource requirement of high energy air shower simulation is called "thin sampling" or "thinning" [159, 160]. Instead of tracking and storing each particle above the low energy threshold. An additional threshold, the thinning threshold $E_{\rm thin} = \epsilon_{\rm thin} E_0$, is introduced below which only a few particles are tracked, but they represent the group of particle through a weight. Suppose an initial particle

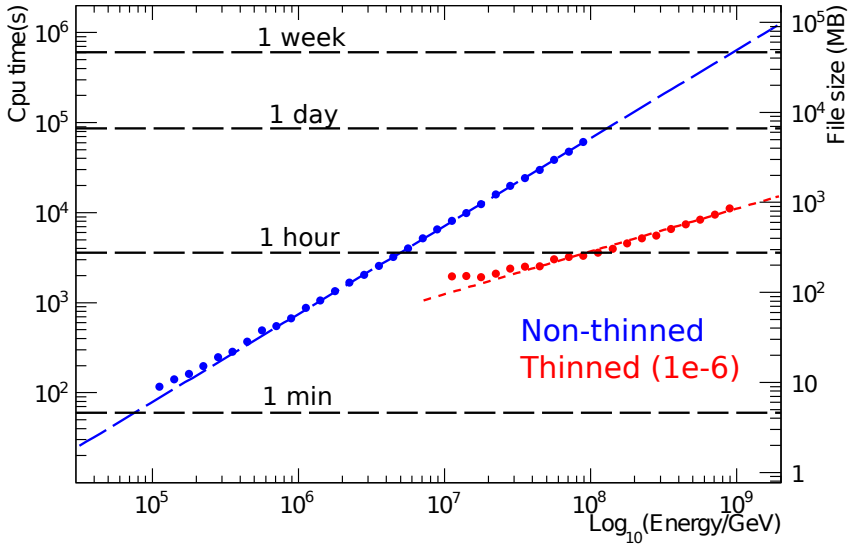

Figure 3.4: Cpu time (left) and file size (right) for one proton shower simulated with CORSIKA, SIBYLL-FLUKA on 2 GHZ machines compared with and without thinning.

with energy E_i interacts and creates five new particles of which two have energies E_j above the thinning energy E_{thin} and the other three below. The particles with $E_j > E_{\text{thin}}$ are kept and tracked further, while the other three are thinned. This means that one of those three particles is chosen, according to the probability $p_j = E_j / \sum_j^3 E_j$, and will be assigned a weight $w_j = 1/p_j$. Then that particle, with energy E_j and weight $\sum_j^3 E_j/E_j$, represents the three particles and will be tracked further. If the sum of the secondary particle energies exceeds the thinning energy threshold, the probability $p_j = E_j/E_{\text{thin}}$ is used instead. Roughly speaking this means that instead of tracking one million of low energy particles, one particle is tracked with a weight of a million. The decrease in file size and cpu time depends of course on the chosen thinning level. For our simulations we use the thinning level ϵ_{thin} of 10^{-6} [161]. Above $10^{8.4}$GeV, the thinning level is relatively less strong at $273./E_0 (\sim 10^{-6} - 10^{-7})$ to prevent any high energy muons ($E_\mu > 273$ GeV) from being thinned because later in the detector simulation InIce muons are not dethinned.

However, with low particle energy thresholds a few particles could have huge weights up to $w_j = E_{\text{thin}}/E_{\text{thr}} = 10^3\text{GeV}/10^{-5}\text{GeV} = 10^8$ for electrons from EeV showers. From these few particles with huge weights artificial fluctuations arise from the thinning. To avoid these artificial fluctuations, a maximum weight $w_{\max}$ is imposed above which no further thinning is applied [162]. Because the weight distribution scales with the primary energy, we use an energy depending weight limit of $w_{\max} = E_0 \cdot \epsilon_{\text{thin}}$, which will be fixed for energies above $10^{8.4}$ GeV due to the energy dependent thinning level.

In CORSIKA, one can even specify different thinning levels for the hadronic and electromagnetic component. For our simulations it is most important to thin the electromagnetic component and prevent the hadronic component from being thinned to be able to have a more accurate simulation of the high energy muon component of the showers at the highest energies. The hadronic thinning level is set at $10/\epsilon_{\text{thin}}$ times lower than the electromagnetic thinning level, which in practise means that hadronic particles are not thinned. The gain in cputime and diskspace can be seen on Fig. 3.4.

3.1.3 Oversampling

The main problem in simulation is the large cpu time needed to generate enough statistics necessary for a detailed understanding of the intrinsic shower fluctuations and the detector response. To create enough

statistics the technique of oversampling has been used. This means that the same cosmic ray air shower, generated with CORSIKA, will be reused n times to make sure the shower actually triggered the detector. Otherwise the large fraction of cpu time, spent in simulating the interactions of the cosmic ray secondaries in the atmosphere, will be lost to a non triggering shower. The other advantage is that when the same shower hits the detector multiple times, it will not a priori generate the same detector response. The detector response and hence reconstructed properties will depend on where the shower core lands with respect to the array geometry.

The parameters which need to be tuned for resampling are the resample radius R and the number of times the shower will be reused n. The resampling algorithm works as follows : the core position (or center of the shower footprint) will be randomly chosen in a circle with radius R and this procedure will be repeated n times, so n shifted copies of the same shower footprint are made right before the actual detector simulation (well technically this has been optimized, but too much detail...).

The resample radius R is chosen to be larger than the distance where the furthest shower can still trigger the detector. This is to make sure the trigger efficiency of the detector will be correctly simulated and accounted for. Higher primary energies give larger shower footprints and will make the air showers trigger the detector from a larger distance to the center of the array. Therefore an energy dependent resample radius was chosen according to Table 3.1. Fig. 3.5 shows the distribution of distances from core position to center of the IceTop array for air showers that triggered both IceTop and IceCube for proton-induced showers (left) and iron-induced showers (right). The radii chosen according to Table 3.1 are clearly larger than the furthest triggering showers. It must be noted that Table 3.1 was optimized for showers with zenith angles between 0 and 40 degrees, which are those used for the analysis in this thesis. For larger zenith angles the shower footprint for some primary energy will be much larger and showers might trigger from even larger distances, so the resample radii are expected to be larger for inclined showers.

The number of resamples should be large enough to make sure almost every unique CORSIKA shower can be used at least once, but should be low enough to avoid artificial fluctuations due to some types of showers that show up too much in a distribution and could bias the analysis. Based on previous experience we chose a hundred resamples. If artificial fluctuations do show up later, cuts on the resample number (eventID) can still be made.

Energy Range (in $\log_{10}$(E/GeV))	Resample radius (m)	Number of resamples
5.0 - 6.0	800	100
6.0 - 7.0	1100	100
7.0 - 8.0	1700	100
8.0 - 9.0	2600	100
9.0 - 9.5	2900	100

Table 3.1: Table of the energy dependent resample radii and number of resamples.

3.1.4 Simulation production

For the measurement of the primary energy and composition spectrum between 1 PeV and 1 EeV, simulations need to be unbiased in energy spectrum and primary type and cover a larger energy range than the one we want to measure to include all fluctuations. Furthermore, enough statistics are needed to describe the whole phase space in as many observables as possible. Therefore 30000 air showers of four type are simulated between 5.0 (100 TeV) and 8.0 (100 PeV) in $\log_{10}(E_0/\mathrm{GeV})$ in 30 energy bins, or 1000 showers per 0.1 energy bin according to an E^{-1} spectrum. The four types (proton (H), helium (He), oxygen (O) and iron (Fe)) such that they are equidistant in $\log A$ and cover the whole phase space in $\log A$ between proton and iron. CORSIKA can not simulate anything heavier than Fe and from the first neural network composition analysis [163] we learned that additional types, like Silicon, can hardly be separated from Fe. Also disk space

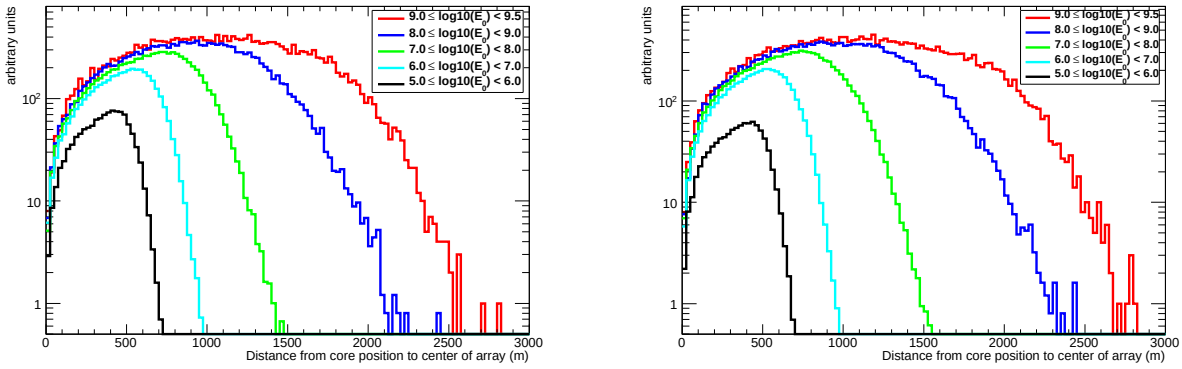

Figure 3.5: Distributions of distances from the core position to the center of the IceTop array for different primary energy ranges. **Left**: Proton simulations without any cuts except passing the coincident filter. **Right**: Iron simulations with the same cuts as the proton simulations.

limitations formed an extra argument for not including Si in the simulation mass production.

To go to higher primary energies, we used thinned CORSIKA showers (see Section 3.1.2). 12000 CORSIKA showers of each type between 7.0 (10 PeV) and 9.5 (3.16 EeV) in $\log_{10}(E_0/\mathrm{GeV})$ in 25 energy bins, or 480 showers per 0.1 energy bin. High energy muons are not thinned, create a lot of stochastic energy losses that are kept in the file and hence still create large files which limited the total number of generated showers per energybin to 480 showers. The overlap energy range between 10 PeV and 100 PeV is created for extra verification of the dethinning algorithms.

For the mass production, we used SYBILL 2.1 above 80 GeV and FLUKA below 80 GeV as hadronic interaction models and for the electromagnetic interactions EGS4. Other high energy hadronic interaction models will be used for systematics studies. The zenith angle from the primary particles is sampled from a $\cos\theta \sin\theta$ distribution between 0° and 40°. The zenith angle range is chosen to be optimal for a coincident event simulation which could trigger both IceTop and IceCube and are contained by both detectors. It is not optimal for studies with the IceTop detector alone for a larger zenith angle range or uncontained coincident events. The $\cos\theta \sin\theta$ distribution accounts for the smaller solid angle ($\mathrm{d}\,\Omega = \sin\theta\,\mathrm{d}\,\theta\,\mathrm{d}\,\phi$) at small zenith angles and atmospheric attenuation at larger zenith angles ($\sim \cos\theta$ because slant depth $X \sim \sec\theta$). The azimuth angle from a uniform distribution over the whole 2π azimuth range. To be able to study atmospheric changes and apply corrections where needed, one reference atmosphere was chosen. In Section 2.3.2 we saw that the average ground pressure in the 2010-2011 data taking period was 692 g/cm^2. Hence we chose the CORSIKA atmosphere model based on the MSIS-90-E parametrization of the South Pole Atmosphere on July 1, 1997 which has an ground pressure of 692.2 g/cm^2 at the South Pole altitude.

Only single air showers are simulated even though in data multiple events can appear during the same global readout window. Overlapping readout windows of multiple, potentially unrelated triggers enlarge the global readout window for one DAQ event. Unrelated IceTop and InIce SMT triggers caused by independent air showers, one that only hits IceTop and the other one that only triggers the IceCube detector, can occur during the same event. Other cases of multiple events during the same readout are multiple independent air showers that only trigger IceTop, typically lower energy events. Also multiple coincidences in the IceCube detector happen, before or after the air shower in which we are interested in that went through both IceTop and IceCube. Even upgoing (atmospheric) neutrinos in coincidence with the IceTop-IceCube air shower happen. These extra events during the same readout can cause an InIce/IceTop SMT trigger by itself or can even happen during the trigger window of the event in which we are interested in. All these cases of independent, extra events (double, triple, ...) are incredibly difficult to simulate and are therefor not simulated for cosmic ray analyses. However, these cases are effectively treated by advanced hit cleaning and event selection methods, discussed in Chapter 5.

We used CORSIKA v.6980 with the steering file from Appendix A. All simulated CORSIKA showers are kept and reused for several detector simulations with different configurations for other analyses. The total CORSIKA library occupies about 150 TB of disk space. In the whole simulation procedure (CORSIKA + detector simulation), the CORSIKA air shower simulation uses most of the cpu time. This is dominated by the low particle threshold needed for the IceTop tank simulation. Another conseqeunce is that millions of low energy particles are kept in the CORSIKA output files with all their properties (position, momentum, etc...) and hence create the large filesizes.

3.2 Detector simulation

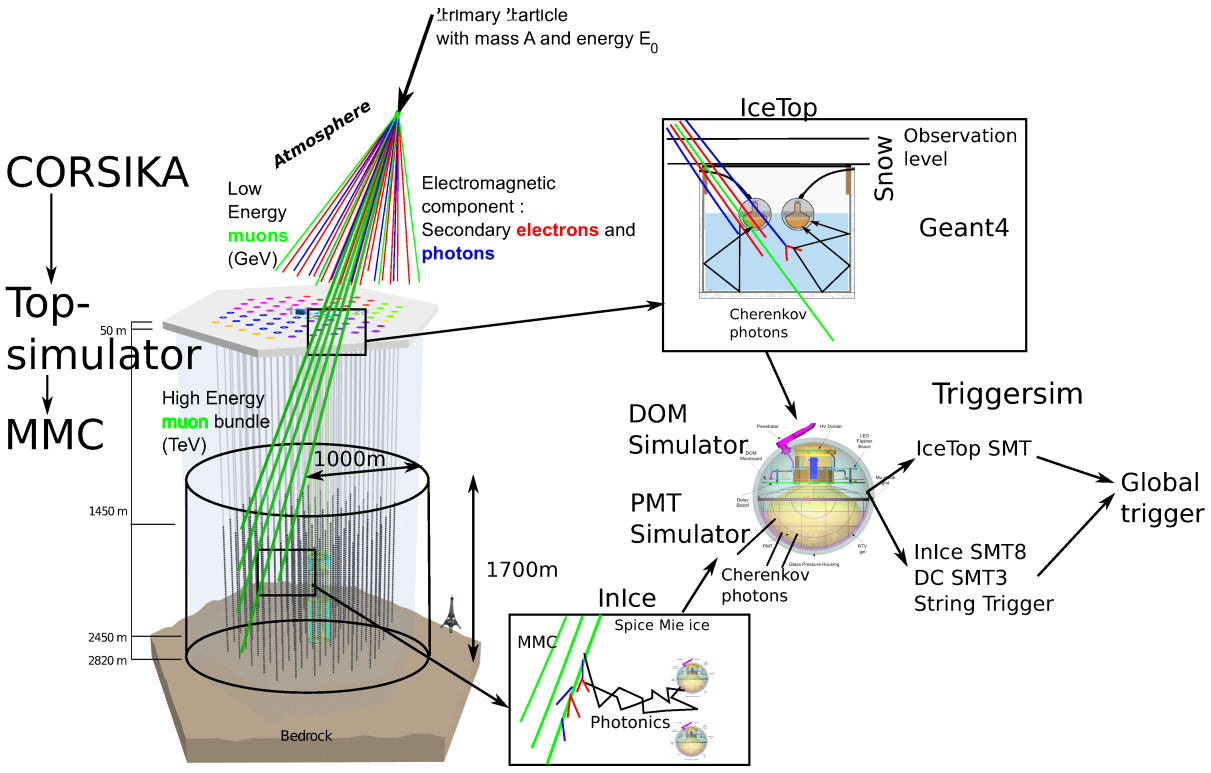

Figure 3.6: Schematic overview of coincident IceTop-IceCube cosmic ray simulations.

Like in nature after simulation of the extensive air showers, the detector response of the IceTop and IceCube detectors to the ground level secondary particles is simulated. The whole procedure is illustrated by Fig. 3.6. After resampling described in Section 3.1.3 n copies of each shower footprint, uniformly distributed over a circle with radius R and the center of the IceTop array as center, exist. A run in simulation is unique shower from a certain dataset, while the event nummer designates the resample number. For each event first the IceTop detector response is simulated, and then the IceCube detector response.

If the air shower has been thinned (see Section 3.1.2), then it contains a set of particles with a weight larger than one. Before the detector response for a weighted particle can be simulated, it first has to be "unthinned". This means that the particle's energy and direction will be cloned a number of times given by the weight of the particle, such that the total energy is conserved ($w_j \cdot E_j = E_i$, the total energy represented by the weighted particle) and uniformly over a well-chosen sampling area. This area and the whole unthinning procedure is optimized in [161] to limit artificial fluctuations and biases (eg. too small sampling area).

For each particle from an event, the IceTop tank response is simulated when the particle intersects the tank cylinder within a 30 cm margin. To speed up simulation IceTop tanks within 25 m of a 5 m by 5 m

pixel are buffered and only those tanks assigned to the pixel where the particle went through are verified for intersection by that particle. The IceTop tank simulation is performed by a detailed Geant4 [164] simulation in which the individual IceTop tank properties, including snow and air above the tanks, are implemented (see Fig. 3.6). Some of the tank properties in Geant4 are parametrized based on single, stand-alone Geant4-based tank simulation, called TankTop [90]. The energy loss, interaction with the IceTop tank material and Cherenkov photon generation is simulated, but the Cherenkov photons (up to several millions) are not tracked. This was done once using TankTop and the relation between the number of photons that hit the PMT photocathode and the number of emitted photons was parametrized to save cputime. The arrival times of the photons are sampled from an exponential distribution with a decay constant that match the one from the waveform decay times in data.

The next step is to make sure the simulated number of Cherenkov photons matches the observed number of signal from the same particles in data. This is accomplished through an absolute calibration of the simulation in exactly the same way as the data are calibrated. A detailed VEM calibration (see Section 2.27) using simulated low energy air showers in an energy range between 3 GeV and 10 TeV according to an $E^{-2.7}$ spectrum and applying the same anti-local coincidence calibration trigger as in data is studied in [165]. The full electronics simulation is added and the simulated charge spectrum has been tuned to the charge spectrum in data by changing the conversion from Cherenkov photons to VEM in order to have the VEM peak, predominantly created by 2-5 GeV muons, at the same place. The remaining uncertainty in this absolute calibration due to atmosphere, hadronic interaction model, composition, etc.. will be the uncertainty in the absolute energy scale of our final result. After the calibrated global conversion from Cherenkov photons to VEM, the VEM calibration from data is used to convert the signal to a tank-dependent number of PE, because all tanks are different.

The muons with energy above 273 GeV are propagated through the Antarctic Ice by a program called Muon Monte Carlo (MMC [109]), shown in Fig. 3.6. 273 GeV is the energy at which 0.1% of the muons still reaches the top of the detector and could create a detectable amount of Cherenkov light in the IceCube detector [166]. The energy loss processes, described in Section 2.2.1, are evaluated according to their cross-sections. When the muons enter a the MMC volume, a cylinder with a radius of 1000 m and height of 1700 m centered at the IceCube detector center (see Fig. 3.6), the energy loss processes with the position, energy and type of process are stored, as well as the position and energy of all muons that enter the MMC volume, at the point closest to the center of the array and when the exit the MMC volume.

The light propagation through the South Pole ice from the muons to the DOMs is impossible to do by directly tracking each emitted Cherenkov photon. Tracking the huge amount of photons from the thousands of muons for the 100 PeV-1 EeV showers would take an unacceptable amount of cputime. Therefore different light profiles for GeV emitters, both pure Cherenkov emission and more diffuse emission from cascade light sources, with different emission angles and at different positions in the detector for DOMs at different distances are simulated once with a chosen ice model (here : Spice-Mie) and the results are stored in large tables. The photon tracking program Photonics [167] handles the photon tracking and tabulating. For each DOM the expected number of photoelectrons and their arrival times are then retrieved from these tables for each muon and for electromagnetic and hadronic cascades, coming from MMC calculations. The energy dependence are treated according to the parametrizations from Eq.2.4 and 2.5. Additionally, noise hits are added for IceCube DOMs to the set of PEs, creating essentially a collection of arrival times. These are then fed into the actual electronics simulation. Several issues have come up with the Photonics program, mainly related to the tabulation and interpolation from the tables. In Chapter 7 the effect of these known bugs will be discussed in more detail.

At this stage in the simulation chain both IceTop and IceCube contain a collection of PEs per DOM from a certain air shower. The PMT and DOM are simulated the same way for both IceTop and IceCube as shown by Fig. 3.6 by software called PMTSimulator and DOMSimulator. The simulated analog PMT-signal is obtained by using Gaussian shaped SPE waveforms and sampling the charge from the measured SPE charge distribution [129] for each PE which are then superimposed. The loss of light from the glass, the gel, the quantum efficiency of the PMT, the angular acceptance of the DOM and the hole ice, the refrozen column of

water during string deployment, is accounted for in the photon propagation. However, this will later prove to be a large uncertainty in the absolute light yield.

The DOM simulation software ("DOMSimulator") applies the toroid droop effect to the the analog pulse from the simulated PMT pulse and adds a pulse shaping for each of the amplifiers before the ATWD. The PMT discriminator is simulated and local coincidence conditions are checked and compared to the neighbouring DOMs. As in data the analog signals are digitized by both ATWD and FADC (using the calibration constants from DOMCal) when the simulated PMT pulse passes the discriminator threshold.

When all raw data from the IceCube and IceTop DOMs have been simulated, the trigger conditions for IceTop and IceCube are first checked independently (by "Triggersim") after which a global trigger with corresponding global readout window is formed. The trigger simulation is carefully checked by applying the trigger simulation software on real data and comparing the trigger times and length with the result from the DAQ. After the full simulation chain, offline level1 and level2 processing is applied and the data is further treated exactly the same as experimental data.

Chapter 4

Reconstruction

The main goal is to map the detector response from an extensive air shower to a set of characteristic observables that uniquely describe its properties. Based on these well chosen shower characteristics, we can then deduce the energy and mass of the primary particle using dedicated simulation.The direction and core location define the position from which we can then deduce radially dependent properties on the surface and the energy deposit profile as the muon bundle propagates through the detector.

4.1 IceTop reconstructions

With the signals detected by the tanks of the IceTop surface array, the core location of the extensive air shower and its direction is determined. Next, the radial distribution of arrival times and charges on the plane perpendicular to the shower axis is fitted by a curvature and lateral distribution function (LDF) respectively. The fit parameters of the curvature and lateral distribution function depend on primary mass and primary energy. Therefore the fit results of the LDF fit will play an important role in this analysis as the main primary energy dependent observables.

4.1.1 First guess

For every advanced likelihood minimization algorithm a good seed is very important. If the seed is already close to the true solution, then the minimizer will have less difficulty in finding the global minimum in a complex n-dimensional likelihood space. Another important property of a first guess algorithm is its speed and its robustness (ie. that it never fails to a solution).

Core position

A fast, simple first guess method for determining the core position of the air shower is based on the so-called center-of-gravity (COG) of hit IceTop tanks. This is the charge-weighted sum of tank positions:

$$\boldsymbol{r}_{COG} = \frac{\sum_{i}^{\mathrm{nTanks}} \boldsymbol{r}_i \cdot Q_i^w}{\sum_{i}^{\mathrm{nTanks}} Q_i^w}, \tag{4.1}$$

with $\boldsymbol{r}_i$ the position of tank i, Q the charge in VEM measured by tank i and w the weighting factor. Larger w gives more weight to tanks with high charges and would pull the COG closer to the tanks with the highest charges. *nTanks* is the total number of hit tanks, but can also mean the number of hit tanks of with the largest charges.

In Fig. 4.1 the cumulative distribution of distances between the true core position and the reconstructed core position (at the surface) is shown for a different number of hit tanks with the largest signal and different

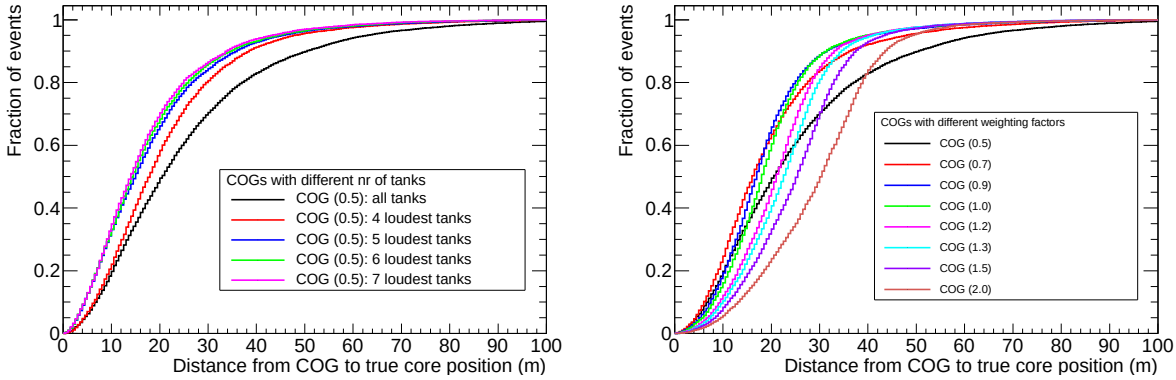

Figure 4.1: Core resolution for the COG of proton-induced showers with more than 10 hit IceTop stations. **Left**: Only the n tanks with the largest signals are used for the COG. **Right**: Different weighting factors used for the COG calculation.

weighting factors. It can be clearly seen that the standard COG definition where all hit tanks are used and a weighting factor of 0.5 is not optimal and could provide a bad seed for the core position. Both increasing the weighting factor and reducing the number of tanks improves the core resolution, defined as the distance which comprises 68.3% of the total number of events. Based on the comparison of both methods in Fig. 4.2 I/we chose to use the standard weighting factor of 0.5, and to sum only over the 7 tanks with the largest signals. The reason why a reduction of number of tanks improves the resolution is the topology. In a large array such as IT-73 the footprint of the air showers can become elongated. A larger number of tanks with a lower charge could therefore pull the COG away from the true core position, which is naturally still closer to the largest signals. Studies showed that this improvement helped likelihood reconstructions, discussed in the next section, a lot.

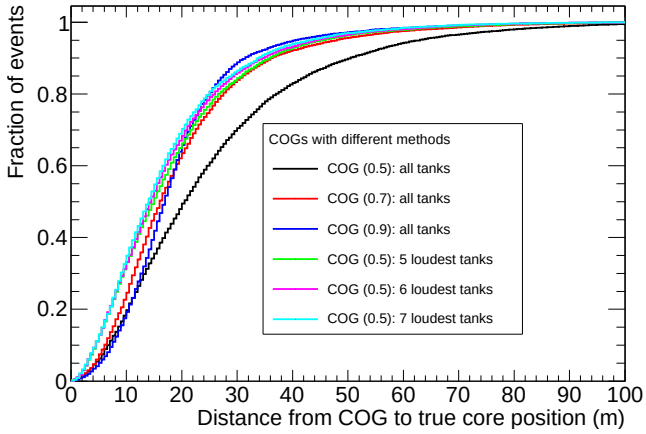

Figure 4.2: Core resolution for the COG of proton-induced showers with more than 10 hit stations. The different number of station-method is compared with the different weighting factors.

Direction

The direction where the extensive air shower comes from can be extracted from the arrival times of the secondary particles in the IceTop tanks. It is characterized by the unit vector $\boldsymbol{n}$ that points in the direction

of movement of the shower. In the IceCube coordinate system, the zenith and azimuth angles are defined with respect to the direction where the events come from, hence $\boldsymbol{n} = (-\sin\theta\cos\phi, -\sin\theta\sin\phi, -\cos\theta)$. For the arrival times of the first secondary particles in each tank i the leading edge times t_i of the IceTop waveforms are used. From the following χ^2 equation, the direction can be calculated :

$$\chi^2 = \sum_i^{\text{nTanks}} w_i (t_i^{\text{meas}} - t_i^{\text{exp}})^2 \qquad w_i = \frac{1}{\sigma_i^2} \tag{4.2}$$

$$t_i^{\text{exp}} = t_0 + \frac{(\boldsymbol{r}_i - \boldsymbol{r}_c)\cdot\boldsymbol{n}}{c} + \Delta t_i(R), \tag{4.3}$$

with c the light speed at which the shower front approximately propagates, t_0 the time at the shower core position $\boldsymbol{r}_c$ and $\boldsymbol{r}_i$ the tank position. The term $(\boldsymbol{r}_i - \boldsymbol{r}_c)\cdot\boldsymbol{n}$ is the projection of the vector from the tank position to the core position onto the direction vector. The extra radius-dependent term $\Delta t_i(R)$ with $R = \parallel \boldsymbol{r}_i - \boldsymbol{r}_c \parallel^2$ denotes the curvature of the shower front.

As a first guess the shower front is approximated as a plane ($\Delta t_i(R) = 0$). This simplifies Eq.4.3 because the shower core position and the time at the shower core are arbitrary on a plane. An additional approximation for a first guess estimation of the direction is to use a constant time fluctuation σ of 5 ns. The analytical solution of the χ^2 minimization of Eq.4.2, derived to t_0, n_x and n_y, can then be written as a matrix equation where we also assumed that all tanks are at the same height in a first iteration ($z_i = z_c$) :

$$\begin{pmatrix} \sum_i w_i & \sum_i w_i x_i & \sum_i w_i y_i \\ \sum_i w_i x_i & \sum_i w_i x_i^2 & \sum_i w_i x_i y_i \\ \sum_i w_i y_i & \sum_i w_i x_i y_i & \sum_i w_i y_i^2 \end{pmatrix} \begin{pmatrix} t_0 \\ n_x/c \\ n_y/c \end{pmatrix} = \begin{pmatrix} \sum_i w_i t_i \\ \sum_i w_i x_i t_i \\ \sum_i w_i y_i t_i \end{pmatrix} \tag{4.4}$$

Because t_0 is arbitrary, we set this to zero and can easily calculate n_x and n_y from the inverse of the above matrix equation. After a first iteration and calculation of zenith θ and azimuth ϕ angles, the following height correction for all signals is applied and the matrix equation is solved again:

$$t_i^{\text{corr}} = t_i + \frac{(z_i - z_c)\cos\theta}{c}, \tag{4.5}$$

with z_c the mean z position of all hit signals, chosen as shower core position estimate. This first guess procedure provides a fast, analytic estimation of the direction and is very robust. Only when the solution $n_x^2 + n_y^2 > 1$, the procedure can not find a first guess direction which could be in the case where only few stations are hit and are all aligned.

4.1.2 Lateral distribution and curvature

With a first estimate of the core position, from the COG method, and the direction, from the planar shower front approximation, the distribution of signals as a function of the distance to the shower axis can be fitted. This lateral distribution is characteristic for the stage of the shower development, the primary mass and primary energy of the extensive air shower. Because we want to deduce the nature and energy of the primary particle we therefore need an accurate fit to the lateral signal distribution.

The initial core position and direction are however not accurate enough to yield a good lateral distribution function (LDF) fit. The COG for example is obviously not the correct core position for showers that land outside the IceTop array. The approximations made for the direction reconstruction for a fast first guess naturally limit its resolution as well. That is why both the core position and direction are refitted together with the LDF in a maximum likelihood procedure that will be explained below term by term.

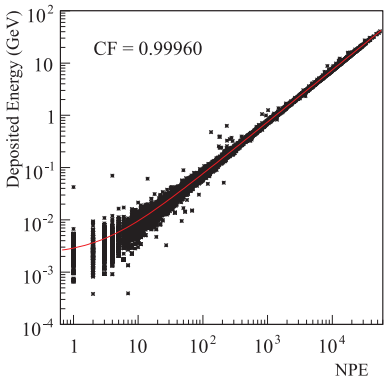

Figure 4.3: The correlation between the energy deposited in an IceTop tank by all particles that enter the tank and the detected number of of photo-electrons by the PMT from [168]. CF is the correlation factor.

Charge likelihood and LDF

The Cherenkov light detected by the PMT (in PE or after tank-to-tank calibration in VEM) scales almost linearly with the Cherenkov emitting path lengths of all charged particles in the tank. The energy loss of the charged particles scales approximately linearly with their path lengths. Therefore the signal detected in the PMTs of IceTop tanks is proportional with the energy deposited by the secondary particles that enter the tank (see Fig. 4.3). This distinguishes IceTop from air shower experiments that use scintillator arrays, which detect particle densities instead of deposited energies.

The lateral distribution from electromagnetic particle densities can be analytically parametrized by the so-called NKG function or similar [41]. Because the IceTop signals are more correlated to the energy deposit and because they include contributions from both the electromagnetic and the muonic component of the extensive air shower, dedicated simulation studies were performed in [168] to deduce the functional form of the lateral signal distribution. It was found that the mean expected signal $S_{\mathrm{exp},i}$ for tank i at distance R_i from the core position can be parametrized as:

$$S_{\mathrm{exp},i} := S_{\mathrm{exp}}(R_i) = S_{R_{\mathrm{ref}}} \cdot \left(\frac{R_i}{R_{\mathrm{ref}}}\right)^{-\beta-\kappa\log_{10}\left(\frac{R_i}{R_{\mathrm{ref}}}\right)} \qquad R_{\mathrm{ref}} = 125\ m, \tag{4.6}$$

a so-called *double logarithmic parabola* (DLP), which becomes clear on log-log scale, with $\kappa = 0.303$, β the slope of the LDF at R_{ref} and $S_{R_{\mathrm{ref}}} = S_{125}$ the normalization of the LDF. The normalization S_{125} is also called the shower size as larger showers naturally give a higher energy deposit and thus also a higher normalization. The shower size is evaluated at 125 m from the shower core because at medium energies the average distance of signals participating in the fit is 125 m [90]. Evaluating the fitparameter at this most stable distance could help the fit procedure although if the fit procedure is robust the reference distance is arbitrary. However, 125 m is the distance at which the shower size S_{125} is least composition-sensitive [163]. The slope β of the DLP relates to the stage of shower development, ie. smaller β gives a steeper LDF which is typical for showers that are earlier in their shower development and therefore most secondaries are still near the core position and have not yet undergone much scattering. Those young showers can come from higher energy primaries and/or higher mass primary. Both β and the shower size parameter S_{125} therefore depend on the primary composition and primary energy.

In addition to a good description of the mean value of the expected lateral signal distribution the distribution around the mean and its fluctuation are also crucial for a good fit. The simulation study from [168] demonstrated that the signals are log-normal distributed. The charge dependence of the width $\sigma_{\log_{10} S}$ of the distributions comes from a data study that compared the signals of tank A and tank B and is reasonably

reproduced by simulations [168, 90]:

$$\log_{10}\sigma_{\mathrm{q},i} = \begin{cases} 0.283 - 0.078\log_{10} S & \log_{10} S < 0.340 \\ -0.373 - 0.658\log_{10} S + 0.158\log_{10}^2 S & 0.340 \leq \log_{10} S < 2.077 \\ 0.0881 & 2.077 \leq \log_{10} S \end{cases}$$
$$\text{with}\log_{10} S := \log_{10} S_{\mathrm{exp},i}$$
$$\text{with}\log_{10}\sigma_{\mathrm{q},i} := \log_{10}\sigma_{\log_{10} S} \tag{4.7}$$

The charge likelihood $\mathcal{L}_{\mathrm{q}}$ based on the signal expectation from Eq.4.6 and the fluctuations from Eq.4.7 can then be described by the product over all hit stations of the log-normal distributed charges:

$$\mathcal{L}_{\mathrm{q}} = \prod_{i}^{\mathrm{nHitTanks}} P(S_i|S_{\mathrm{exp},i}) = \prod_{i}^{\mathrm{nHitTanks}} \frac{1}{\sqrt{2\pi}\sigma_{\mathrm{q},i}} e^{-\left(\frac{\log_{10} S_i - \log_{10} S_{\mathrm{exp},i}}{\sqrt{2}\sigma_{\mathrm{q},i}}\right)^2} \tag{4.8}$$

where nHitTanks does not include tanks which are saturated but are treated separately and discussed later. The parameters that will be fitted in this likelihood are the core position, represented by the R dependence in the LDF, and the two fitparameters β and S_{125} of the LDF.

Currently studies are ongoing to separate the electromagnetic part of the signal and the muonic part of the signal in order to fit a separate NKG-type LDF to the electromagnetic signals and a muon LDF to the muons [169].

Timing likelihood and curvature

The direction reconstruction is improved by fitting a curved shower front instead of a plane. The curvature is a function of the distance to the shower axis, and therefore the core position is not arbitrary anymore, which makes an analytical solution of Eq.4.2 with a curvature term difficult. As the shower core position improves during the LDF fit, we can use the improved core position to fit the shower front curvature at the same time and consequently improving the zenith and azimuth angle reconstruction.

The shower front curvature is parametrized by a paraboloid with a gaussian nose in the center of the shower and comes from a fit to data [90]:

$$\Delta t(R_i) = aR_i^2 + b\left(1 - e^{-\left(\frac{R_i}{\sqrt{2}\sigma_{\mathrm{curv}}}\right)^2}\right), \tag{4.9}$$

with $a = 4.823 \cdot 10^{-4}$ ns/m^2, $b = 19.41$ m and $\sigma_{\mathrm{curv}} = 83.5$ m. Even though the curvature, represented here mainly by parameters a and b, depends on primary mass and primary energy, the parameters are kept constant during the fit and only the direction $\boldsymbol{n}$ is fitted. This might limit the resolution the resolution in certain energy ranges. Studies on how to include a and b as free parameters in a stable fit to try to improve the curvature fit and study the composition and energy dependence of the resulting fitparameters is ongoing.

The arrival time fluctuations $\sigma_{t,i}$ also comes from a fit to data when the detector was in its 26-station configuration [90] and only depends on the distance to the shower axis :

$$\sigma_{t,i} := \sigma_t(R_i) = 2.92 + 3.77 \cdot 10^{-4} R_i^2. \tag{4.10}$$

There are several indications that the fluctuations are overestimated at large distances for large showers and an improvement of the current parametrization is ongoing.

The resulting timing likelihood $\mathcal{L}_{\mathrm{t}}$ based on the expected arrival time of the signals on a curved shower front from Eq.4.3 and 4.9 and its fluctuations from Eq.4.10 are described the following gaussian likelihood:

$$\mathcal{L}_{\mathrm{t}} = \prod_{i}^{\mathrm{nHitTanks}} P(t_i|t_{\mathrm{exp},i}) = \prod_{i}^{\mathrm{nHitTanks}} \frac{1}{\sqrt{2\pi}\sigma_{t,i}} e^{-\left(\frac{t_i - t_{\mathrm{exp},i}}{\sqrt{2}\sigma_{t,i}}\right)^2}, \tag{4.11}$$

where both the shower core position in the radial dependence of the curvature and the direction can be fitted.

No-hit likelihood

Unhit stations also carry information that can be used in the LDF fit because the probability that a certain signal expected not too far from the core gives a measured signal below the tank threshold is not zero. A so-called no-hit likelihood helps to push the minimizer away from core locations in parts of the array where there are tanks which are not hit. The probability that a tank is not hit depends purely on the tank signal threshold S_{thres} and is the integral over the gaussian distribution of all possible signals from a certain signal expectation $S_{\mathrm{exp},i}$ for tank i to $S_{\mathrm{thres}} = 0.1657$ VEM (or roughly 20 PE, corresponding to the MPE PMT discriminator threshold).

Due to the LC condition, only hit HLC stations carry the full waveform information while hit tanks without hit neighbouring tank only carry an SLC chargestamp. SLC hits were for this analysis not yet used in the reconstruction because they were not well calibrated and simulated. That is why there are either hit stations or unhit stations in the set of hits used by the reconstruction. In the approximation that the 2 unhit tanks of a station are correlated, we get the following expression for the no-hit likelihood $\mathcal{L}_{\mathrm{nohit}}$:

$$P_{\mathrm{nohit},i} = \int_{-\infty}^{\log_{10} S_{\mathrm{thres}}} \frac{1}{\sqrt{2\pi}\sigma_{q,i}} e^{-\left(\frac{\log_{10} S_i - \log_{10} S_{\mathrm{exp},i}}{\sqrt{2}\sigma_{q,i}}\right)^2} \mathrm{d}\log_{10} S_i \tag{4.12}$$

$$= \frac{1}{2}\left(\mathrm{erf}\left(\frac{\log_{10} S_{\mathrm{thres}} - \log_{10} S_{\mathrm{exp},i}}{\sqrt{2}\sigma_{q,i}}\right) + 1\right)$$

$$P_{\mathrm{hit},i} = 1 - P_{\mathrm{nohit},i}$$

$$\mathcal{L}_{\mathrm{nohit}} = \prod_{i}^{\mathrm{nUnhitStations}} (1 - P_{\mathrm{hit},i}^2), \tag{4.13}$$

where the first two equations express the probabilities for (un)hit tanks [90].

In reality the charge thresholds for each tank are slightly different, because they are set in mV, based on a relation between the DAC number and the analogue value in mV, and the correspondence with the charge threshold varies slightly between each tank. Also the treatment of SLC tanks in tank-based description of the no-hit likelihood is currently under investigation.

Saturation Treatment

The PMTs of the DOMs in an IceTop tank are saturated when the pulse amplitude starts to behave non-linear as a function of the integrated charge as illustrated by Fig. 2.29. From Fig. 2.29 we learn that LG DOMs start to saturate at about 600 VEM (90000 PE) and HG DOMs from about 20 VEM (3000 PE). The saturation thresholds for HG and LG DOMs are chosen at the fixed values in PE and converted to VEM on a tank-to-tank basis. In Section 2.6.2, we explained that the LG DOMs are used for analysis when the HG DOM charge is larger than the HG-LG crossover value from the VEM calibration. However, in some cases no matching LG pulse is found because the LG pulse was earlier or later than our chosen maximum time difference (see Section 5.1.1) or still digiziting previous waveforms. The HG pulses are then used instead with the HG-LG crossover value as saturation threshold.

Saturated tanks are treated separately in the likelihood description because the measured charge from saturated PMTs is an underestimation of the real charge due to the non-linear behaviour of the PMT. The real, unsaturated charge follows the log-normal distribution around the expected charge from Eq.4.8. If the charge is saturated the real value could have been anything above the saturation threshold $S_{\mathrm{sat},i}$ for tank i. Hence, the probability that a tank is saturated for an expected signal $S_{\mathrm{exp},i}$ can be expressed as the integral of the log-normal distributed expected charges over all possible measured charges above $S_{\mathrm{sat},i}$. The saturation

likelihood is then the product over all saturated tanks :

$$\mathcal{L}_{\text{sat}} = \prod_{i}^{\text{nSaturatedTanks}} \int_{\log_{10} S_{\text{sat},i}}^{+\infty} \frac{1}{\sqrt{2\pi}\sigma_{q,i}} e^{-\left(\frac{\log_{10} S_i - \log_{10} S_{\text{exp},i}}{\sqrt{2}\sigma_{q,i}}\right)^2} \mathrm{d}\log_{10} S_i$$
$$= \prod_{i}^{\text{nSaturatedTanks}} \frac{1}{2}\left(1 - \text{erf}\left(\frac{\log_{10} S_{\text{sat},i} - \log_{10} S_{\text{exp},i}}{\sqrt{2}\sigma_{q,i}}\right)\right). \tag{4.14}$$

The time likelihood for saturated tanks is the same as for unsaturated tanks, because PMT saturation does not affect the LE time of the waveforms.

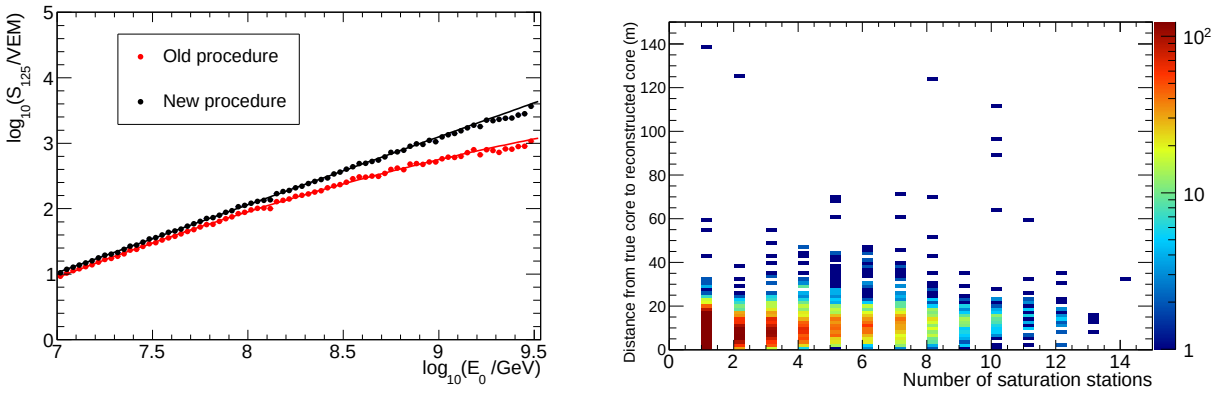

Figure 4.4: **Left**: The fitted shower size $\log_{10}(S_{125})$ as a function of the primary energy for proton MC between 10 PeV and 3 EeV compared between a likelihood procedure that does not include the saturation term (red) and one that does (black). The fitted line is first order (black) and second order (red) polynomial to illustrate the non-linearity. **Right**: Distance from true core position to reconstructed core position, when including the saturation term in the likelihood, as function of the number of saturated stations for the same events as the left plot.

In Fig. 4.4 the performance of the saturation term is illustrated. The left plot shows the difference between the old likelihood procedure from [90] and the new procedure explained here which includes the saturation likelihood term. If the saturation is not accounted for in the fit, then the relation between the shower size parameter S_{125} and primary energy E_0 clearly behaves non-linear at the highest energies. The proper treatment of saturation also results in a reconstructed core position that does not depend on the number of saturated stations in the event (right plot on Fig. 4.4). The effect of the saturation likelihood is also visible on LDF of the large event at the bottom of Fig. 4.10, where the LDF would try to go through the saturated points close to the core, which is not the case thanks to the saturation treatment.

The saturation likelihood however prefers to push signal expectation far from the saturation threshold but due to the behaviour of the error function, there is no strong change in the probability for very high expected charges. This prevents the likelihood to stress the region close to the core too much and still results in proper fits. Although this is a simple way to treat saturation in the likelihood, it does behave properly and solves the non-linear behaviour in the shower size to primary energy relation. Potential improvement could lie in the usage of the individual DOM-wise saturation curves instead of integrating over a fixed saturation threshold (in PE) for all DOMs. In addition the relation between the saturated integrated charge and the actual charge could be studied in the lab and used to correct the saturated charges. However, as seen in Fig. 2.29, the relation between unsaturated and saturated charge will be different for each PMT and should be deduced from data.

Snow correction

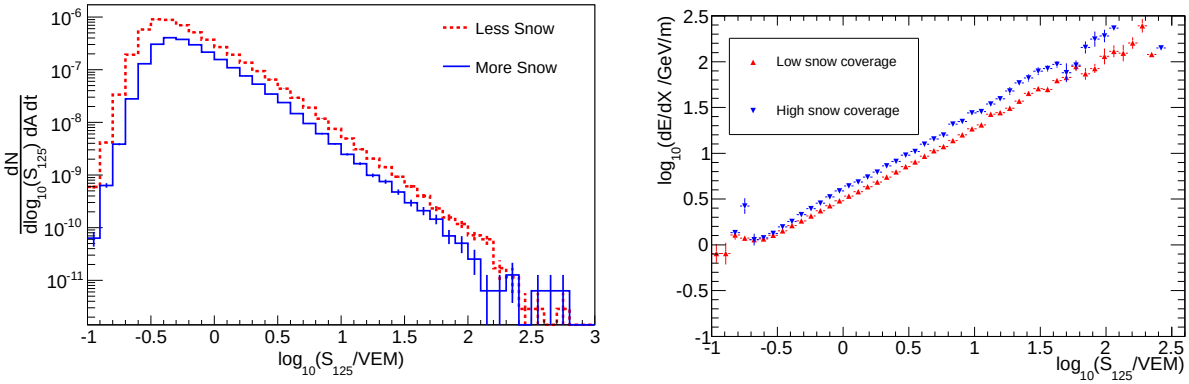

Figure 4.5: The effect of snow on reconstruction shown in two different ways. **Left:** Shower size spectra for a subarray with less snow compared to one with more snow [170]. **Right:** Reconstructed energy loss in IceCube as function of S_{125} for coincident IceTop-IceCube events also compared between subarrays with different snow coverages.

In Section 2.3.1 the varying snow heights that accumulated on the IceTop tanks are discussed. The LDF is derived based on simulation which did not include snow. The measured tank signals on the other are affected by this extra snow layer because the secondary particles lose energy or are fully absorbed by the snow. This results in a location-dependent reduction of the measured signals. The main effect is that the fitted shower size parameter S_{125} with these reduced signals also decreases. Without a proper snow correction this would mean that the relation between the primary energy of the shower and S_{125} depends on the location of where the shower lands in the array and its orientation, as different hit stations could have a different effect on the fitted S_{125}. Fig. 4.5 illustrate this nicely in two different ways. The array is divided in an *older* part which has more snow coverage than the later deployed, *newer* part according to the red subarray (*old*) and black subarray (*new*) on the left plot of Fig. 2.15. The shower size spectrum, corrected for the different geometric area, for the subarray with more snow on the left plot of Fig. 4.5 is clearly shifted to the left because of the signal attenuation by snow. However, both spectra are caused by the same primary energy flux.

For a fixed primary energy we should have the same S_{125} independent of where the showers land. However, with IceTop alone the primary energy is unknown in data. For coincident IceTop-IceCube events we can use the detected energy loss in IceCube as an estimate for the primary energy because snow does not affect the IceCube energy loss reconstruction, discussed in the next Section. The advantage of this approach is that it does not depend on the knowledge of the effective area of each of the subarrays. To prevent ambiguous showers which land near the separation of the *old* and *new* subarray that have a large variation in snow coverage of its stations and could land in either sample, the *old* and *new* subarray are defined as shown on the right plot of Fig. 2.15. The region above the dashed line has a high snow coverage, while events that fall in the region below the solid line have a low snow coverage. The right plot of Fig. 4.5 reveals that for the same average energy loss in IceCube (or roughly primary energy) a lower S_{125} is found for events that land in the subarray with a higher snow coverage as expected. Therefore after a snow correction with the correct snow attenuation length the relation between energy loss and S_{125} should be the same over the whole array.

To properly account for the signal reduction we apply the following snow correction :

$$S_{\mathrm{corr},i} = S_{\mathrm{meas},i} \cdot \exp\left(\frac{d_{\mathrm{snow}} \sec\theta}{\lambda_{\mathrm{eff}}}\right), \tag{4.15}$$

with d_{snow} the measured monthly snow heights, θ the zenith angle of the shower and λ_{eff} an effective snow attenuation length. The shower signals that go into Eq.4.8 are the snow corrected signal $S_{\mathrm{corr},i}$. Fig. 4.6

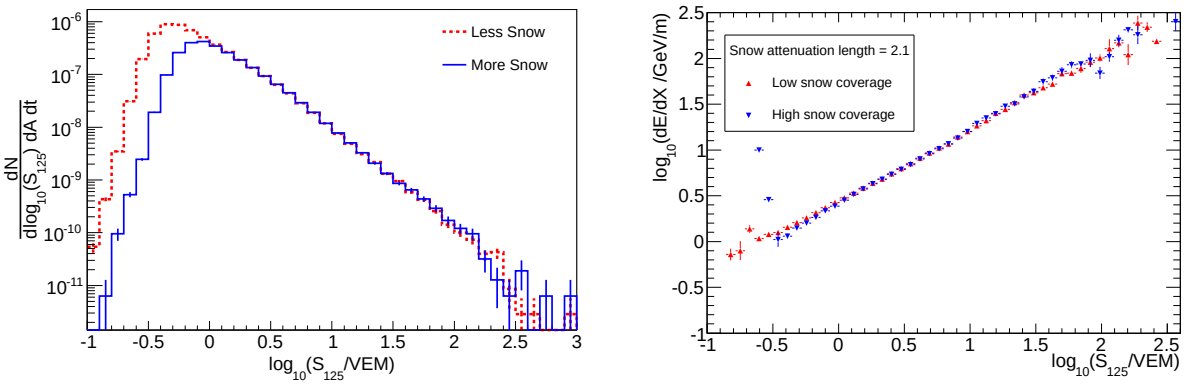

Figure 4.6: The same plots as Fig. 4.5, but after snow correction with a snow attenuation length of 2.1 m.

shows both the S_{125} spectra and IceCube energy loss as function of S_{125} after the snow correction with an optimal effective snow attenuation length of 2.1 m obtained indepently from the two studies discussed above. After the snow correction, there is no more location-dependence anymore of the reconstructed S_{125}, demonstrated by Fig. 4.7 which shows the distribution of core locations above the detector threshold of $\log_{10}(S_{125}/VEM) = 0.2$ and compared to the right plot of Fig. 2.15.

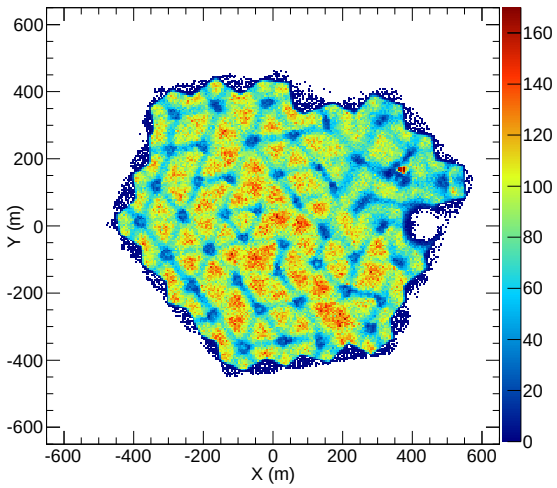

Figure 4.7: Distribution of core locations after snow correction for events above the threshold of $\log_{10}(S_{125}) = 0.2$.

Of course the different snow heights for one period in time (Feb. 2010) are included in simulation to be able to study the behaviour of snow in simulation and to make sure the energy threshold of the detector, which are xy-dependent due to the snow, match with the energy threshold in data. However, in MC the snow attenuation seems to be less strong, because the snow correction works gives a perfect correction with an attenuation length ot 4.0 m in both the proton and iron simulated data (see Fig. 4.8). The reason for this data/MC discrepancy is currently still not well understood. As for both data and MC the snow effect is corrected out of the S_{125}, this data/MC discrepancy is not worrysome but indicates we have to cut away the threshold region in the analysis later.

Muons are highly penetrating particles and are not affected by a few meters of snow on the IceTop tanks.

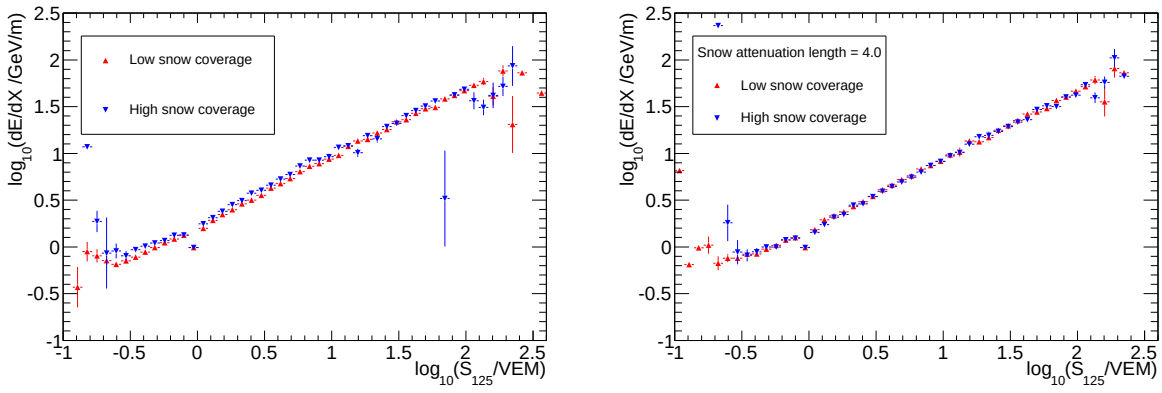

Figure 4.8: Energy loss in IceCube as function of S_{125} for simulated proton showers both before (left) and after (right) snow correction, here with an optimal attenuation length of 4.0 m.

They contribute to the detected signals which we currently correct in total for snow attenuation. This is a good first order approximation as the shower signals are dominated by electromagnetic particles but at distances far from the core position, the muon contribution to the signal becomes larger and the approximation becomes less correct. In [171] a radius-dependent snow correction is being investigated. Based on a rough first estimate of the energy and the theoretical ratio of muonic to electromagnetic component as function of distance to the shower axis, the electromagnetic part of the signal can be snow corrected while the muonic part can be left unharmed. This becomes easier once separate muon and electromagnetic LDFs are fitted instead of a global LDF to the total signal.

Fit procedure

The full loglikelihood L is the sum of the logarithm of the four likelihoods and depends on the shower core position $\boldsymbol{r}_c = (x_c, y_c)$, the time t_0 at when the shower front passed the core, the direction of the shower $\boldsymbol{n}$ and the LDF parameters S_{125} and β:

$$L(\boldsymbol{r}_c, t_0, \boldsymbol{n}, S_{125}, \beta) = \log \mathcal{L}_q(\boldsymbol{r}_c, S_{125}, \beta) + \log \mathcal{L}_t(\boldsymbol{r}_c, t_0, \boldsymbol{n}) + \log \mathcal{L}_{\text{nohit}}(\boldsymbol{r}_c, S_{125}, \beta) + \log \mathcal{L}_{\text{sat}}(\boldsymbol{r}_c, S_{125}, \beta). \tag{4.16}$$

The solution of this equation are the fit parameters that maximize the loglikelihood, or minimize the negative loglikelihood and thus describe the data, arrival times and tank charges, best. The complicated 7-dimensional likelihood parameter space can have many local minima. A fit procedure that narrows down the parameter space step by step, only fits few free parameters at the same time and starts from a good initial guess will have a higher chance of finding the global minimum without too many iterations.

The fit procedure used in this analysis differs from the old procedure described in [90] and solves several issues. The new procedure is optimized for contained events which hit more than 5 stations. Five stations are needed to keep number of degrees of freedom in the fit higher than one, required for a reliable fit. The procedure happens in three steps:

1. Starting from the seed COG core position, only the LDF is fitted and the timing likelihood is not included, ie. the direction is kept fixed at the seed plane wave direction. Both the core position and the LDF parameters are free in the fit. β is bound between 2.9 and 3.1 for a more stable first LDF fit. The core position is only allowed to move in a box with 400 m sides centered around the COG with an initial stepsize of 10 m. As shown earlier in Fig. 4.2, the resolution of the COG is already quite good, so the true core position can not be that far from the COG. The box prevents the minmizer from wandering off to some unrealistic local minima.

2. With the fit parameters as a seed from the first step, both the core position, LDF and direction are fitted all at once, which means the timing likelihood is included and a curved shower front is fitted. β is still bound but between 2.0 and 4.0 now. Because the main goal of this 7-parameter fit is to improve the direction, the core is bound in a much smaller box with sides of 30 m and centered around the core position found in the previous step, and an initial stepsize of 2 m for both x_c and y_c.

3. The timing likelihood is still used in the fit, but the direction found in step 2 is kept fixed now and the LDF and core position are refitted one last time. β is bound between 0 and 10, which is beyond all realistic slopes and hence means that β is unbound. The core is less bound than the previous step in a 70 m box, and an initial stepsize of 1 m.

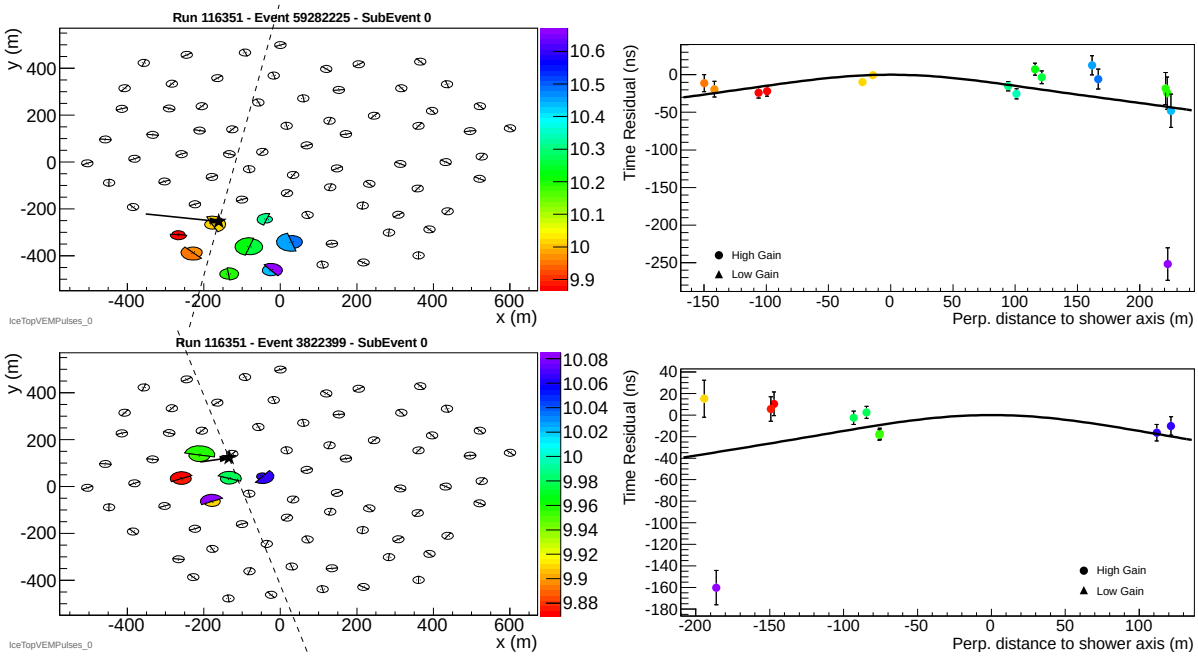

Figure 4.9: Two examples of events with tanks that have arrival times later than 80 ns after the shower front arrives. **Left**: Top view of the events. The colours represent the arrival times in μs, the dashed line is perpendicular with the azimuth angle and the size of the arrow proportional to the zenith angle. The half spheres are proportional to the charges in the tanks. **Right**: Time residual Δt as function of the perpendicular distance to the shower axis. Negative distances mean tank positions hit before the shower front crosses the core position (*downstream*).

The three-step procedure with a decreasing parameter space for the core position, to prevent the minimizer from wondering off to distant local minima, and an increasing parameter space for β, to focus more on an accurate LDF fit in the last step, all make sure that the search for the global minimum is well guided. The algorithm used for the minimization of the negative loglikelihood is SIMPLEX [172][1] with a maximum number of iterations of 2500. During each iteration of the minimization pulses which are closer than 5 m from the core position are not included in the fit, because the LDF becomes unphysical at very small distances. For the curvature fit, tanks which have arrival times that deviate more than 80 ns from the expectation are removed from the fit. Even though they are not noise hits and seen both in data (two examples are shown in Fig. 4.9) and in MC, they do confuse the curved shower front fit and often the whole likelihood as well. The minimizer tries to put the core position far away from these tanks, because then their (overestimated) timing fluctuations will fake that the times are consistent with the shower front expectation.

[1]The fitting is done using the Minuit [173, 174] libraries.

For data it is important that the seed core position and direction are not biased by noise stations from double coincidences (different showers hitting the IceTop array at the same time). The hit cleaning method explained in Section 5.3.2 must be applied to the hits used by the seeding algorithms in order to provide unbiased seeds to this maximum likelihood procedure.

For low energy showers, which hit 3 to 4 stations, only the first step of the procedure without the timing likelihood is used. These events are not used in the analysis presented in this theiss but the performance is being studied dedicately in [92].

Fit performance

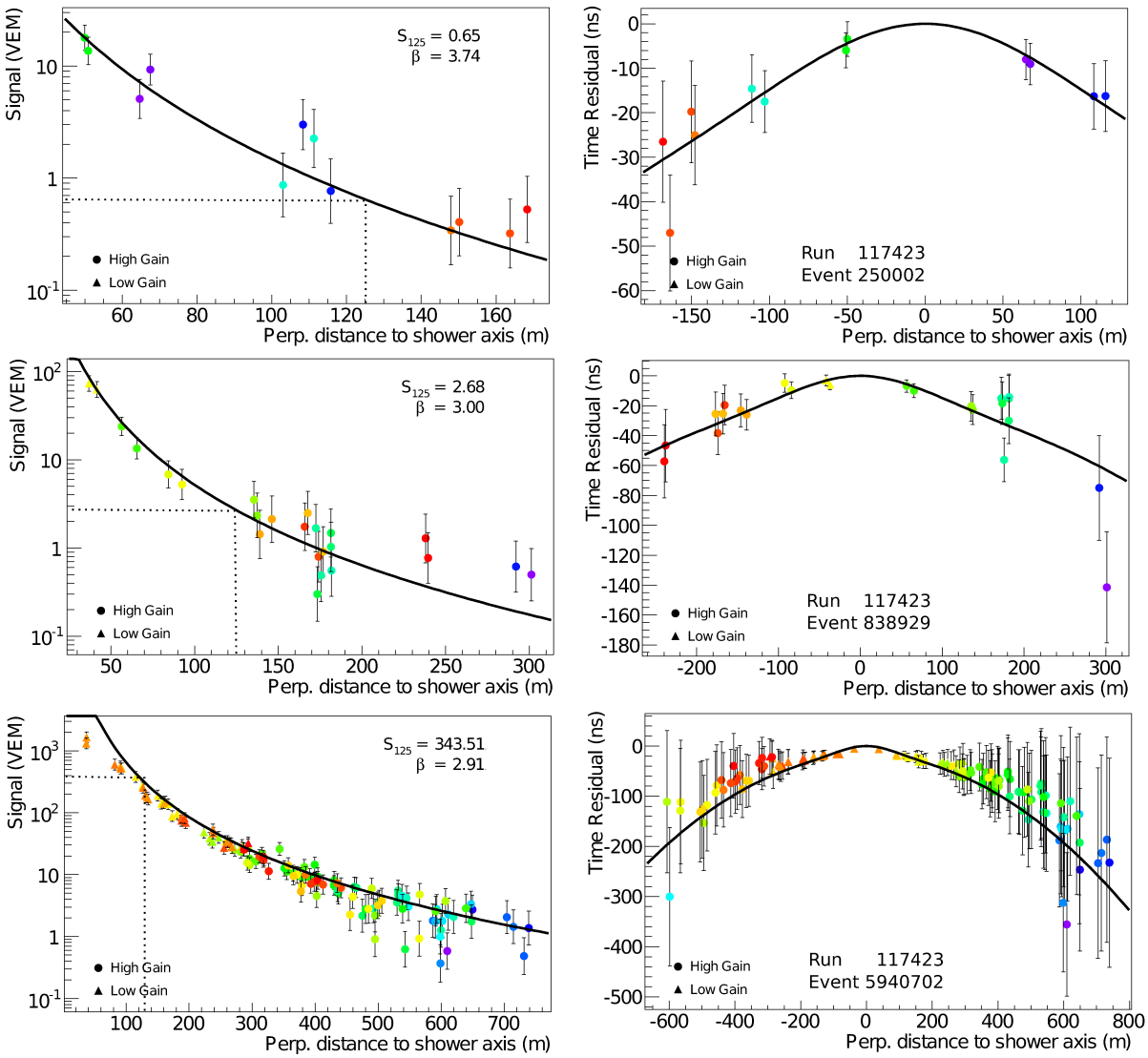

Figure 4.10: Examples of a small event (top), a medium event (middle) and a large event (bottom) with the LDF fit result on the left and the curvature fit on the right. The dotted line on the LDF fits show the signal at 125 m from the core, S_{125}

Fig. 4.10 demonstrates the LDF and curvature fits through a small event that hit 6 IceTop stations, a medium event that hit 12 Icetop stations and a large event that hit 64 IceTop stations. The LDF and curvature fits describe the data in all cases very well. For the large event the LDF goes more clearly above the data points because the data points are here not snow corrected while the fit is and very close to the core the signals

are saturated. The limitation of a fixed curvature is also clear in the large event which does not describe the curvature as good as for the other two events. The real timing fluctuations on the points is also much smaller than the error bars for the overestimated fluctuations indicate, as mentioned earlier.

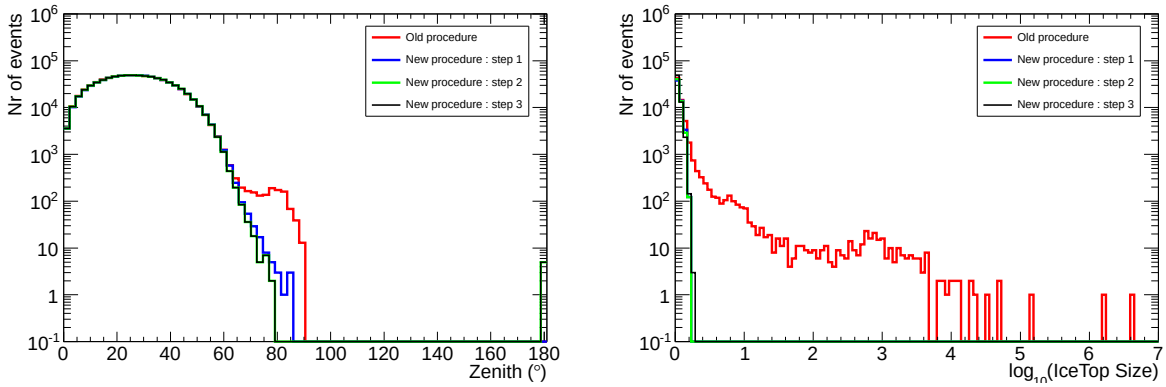

Figure 4.11: The reconstructed zenith angle (left) and IceTop size (right) distribution for data compared between the old procedure from [90] and the three steps of the fit procedure described here.

In Figs.4.11 to 4.13 the old procedure decribed in [90] is compared to the three steps of the new procedure described above based on three days of data (Aug. 12, 2010, Sept.12, 2010 and Oct.13, 2010). Fig. 4.14 uses proton simulations to compare angular resolutions and core resolutions. The only quality cuts applied are a minimum required of 5 hit stations and successful, converged reconstruction. The old procedure loses 5% of the events because they did not converge, while the new procedure does not have this problem but loses 5.5% because after the hit cleaning from Section 5.3.2 less than five good stations remain in the set of pulses used for reconstruction.

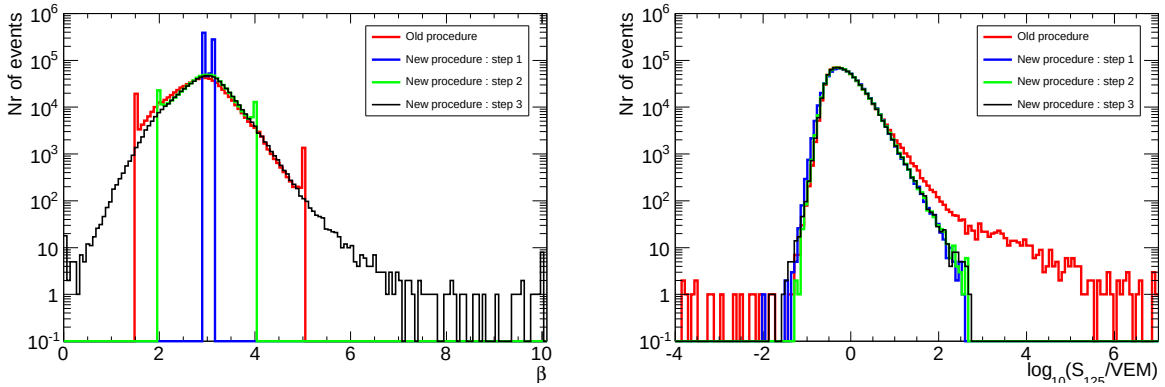

Figure 4.12: The reconstructed β (left) and S_{125} (right) distribution for data compared between the old procedure from [90] and the three steps of the fit procedure described here.

The main improvement obtained with the new procedure can be observed mainly in the tails of the distributions. In the zenith angle distribution from the left plot of Fig. 4.11 there is an unphysical bump near the horizon (90°) in the old procedure while the improved, new procedure does not have this artefact anymore. The new procedure reconstructed five events ($6 \cdot 10^{-4}$%) as vertically upgoing. Each of these events is investigated in detail and no reasonable reconstruction is possible for these events, so these will be cut out later by quality cuts. The IceTop size distribution from the right plot of Fig. 4.11, which quantifies by which factor the contour of the IceTop array has to be scaled so the core position lies on the contour,

illustrates the importance of the bounds on the core position in the fit procedure. The tail, only visible for the old procedure, shows reconstructed core locations which are unrealistically far from the IceTop array and clearly ended up in far away local minima.

The β distribution from the left plot of Fig. 4.12 illustrates the stepwise loosening of the bounds and that the bounds in the last step are safe. The peaks in each distribution come from events where the minimizer gets stuck on the boundary of this fit parameter and typically means the results are unreliable. This meant that a quite strong quality cut was needed with the old procedure that removed 3% of the events. The new procedure exhibits a smooth β distribution not affected by the boundary conditions. In addition the fraction of events that would have been cut by the same quality as for the old procedure is only 0.1%. In Section 5.4.1, we will discuss whether a cut on β is still necessary.

The S_{125} distribution, which is closely related to the primary energy distribution because of the relation in Fig. 4.4, reveals both unrealistically small values and too many large values in the old procedure. These are caused by the LDF either missing all the data points or where the core is misplaced and the measured signals then misrepresent a bad LDF fit at large distances from the core, hence resulting in large S_{125} values. In both cases the minimizer still converged to a local minimum in the likelihood space. In analyses based on the old procedure, these events had to be cut away later by a set of quality cuts, while here with the new procedure they are properly treated by the reconstruction itself.

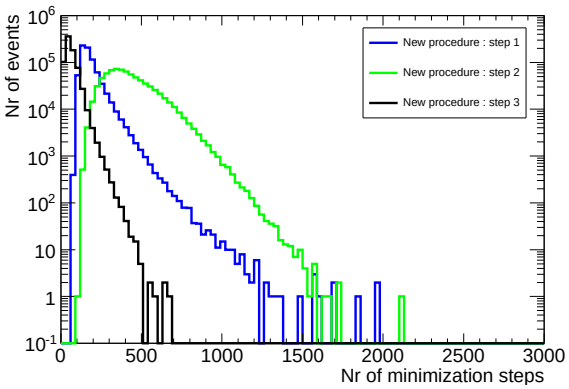

Figure 4.13: Distribution of number of iterations needed by the SIMPLEX minimizer to converge for the three steps of the fit procedure.

In Fig. 4.13 the number of minimization steps required by the SIMPLEX minimizer for convergence motivate the chosen maximum number of iterations of 2500 in the fit procedure. The second step needs more iterations because the minimizer looks for a minimum in a 7-dimensional parameter space instead of the 4-dimensional space from step one. In the third step the minimizer converges much faster because it is also much closer to the global solution thanks to the previous two steps.

From these comparison we conclude that the new procedure solves several issues seen with the procedure from [90] and that not well reconstructed events which had to be cut out by several quality cuts are now properly treated by the new procedure. With only the criterium that at least five good stations are needed for the fit, all distributions look smooth and ready for an energy and composition analysis.

The reconstruction quality based on proton simulations between 100 TeV and 100 PeV is illustrated by Fig. 4.14 and compared between all events (left) and events that fall inside the IceTop array, called *contained events* (right). The improvement of the direction reconstruction when a curved shower front is used instead of planar shower front (blue) is clearly shown. The new procedure improves on the old procedure mainly in the tail of the distribution and probably comes from the treatment of signals that deviate a lot from the expected arrival times and from a better core reconstruction.

The core reconstruction, presented by the lower two plots of Fig. 4.14, of the COG seed was already quite good because certainly for contained events the core is always near the stations with the largest signals.

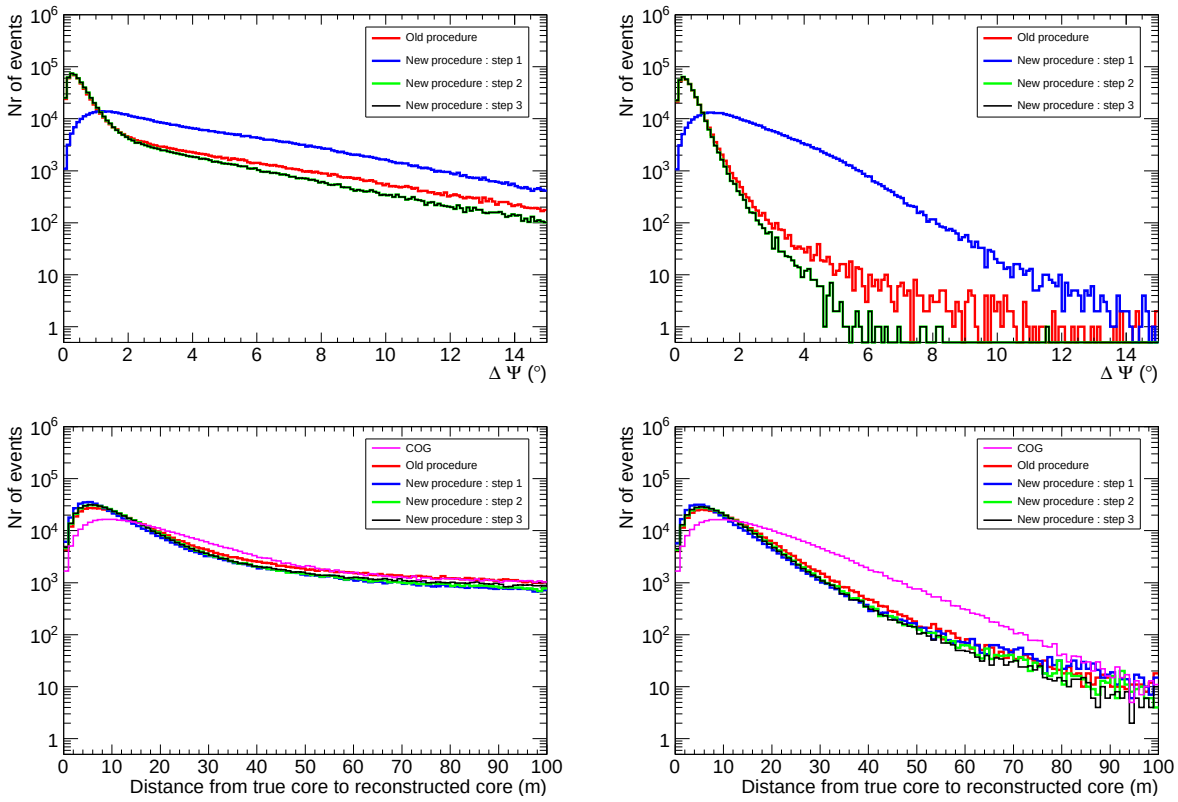

Figure 4.14: **Top**: Opening angle between the true direction and the reconstructed direction for all events (left) and contained events (right). As the direction is held fixed in step one, the blue distribution shows actually shows the reconstruction quality of the seed direction based on a planar shower front. **Bottom**: Distance between the true core position and the reconstructed core position for all events (left) and contained events (right).

The lateral distribution fit improves on the core reconstruction with the new procedure showing a better performance than the old procedure, probably due to the decreasing freedom in the parameter space for the core in each step.

Contained events (right) both have a much better direction reconstruction and core position reconstruction. Therefore we will only use contained events in this analysis. The reconstruction of uncontained events need a dedicated treatment which is currently under development but this is outside the scope of the work presented here.

4.2 IceCube reconstructions

The IceCube detector observes the Cherenkov light pattern from the high energy bundles of muons that propagate through the Antarctic ice and from their accompanying energy losses, which create Cherenkov light emitting cascades. From the arrival times of the signals in the DOMs the track direction can be obtained through a maximum likelihood procedure [175]. However, we will not go in detail here because the IceTop direction performs much better than the best IceCube track reconstruction and no IceCube track reconstruction is used in the analysis presented here for reasons discussed in Section 5.3.1.

The amount of light detected by the IceCube in each DOM relates to muon bundle energy loss, which depends on the muon multiplicity. The number of high-energy muons at some fixed slant depth X in the ice is the most important probe to the primary cosmic ray composition, as illustrated by Fig. 4.15. The

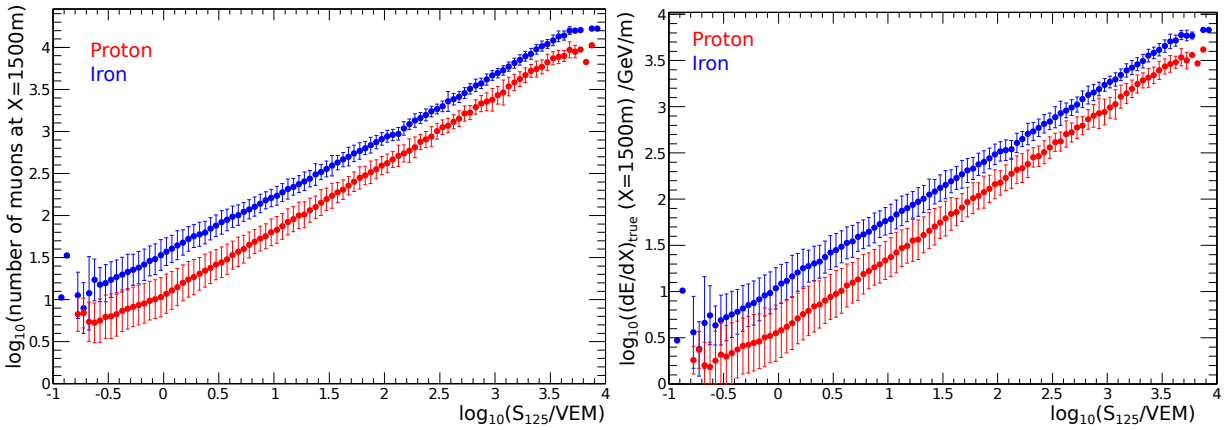

Figure 4.15: **Left**: Number of muons after the muon bundle travelled through 1500 m of ice as function of S_{125} for proton (red) and iron (blue) simulations between 100 TeV and 3 EeV, with the RMS as error bars. **Right**: Muon bundle energy loss, at the same slant depth as the left plot, as function of S_{125}.

muon multiplicity from iron-induced showers is very well separated from the the muon multiplicity from proton-induced showers except at the lowest energies where the distributions start to overlap a little. This is expected from the Elbert formula at low energies, see Fig. 1.25. The muon bundle energy loss is expressed as a function of the muon multiplicity by:

$$\left(\frac{\mathrm{d}\,E_{\mu,B}}{\mathrm{d}\,X}\right)(X) := \left(\frac{\mathrm{d}\,E_{\mu}}{\mathrm{d}\,X}\right)_{\text{bundle}}(X) = \int_{E_{\min}}^{E_{\max}} \frac{\mathrm{d}\,N_{\mu}}{\mathrm{d}\,E_{\mu}}(A, E_0, \theta, E_{\mu}, X)\frac{\mathrm{d}\,E_{\mu}}{\mathrm{d}\,X}\,\mathrm{d}\,E_{\mu}, \tag{4.17}$$

where the muon multiplicity $N_{\mu} = \int_{E_{\min}}^{E_{\max}} \frac{\mathrm{d}\,N_{\mu}}{\mathrm{d}\,E_{\mu}}\,\mathrm{d}\,E_{\mu}$ and with $E_{\min}$ the energy needed to reach depth X and $E_{\max} = E_0/A$ the maximum energy muons from a primary with energy E_0 and mass A can have. The energy loss smears the muon multiplicity distribution but the right plot of Fig. 4.15 still shows a good separation between the proton-and iron-induced muon bundle energy loss distributions. Therefore, the main composition sensitive information detected by IceCube is the muon bundle energy loss $(\mathrm{d}\,E_{\mu,B}/\,\mathrm{d}\,X)(X)$ at a chosen slant depth. Studies from [176] have shown that energy losses at narrower depths have slightly better composition separation, hence from now we always take the energy loss at the top of the IceCube detector, $(\mathrm{d}\,E_{\mu,B}/\,\mathrm{d}\,X)$ (X = 1500 m), as *the* muon bundle energy loss.

In addition to the average muon bundle energy loss, Fig. 1.26 hints another difference between proton and iron bundles that can be exploited. For low to medium primary energy showers, the probability to have an extremely high energy muon in the bundle is larger for proton than for iron. These very high energy muons have a higher probability to create large local energy depositions from Bremsstrahlung. As a consequence there can be higher extreme stochastic energy losses in the energy loss profile for proton bundles than for iron bundles.

The overall stochasticity of the energy loss profile, manifested by the number of stochastic energy losses, is an extra property sensitive to the muon multiplicity. Iron bundles have more muons that proton bundles which increases the probability to create (low energy) stochastic energy losses at the same place in the place in the detector. This results in higher than every average energy losses, named *stochastics*, from the whole bundle at certain track segments. Counting these *stochastics* therefore gives us an extra composition-sensitive property. Consequently iron bundles have more *stochastics*, but the energy losses from proton bundles can be more extreme.

Hence the goal for IceCube reconstructions exists in obtaining the energy loss profile in track segments along the muon bundle as a function of slant depth. Then the average energy loss is fitted to the segmented energy losses. The stochastic energy loss behaviour is acquired by an optimal selection of large deviations,

the *stochastics*, from the fitted average energy loss. The properties of the selected *stochastics* and the average energy loss are the composition-sensitve observables, needed by the coincident IceTop-IceCube composition analysis presented in this thesis.

The larger muon multiplicity for iron bundles also creates wider muon bundles, demonstrated in Fig. 1.28, because lower energy muons have larger transversal momenta and are situated further from the shower axis (see Fig. 1.27). A reliable reconstruction of the bundle radius could yield another composition observable but this has been proven to be very difficult.

4.2.1 Unfolding the energy loss pattern

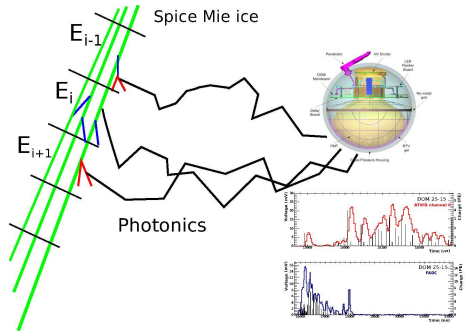

Figure 4.16: Cherenkov light emitted from distinct muons at different track segments i along the muon bundle from various sources, detected by the same DOM. The ATWD and FADC waveforms show the time profile of the detected photons.

In Section 2.2.1 we have seen that the emitted Cherenkov light scales with the energy of the electromagnetic and hadronic cascades generated by stochastic energy loss from high energy muons. The attenuation of the photons in the South Pole ice does not change that energy dependence. Due to the small scattering length, but large absorption length in the ice photons from bright cascades can travel very far. The IceCube PMT thus detects photons originating not only from the Cherenkov cone that directly illuminates the PMT but also from other places along the track. This is illustrated in Fig. 4.16. Along the muon bundle cascades with energy E_i from energy losses of one or multiple muons of the bundle at track segment i emit photons that scatter through the detector. Several track segments contribute to the total charge seen by the PMT. The total charge Q_k measured in DOM k is therefore:

$$\begin{aligned} Q_{\text{exp}} := Q_k &= E_1\lambda_1(DOM_k) + E_2\lambda_2(DOM_k) + \cdots + E_n\lambda_n(DOM_k) + \nu_k \\ &= \left(\frac{\mathrm{d}\,E_{\mu,B}}{\mathrm{d}\,X}\right)_1 \lambda_1(DOM_k) + \left(\frac{\mathrm{d}\,E_{\mu,B}}{\mathrm{d}\,X}\right)_2 \lambda_2(DOM_k) + \cdots + \nu_k \\ &= \sum_i^{\text{nTrackSegments}} \left(\frac{\mathrm{d}\,E_{\mu,B}}{\mathrm{d}\,X}\right)_i \lambda_i(DOM_k) + \nu_k \end{aligned} \tag{4.18}$$

with $\left(\frac{\mathrm{d}\,E_{\mu,B}}{\mathrm{d}\,X}\right)_i := \left(\frac{\mathrm{d}\,E_{\mu,B}}{\mathrm{d}\,X}\right)(X_i)$ where X_i is the slant depth of track segment i. $\lambda_i(\text{DOM}_k)$ is the expected charge from a 1 GeV cascade on tracksegment i at DOM j. ν_k is the PMT noise term, which is of course independent of the physics of the muon bundle but contributes to the detected charge.

In addition to the fact that several track segments contribute to the total charge detected by DOM k, the different pulses of a waveform also carry different contributions from different track segments. The first pulse arises from the first arriving arriving photons emitted by the Cherenkov cone that illuminates the DOM, only called direct photons as they travel almost unscattered to the DOM. Later pulses are from photons that endured some scattering, and could come from neighbouring segments to the one that emitted the direct

photons. Eq.4.18 remains unchanged to account for this, but index k now has the meaning of a time bin within a certain DOM [133].

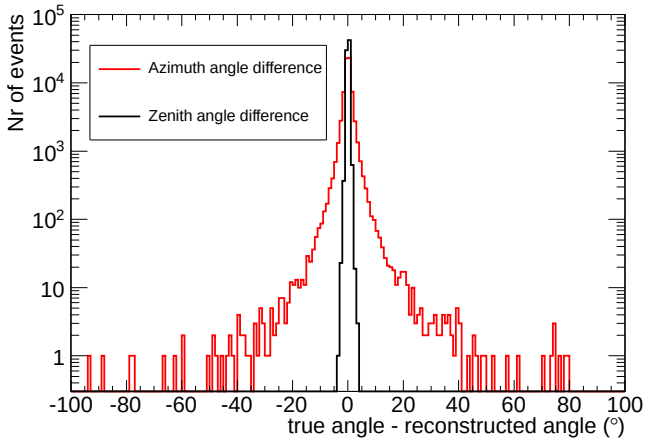

Figure 4.17: The difference between the true zenith (black) or azimuth angle (red) and the reconstructed angle.

An accurate energy loss reconstruction tries to solve Eq.4.18 with respect to the unknown energies E_i at some well chosen track segments for each DOM and even for each pulse. Crucial for a good quality energy loss reconstruction is a well reconstructed track, which for muon bundles has the meaning of the shower axis or central bundle axis. If the reconstructed track is further away from a certain DOM than the true track, then the energy loss reconstructed will misinterpret the measured charge as coming from a much brighter cascade than was actually the case. After cuts, described in Chapter 5, the IceTop track reconstruction gives a very good angular resolution between 0.3° and 1.0° and a very good core resolution at the surface of 6-10 m (see Fig. 5.40). However, the azimuth angle is not as well reconstructed as the zenith angle illustrated by Fig. 4.17. Several scans in the azimuth-zenith angle likelihood space for all known likelihood descriptions used in several track reconstructions were performed and no improvement over the current reconstruction was found. This could limit the performance of the energy loss reconstruction, described below.

The algorithm

The energy loss pattern from a cosmic ray muon bundle does not only give rise to the waveform in one DOM, but to the waveforms in all hit DOMs. Eq.4.18 can then be described by the matrix equation :

$$\begin{pmatrix} \lambda_1(DOM_1) & \lambda_2(DOM_1) & \cdots & \lambda_n(DOM_1) \\ \lambda_1(DOM_2) & \lambda_2(DOM_2) & \cdots & \lambda_n(DOM_2) \\ \vdots & \vdots & \ddots & \vdots \\ \lambda_1(DOM_m) & \lambda_2(DOM_m) & \cdots & \lambda_n(DOM_m) \end{pmatrix} \begin{pmatrix} \left(\frac{\mathrm{d}\,E_{\mu,B}}{\mathrm{d}\,X}\right)_1 \\ \left(\frac{\mathrm{d}\,E_{\mu,B}}{\mathrm{d}\,X}\right)_2 \\ \vdots \\ \left(\frac{\mathrm{d}\,E_{\mu,B}}{\mathrm{d}\,X}\right)_n \end{pmatrix} + \begin{pmatrix} \nu_1 \\ \nu_2 \\ \vdots \\ \nu_m \end{pmatrix} = \begin{pmatrix} Q_1 \\ Q_2 \\ \vdots \\ Q_m \end{pmatrix}$$

$$\Rightarrow \mathbf{\Lambda} \cdot \vec{E} = \vec{Q} - \vec{\nu}, \tag{4.19}$$

where m goes over all pulses of all DOMs (both hit and unhit) and n is the number of tracksegments based on a chosen segment spacing. The detector response matrix $\mathbf{\Lambda}$ is obtained from simulations. Using the Photonics program, as explained in Section 3.2, tables with the expected number and arrival times of Cherenkov photons from 1 GeV cascades are generated. The photon propagation is based on the Spice-Mie ice model. To prevent binning artefacts from unaccurate bin-to-bin interpolations during the readout of the tables, the tables are

fitted by smooth B-splines [177] and the coefficients are stored in so-called spline tables. The matrix $\mathbf{\Lambda}$ for a certain track is then built up from lookup operations to these spline tables for each event.

The unfolding procedure to obtain the segmented energy losses exists in inverting the above matrix equation [133]. Solving the matrix equation with simple linear algebra would result in alternating positive and negative solutions for the energies of the segments. This is a typical problem in unfolding and is caused by the fact that the measured DOM charges (or pulse charges) are not the exact solution of the matrix equation, but come from a Poisson distribution around the average values. Regularisation is the mathematical technique that solves this problem because it prevents large unrealistic variations in the solution. Similar as in the unfolding used to extract the pulse charges from IceCube waveforms, the condition that the solution has to be positive provides the required regularization. For the unfolding the NNLS algorithm from [134] is used.

The unfolding however only provides a good seed for a maximum loglikelihood procedure that further improves the result by allowing Poisson fluctuations of the measured charges:

$$\mathcal{L}(\vec{Q}_{\mathrm{meas}}|\vec{Q}) = \prod_{k}^{\mathrm{mTimeBins}} \frac{(Q_k)^{Q_{\mathrm{meas},k}}}{Q_{\mathrm{meas},k}!} \cdot e^{-Q_k}$$

$$L = \log \mathcal{L} = \sum_k Q_{\mathrm{meas},k} \log(Q_k) - \sum_k Q_k - \sum_k \log(Q_{\mathrm{meas},k}!) \tag{4.20}$$

with $Q_{\mathrm{meas},k}$ the measured charges in time bin k of some DOM, and Eq.4.18 for the expected charges Q_k. The matrix equation from Eq.4.19 is actually the first order approximation of the above Poissonian likelihood (in the Gaussian error regime).

Procedure

Before the actual unfolding procedure is executed, a proper pulse selection is necessary which is described in detail in Chapter 5. Additionally, waveforms with calibration issues are tagged during the calibration and saturated parts of the waveforms are marked. These are also excluded from the energy loss fit procedure.

Of course not the whole energy loss profile from when the muon bundle penetrates the ice until all muons are absorbed can be reconstructed. We chose the same slant depth range between 1300 m and 2600 m for each event because we want to compare the energy loss profile after the muon bundle propagated through the same amount of ice, independent of the zenith angle of the shower axis. The range is optimized in order to include segments above the top of IceCube that create light in the top DOMs and segments at the bottom of IceCube that create detectable light for inclined bundles (zenith angle up to 30°) in the bottom DOMs.

The track segments are chosen to be 20 m long. Ideally very small track segments would result in a more accurate description of the energy loss pattern. However, this enlarges the response matrix $\mathbf{\Lambda}$ and thus also the number of lookup operations to the spline tables. Several segmentations were tried, but the gain in performance between 10 m and 20 m segments was small compared to the much higher computation time needed per event. The chosen track segment spacing also corresponds closer to the DOM spacing of 17 m, which limits the resolution with which the detector sees the track.

Implicitly the energy loss reconstruction assumes that the light comes from a single muon and not from individual, parallel muons inside a muon bundle. For the muon bundle energy loss reconstruction we therefore assume that the muons are packed together at the bundle axis. As an attempt to account for a bundle width we added a Gaussian jitter with a width of 30 ns to the expected arrival times from the spline tables.

DOM efficiency correction

Due to a shadow effect of the DOM cable, the angular acceptance of the DOM, the glass, the optical gel and the quantum efficiency Cherenkov photons incident on the DOM are lost. The ratio of the number of photo-electrons that get to the photocathode of the DOM over the total number of photons that hit the DOM is called the DOM efficiency and depends on the wavelength of the wavelength of the photons and the area of the DOM which is hit. Therefore the measured charge in the DOMs depends on the efficiency of the DOM.

This is accounted for by the simulation of the photon propagation takes these efficiencies when calculating the expected charge. Because the ratio of measured charge and expected charge gives the energy loss, this means the DOM efficiency is corrected out.

However, recent studies [133] to improve the knowledge and uncertainty of the DOM efficiency in situ have shown that the DOM efficiency is 10% higher than assumed before. The study is still ongoing, so the value and its uncertainties are not final. For the energy loss reconstruction any DOM efficiency can be included during the calculation of the expected charges for the response matrix $\mathbf{\Lambda}$. For the new nominal value, this means the setting we use for the algorithm is 0.99 as DOM efficiency (= 1.1·(100% - 10% cable shadowing not including in the photon propagation simulation)).

Performance

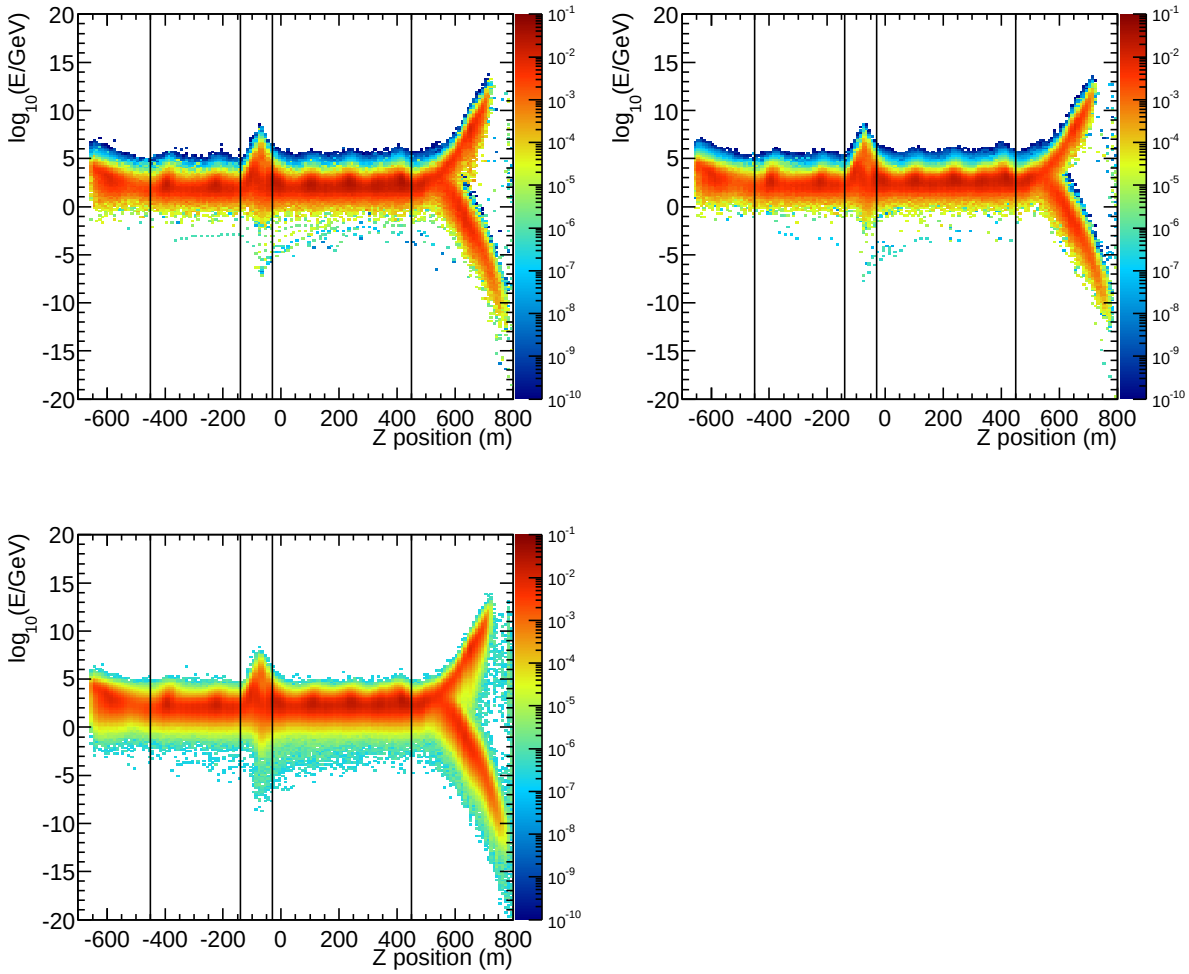

Figure 4.18: The energy of the reconstructed cascades as a function of their z position in the detector for proton simulations (top left), iron simulations (top right) and data from June and July 2010 (bottom left). The colour code shows the rates in Hz. The cuts discussed in the text are illustrated by the vertical lines.

If we look at the distribution of reconstructed energies of the cascades as a function of their z position in the detector (Fig. 4.18) some issues inherent to segmented energy loss reconstruction become apparent. At some places in the detector there are anomalously higher ($\sim 10^{13}$ GeV) and lower energies ($\sim 10^{-13}$ GeV) of

the reconstructed cascades then in the rest of the detector. The locations in the detector where the unfolding gives unphysical solutions are outside the IceCube volume (above 450 m and below -450 m in Fig. 4.18) and in the big dust layer (between -140 m and -30 m). This is the result of a local ill-defined problem.

The light detected by the top DOMs could for example come from a track segment nearby with medium energy loss or from a much brighter segment further away. As there are only a very few DOMs that carry information about those segments, the problem is hard to solve and yields in large fluctuating solutions as clearly shown by Fig. 4.18. The same is valid for segments outside the walls of the IceCube volume or below the bottom of IceCube. There are not enough DOMs surrounding the segments to result in a well defined problem that could be accurately solved by the unfolding. In the large dust layer in the center of IceCube, the large absorption makes sure that only very few photons are detected by the DOMs in the dust layer and that they must be close to the track to see some light. Because of the large fluctuations on the few number of detected photons by few DOMs in the dust layer the problem is also not well-defined and again gives large fluctuations.

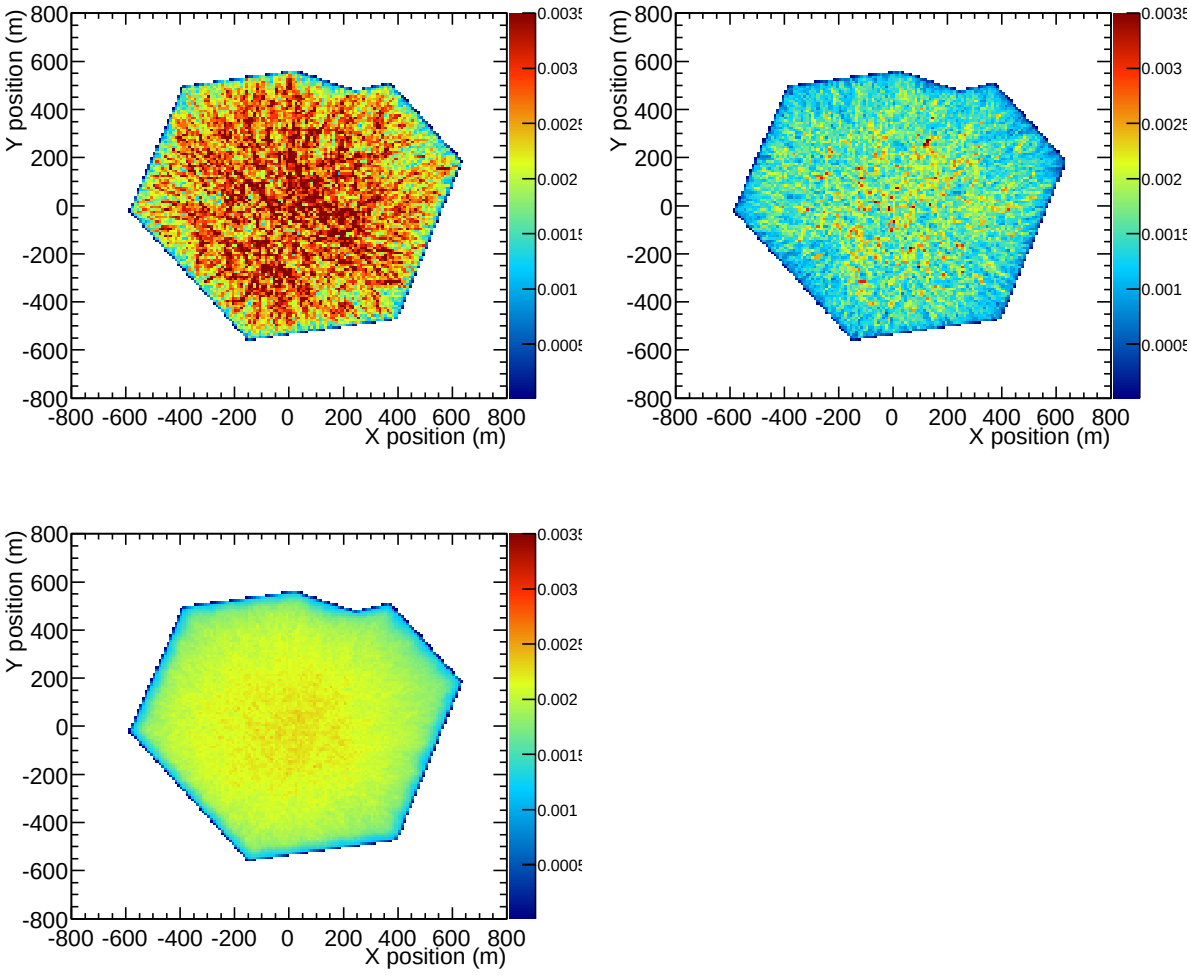

Figure 4.19: The map of where the energy loss cascades are reconstructed for proton simulations (top left), iron simulations (top right) and data from June and July 2010 (bottom left), where the colour code shows the rate in Hz.

The information about how much the data is defined by a particular segment is mathematically stored in the Fisher information matrix, which can analytically be derived from the likelihood equation, Eq.4.20.

The covariance matrix could then in principle be used to calculate the errors on the reconstructed energies. However, because of a very small determinant of the Fisher information matrix, the inversion is practically impossible. The study on how to correctly use the information stored in the Fisher information matrix to judge on the energy reconstruction quality of each segment is ongoing.

Alternatively regularization terms can be added to force the solution in the dust layer and outside the detector to be smoother and hence reduce the ambiguity. The technical implementation of this regularization was not yet ready during the development of the analysis presented here. The solution to this problem used in my analysis is to cut away the track segments outside the IceCube volume and inside the dust layer. Fig. 4.18 does show a very nice agreement between data and MC (top two plots), which strengthens our trust in the validity of the energy loss reconstruction and in the choice of the cuts.

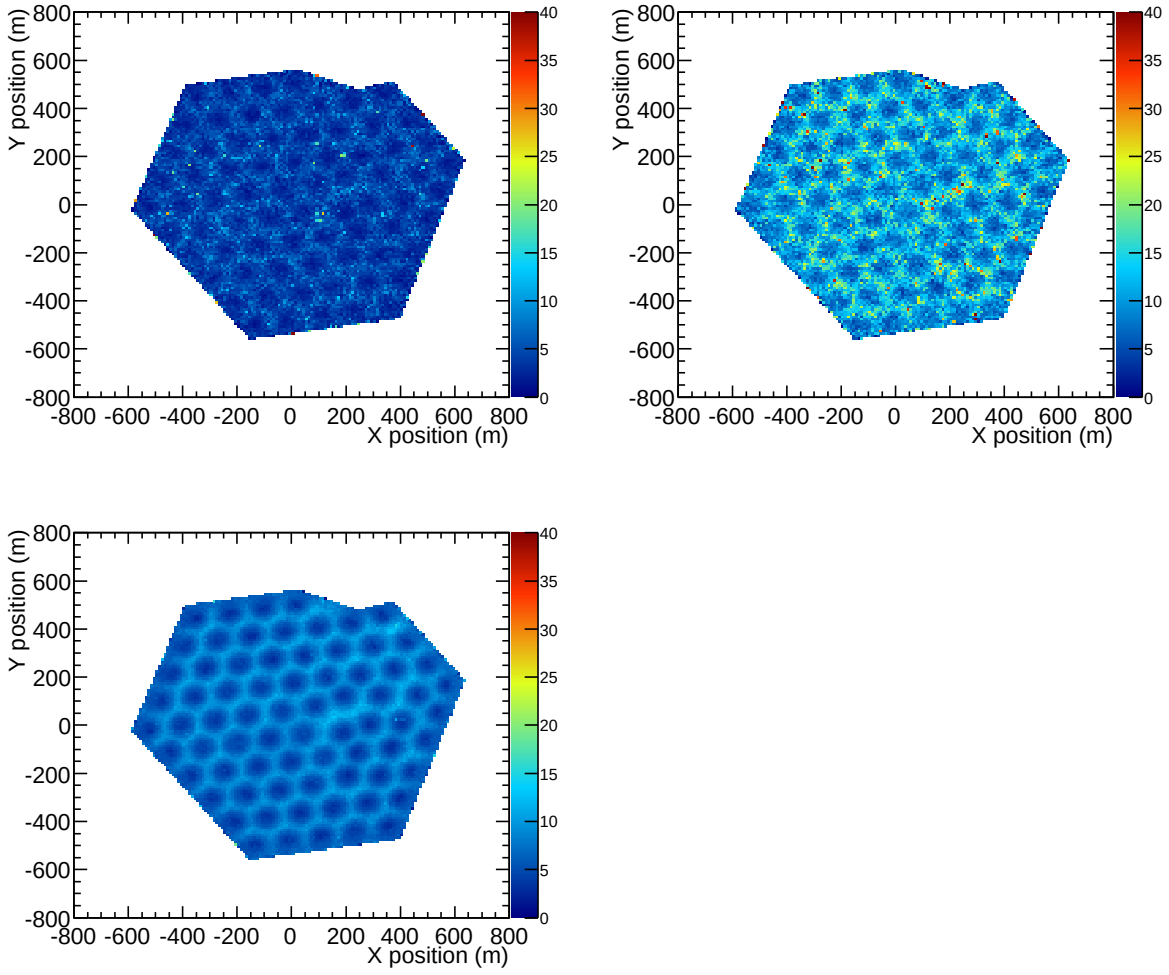

Figure 4.20: The map of where the energy loss cascades are reconstructed for proton simulations (top left), iron simulations (top right) and data from June and July 2010 (bottom left), where the colour code shows the average energy loss in GeV/m in that xy-bin.

The reconstructed energies of the 65 20 m long track segments do not all yield non-zero values. Because of the same reason as explained above, segments which are in between strings generate light that is not detected by many DOMs and are therefore difficult to have a well-reconstructed energy loss. In other words, due to the finite detector spacing, only parts of the energy loss profile are sampled by the detector. The position of the track segments with non-zero reconstructed energies, called reconstructed cascades from here

on, for both simulation and data is plotted in Fig. 4.19. The sharp IT-73 geometric area is visible because the cascades which are reconstructed outside the IceCube volume or in the dust layer are cut away. The reconstructed non-zero cascades have no position dependence and are consistent between proton and iron MC and data.

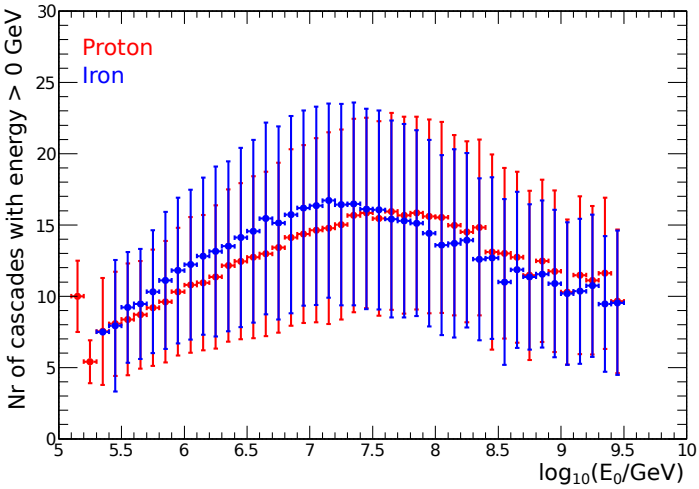

Figure 4.21: Average number of reconstructed cascades with a non-zero energy as a function of primary cosmic ray energy for proton (red) and iron (blue) simulations. The error bars denote the RMS of the distribution.

The average energy losses of those segments depict a clear structure in Fig. 4.20. Cascades near the IceCube strings have lower reconstructed average energy losses than cascades in between strings. This might be related to the fact that less information is known from DOMs far away from a track segment right in between two strings and is compensated by systematically larger energy losses to account to compensate for the lack of information. The regularization, currently under study, should smoothen this xy-dependence of the energies of reconstructed cascades out. However, this is nothing to worry about as the variation is not large and the effect both visible in data and MC.

Another potential issue is demonstrated by Fig. 4.21. One would expect that the brighter the track, the more DOMs see more light from the whole track, so the number of reconstructed cascades with a non-zero energy should increase with primary energy until all segments can be well reconstructed. This seems to be only true up to primary energies of about 20 PeV after which there is a decrease which starts at a different energy for proton and iron simulations. Around those energies the muon bundle diameter is about 100-120 m (Fig. 1.28), which is also the string spacing. This means that the approximation that all muons are packed together at the shower axis seems to break down. As a result the resolution of the muon bundle energy loss reconstruction might be affected at the high energy. To properly account for the bundle radius is however very difficult but should be studied in the future to improve the reconstruction at high energies.

4.2.2 Selection of extreme stochastic energy losses

The result of the reconstructed energy loss profile, before the cuts on cascades in the dust layer and cascades outside the detector, can be seen in Fig. 4.22 for a HE event. The reconstructed energy from the unfolding procedure described above is translated to an energy loss by a division by the length of the track segment. From this energy loss profile we want to acquire an average energy loss and some qualitative parameters that describe the stochasticity of the bundle. Those parameters should be composition-sensitve observables that can be used together with the mainly energy dependent shower size from IceTop for the IT-73/IC-79 primary composition analysis. In order to find the best observables we typically look for parameters that have large separation between proton and iron-induced air showers, or have different shapes of distributions.

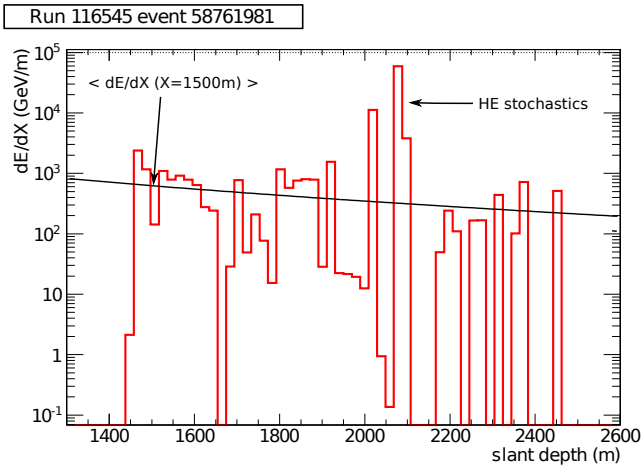

Figure 4.22: Example of the energy loss reconstruction of large event, where the solid line demonstrates the average energy loss fit and the dashed line the energy loss fit after subtraction of the selected extreme cascades or *stochastics*. The properties of the stochastics selection are mentioned in the top right corner.

The algorithm

To interpret the reconstructed segmented energy losses and determine the average energy loss at a fixed slant depth in the ice we perform a fit with the expected muon bundle energy loss as fit function. The solution from Eq.4.17, derived in Appendix B, is:

$$\left(\frac{\mathrm{d}\,E_{\mu,B}}{\mathrm{d}\,X}\right)(X) = \left(\frac{\kappa A}{\cos\theta}\right)\cdot e^{-bX}\cdot\gamma_\mu\cdot\left(\frac{E_0}{A}\right)^{\gamma_\mu-1}\cdot \left[\left(-\frac{E_0}{A}\right)^{-\gamma_\mu}\left(\frac{a}{\gamma_\mu}-\frac{b}{1-\gamma_\mu}\cdot\frac{E_0}{A}\right)+E_{\mathrm{min}}^{-\gamma_\mu}\left(\frac{a}{\gamma_\mu}-\frac{b}{1-\gamma_\mu}\cdot E_{\mathrm{min}}\right)\right], \tag{4.21}$$

with $E_{\mathrm{min}} = a/b(e^{bX}-1)$. $a = 0.25958$ GeV mwe^{-1} $= 0.23881$ GeV m^{-1} is the ionisation energy loss constant and $b = 3.5709\cdot10^{-4}$ mwe^{-1} $= 3.2852\cdot10^{-4}$ m^{-1} is the radiative energy loss constant from the average energy loss for muons [2]. $\kappa = 14.5$ GeV and $\gamma_\mu = 1.757$ are parameters from the Elbert formula (Eq.1.48). In an unweighted χ^2 minimization the fit parameters A and E_0 can be determined for each event. However, there is a large degeneracy between A and E_0. High energy proton bundles have an almost identical energy loss behaviour as lower energy iron bundles. Therefore, we only fitted E_0 as if all bundles were caused by oxygen primaries with $A = 16$. This means we cannot interpet the fit parameters E_0 and A as real primary energies and masses, but that is not a problem for a good average energy loss fit. a, b, κ and γ_μ can also float freely in the fit, but for fit stability reasons they are kept constant at their nominal values. An example of the fitted average muon bundle energy loss is illustrated by the solid line in Fig. 4.22.

Performance

The performance of the average energy loss fit to the reconstructed segmented energy loss is visible in Fig. 4.23. The left plot shows the resolution and bias, calculated by a gaussian fit to the ratio of reconstructed energy loss to true energy energy loss, for simulations with a primary energy above 1 PeV. Although the tail of the distributions are not well described by the gaussian, the width of the gaussian is still a good

[2] Both values are taken from [111] and are consistent within the uncertainty on the values quoted in Section 2.2.1 that come from [109].

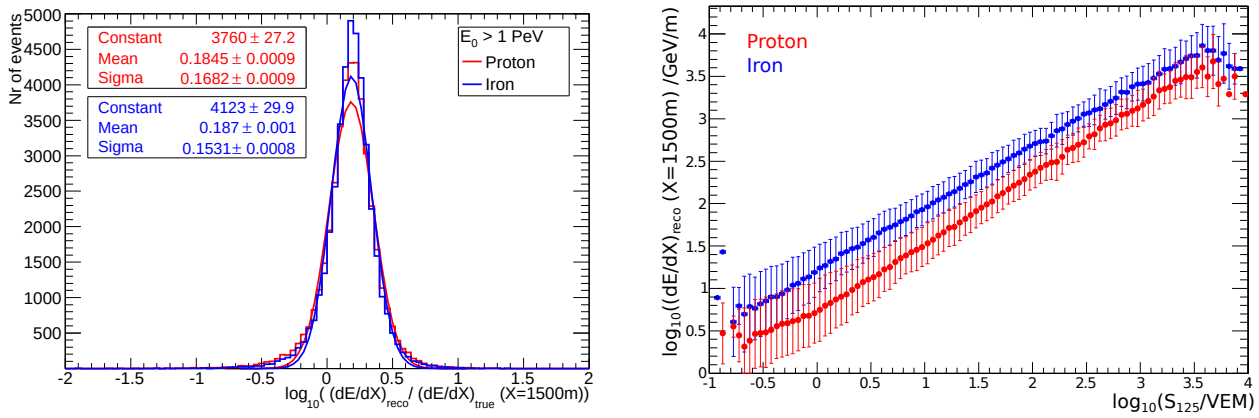

Figure 4.23: **Left**: Resolution of the energy loss reconstruction for both proton (red) and iron (blue) simulations above a primary energy of 1 PeV. **Right**: Reconstructed energy loss as a function of S_{125} for proton (red) and iron (blue) simulations, with the RMS as error bars.

measure for the resolution. The overall resolution for proton showers is 0.168 (or 39%) and for iron showers 0.153 (or 35%) and an average shift of 0.185 in $\log_{10}(\mathrm{d}\,E/\,\mathrm{d}\,X)$.

If these resolutions are compared with other energy loss reconstruction methods, then it becomes clear that the resolutions obtained here are quite good. The reconstruction of the average energy loss over the whole detector at the center of one segment instead of 35 segments [178, 179], an energy resolution of 0.27-0.29 depending on the event selection was obtained [180, 181]. A different method based on the truncated mean of the energy losses yields 0.22 [181].

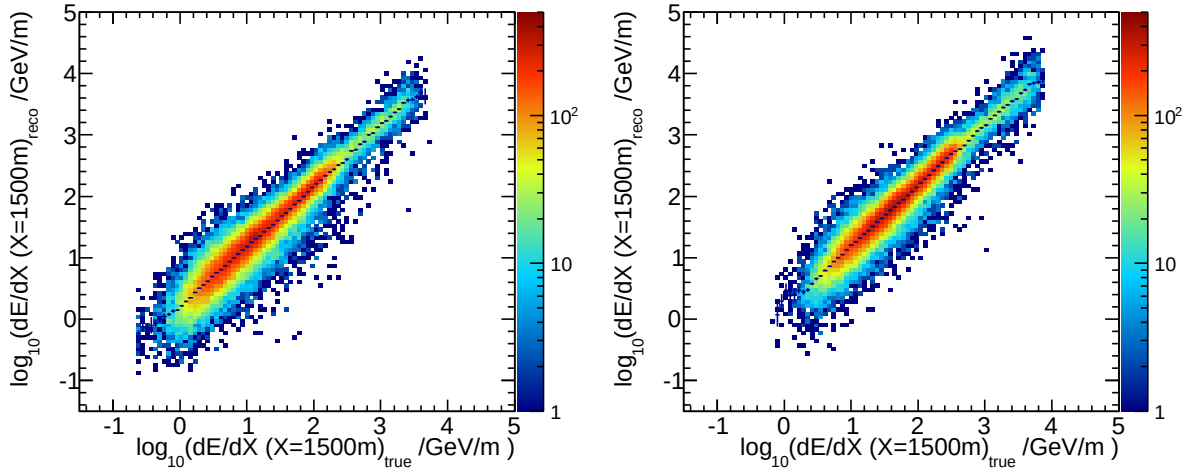

Figure 4.24: Reconstructed muon bundle energy loss as a function of the true muon bundle energy loss for proton (left) and iron (right) simulations.

There are two main reasons that contribute to the difference between the energy loss resolution obtained here and the two other methods. The first reason is that the other methods reconstruct energy proxies at the point on the muon track of single muons closest to the center of the array. For cosmic ray induced muon bundles this means that depending on their zenith angle a different amount of ice has been propagated. This creates a smearing and worsens the resolution. The second reason is that the other two methods compare the

reconstructed energy loss with the muon energy. The muon energy loss process is for high energy muons very stochastic and creates fluctuations which smears the resolution again.

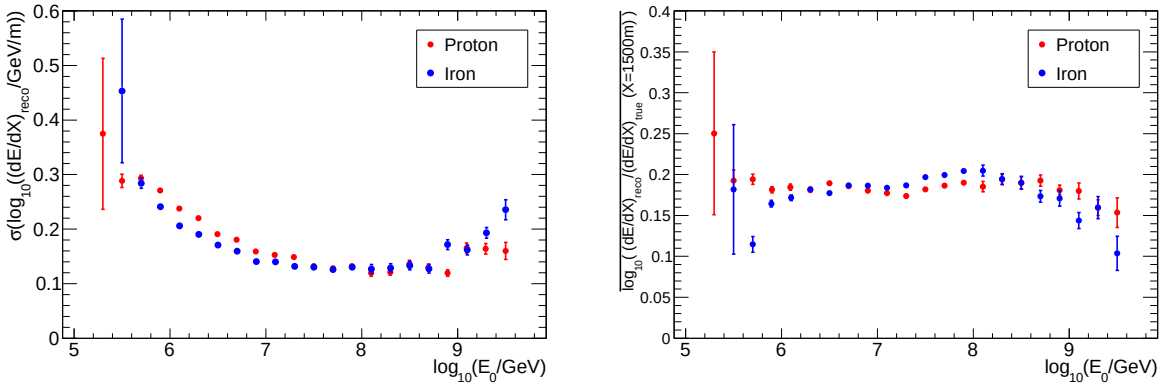

Figure 4.25: Resolution (left) and bias (right) of the energy loss reconstruction for proton (red) and iron (blue) simulation as function of primary energy.

For cosmic ray composition studies we do not to need to know the energy of the muon bundle as it propagates through the detector. We could unfold the reconstructed energy loss profile to the muon bundle energy profile and unfold that to acquire the muon multiplicity as function of the slant depth. These two unfolding procedures potentially create extra uncertainties in the final property, like the muon multiplicity, used for the actual composition analysis. The main objective for the multivariate composition analysis, discussed in Chapter 6 , is to have a set of variables that provide a good separation between proton and iron and thus have a good composition-sensitivity. The right plot in Fig. 4.23, where the reconstructed energy loss is plotted as a function of the primary energy-dependent S_{125}, demonstrates we already succeeded in this goal with the reconstructed muon bundle energy loss. The intermediate step of deconvoluting it first to a muon multiplicity is not necessary and can be taken care of by the multivariate analysis.

If we compare the right plot of Fig. 4.23 with the right plot of Fig. 4.15 a larger spread of the proton and iron distributions becomes clear due to the resolution of the energy loss reconstruction. Mainly at higher energies the overlap increases because of the reconstruction issues discussed above that result in a worse resolution and a larger smearing.

The relation between the reconstructed energy loss and the true energy loss at a slant depth of 1500 m is smooth and nicely linear for both proton and iron bundles (Fig. 4.24). The energy dependence of the resolution and the bias is depicted in Fig. 4.25. Because the unfolding starts to suffer from the huge bundle width, the resolution increases at the highest energies and earlier for proton than for iron. The bias is quite flat over the whole energy range and very similar for proton and iron showers.

Selection of high energy stochastics

After the determination of the average energy loss as function of the slant depth along the muon bundle, we need to describe the stochasticity of the muon bundle in order to find uncorrelated composition-sensitive variables. A dedicated study is performed in [182] where several methods are investigated to select extreme stochastic energy losses. This resulted in two types of selection criteria:

$$\text{Type 1}: \frac{\mathrm{d}\,E}{\mathrm{d}\,X}(X_i) > a \cdot \left\langle \frac{\mathrm{d}\,E_{\mu,B}}{\mathrm{d}\,X} \right\rangle + b \cdot \left(\frac{\mathrm{d}\,E_{\mu,B}}{\mathrm{d}\,X}(X_i) \right)^{c}_{\text{reco}} \tag{4.22}$$

$$\text{Type 2}: \frac{\mathrm{d}\,E}{\mathrm{d}\,X}(X_i) > a + b \cdot \left(\frac{\mathrm{d}\,E_{\mu,B}}{\mathrm{d}\,X}(X_i) \right)^{c}_{\text{reco}}, \tag{4.23}$$

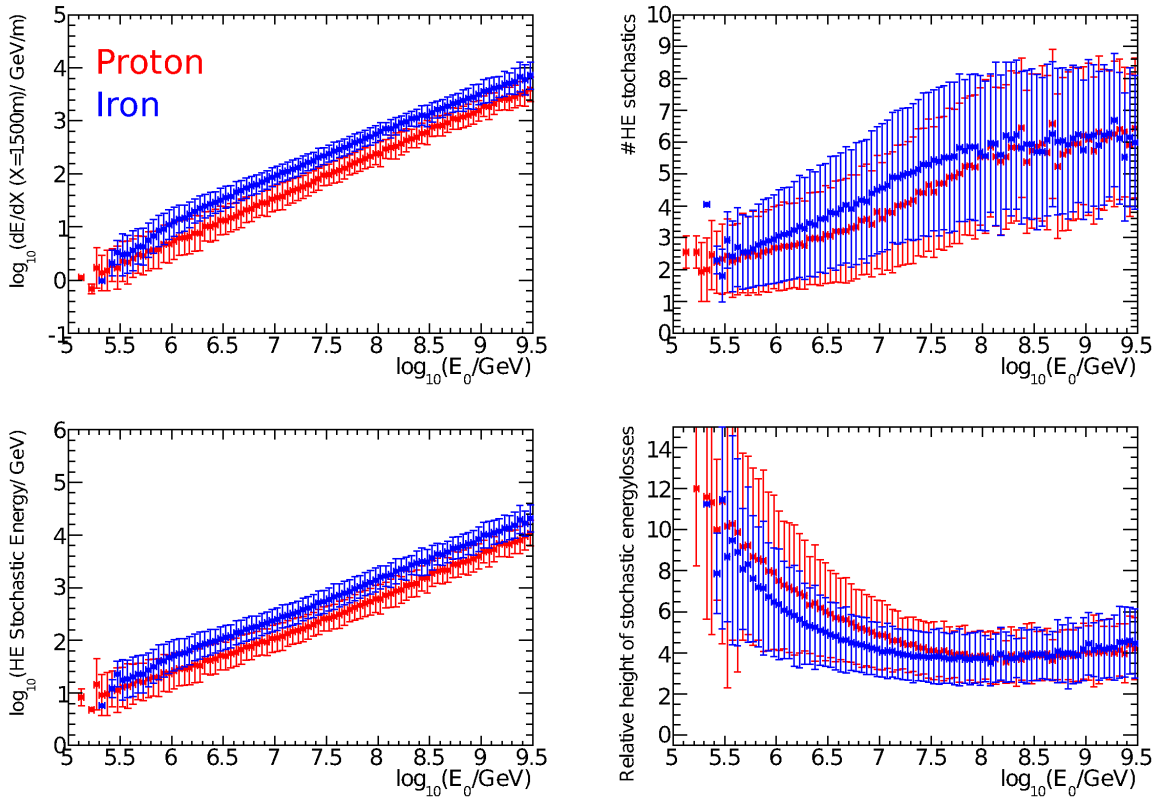

Figure 4.26: Characteristics of the standard selection for big stochastic peaks, with a = 0, b = 5 and c = 0.8. **Top left**: Reconstructed average energy loss as function of primary energy for proton (red) and iron (blue) simulations. **Top right**: The number of selected stochastic peaks as function of primary energy. **Bottom left**: Average energy of the selected stochastics as function of primary energy. **Bottom right**: Average ratio of the energy loss of the selected cascades and the fitted average energy loss as function of primary energy. The error bars in all plots are the RMS spread of the distribution.

where a, b and c are parameters that defined which kind of stochastic energy losses are selected and how strong the selection is. The characteristics of these so-called selected energy loss *peaks* are then compared between proton and iron simulations. The study from [182] proved the potential for using information from the stochasticity of muon bundles but was based on the true energy losses from MC, because the unfolding procedure discussed above was not yet available at the time.

The unfolded segmented energy loss pattern, as shown in Fig. 4.22, does not yield the exact energy loss pattern, but a representation of the energy loss pattern that best describes the observed IceCube waveforms (ie. which maximimizes our likelihood description of the energy loss). The gaps seen in Fig. 4.22 can therefore not be interpreted as segments on the muon bundle track where no energy lost, but rather stem from pieces of the track not (well) sampled by the detector (eg. because of track topology)

Hence, the parameters a, b and c from Eq.4.22 are reoptimized based on the reconstructed energy losses from the unfolding instead. Fig. 4.26 and 4.27 present the properties of the two optimal selection criteria. They are both based on selection method Type 2 from Eq.4.22. The *standard selection* (Fig. 4.26) uses $a = 0$, $b = 5$ and $c = 0.8$, while the *strong selection* (Fig. 4.27) uses $a = 0$, $b = 7$ and $c = 0.9$. This means that the selected peaks must have a much higher reconstructed energy loss than the average than for the standard selection. Over the whole energy range, proton and iron distributions are well separated in the average energy loss (top left in both figures), as expected from Fig. 4.23 because S_{125} is a good estimator for the primary energy E_0. The fact that the average energy loss has a very high correlation with the muon multiplicity at the

same depth, also clear from Eq.4.17, is illustrated by Fig. 4.28.

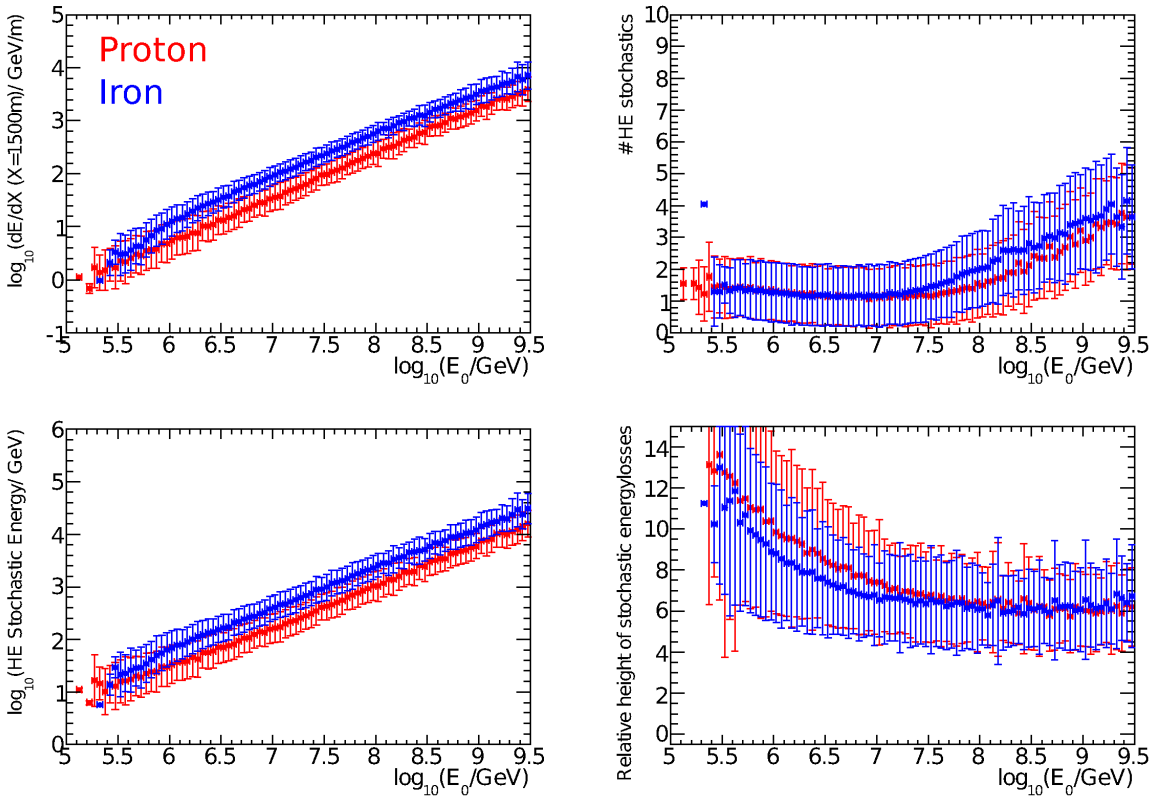

Figure 4.27: Characteristics of strong selection for big stochastics peaks, with a = 0, b = 7 and c = 0.9, demonstrated by the same plots as Fig. 4.26

In the other three variables, the distributions have a larger overlap, but the means and tails are still different for proton and iron over a large part of the primary energy. That indicates that proton and iron exhibit a different behaviour, with different shapes of the distribution for each primary energy bin. The average energy of the selected stochastics peaks (bottom left on both figures) has the best proton-iron separation for both standard and strong selection, but this correlates very highly with the average energy loss and thus does not provide extra information about the primary composition.

The number of selected stochastics performs best beyond the 1 PeV (the energy threshold of this analysis) up to 100 PeV for the standard selection, while from about 30 PeV the stronger selection performs better in separating proton and iron. In both cases there are more high energy cascades selected for proton bundles than for iron bundles. This is expected from the discussion at the beginning of this section, where we explained that due to large number of muons, a selected high energy peak probably carries contributions from several muons and therefore relates to the muon multiplicity. The correlation of the selected number of stochastics with both methods with the muon multiplicity at the center of the detector is reflected by Fig. 4.29. The standard selection performs better at low muon multiplicities while the strong selection performs better for bundles with at least 100 muons.

The ratio of the energy loss of the selected peak and the average muon bundle energy, also called *relative height of stochastic energy loss*, (top right) is higher for proton bundles than for iron bundles up to about 30 PeV where they start to become equal. Also the distribution for proton bundles has much larger tails in that energy region than for iron bundles. This nicely illustrates what we expected from the Elbert formula (Fig. 1.26), namely that the probability to have an extreme high energy muon is larger for proton bundles. An additional advantage of this variable is that it does not depend on the knowledge of the absolute light yield in

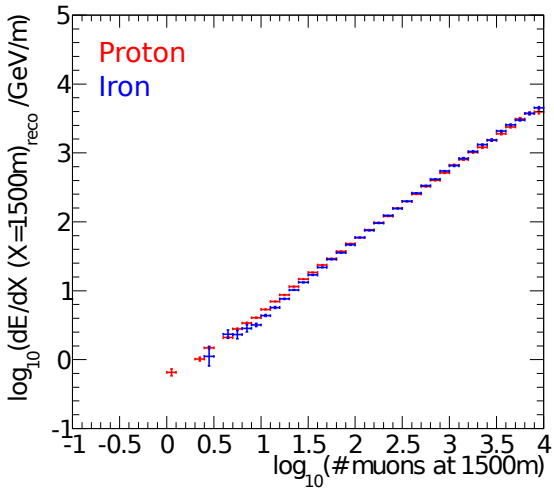

Figure 4.28: Correlation between the the reconstructed average muon bundle energy loss and the number of muons at a slant depth of 1500 m for proton (red) and iron (blue) simulations.

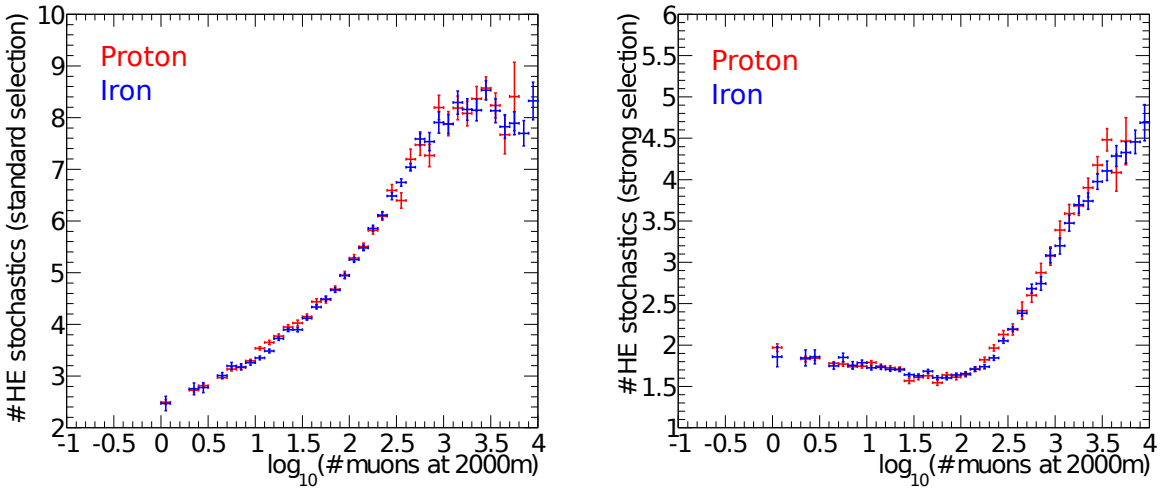

Figure 4.29: Correlations between the the number of selected high energy stochastics from the standard selection (left) and strong selection (right) with the number of muons at the center of the detector for proton (red) and iron (blue) simulations.

the detector, which we will show later is a large uncertainty.

The correlation matrix of all variables with a great potential for this composition analysis are shown in Fig. 4.30. The plots demonstrate the correlations for proton showers over the full simulated primary energy range. The correlation coefficients are drawn for both proton and iron simulations. Even though one would expect large correlations between some of these composition-sensitive variables, Fig. 4.30 proves that most correlations are reasonable to small. This indicates that each of the variables provide extra information, to determine the primary energy and primary mass of cosmic rays.

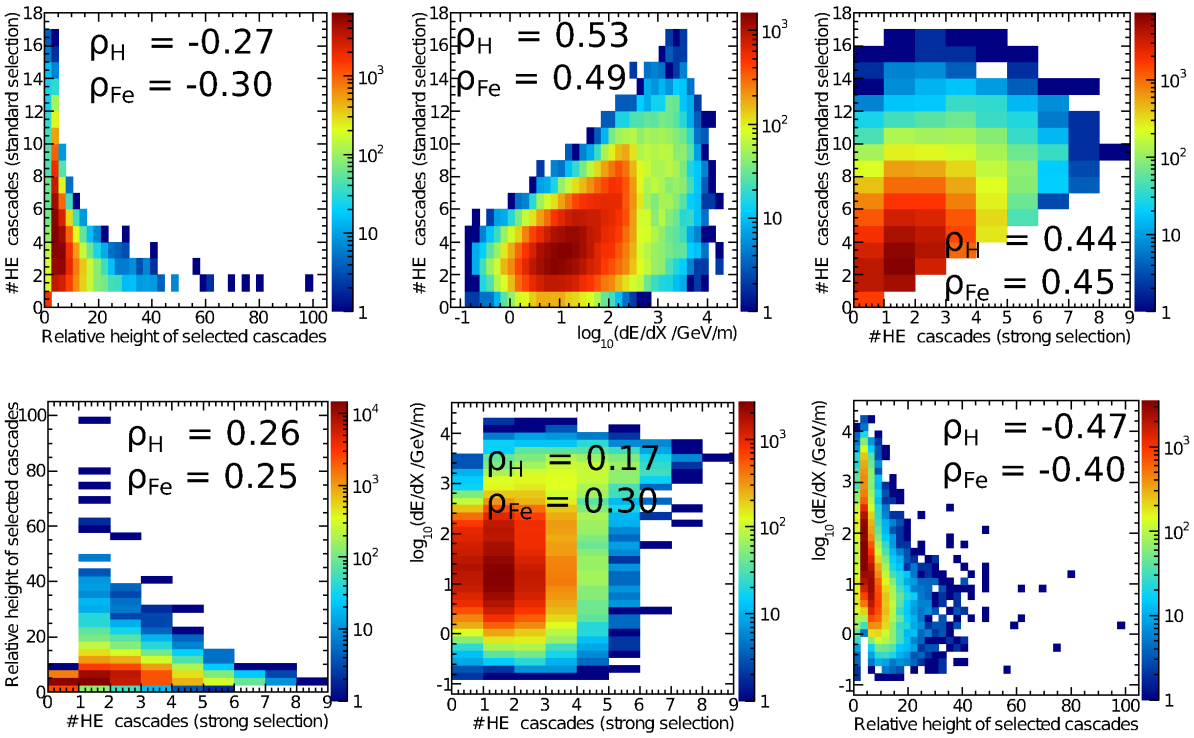

Figure 4.30: Correlations between the variables obtained from the standard (Fig. 4.26) and strong (Fig. 4.27) stochastics selection, shown for proton simulations. The correlation coefficients drawn are both for proton and iron simulations (after all quality cuts, discussed in Chapter 5).

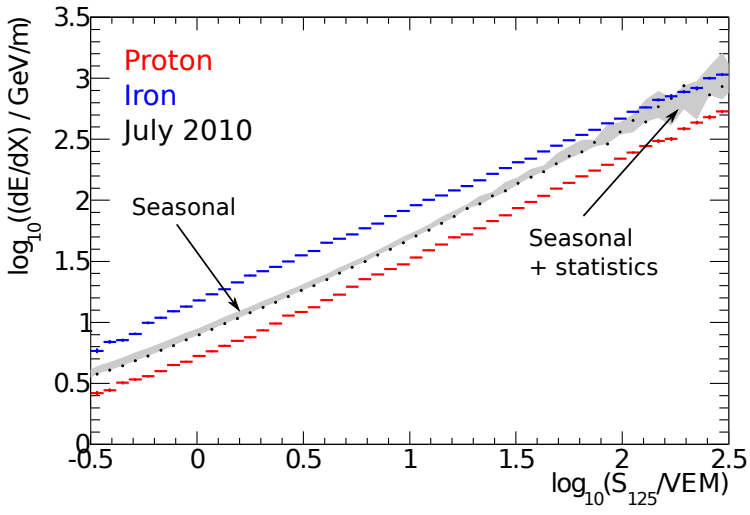

Figure 4.31: Reconstructed energy loss as function of S_{125} for data relative to the proton and iron simulations. The grey band illustrates the maximum variation of the mean energy loss of each month over the whole IT-73/IC-79 data taking period. The black data points are the means of July 2010. All error bars are errors on the mean of the distribution in each S_{125} bin.

Seasonal correction

The seasonal atmospheric variations change the temperature profiles of atmospheric temperature as function of atmospheric depth throughout the year, illustrated for example by Fig. 2.20. As a consequence the air density at different heights in the atmosphere changes. The muon multiplicity at the IceCube depth from cosmic ray air showers depends on the interplay between interaction and decay of secondary high energy pions and kaons. Because the interaction probability depends on the air density, the muon multiplicity measured in IceCube also reflects seasonal variations.

In simulation it is unrealistic to produce a large dataset for each atmospheric temperature profile seen in data. Therefore we chose the CORSIKA July atmosphere, based on July 1, 1997 as reference atmosphere to deduce the relation between primary composition and reconstructed observables, like the average muon bundle energy. The maximum variation of data in the energy loss - S_{125} space relative to the proton and iron simulations is demonstrated by the grey band in Fig. 4.31 and is about 10-15%. This would mean that the primary composition, derived from this figure, changes by 10-15% or also that there is an extra systematic uncertainty of 10-15% on the composition measurement if this is not accounted for. Here we will explain the method developed in [183] to correct the data for the seasonal changes relative to the simulated reference month.

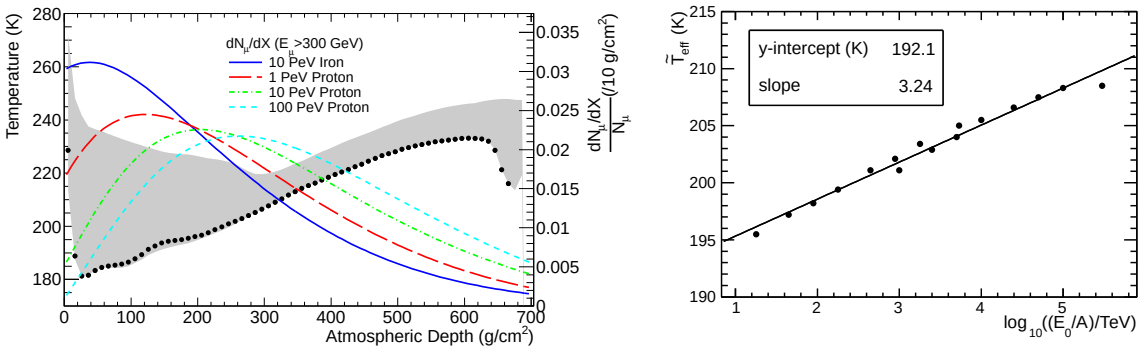

Figure 4.32: **Left**: Atmospheric temperature profile variation over the IT-73/IC-79 data taking period, with the black points representing the mean temperature profile for July 2010 and the grey band the maximum variation. The 4 curves are fits to the normalized muon longitudinal profiles $\left(\frac{1}{N_\mu}\frac{\mathrm{d}N_\mu}{\mathrm{d}X}\right)$ for proton showers of 1, 10 and 100 PeV and 10 PeV iron showers, with a muon threshold of 300 GeV. **Right**: The effective temperature, as defined in the text, for July 2010 as a function of primary energy per nucleon.

It is well known [126, 123] that the correlation between the muon flux and an effective temperature as defined (NOTE: Add Equation Number from Section ENVIRONMENT) in [126, 32] results in a linear relation quantified by a so-called temperature coefficient. In studies of the relation between IceCube rate variation and the effective temperature variation [125] the temperature coefficient α_T is found to be 0.9. In the calculation of the effective temperature a cosmic ray flux and composition is assumed, because the cosmic ray flux causes the muon rate at ground level. Here, we are interested in the muon multiplicity variation for one shower with a certain energy E_0 and mass A. Therefore we redefine the effective temperature $\tilde{T}_\mathrm{eff}$ as the temperature at atmospheric depth X[3] weighted by the number of muons produced there $\mathrm{d}\,N_\mu/\,\mathrm{d}\,X\,\mathrm{d}\,E_\mu(E_0, A)$

[3] In this discussion X is mainly used for atmospheric depth, except in the symbol for reconstructed energy loss, where it means slant depth in the ice.

and integrated over the whole atmosphere:

$$\tilde{T}_{\text{eff}}(E_0, A) = \frac{\iint \frac{\mathrm{d}\,N_\mu}{\mathrm{d}\,X\,\mathrm{d}\,E_\mu}(E_0, A)T(X)\,\mathrm{d}\,X\,\mathrm{d}\,E_\mu}{\iint \frac{\mathrm{d}\,N_\mu}{\mathrm{d}\,X\,\mathrm{d}\,E_\mu}\,\mathrm{d}\,X\,\mathrm{d}\,E_\mu} = \frac{\int \frac{\mathrm{d}\,N_\mu}{\mathrm{d}\,X}(E_0, A)(E_\mu > 300\ \text{GeV})T(X)\,\mathrm{d}\,X}{\int \frac{\mathrm{d}\,N_\mu}{\mathrm{d}\,X}(E_\mu > 300\ \text{GeV})\,\mathrm{d}\,X}. \tag{4.24}$$

The muon energy threshold of 300 GeV is the minimum energy a muon needs to propagate to the IceCube depth and generate light visible by the IceCube DOMs. The calculation of the effective temperature is demonstrated by Fig. 4.32. The average temperatures T for July 2010 (black points) and the maximal variation during the IT-73/IC-79 data taking period (grey band) are plotted as a function of the atmospheric depth X. The atmosphere data used are provided by balloon measurements from the Antarctic Meteorological Research Center (AMRC [119]) and are extended to larger altitudes with data obtained from the Atmospheric Infrared Sounder (AIRS), one of the six instruments on board of the NASA Aqua Research satellite [184].

From dedicated MC simulations using the real atmosphere profile from data, the muon production longitudinal profiles are derived and plotted for three primary energies and two primaries. These show clearly that the atmospheric depth where most muons are produced and where the variation will most affect the muon multiplicity variations increases as a function of energy per nucleon. Hence, variations at different atmospheric depths will not affect low energy showers and high energy showers in the same way. This motivates the new definition of the effective temperature. The new effective temperature calculation follows then easily from Fig. 4.32.

Only discrete primary energies were simulated, while in data there is a continuous range of primary energies. For each month we fitted the new effective temperature as function of energy per nucleon (see right plot of Fig. 4.32) and use that relation further to study the correlation with the variation in reconstructed energy loss.

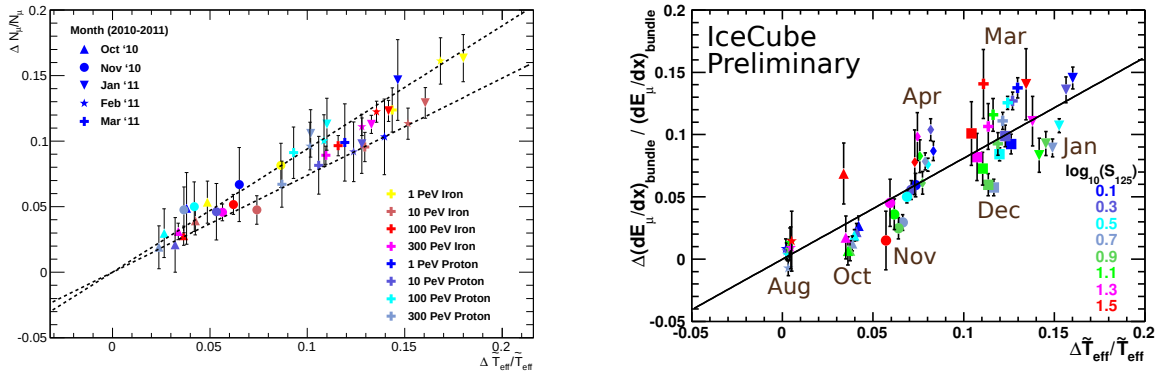

Figure 4.33: **Left**: The variation in muon multiplicity with respect to the muon multiplicity in July 2010 as a function of the variation in $\tilde{T}_{\text{eff}}$ for 5 different real atmospheres, 4 primary energies and proton and iron primaries. The dashed lines are the $\tilde{\alpha}_{MC}$ = 0.74 and 0.94 lines to show the variation in obtained temperature coefficients. **Right**: The variation in muon bundle energy loss as a function of the difference in $\tilde{T}_{\text{eff}}$ for all months in the IT-73/IC-79 data taking period compared to the reference month July 2010. The different colours show the different $\log_{10}(\text{S}_{125}/\text{VEM})$ bins.

Dedicated MC simulations, using the real temperature profiles from the atmospheres of month between June 2010 and May 2011, are performed for two reasons. The first reason is to obtain the muon longitudinal production profiles for the calculation of the effective temperature. Secondly, we need to verify whether a linear relation exists between the effective temperature variation $\Delta\tilde{T}_{\text{eff}}/\tilde{T}_{\text{eff}}$ and find its temperature coefficient

$\tilde{\alpha}_{\rm MC}$. The left plot of Fig. 4.33 shows the variation in muon multiplicity between a particular month and the reference month (July 2010), $\Delta N_\mu/N_\mu$, as a function of the variation in $\tilde{T}_{\rm eff}$ for four primary energies and for both proton and iron showers. A linear relation is visible and the temperature coefficient $\alpha_{\tilde{\rm MC}}$ is 0.84±0.10, with the spread of the points as error.

Because the seasonal variation of the data variables needs to be corrected, a similar study is performed on data. In data however, we do not measure the muon multiplicity and we do not know the primary energy and primary mass to calculate $\tilde{T}_{\rm eff}$. In data, the events are first binned in $\log_{10}(S_{125})$. For each bin, the peak position of the reconstructed energy loss is fitted with a gaussian and compared to the fitted peak position of the reference month for the same S_{125}-bin. To calculate the effective temperature for that bin, the $S_{125} - E_0$ conversion from the IT-73 energy spectrum analysis [170] has been used, and an average $\log A$ of 1.9 (roughly consistent with most previous measurements, although a new iteration could use the $\log A$ of this analysis). Even though the muon multiplicity is not directly reconstructed, the linear relation from Fig. 4.28 conveys a similar temperature coefficient should exist. Indeed, the temperature coefficient found on the right plot of Fig. 4.33 is 0.81±0.28, where the error is obtained from a separate fit to each S_{125} bin in order to show the maximal spread. This is compatible with the values from MC simulations. However, a much larger spread is visible in data.

The larger spread in data comes from two effects. First, there is a hysteresis visible on the right plot of Fig. 4.33, which is anti-clockwise going from Aug.2010 to May 2011. From August 2010 to Jan. 2011 the points are below the fitted linear curve, while they are above the line from Feb.2011 to May 2011. This effect is not seen in simulations and could be caused by the influence of the chosen hadronic interaction (SYBILL 2.1) for the muon longitudinal profiles, a seasonal variation of S_{125}, the energy threshold chosen for the muon longitudinal profiles (300 GeV) or the energy dependence of the composition. However, all of these effects were studied and none of them could explain the hysteresis.

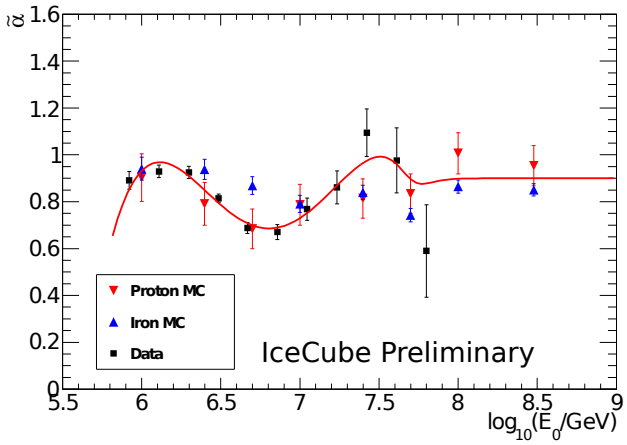

Figure 4.34: Energy dependence of temperature coefficient $\tilde{\alpha}$ for data and MC obtained from fits based in Fig. 4.33. The solid red line is a fourth order polynomial fitted to data and extended at the highest energy based on MC. For data, the conversion from S_{125} to E_0 is done based on [170].

The second effect that increases the spread of the data points on the right plot of Fig. 4.33 is an energy dependence that is not completely accounted for by $\tilde{T}_{\rm eff}$. For each of the months there is U-shaped energy dependence larger than the error bars on the points. The energy dependence becomes even more clear if we fit the temperature coefficient separately for each S_{125}-bin and convert these to primary energy. For the simulation from the left plot of Fig. 4.33 the energy dependence can directly be extracted. The result is shown in Fig. 4.34 where the U-shaped energy dependence becomes much more clear. For MC there is a smaller energy dependence than for data. The physical reason for this energy dependence is unknown, and investigations are ongoing. Data from 2011 to 2013 is ready to be analyzed. With more data both the

hysteresis and the energy dependence could be studied over a larger time scale and to higher energies.

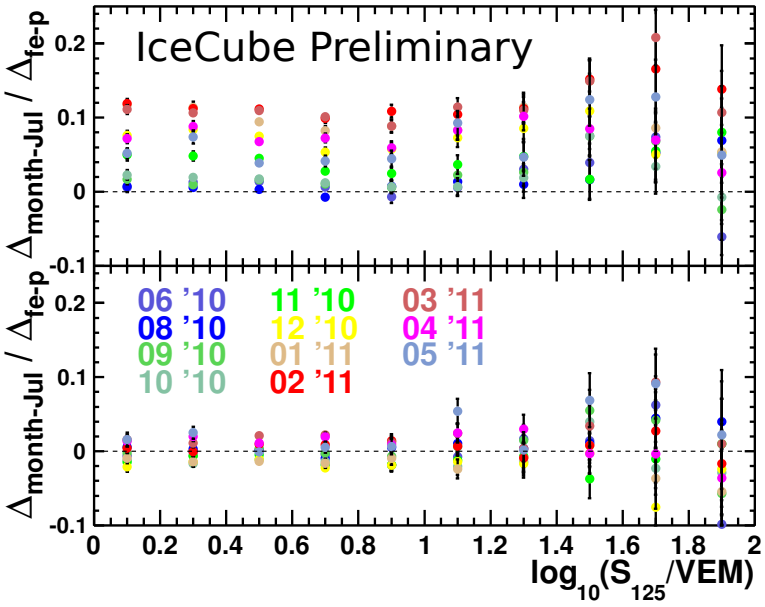

Figure 4.35: The uncorrected (top) and corrected (bottom) $\Delta \log_{10}(\mathrm{d}\, E_{\mu,B}/\,\mathrm{d}\, X)$ for all months with July 2010 as a reference ($\Delta_{\mathrm{month-Jul}}$), as a function of $\log_{10}(S_{125})$. The difference is normalized to the difference in $\Delta \log_{10}(\mathrm{d}\, E_{\mu,B}/\,\mathrm{d}\, X)$ between proton and iron ($\Delta_{\mathrm{Fe-p}}$), obtained by fitting the proton and iron curves in Fig. 4.31.

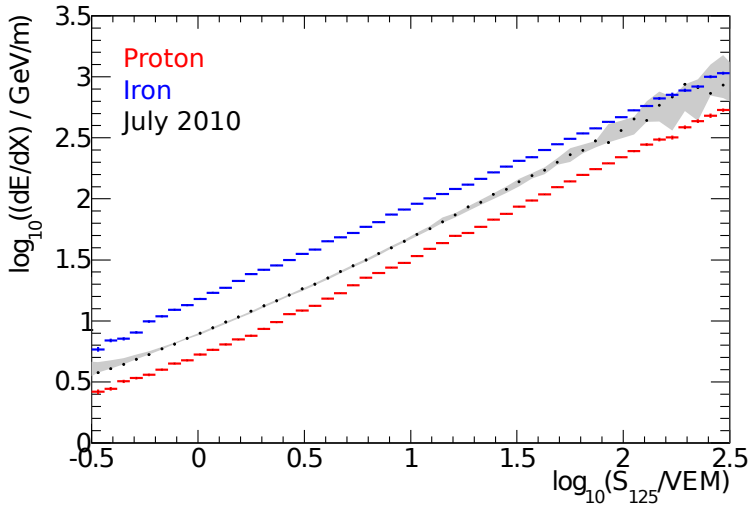

Figure 4.36: Same figure as Fig. 4.31, but after the seasonal correction explained in the text.

The correction of the reconstructed variables from the average and stochastic behaviour of muon bundles is done based on the temperature coefficient $\tilde{\alpha}_{\mathrm{data}}$ from Fig. 4.34. The energy dependence is fitted with an empirical fourth degree polynomial, extended at the highest energies by a constant. This is done because the

last point from data is unreliable due to low statistics and the average between proton and iron MC is used instead. If a constant $\tilde{\alpha}_{\mathrm{data}}$ is utilized, then the seasonal correction induces an energy dependent effect on the composition result, which of course is not desired. A comparison between the uncorrected energy loss relative to the difference between proton and iron as a function of S_{125} and the corrected one is illustrated by Fig. 4.35 for each month used in the IT-73/IC-79 analysis. The large monthly shift up to 10-15% is corrected to a 3-5% variation but without a shift relative to the reference month. This means that the composition result for all months will be smeared a little bit but not systematically shifted anymore on monthly basis. There is also no energy dependence visible after the correction, due to the inclusion of the energy dependence in the temperature coefficient. At the highest energies a larger spread is visible but the error bars are also larger because of lower statistics. More data will extend the study to higher energies. Fig. 4.36 shows the correction version of Fig. 4.31 and nicely illustrates that after the correction the grey band that shows the maximum spread disappears.

The other variables that described the stochastic behaviour of muon bundles are corrected based on their relation with the muon multiplicity.

Chapter 5

Hit Cleaning and Event Selection

Cosmic rays constitute a large background for most neutrino analyses. Cuts in those analyses are mainly designed and optimized to separate signal from background. A measurement of cosmic ray composition does not need to separate signal from background. However, for the event selection of coincident events that pass through both IceTop and IceCube, the background of random coincidences need to be removed.

Cuts are further required to acquire a set of events that are well reconstructed and have a good reconstructed core position and direction. The main criteria is that showers are contained within the IceTop and IceCube array. This means that the true core position is within the boundaries of IceTop and that the track afterwards passes through the IceCube volume. Additionally quality cuts to ensure good reconstructions are required.

Before reconstructions can be performed, a hit cleaning is carried out. Pulses that are not related to the actual event, due to multiple events in either IceTop or IceCube during the same event readout, or that are caused by noise, confuse the reconstruction algorithm and are therefore cleaned before the reconstruction procedure is executed.

5.1 Standard Pulse Selection

5.1.1 IceTop Pulse Selection

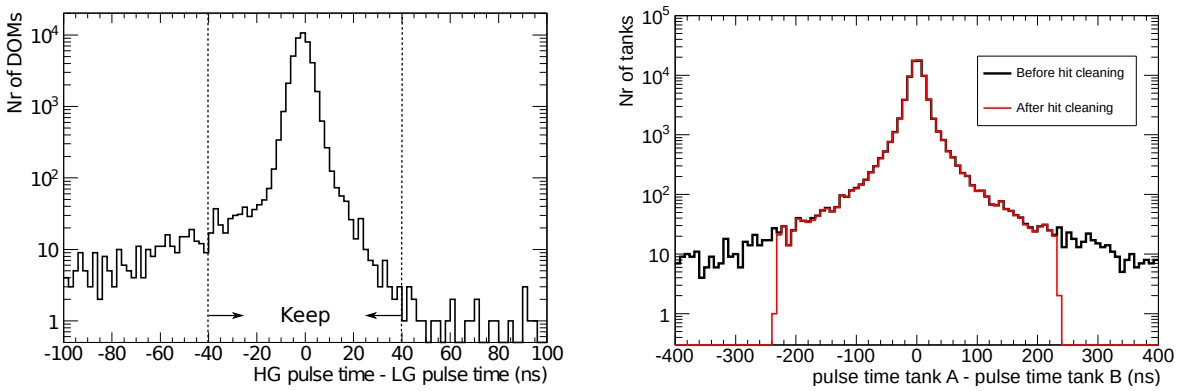

Figure 5.1: **Left**: Time difference between signals in HG DOMs and waveforms in LG DOMs in the same IceTop tank from data. **Right**: Time difference between the signals in tank A and signal in tank B from the same IceTop station from data.

For the reconstruction of core position, direction and LDF based on IceTop signals, only HLC tank

signals are currently used. When both the HG DOM and the LG DOM detected a signal in tank, we first determine whether they belong to the same event. The distribution of time differences between HG pulses and LG pulses in the same tank for data (left plot of Fig. 5.1) shows a gaussian distribution centered around zero with a non-gaussian tail at large negative values. The tail is caused by waveforms with multiple peaks in the HG DOM of which the first ones are not seen by the LG DOM because the amplitude is below the PMT discriminator threshold. Fig. 5.2 shows both HG and LG waveforms of one tank for one event. The first peak is not seen by the LG DOM and the LG DOM only triggered on the second peak [185]. Because no multi-peak extraction is not yet done in IceTop, the time of the first peak in the HG DOM is compared to the time of the peak in LG DOM, which matches the second the peak in the HG DOM. The LG pulse time for this class of waveforms is systematically much later than the HG pulse time, and creates the non-gaussian tail. The multi-peak HG waveforms typically happen at a few hundred meters from the core and are typically unsaturated. Therefore the mismatching between HG and LG DOMs does not create a problem as the LG waveforms is not used anyway.

To decide whether HG and LG pulses belong to the same tank signal, we chose an absolute time difference of 40 ns. Based on the charge of the high gain DOM and whether the HG and LG pulse belong to the same event, the tank signal is formed The following three situations exist:

1. The HG pulse charge is below the HG-LG cross-over value from VEMCal: The tanksignal consists of the HG pulse charge and the HG pulse time.

2. The HG pulse charge is above the HG-LG cross-over value and a matching LG pulse within 40 ns is found: The tanksignal consists of the LG pulse charge and the (more accurate) HG pulse time.

3. No matching LG pulse is found when the HG pulse charge is above the HG-LG cross-over value: The tank signal consists of the HG pulse time and an undeterminted (NaN) charge. These signals are not used by the first guess core and direction reconstruction, and treated properly as saturated hits by the LDF reconstruction procedure.

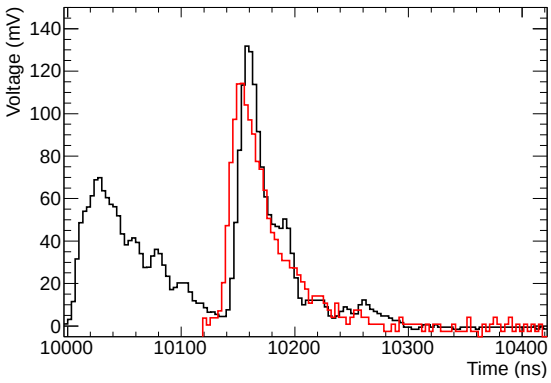

Figure 5.2: The black waveform is from HG DOM 28-63, while the red waveform comes from LG DOM 28-64. The LG waveform starts later because it didn't trigger on the first pulse. The voltage of the waveform from the LG DOM is amplified by a factor of 25 in the plot for clarity.

After the construction of tank signals, the tank signals between tanks of the same IceTop station are compared to see whether they belong to the same event or whether one of the tanks is from an earlier or later noise, single tank hit. The distribution of time differences between tanks of the same station, called the *intra-station time difference*, for data is shown in Fig. 5.1. For a planar shower front one would expect very small time differences for vertical showers to time differences up to 30 ns for horizontal showers (if the shower front propagates with the light speed c and with a tank spacing R_{tank} of 10 m). The spread of the

distribution, for data in large zenith angle range, is however much larger due to the curvature of the shower front and intrinsice shower fluctuations. The maximum allowed absolute time difference between two tanks in the same station to belong to the same event is chosen to be 200 ns + R_{tank}/c. If tanks of the same station do not belong together, they are discarded and thus not used for any reconstruction.

The last step of the standard IceTop hit cleaning is to construct the set of IceTop signals that belong to the same event. This event-building is based on IceTop stations, which are formed from the average position of the two hit tanks from the same station and with the average pulse time of both tanks. The station signals are ordered in time. If the absolute time difference between a station and the previous station in the time ordered set is larger than 200 ns + R_{station}/c, with R_{station} the distance between the two station, then a new event consisting of this station and later stations is started. Late HLC station signals are typically formed by PMT afterpulses[1]. Therefore second events formed by this part of the standard IceTop hit cleaning procedure are often uninteresting sets of afterpulses. Multiple IceTop events can also happen during the same event readout. This procedure should in principle correctly treat these and create separate events. However, as we will show in Section 5.3.2, this does not happen but will be better accounted for in this analysis.

5.1.2 IceCube Pulse Selection

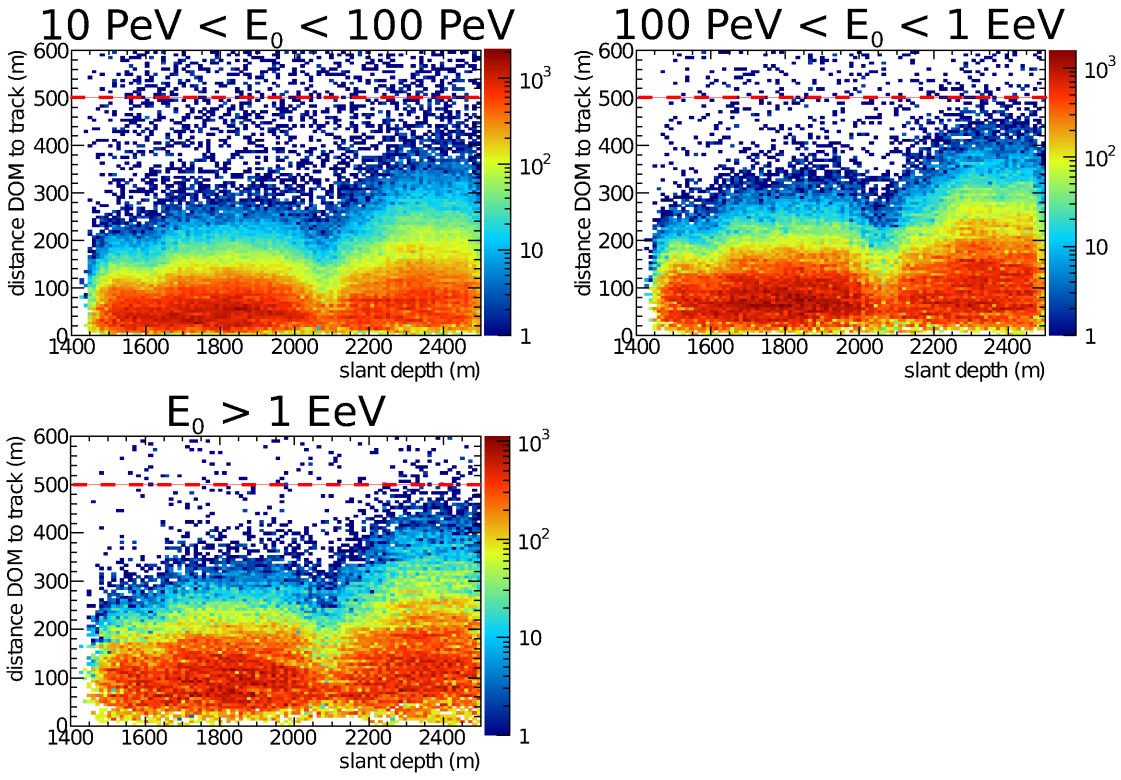

Figure 5.3: Distance from hit IceCube DOM to track as a function of slant depth for different primary energy ranges using iron simulations. The red dashed line shows the cut above which (predominantly noise) hits are cleaned.

The unfolding procedure to reconstruct the segmented energy loss in IceCube along the muon bundle uses both SLC and HLC pulses from the feature extracted waveforms of hit IceCube DOMs. Both the hit DOMs and the unhit DOMs carry information because the expected number of photo-electrons can be larger than

[1] Afterpulses are created when some photo-electrons ionize the residual gas inside the PMT. The positive ions are attracted by the cathode, generates a new, late photo-electron which then results in a late pulse.

zero for some unhit DOMs. Therefore the calculation of the response matrix in principal performs lookup operations for all pulses of the hit DOMs and for all unhit DOMs in the IceCube detector. To reduce the time spent per event to calculate the energy loss profile without loss of accuracy a conservative DOM selection is done.

The DOM selection is based in Fig. 5.3 which shows the distance of the hit DOMs as a function of the slant depth along the muon bundle, in three energy regions for iron bundles. Up to 200-300 m the hits are clearly dominated by photons from the muon bundle while further away the hit DOMs come from the simulated random noise. We chose a conservative maximum distance of 500 m motivated by hit DOMs deep in the ice where the ice is clearest for the largest muon bundles (above 1 EeV). The DOM selection is based on iron bundles because they have larger bundle width and c arry much more muons resulting in DOMs that can be hit further away from the bundle. Above the red dashed line in Fig. 5.3 the DOMs are cleaned and not used for the reconstruction anymore.

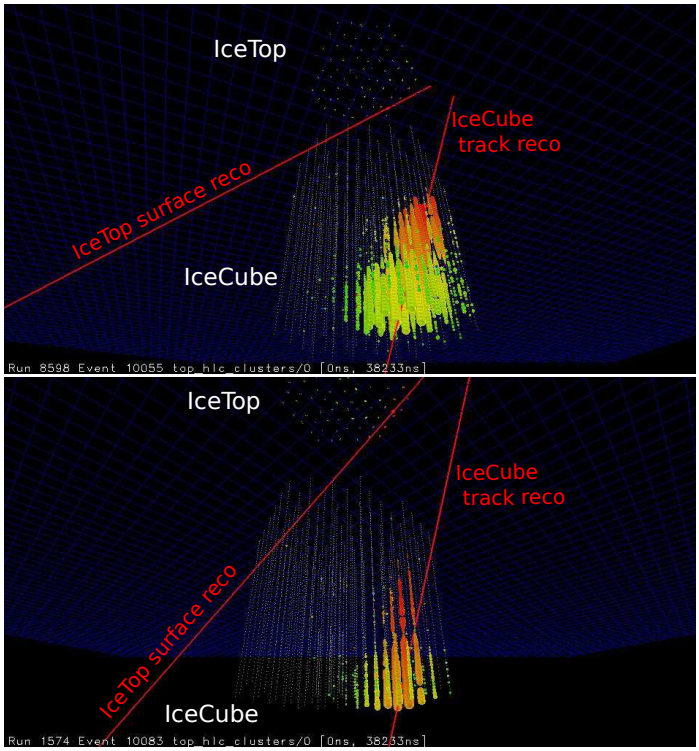

Figure 5.4: Two rare events that survived all containment cuts and IceTop quality cuts. In this case the IceCube track reconstruction did a better job and shows they are uncontained events. The hit cleaning which removes all hits outside a cylinder with a radius of 500 m gets rid of these as bonus.

Fig. 5.4 demonstrates an additional bonus of this hit selection. The two only events passed all the containment cuts, explained below, and are clearly reconstructed with a core position in IceTop. However, the real shower missed IceTop and entered IceCube from the side. In this case the IceCube track reconstruction performs much better and proves the real core position is not contained by IceTop. These events are unwanted and are still removed thanks to the hit cleaning in a 500 m cylinder around the reconstructed track which in both these cases removes all the hits and results in the event to be removed.

The simulation, based on lookup operations in photon tables generated by Photonics (see Chapter 3), has known issues because the extrapolations of the expected number of photo-electrons stored in those photon tables are incorrect and create binning effects because of the binning of the photon tables. This effect mainly plays a role at very close distances from the Cherenkov emitting source to the DOM. In Fig. 5.5 the ratio of the total charge in one DOM over the the total charge in the event is compared between data and MC. DOMs

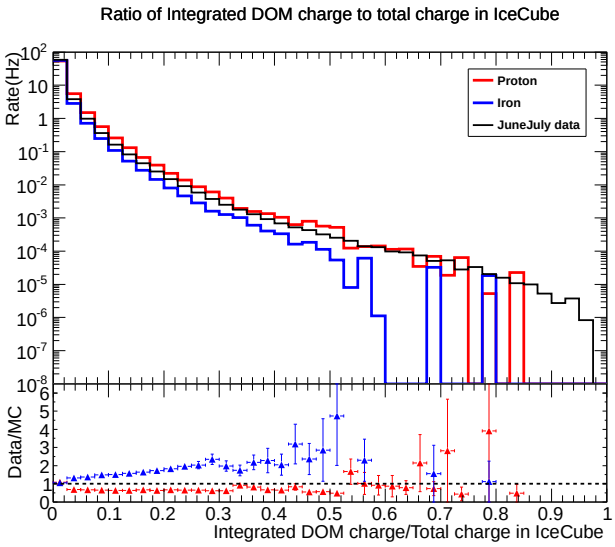

Figure 5.5: Distribution of the ratio of total charge in one DOM over the total charge in the whole event for proton (red) and iron (blue) simulations compared to data from June and July 2010.

that carry a large fraction of the total charge of the event are due to this Photonics issue, not well simulated and could bias the energy loss reconstruction. We therefore remove DOMs which carry a fraction of the total charge in the event larger than 0.3 or 30%.

5.2 Containment

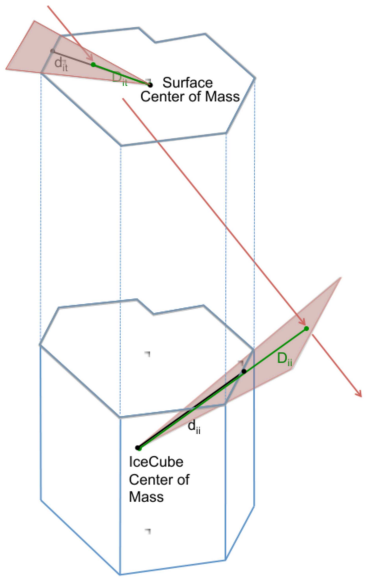

Figure 5.6: Schematic drawing to illustrated the definition of IceTop containment or IceTop size (=$D_{\mathrm{it}}/d_{\mathrm{it}}$) and IceCube containment (=$D_{\mathrm{ii}}/d_{\mathrm{ii}}$).

The most important and strongest cut that ensures a good quality in the core reconstruction, the direc-

tion reconstruction, the LDF fit and the energy loss reconstruction is containment. In the previous Chapter, Fig. 4.14 already clearly proved that contained showers have a better core and angular resolution than uncontained showers. High quality reconstruction of uncontained air showers requires designated reconstruction algorithms. The study on how to adapt current reconstruction algorithms, presented in Chapter 4, to uncontained showers is currently ongoing. In addition the trigger probability of uncontained showers is biased by upfluctuating events. This means that for a certain primary energy and direction, fluctuations with larger signals on the edges are more likely to trigger the detector than fluctuations of the same type of shower to lower signals. That effect need to be properly accounted for in an analysis and is outside the scope of this thesis.

The IceTop containment, also called *IceTop size* or *IceTop scale*, is defined in Fig. 5.6 as the ratio of the distance D_{it} of the core position to the center of polygon connecting all outer IceTop stations over the distance d_{it} from the side of the polygon to its center. In other words, *IceTop size* is the factor by which the IceTop boundary has to be scaled in order to contain the core position.

The IceCube containment is the ratio of D_{ii} to d_{ii} in Fig. 5.6 and is the three-dimensional analogue for IceTop containment. It is the factor by which one has to scale the IceCube volume in order to contain the point on the track closest to the center of the IceCube volume.

5.2.1 IceTop containment

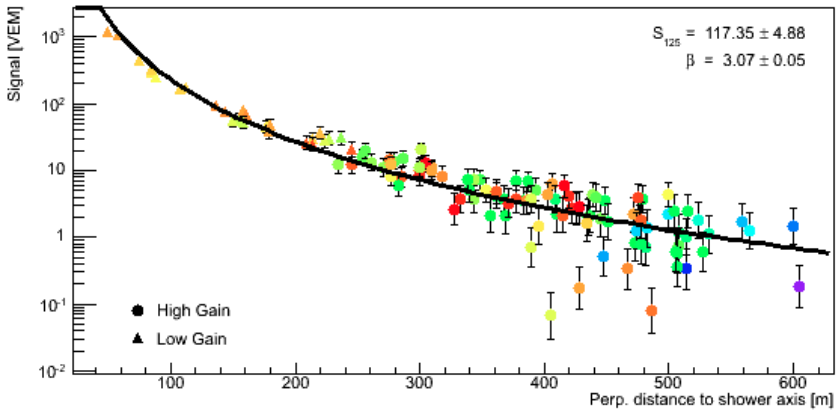

Figure 5.7: LDF of big IceTop event to demonstrate the LDF principle, explained in the text.

Here we develop a procedure to select contained events without depending on any, possibly biased, reconstructions. To know if the air shower landed outside the array or inside the array we rely on the *LDF principle*. According to the LDF, most particles and thus also the largest signals are nearest to the true core position, illustrated by the LDF in Fig. 5.7. Consequently the true core position is closest to the station with the largest signals. Therefore we require that the station with the largest charge, defined as sum of the two tank charges, is not one of the stations on the border of the array. This *loudest station* cut removes a large part of uncontained and keeps most contained events, but still a large distribution of uncontained events is visible in the true IceTop size distribution (cyan distribution in Fig. 5.8).

The remaining uncontained events are so-called *tail events*. The air showers land very far from the boundary of the IceTop array, but still trigger the array and only the outer boundary or the tail in the LDF is detected. Those events sneak past the loudest station cut because the muons at large distances from the core create larger signals that the decreasing electromagnetic part. As as consequence stations inside the array have a larger total charge than the station on the boundary of the array which is closer to the true uncontained core. Also local fluctuations cause larger signals further away from the core and create a loudest station inside the array boundary.

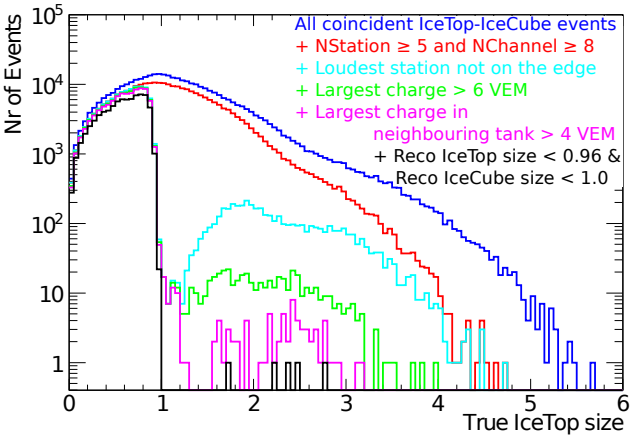

Figure 5.8: True IceTop size distribution for proton simulations after each of cut.

The tail events also do not follow the LDF principle anymore. Suppose the large event from Fig. 5.7 lands more than 450 m away from the array boundary. The tail of this event still triggers the detector and the yellow point has the highest charge and is contained by the array in that case. If we can characterize the signature of these tail events, these can be removed for a more efficient contained event selection.

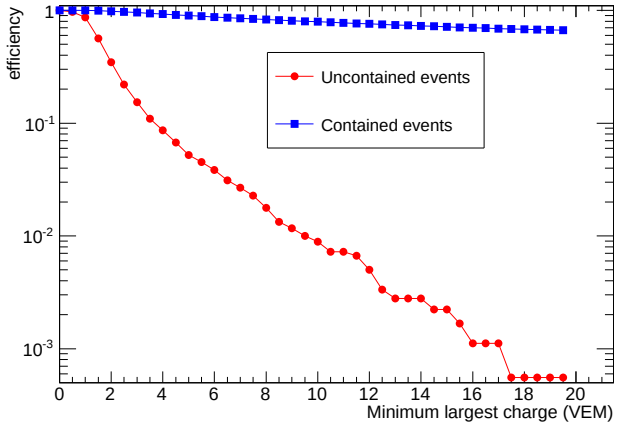

Figure 5.9: Efficiency of the largest charge (Q1) cut for contained and uncontained events. The containment efficiency is defined as the total number of kept contained events (IceTop size < 0.9) after the cut divided by the total number of contained events without any cuts. The efficiency for uncontained events or uncontainment efficiency is defined as the total number of kept uncontained events (IceTop size > 1.1) after the cut divided by the total number of uncontained events without any cuts.

Already from Fig. 5.7 we see that the LDF becomes flatter for very low absolute charges. Therefore a cut on the minimum largest charge (Q1) is investigated in Figs.5.9 and 5.10. The first figure shows fraction of contained events kept after the cut, relative to the contained events after the loudest station cut (blue) compared to the fraction of uncontained events that remain after the cut (red) as a function of the value for the largest charge cut. In order to keep as many good, contained events as possible the value of 6 VEM was chosen. The left plot of Fig. 5.10 demonstrates the clear separation between the Q1 distributions for contained events and the low Q1 charges for uncontained events with the chosen cut superimposed as dashed line. Of course we want to know which contained we actually removed. This is shown by the the true

energy distribution as a function of the true IceTop size for the removed events (right plot of Fig. 5.10). The contained events we lose are low-energy showers near and below the detector threshold of 1 PeV, while the higher the energy of the events the more uncontained they are as we are looking at the end of the tail of those showers. In both plots of Fig. 5.10 the loudest station has already been applied.

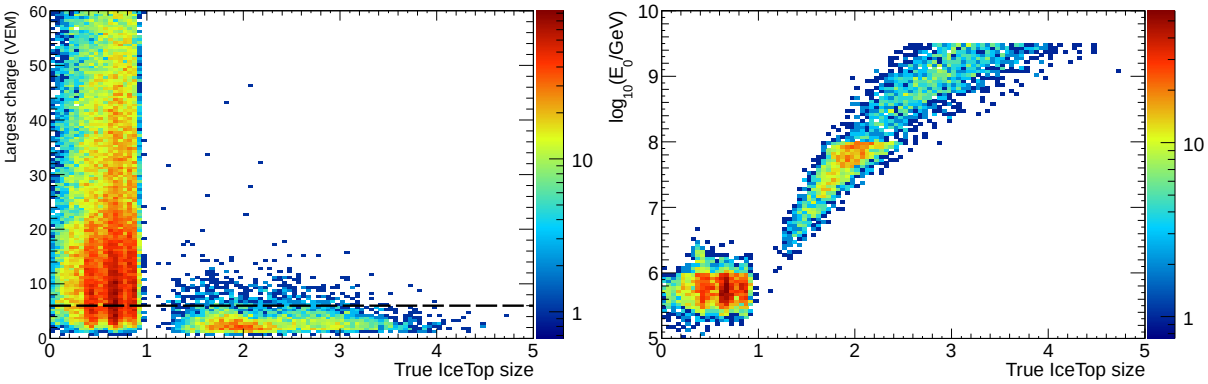

Figure 5.10: **Left**: Q1 as a function of true IceTop size for proton simulations. The dashed line shows the Q1 value below which events will be cut. **Right**: Primary energy as a function of true IceTop size for events that are cut away (Q1 $<$ 6 VEM).

On Fig. 5.8 the green distribution shows that the cut efficiently removes a large part of the uncontained events while keeping the contained events, but still some uncontained events slip through the mazes of the net. These are again created by charge fluctuations, typically for muons that can generate charges above 6 VEM even though the core position is very far away. Fig. 5.11 is similar as Fig. 5.9 and shows the cut optimization of three possible cuts that should remove the last uncontained events without removing any contained events. This time the efficiencies are calculated relative to the number of (un)contained events after the loudest station cut and the largest charge cut. The three candidate cuts are the second largest charge (Q2), the charge of the neighbouring tank of the tank with the largest charge (Q1b) and the ratio Q1/Q1b. The best efficiency can be reached by a cut on Q1b at 4 VEM. This cut variable best characterized a charge fluctuation, because if the largest charge is a local upfluctuation, then its neighbouring tank should not be one.

The Q1b distribution as function of the true IceTop size after the previous containment cuts are depicted on the left plot of Fig. 5.12 while the right plot again shows the primary energy distribution of the removed events. Also in this case the removed, contained events are from the low energy region, but might shift the energy threshold to slighly higher energies.

The Q1b cut effectively removes almost all of the remaining uncontained (magenta distribution on Fig. 5.8) and keeps the contained events. The energy dependence of this sequence of containment cuts is illustrated by Fig. 5.13. The station density cut is a quality cut that will be discussed in Section 5.4. The left plot shows the energy dependence of how many good events we lose. The loudest station has a very small energy dependence but removes about 8% contained events. This is expected because on both sides of the boundary of the array showers create a largest station on the boundary, so these events are almost removed by this cut. Both Q1 and Q1b cut efficiently keep almost all contained events but shift the energy threshold as expected. The right plot demonstrates how efficient each cut removes the unwanted events. Each cut reduces the fraction of uncontained events by a factor of 10 and is therefore very efficient. However, it becomes increasingly difficult to get rid of the uncontained events above 1 EeV. One last cut is necessary for those events.

The easiest way to select possible contained events is by performing on a cut on where the reconstructed shower lands, ie. on the reconstructed IceTop size. The reason why we avoided this so far is very well illustrated by the left plot of Fig. 5.14. If we would only rely on the reconstructed core position, ie. reconstructe

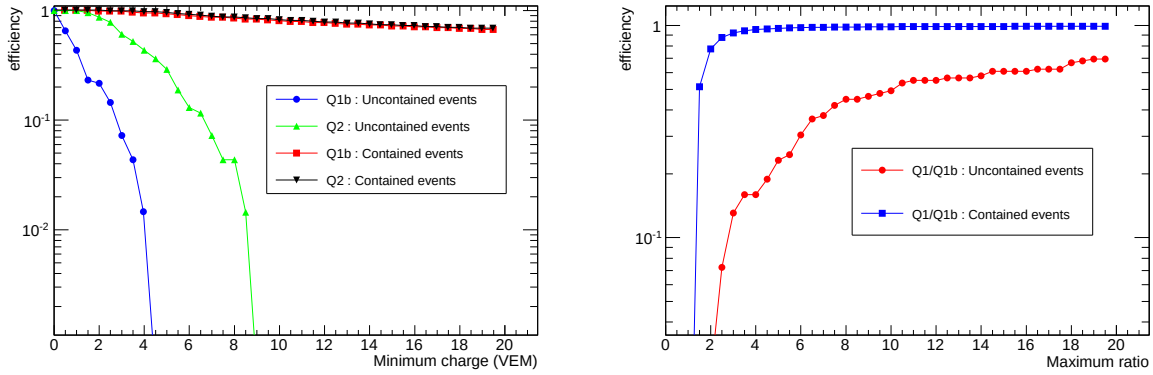

Figure 5.11: **Left**: Efficiency of a second largest charge (Q2) cut and of a cut on the minimum charge of the charge in the neighbouring tank of the tank with the largest charge (Q1b). The efficiencies are defined the same way as for Fig. 5.9, but with the largest charge already applied on both numerator and denominator. **Right**: Efficiency of a cut on the maximum Q1/Q1b ratio. The efficiency is plotted both for contained and uncontained events.

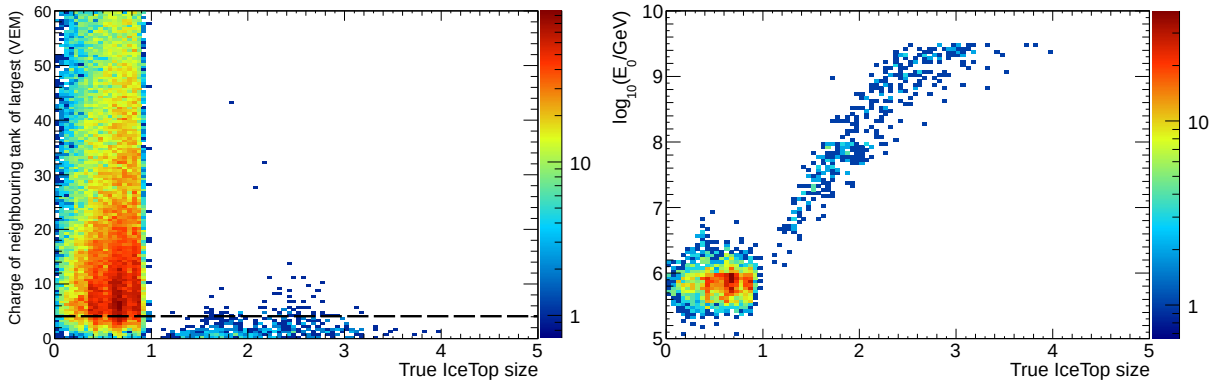

Figure 5.12: Same plot as Fig. 5.10, but after the Q1 cut and for Q1b instead of Q1.

IceTop size, a large set of uncontained remain. These events have a true IceTop size above one and a reconstructed IceTop size below one. Those remaining uncontained events are not well reconstructed or mimic contained events and are therefore not accounted by a simple cut on reconstructed IceTop size. The situation after our set of containment cuts that do not depend on reconstruction is completely different. The right plot of Fig. 5.14 demonstrates that our cuts removed this class of events before the reconstruction is performed. Now, a cut on reconstructed IceTop size is valid and necessary to remove the very last few, uncontained , very high energy events. The maximum reconstructed IceTop after this last cut is 0.96 (black solid line).

5.2.2 IceCube containment

After the IceTop containment cuts to make sure the true core position is contained by the IceTop array, we also require the reconstructed track to go through the IceCube volume. The main reason for an IceCube size cut is the reconstruction quality for the segmented energy loss reconstruction. In Section 4.2.1, we explained that track segments far from the DOMs are not well constrained and that reconstructed energy losses on track segments outside the detector are therefore unreliable. A conservative IceCube size of 1.1 means that the point of closest approach to the center of the IceCube array of the reconstructed muon bundle track must be

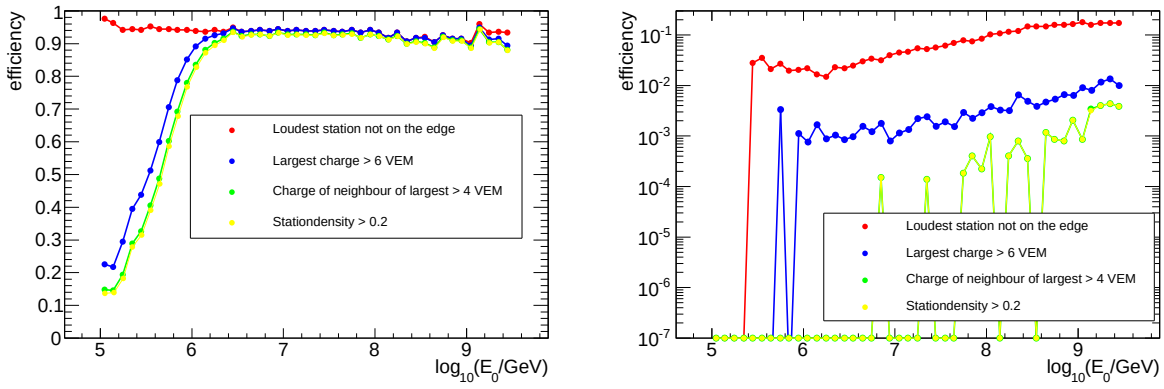

Figure 5.13: **Left**: Containment efficiency as function of primary energy for the different containment cuts applied sequentially. **Right**: Uncontainment efficiency as function of primary for the different containment cuts.

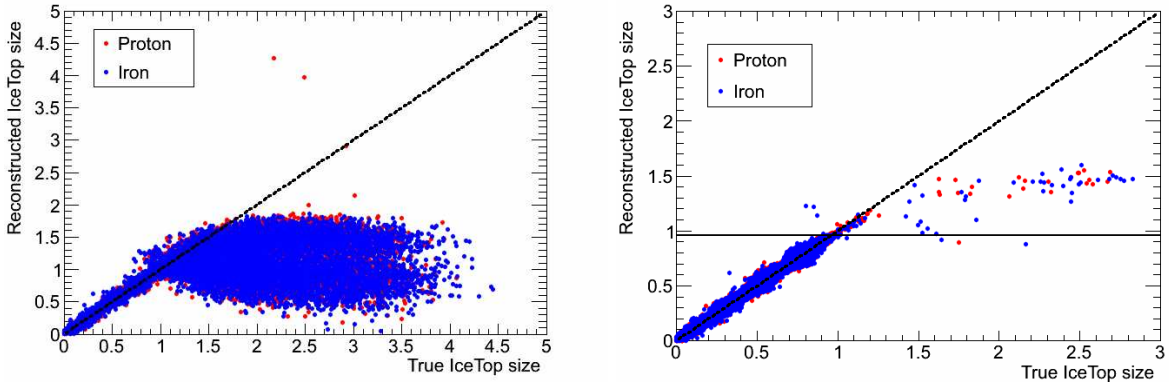

Figure 5.14: **Left**: Reconstructed IceTop size as function of true IceTop size for coincident proton (red) and iron (blue) simulations without other cuts. **Right**: The same as the left plot but after IceTop containment and quality cuts. The solid horizontal line shows the extra IceTop cut used in this analysis.

within 1.1 times the IceCube volume or also must be contained by the IceCube volume. Fig. 5.15 however shows that the effective area obtained after the IceTop containment cuts and this IceCube containment cut is not flat as a function of the primary energy. Even more worrysome is that there is composition dependence of the effective area, which is undesirable because we do not a priori know the composition but want to measure the composition. For the measurement of the cosmic ray energy spectrum a composition-independent effective area is needed. The reason for this composition dependence can be understood from the fact that the muon rich iron showers have a larger probability to trigger the detector for not fully contained showers than for muon poor proton showers. The energy dependence comes from the increasing muon multiplicity which increases the IceCube trigger probability. The solution to this effective area problem is to cut stronger and to require the reconstructed IceCube size to be below 1.0. The effective area after that cut is flat and the same for both proton and iron showers.

An additional advantage of the containment requirement by the IceCube volume of the track is that this provides an extra handle against random IceTop - IceCube coincidences. If the reconstructed track is contained by the IceTop array and goes through IceCube and if the hits are causally connected, the event comes a real air shower that went through both detectors and not by random coincidences. This will be illustrated in more detail in the next Section.

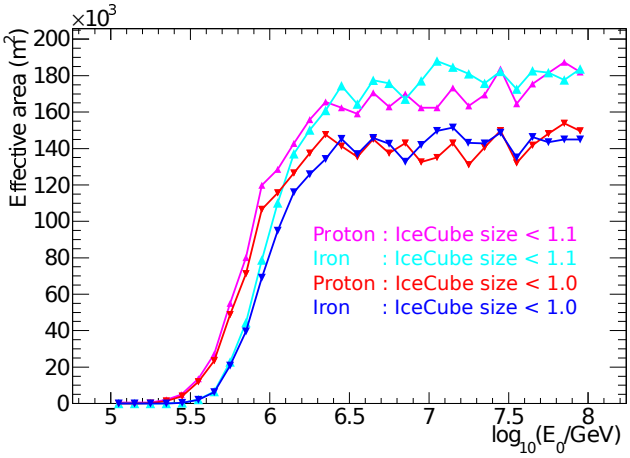

Figure 5.15: Effective area as a function of primary energy after the IceTop containment cuts. Two different IceCube size cuts of 1.0 and 1.1 are compared for proton and iron simulations.

5.3 Random coincidences and multiple coincidences

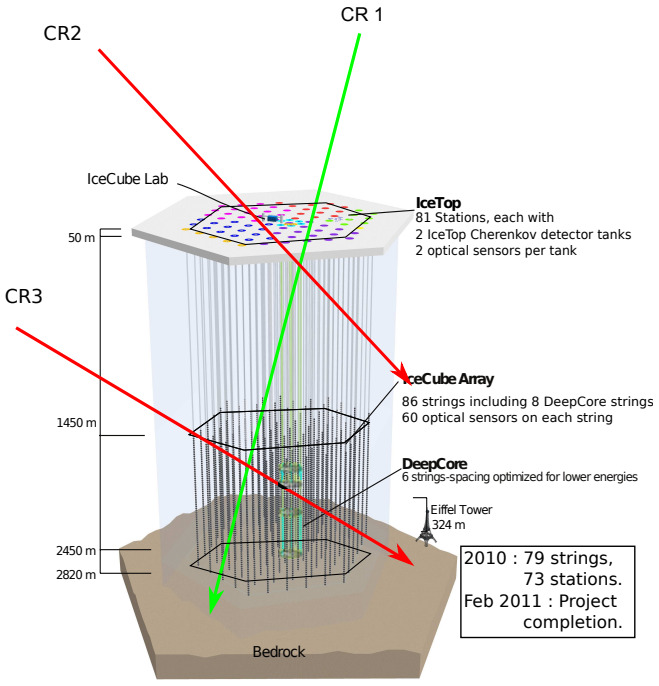

Figure 5.16: Illustration of random IceTop-IceCube coincidences (CR2 and CR3), double IceTop-IceTop coincidences (CR1 and CR2) and double IceCube-IceCube coincidences (CR1 and CR3). The event selection should remove the first case and clean the hits from CR2 and CR3 in the second and third case.

The trigger readout window in which IceTop and IceCube hits are added to the same event is ± 10 μs around the IceTop SMT Trigger. Within these 20 μs there could be other IceTop air showers or IceCube muons or neutrino's triggering the detector. The readout window gets extended (and could even go up to 80 μs) and multiple IceTop and/or IceCube SMT triggers exist within the same DAQ event readout, illustrated by Fig. 5.16. If the hits of the new (second or maybe third) IceCube muon and/or IceTop air shower are

coming in closer than 5 μs after the previous event (within the LC time window), no new trigger is formed, but the extra event happens around the same trigger. In Fig. 5.16 CR1 is the air shower that passed through both IceTop and IceCube. This is the type of events we want to study in the analysis presented in this thesis. CR2 is an additional air shower hitting IceTop during the same event readout, creating double IceTop events. Additional muons or neutrinos (CR3) can also pass through the IceCube volume during the same event readout as CR1. The possibility that there are double IceTop-IceCube coincidences, air showers that pass through both IceTop and IceCube during the same readout (two cases of CR1 in Fig. 5.16 during the same event readout), is however negligible for 2010-2011. In later data taking periods new triggers were added with very long readouts, which makes that particular case of multiple coincidences not negligible anymore.

It also happens that there are independently air showers hitting the IceTop detector while during the same event readout muons not from that shower pass through IceCube. The current coincident filter sees these events as coincident IceTop-IceCube events although they are actually random coincidences (CR2 and CR3 mimicking CR1 in Fig. 5.16). The trick in an IceTop-IceCube coincident analysis is to figure out first whether there really was an air shower that first triggered IceTop, travelled through the ice and then triggered IceCube. This means getting the random coincident events need to be removed. Then a correct hitcleaning will separate the independent IceTop triggers and the low energy (or noise) hits within the same IceTop trigger. A similar cleaning is needed to separate the IceCube coincidences, select the right one and clean the hits not related to the actual IceTop-IceCube coincident air shower. This procedure is described below.

5.3.1 Random IceTop-IceCube Coincidences

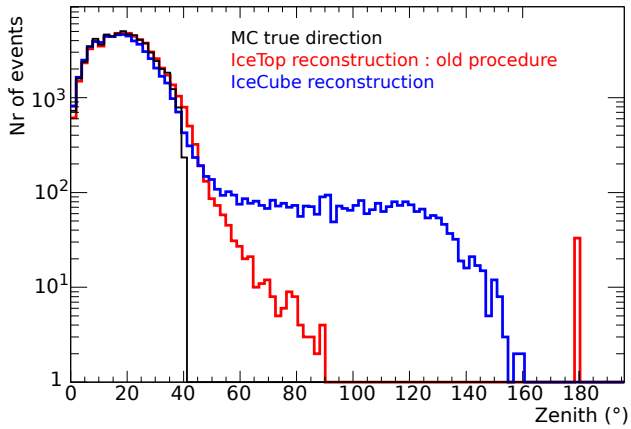

Figure 5.17: Comparison of independent IceTop (red), IceCube (blue) and the MC true zenith angle distribution for proton simulations. The IceTop reconstruction shown here is from the old procedure described in [90].

The simplest way to remove events that passed the coincident filter, but come from random IceTop-IceCube coincidences it by employing independent IceTop and IceCube direction reconstructions and performing a cut on the angular difference between both reconstruction. In addition, one can could cut on the time difference between the reconstructed time at the IceCube track vertex and the time at the reconstructed core position. Fig. 5.17 demonstrates why this approach is not a good idea. The reconstructed zenith angle distribution by the IceTop reconstruction and an IceCube track reconstruction are compared to the true zenith angle distribution without any cuts applied. The IceTop reconstruction performs much better and follows the true zenith angle distribution while a large shoulder exists for the IceCube track reconstruction. If we would cut on the difference between both direction reconstruction, then we lose events that are well reconstructed by IceTop but misreconstructed by IceCube and consequently misidentified as random coincidences. This figure

also shows that the IceTop reconstruction outperforms the best IceCube track reconstruction. No IceCube track reconstruction is therefore used in the analysis presented in this thesis.

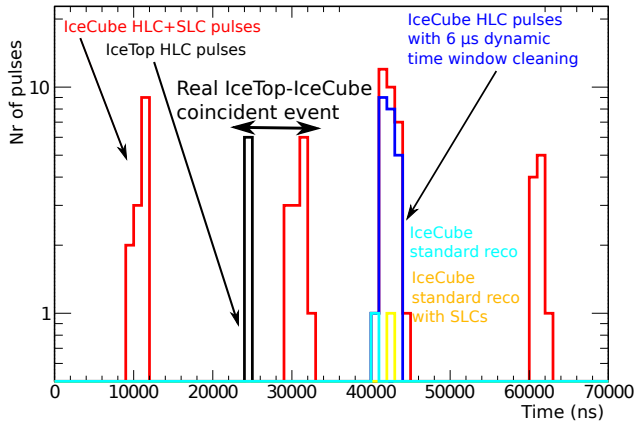

Figure 5.18: Pulse time distribution of event 1621485 from run 116489, where multiple IceCube triggers happened during the same event readout. All IceCube pulses, including both HLC and SLC pulses, are shown in red and the IceTop HLC pulses in black. The IceCube pulses after the standard, 6μs dynamic hit cleaning are shown in blue and the time at the reconstructed track vertex for standard IceCube track reconstruction in cyan (using HLC alone) and yellow (using both HLC and SLC).

The procedure for selecting the pulses that belong to the real IceTop-IceCube coincident event if there is one developed below is motivated by the event in Fig. 5.18. It shows the time distribution of the pulses for both the IceTop and the IceCube pulses. The set of pulses from the IceTop event is around 25μs. During the event readout several IceCube triggers were fired and several discrete sets of pulses from different events are visible (red distribution). The standard IceCube hit cleaning procedure, called *dynamic hit cleaning*, selects the largest set of pulses and only keeps the pulses in a 6μs time window centered at this largest set of pulses. Although one expects that this always selects the event that comes from the big muon bundle that passed through IceTop, this is not the case here. The IceCube pulses that belong to the coincident event are hit roughly 4.5μ - 7 μs later (for a muon bundle that propagates through 1500 m of ice at the light speed). The algorithm we need should always look for a set of IceCube pulses that is causally connected with the IceTop pulses and perform the 6μs cleaning around this set of pulses. If they are not found, then the event is a random coincident event.

The procedure we constructed to select the set of pulses belonging to the IceCube SMT trigger that is causally connected with the IceTop SMT trigger (typically at 10μs) , is called *coincident time window cleaning* and is demonstrated by Fig. 5.19. For simulation the distribution of trigger length as a function of the trigger time for IceCube SMT8 triggers is shown for events that pass the coincident filter. The initial situation is shown by the top two plots, where the top right plot only shows the contained events above 1 PeV. The basic principle of the algorithm is that we expect the IceCube trigger to come 4.780 μs to 7μs later than the IceTop trigger from causality. These are also the triggers that are selected by the algorithm, shown by the area between the two dashed line. The pulses are then selected in a window between 300 ns before start time of the trigger and 400 ns after the end time of the trigger.

The first problem with this method is that clearly the minimum time difference between the IceTop and IceCube trigger is too sharp and good, coincident events are removed (because random coincidences are not simulated). A looser minimum time difference is more conservative, but allows for random coincidences to be selected and is unphysical because it violates causality. A detailed study of these events unveiled that the IceCube SMT trigger did not start by the first muon bundle induced physics hit but from random HLC noise pairs. The solution to that problem is to remove the HLC noise pairs and bad DOMs, that might have

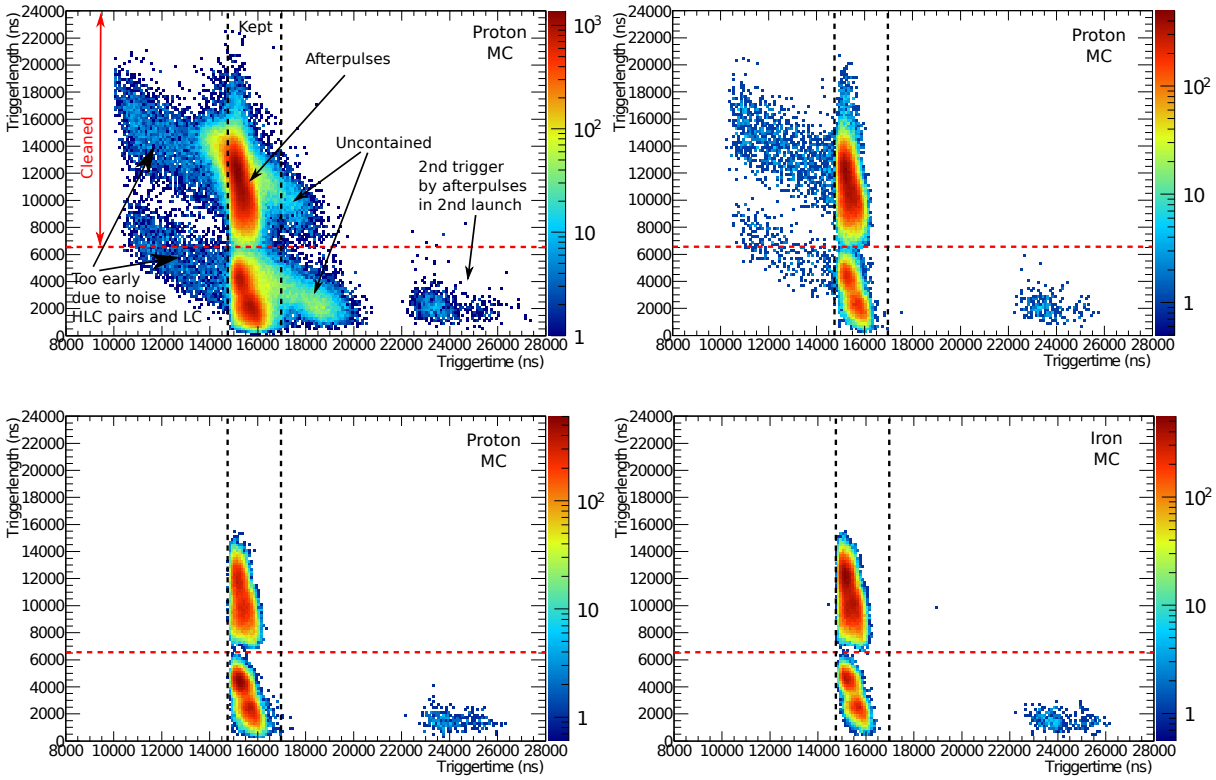

Figure 5.19: Trigger length as a function of the IceCube SMT8 trigger time for proton simulation (top left), proton events above 1 PeV which are contained by both IceTop and IceCube (top right), after retriggering as explained in the text (bottom left) and retriggered, contained iron simulations above 1 PeV (top right). The region between the dashed lines are the events that will be kept, pulses above the red dashed line will be cleaned.

triggered the detector but are untrustworthy, and retrigger based on the set of noise cleaned DOM hit. In this way the trigger times do not violate causality anymore but started at the first physics hit.

After removing the known bad DOMs, the so-called *seeded RT cleaning* algorithm removes the HLC noise pairs. This algorithm looks for a cluster of three hit HLC DOMs around each HLC DOM within a distance R = 150 m and a time difference T = 1000 ns. In order words it looks for clusters formed by at least two nearby HLC pairs. If no such clusters are found the event is discarded. Noise HLC pairs typically come alone and are randomly distributed over the detector, while physics HLC pairs from muons are grouped in larger clusters.

After the seeded RT cleaning, still some events have IceCube trigger times that violate causality. There the triggers are not caused by HLC noise, but by noise hits on a string where the physics HLC pairs arrive a bit later. Because the noise hits are within the 5μs time window to form an SMT8 trigger, the trigger uses the time of the earlier noise hit as start time for the trigger. The early noise hits can also be removed as illustrated by Fig. 5.20. For each hit DOM, the average time difference between its own hit time and the time of the hit LC neighbours (meaning up to two DOMs above the current DOM on the same string and up to two DOMs below) is plotted as function of the DOM hit time. Early noise hits are surrounded by the later physics hits and therefore have a systematically lower average time difference. The solid line of Fig. 5.20 is the earliest DOM hit we expect from causality. A clear separation is visible between the noise DOMs and the physics DOMs and the cut we will apply is to require minimum average time difference of -300 ns, shown by the dashed line.

After the hit cleaning and retriggering we get the bottom two plots of Fig. 5.19. Almost every single

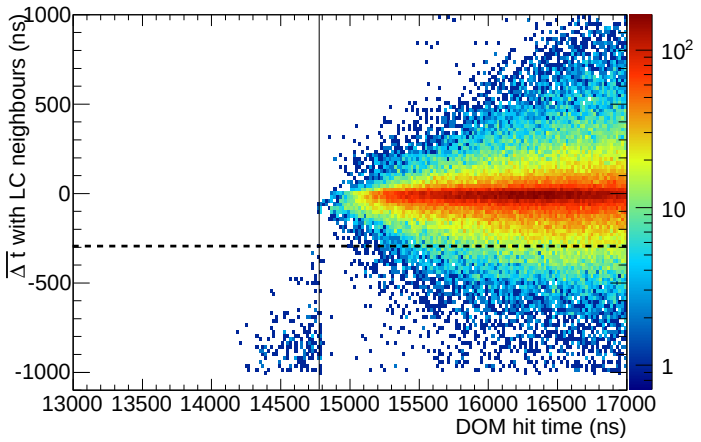

Figure 5.20: Average time difference between a hit and all his LC neighbours (nearest and next-to-nearest neighbours) as function of the hit time from simulation.

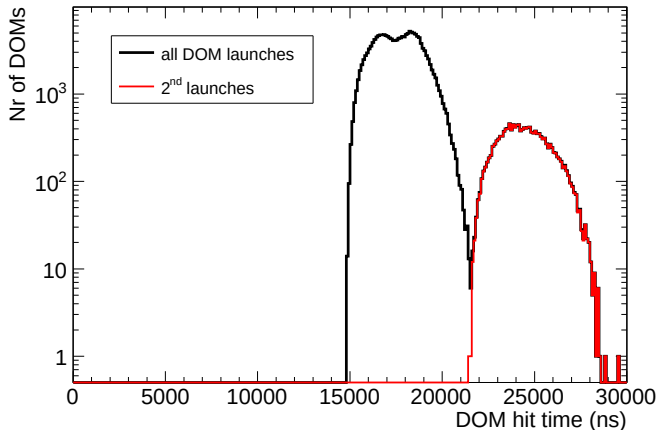

Figure 5.21: The DOM hit time distribution from MC for all DOMs (black) and second launches in a DOM (red), typically from afterpulses.

event now falls within the physically expected boundaries for the differences between the IceTop and IceCube trigger time of coincident events for both proton (left) and iron (right) simulations. The reason for trigger lengths larger than 6.5μs are PMT afterpulses. The PMT afterpulses create a second launch in the DOM. Because the time difference between the first hits from afterpulses and the the last physics hits is smaller than 5μs the triggerlength is extended and can even go up to 16μs. Fig. 5.21 nicely demonstrates that these DOM hits are indeed from second launches caused by afterpulses. The time distribution for all hit DOMs is plotted together with the time distribution of second launches which are the sole responsible for the second peak and therefore the second distribution at large trigger lengths. The triggers at 24μs are even generated only by second launches from afterpulses. To remove the pulses from these second launches, the coincident time window cleaning uses a maximum time window of 6.5μs starting from the trigger start time minus 300 ns (to account for PMT transit time) when the triggerlength becomes too large.

The reason why there are less events with a trigger length at 3μs is the dust layer. 3μs is the time needed for muon bundle to reach the dust layer and for low energy muon bundles the hits from muons that just reach the dust layer are less likely to not reach the DOMs.

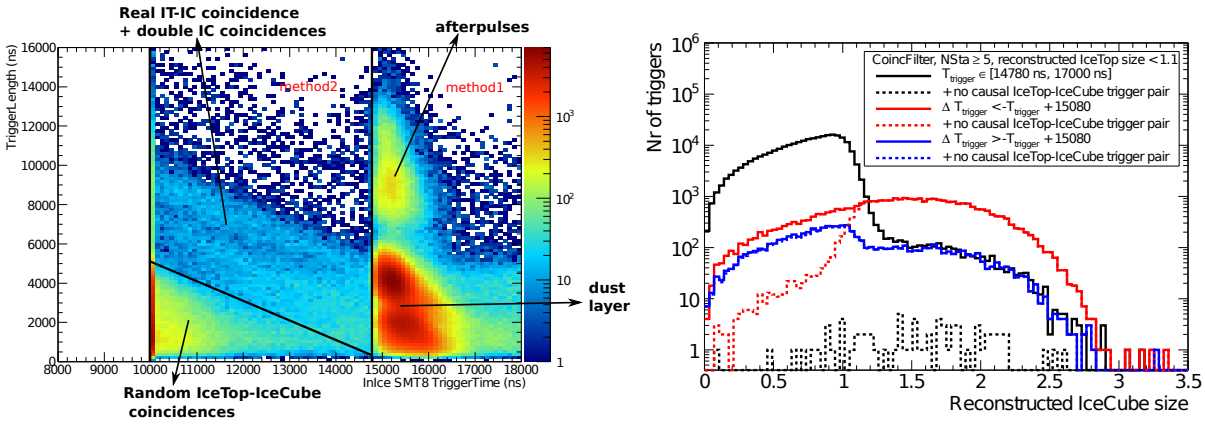

Figure 5.22: **Left**: Trigger length as a function of the IceCube SMT8 trigger time for 5 days of June 2010 data. The solid black lines show the events selected by the causal trigger selection algorithm, explained in the text, for method one (region at the right-hand side of the right line) and for method two (selects event in the region above the slanted solid line in addition to the region from method one) **Right**: IceCube size distribution for different region in the trigger length $\Delta T_{\text{trigger}}$ - trigger time T_{trigger} parameter space from the left plot. The events in this plot passed the coincident filter, have at least 5 hit IceTop stations and a reconstructed IceTop size smaller than 1.1. The blue distribution are from events that have IceCube trigger length above the slanted solid line from the left plot, while the red distributions are formed by events below the slanted solid line. The causal IceTop-IceCube trigger pair is here defined as events selected by method one, where the trigger time difference between IceTop and IceCube SMT8 fall in the [4μs, 7μs] window.

However, if we look at same distribution as Fig. 5.19 for data, after retriggering, on the left plot of Fig. 5.22, many events with trigger times earlier than 4.780 μs after the IceTop trigger appear. The trigger times can of course not be earlier than at 10μs because the readout window extends to 10μs before the start time of the first trigger and defines $T = 0$ ns. The unsimulated, good IceTop-IceCube events with a trigger time earlier than expected by our standard trigger selection method, explained above (*method 1*), are events where a muon or neutrino passes through IceCube just before the coincident air shower arrives. These events antedate the trigger time but also extend the trigger length. If there are real hits coming from an IceTop-IceCube coincidence, the trigger time is at least 4.780μs later than the IceTop trigger and the minimum trigger length is 300 ns. If an earlier event antedated the event so that the trigger is at the same time as the IceTop trigger, then the minimum trigger length must be at least 5180 ns in order to contain 300 ns worth of hits from the actual coincidence. The points (10000, 5180) and (14780, 300) in the trigger length - trigger time space, define the solid line shown in the left plot of Fig. 5.22. Above the solid line real coincident events are still possible because of the extended trigger length. Therefore, a new selection procedure (*method 2*) for candidate causal triggers adds the region above before 4780 ns and above the solid line to the allowed region.

The right plot of Fig. 5.22 describes the reconstructed IceCube size distribution of events contained by IceTop in each of the three regions from the left plot. Events that are selected by method 1, with a trigger time between the 14780 ns and 17000 ns form the black distribution. Events that are not selected because a causal IceTop-IceCube trigger pair has not been found by method 1, are shown by the dashed distributions. The bulk of the events are contained tracks and for almost all of them a matching IceTop-IceCube trigger is found. The red distribution is formed by events with trigger lengths below the slanted line in the left plot. The events from the red dashed distribution are dominated by random coincidences, because for most events the reconstructed IceCube size from the IceTop direction reconstruction is larger than one and thus does not create IceCube hits. The IceCube trigger must come from an unrelated event. The dashed distribution that some events are still selected by method 1. This is because of multiple IceCube trigger of which one satisfies the selection criterium from method 1 and the other trigger is from an unrelated event. The blue distribution

are formed by events that are selected additionally by method 2. Because the dashed and solid distributions are the same, these events are lost if selection method 1 is used. However, we can see that a large fraction of these events, contained by IceTop, also go through the IceCube volume and therefore must consist of the real IceTop-IceCube coincidences in which we are interested.

An additional 1.5% good events are selected if selection procedure 2 is used instead of method 1. Due to the good quality of the IceTop direction reconstruction after containment cuts, the final criterium to make sure no random coincidences survive the cuts, is a cut on reconstructed IceCube size as motivated by Fig. 5.22 and further explained in the Section 5.4.

5.3.2 IceTop Multiple Coincidences

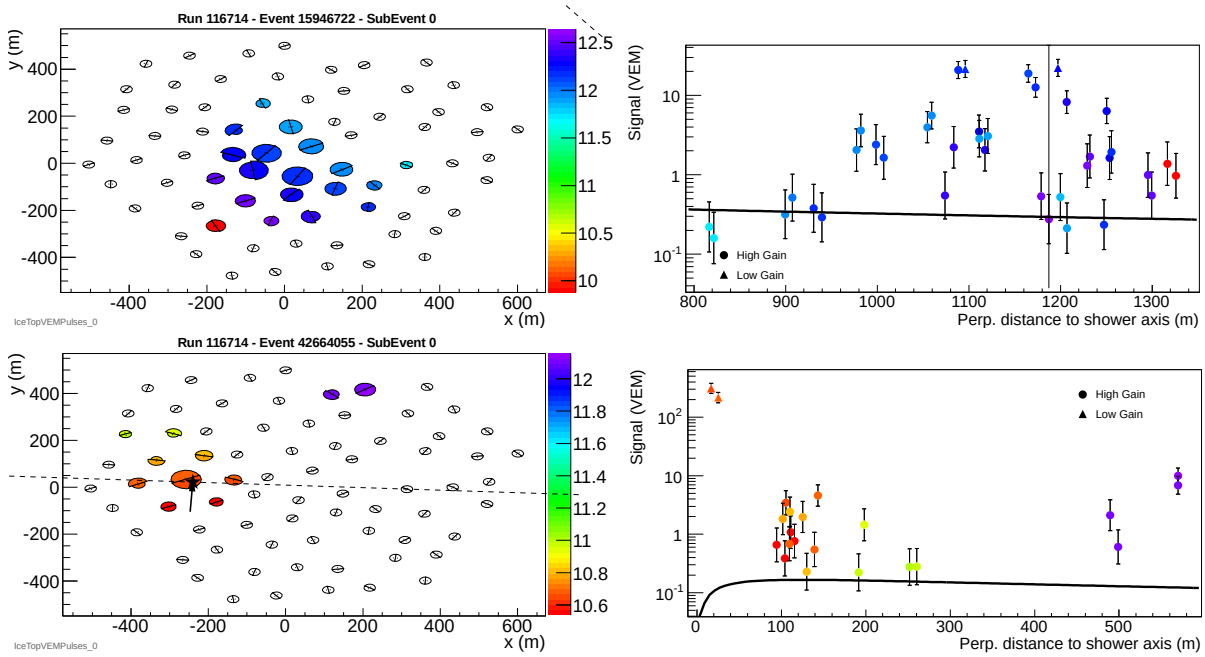

Figure 5.23: Two examples of events where two air showers landed on the IceTop array within the same event readout. **Left**: Top view of the events (definition of symbols is the same as for Fig. 4.9 **Right**: Result of the failed LDF reconstruction that tried to fit both independent events at once. The error bars are the charge fluctuations from Eq.4.7.

In principle multiple IceTop showers that land on the array during the same event readout should have been cleaned by the standard pulse cleaning from Section 5.1. By studying the events with low reconstructed β in data the events from Fig. 5.23 were found. Both LDF fits clearly failed because of one or multiple IceTop stations that comes from a low energy air shower during the same readout that hit the detector earlier or later and confuses the LDF fit. In the event at the top of Fig. 5.23, the 2.5μs earlier hit station is very close the stations connected to the second event. In the other event at the bottom of the same figure, two IceTop stations from a much later low energy event are well separated from the earlier nine-station event.

The reason why the standard pulse cleaning failed for these events is illustrated by the left plot of Fig. 5.24. The distances between stations with the closest time difference, used in the standard pulse cleaning, is plotted for events for very small or very large β that signal these type of events. A large tail to very large interstation distances exists. Because the interstation distance per c is added to the allowed time difference between station, stations from unrelated showers are kept.

A more advanced hit cleaning, similar as the one used above for cleaning the DOM hits, is used to get rid of these clusters. The so-called *seeded RT cleaning* algorithm, first looks for a cluster of 5 HLC hits around

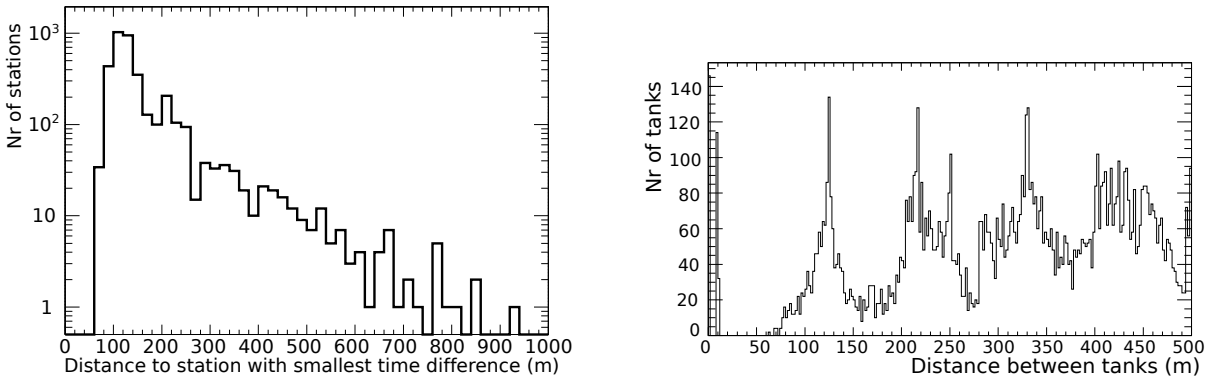

Figure 5.24: **Left**: The distance between a station and its neighbour with the smallest time difference in the event, for data where the fitted LDF slope $\beta < 1.5$ or > 6. **Right**: Distance between each IceTop tank and all its neighbouring tanks.

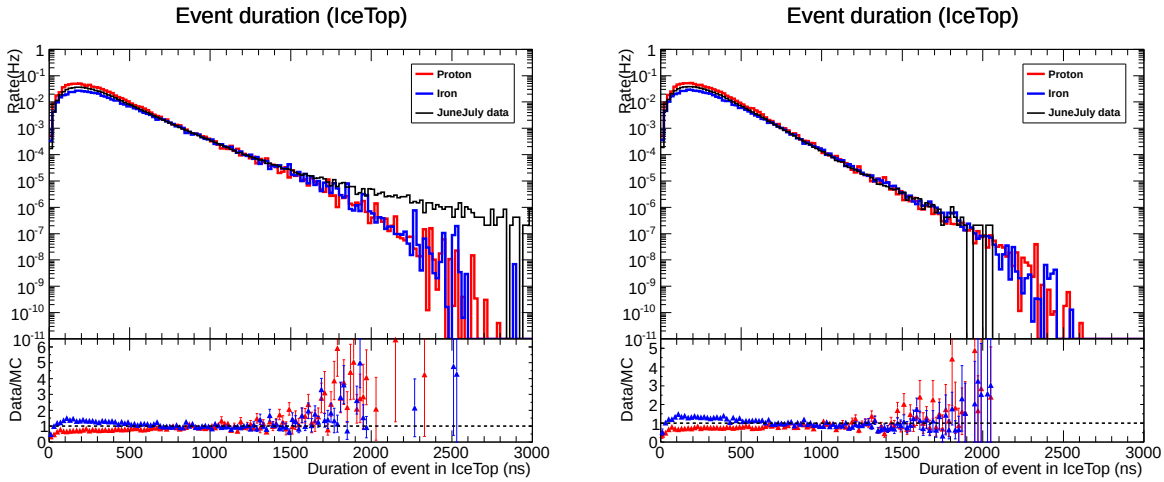

Figure 5.25: Distribution of the IceTop event duration, defined as the time difference between the last pulse and the first pulse, of data from June and July 2010 with proton and iron simulations before the seeded RT cleaning (left) and after the seeded RT cleaning (right)

each HLC hit within a distance R = 180 m and a time T = 450 ns. This means a cluster of at least three stations which are both close in space and time. After it has selected all clusters that satisfy this condition, more HLC are added to the selected pulses in an RT distance of the selected cluster. These additional HLC hits do not need to satisfy the three station cluster criteria anymore. Three iterations are performed to keep on adding more HLC stations in an RT distance of the DOMs selected after the previous iteration. This algorithm cuts on the time difference between neighbouring tanks and stations instead of first time ordering the hits and only comparing the time difference between the closest stations in time.

The distance of 180 m is chosen to make sure the circle around each IceTop tank includes all its neighbouring tanks and is based on the distribution of distances between all tanks (right plot on Fig. 5.24). The peaks are the distances where most neighbouring tanks are located. Consequently the seeded RT cleaning requires that at least a cluster of 3 neighbouring stations exist and that events that do no have this are removed. Of course this also takes care of multiple IceTop events and removes the extra earlier or later extra low energy event. Rare cases where the extra event also has three stations are not cleaned.

Fig. 5.25 nicely demonstrates the effectiveness of this hit cleaning. Events with long event durations, from early or late noise stations or multiple showers, are not simulated and more prominent in data then in MC. After the hit cleaning (right plot) however only the stations the actually belong to the event contribute to the total event duration and result in a good agreement between data and MC.

The set of cleaned pulses is only used for the first guess reconstruction and the LDF reconstruction, because also potential muons far from the core of real event are cleaned by this event. As these are not treated separately in the LDF anyway, the LDF fit performs better without this not well modeled outliers.

5.3.3 IceCube Multiple Coincidences

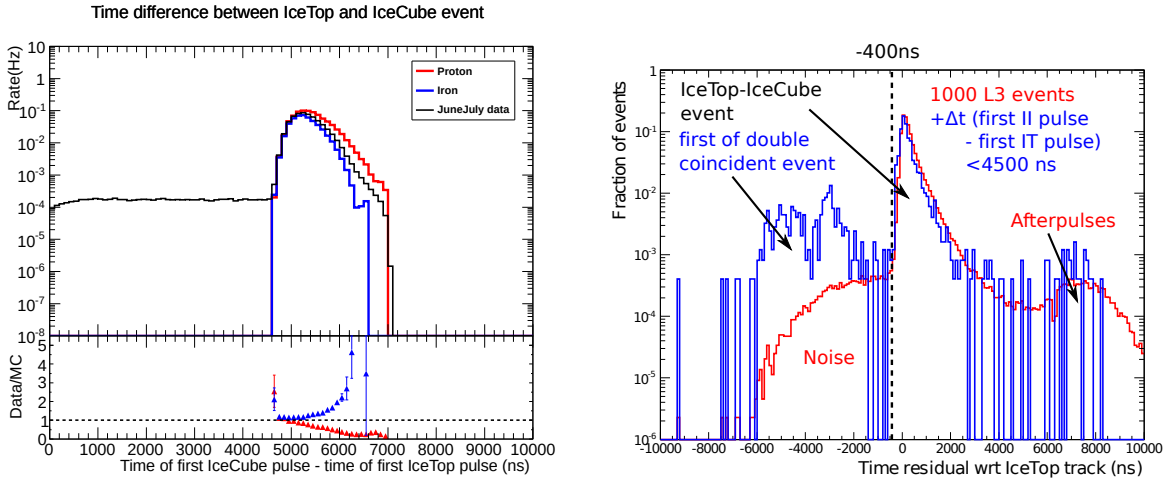

Figure 5.26: **Left**: Time difference Δt between the first IceTop pulse and the first IceCube pulse in an event compared between data and MC after containment cuts and removal of random coincidences (L3). **Right**: Time residual of the IceCube hits relative to the reconstructed IceTop track at L3 for 1000 events from data (red) and with an additional criterium that $\Delta t < 4500$ ns (blue), which is not simulated as shown on the left. Both distributions are normalized to compare the shapes better. The minimum time residual cut we will use for the hit cleaning is illustrated by the dashed line.

After the removal of the random IceTop-IceCube coincident events and cleaning the IceCube hits around the selected IceCube trigger, the distribution of the time differences between the first IceCube pulse and the first IceTop pulse is compared between data and simulation on the left plot of Fig. 5.26. One expects the IceCube DOMs to be hit about 4.5μs to 7μs later than the IceTop DOMs due to the propagation of the muon at nearly the speed of light. The uniform distribution below 4.5μs is not simulated and hints that still random IceTop-IceCube events passed through our event selection. A cut in this distribution could solve this.

However, if we study these events more in detail on the right plot of Fig. 5.26, we see that these events are not random coincidences and good events would have been cut by ignorance. The figure shows the time residual[2] distribution relative to the reconstructed shower direction and after containment and quality cuts for data. If we look at the shape of the time residual distribution for those events with IceCube DOMs that are hit earlier than expected, we see an extra population of hits showing up above the expected noise hits. These (unsimulated) hits come from a real event, either a muon or a neutrino, passing through the IceCube array right before the coincident IceTop-IceCube shower passes through the detector. The two unrelated events are close enough in time that they form one, long trigger. Instead of completely removing these events based on a cut on the data/MC discrepancy from the left plot of Fig. 5.26, we found a way to systematically tag

[2]The time residual is the time difference between the observed pulse time and the expected Cherenkov arrival time from photons hitting the DOM unscattered.

these events and have a method for removing the earlier hits. The earlier hits from the other event would completely confuse the energy loss reconstruction if not removed. The hit cleaning simply requires that the time residual of each DOM should be above -400 ns. Intuitively this means we are following the Cherenkov cone of muon bundle, reconstructed by IceTop, as it propagates through the IceCube detector and remove all hits that happened before the Cherenkov cone passes through the array.

Figs.5.27, 5.28 and 5.29 shows three different examples from the same data run, before (top) and after (bottom) the hit cleaning. The hit cleaning clearly performs outstanding. The first example (Fig. 5.27) shows two well separated tracks of which the later one is the event in which we are interested. Because of the geometrical spacing of the hits, this event can easily be divided in two sub-events by other algorithms. The second example (Fig. 5.28) depicts a muon that passes through the strings that will be hit shortly afterwards by the real IceTop-IceCube coincident event. Both tracks cross each other, are more difficult to separate and definitely fails energy loss reconstruction if not properly cleaned. The third example (Fig. 5.27) is probably even more rare and maybe unexpected. A muon neutrino, because the first hits are inside the IceCube volume and after interaction resuls in a muon track, passed through the strings which are shortly afterwards hit by the IceTop-IceCube air shower. Also the unexpected neutrino background events are properly cleaned by the simple time residual cut.

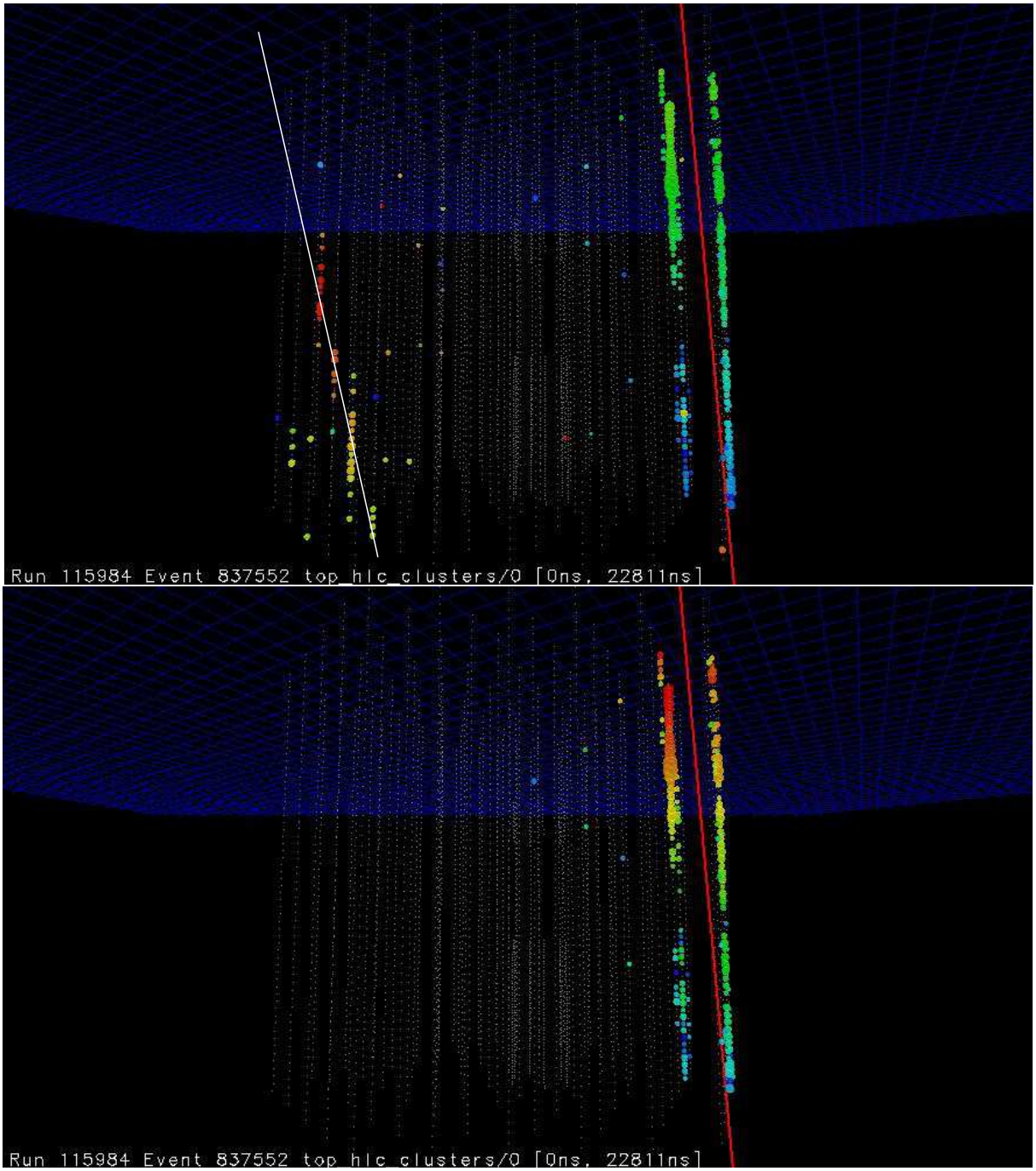

Figure 5.27: Example of an IceTop-IceCube event together with an unrelated IceCube event from data, where the IceCube track is well separated from the IceTop-IceCube air shower. The red line is the reconstructed track, while the white line is drawn to guide the eye. The lower figure shows the same event after the hit cleaning explained in the text. The colour code shows the pulse arrival times (from red to blue) and the size of the hit DOMs scales with the measured charge in the DOMs.

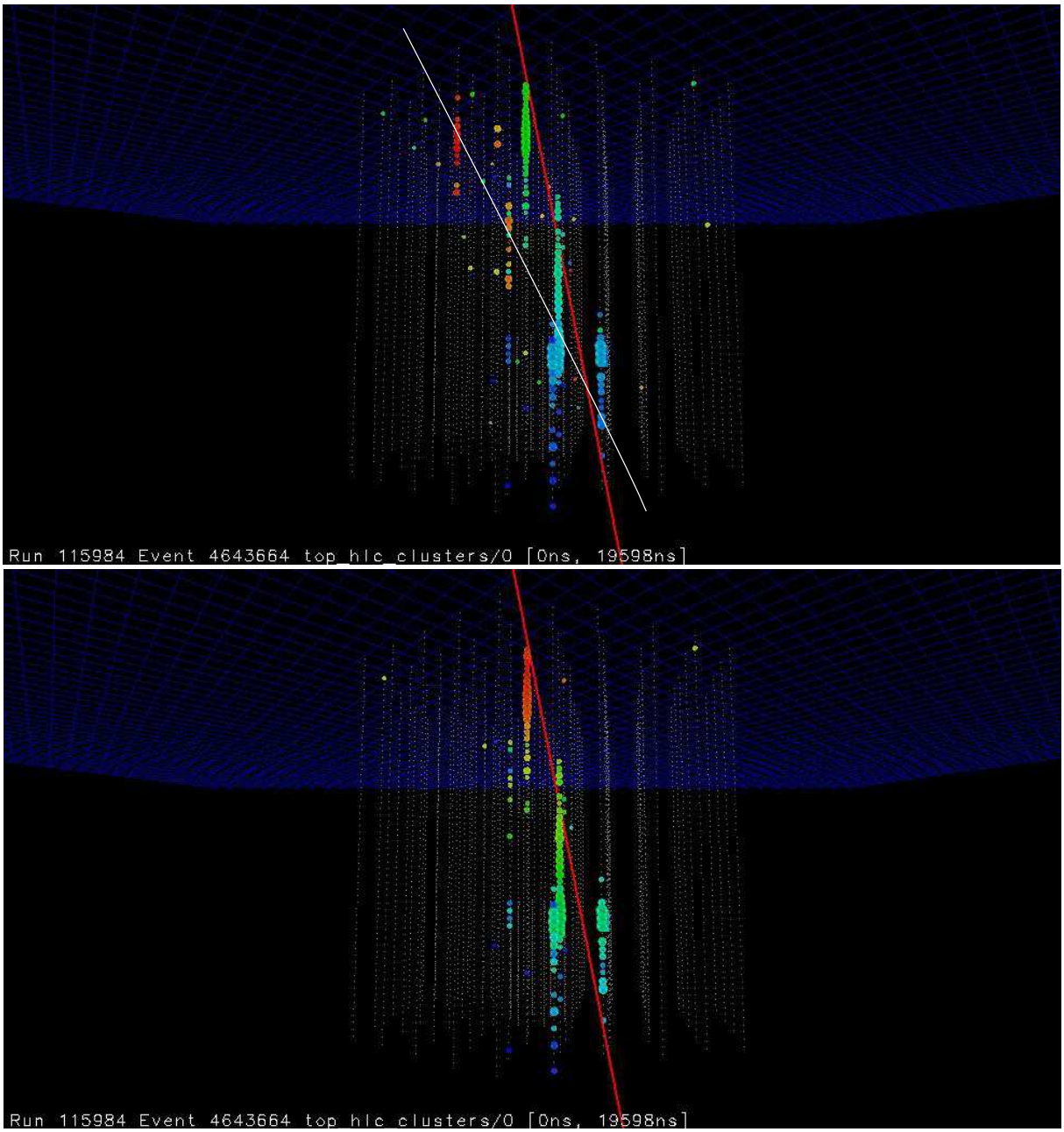

Figure 5.28: Example of an IceTop-IceCube event, with the red line as reconstructed track, together with an unrelated IceCube event from data. Here the IceTop-IceCube event crosses the earlier, unrelated IceCube event (white line) which complicates a standard pulse selection. The lower figure shows the same event after the hit cleaning, explained in the text.

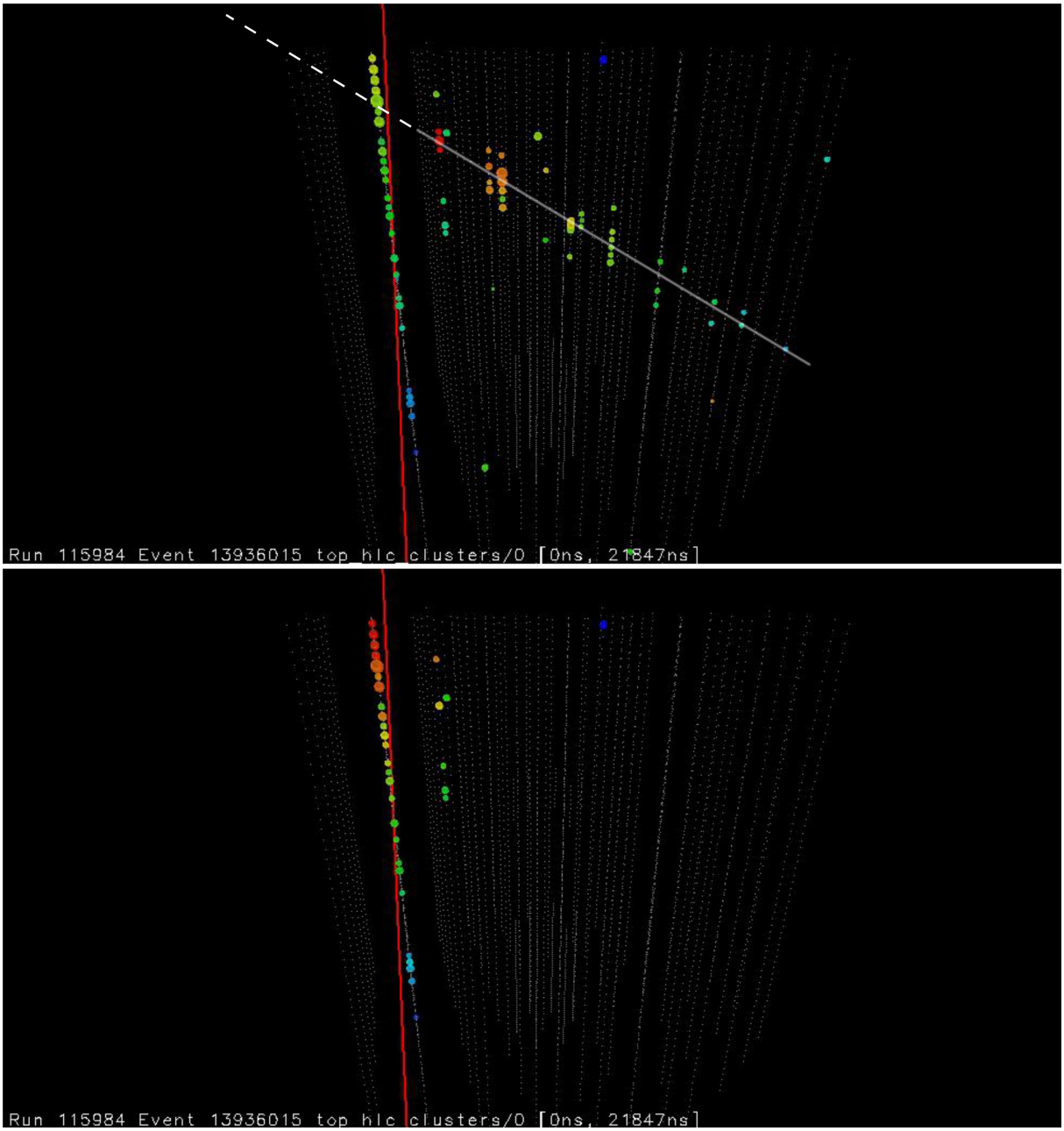

Figure 5.29: Example of an IceTop-IceCube event together with an unrelated IceCube event from data. In this case the earlier IceCube track (white line) probably comes from a muon neutrino, because the first hits are not from the top DOMs as one would expect from a cosmic muon. The lower figure shows the same event after the successful hit cleaning, explained in the text.

5.4 Quality Cuts

The quality cuts discussed in this section quantify if the reconstruction procedure was successful and reconstructed variables make sense. The very first quality requirement after the filter selection of events that passed the coincident filters is that the event must have at least five hit IceTop stations after the standard hit cleaning and eight IceCube HLC DOMs after the pulse cleaning from the coincident time window cleaning procedure. Five IceTop stations are needed to have enough degrees of freedom for an LDF fit with curved shower front. The eight IceCube HLC DOMs form the basic SMT trigger requirement, but this is re-evaluated after the hit cleaning that removes all hits if no causally connected IceCube SMT8 trigger with the IceTop SMT6 trigger has been found. This cut therefore removes the random coincidences where the IceCube pulses were cleaned with the method explained above.

5.4.1 IceTop reconstructions

The IceTop reconstruction algorithms return as status to signal whether the reconstructed converged to a result or not. Of course this is an essential requirement before we can even consider the results of the fit. In reality, this cut removes events which had insufficient hits for the reconstruction or where the first guess algorithms already did not have enough hit stations (the planar shower fit requires 3 stations). Even though we already required five stations after the standard hit cleaning, the additional hit cleaning explained in the previous section reduced the number of good IceTop stations for reconstruction sometimes below five.

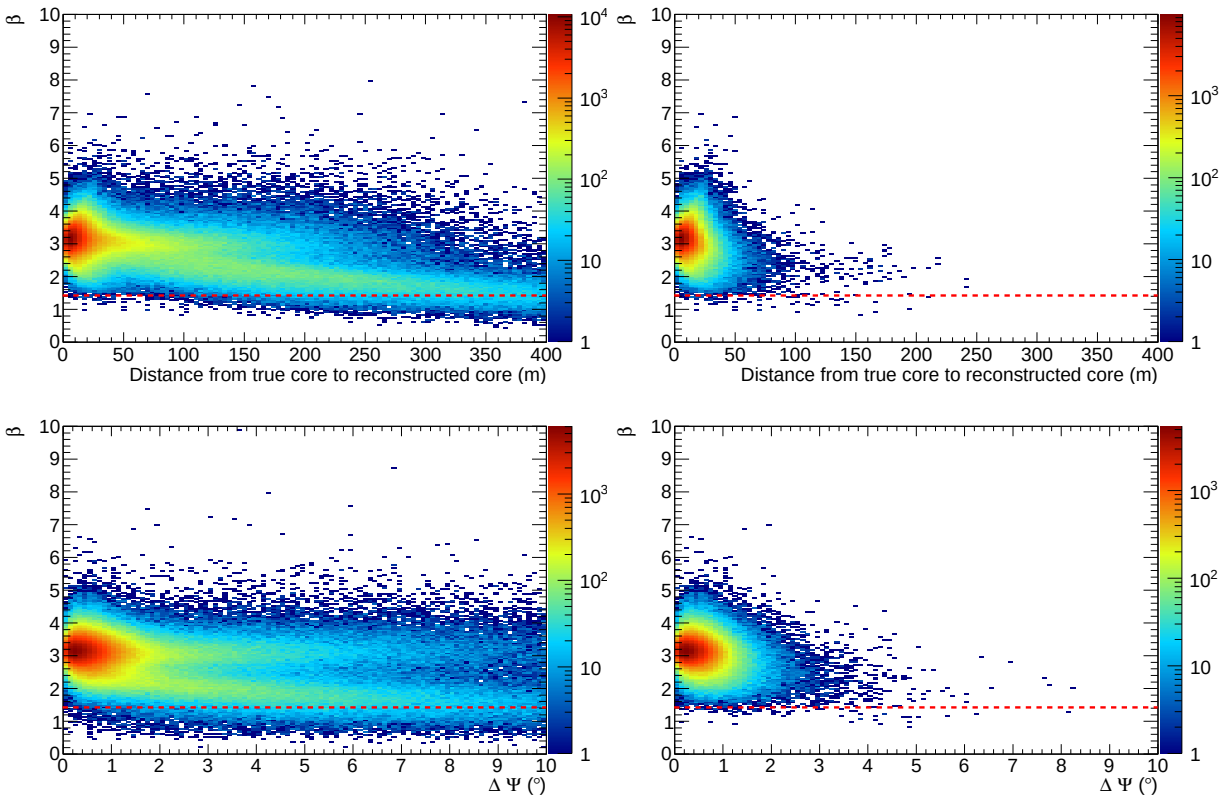

Figure 5.30: **Top**: The slope β of the reconstructed LDF as a function of the distance from the true core position to the reconstructed core position for proton simulations (left) and for the contained proton events (right). **Bottom**: Reconstructed β as a function of the angle $\Delta\Psi$ between the true direction and the reconstructed direction for proton simulations (left) and for the contained proton events (right)

In Chapter 4, the slope of the LDF β has been introduced and hinted that quality cuts on β might be

required. Fig. 5.30 clarifies the relation between the reconstructed β and the core reconstruction (top) and the direction reconstruction (bottom), for all events (left) and contained events (right). After containment cuts it becomes clear that low β typically give a worse reconstruction quality. The minimum β value of 1.4 is chosen as quality and illustrated by the red, dashed line. Large β values are not related to bad reconstructions but the maximum allowed β is 9.5 because β was bound to be between 0 and 10. Fig. 5.30 shows also that this cut does not remove many events, while the typical β cut based on the old IceTop reconstruction procedure removed 3% of the events.

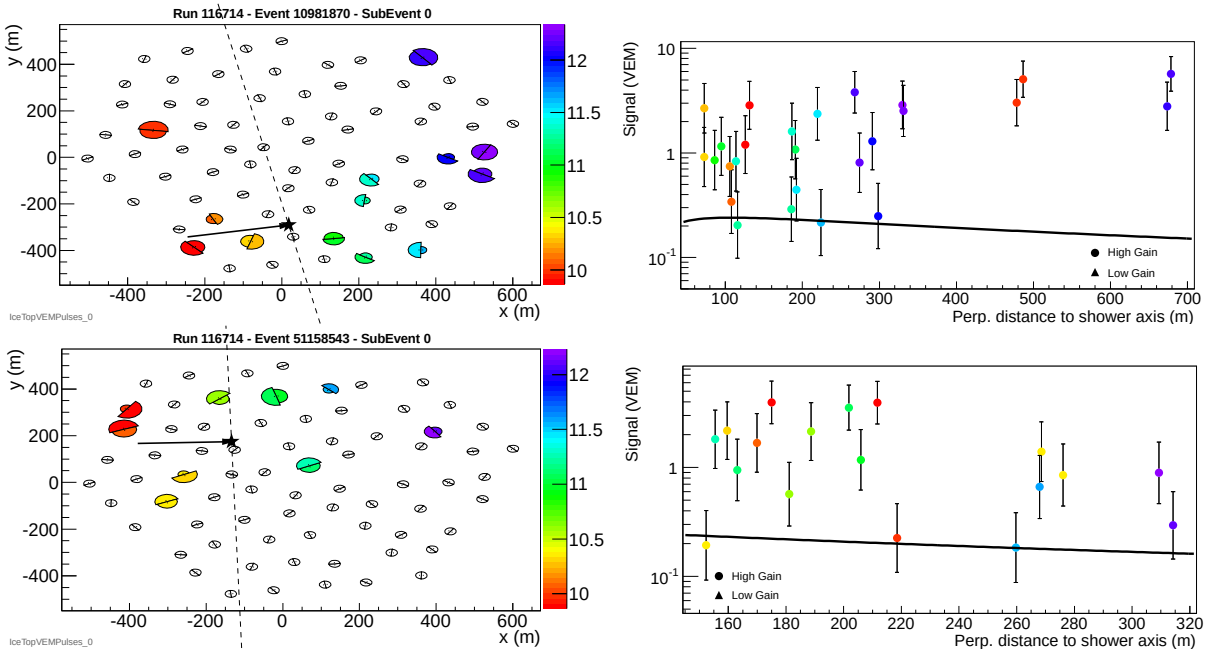

Figure 5.31: Two examples of events with low station density. **Left**: Top view of the events (definition of symbols is the same as for Fig. 4.9) **Right**: Bad LDF reconstructions.

During the development of the new IceTop reconstruction procedure several events were found in data that are impossible to reconstruct. Two examples of these events are shown in Fig. 5.31. It seems impossible to find where the real core position is and the LDF fit can not describe the random set of charges seen here. From the timing behaviour these events could be caused by very inclined showers that are muon-rich, hence the 1-2 VEM hits, because the electromagnetic particles are absorbed by the larger atmosphere. Both the trigger as the reconstruction algorithms are not yet ready to properly account for these so-called *horizontal* showers. Other reasons could be that this type of events come from a collection of noise stations that accidentally triggered the detector.

To quantify these unreconstructable class of events, a quantity called *station density* is constructed. The station density is the ratio of the number of hit stations to the total number of stations in a circle centered at the COG and with a radius that extends to the furthest hit station. A low station density means the COG is in the middle of large set of scattered stations. This quantity is also useful to study weird event topologies and to track multiple IceTop showers hitting the array at the same time. Because data and MC agree quite well in the distribution of this topological, new variable (Fig. 5.32) a conservative cut of 0.2 as minimum station density is chosen.

Fig. 5.33 shows the IceTop size distribution as a function of primary energy for the events that are removed by this cut alone.Only a very few number of events are removed in MC and they are only low energy events. However, the simulations do not produces highly inclined showers, because we only simulated up to a zenith angle of 40 degrees. Also multiple IceTop showers are not simulated as mentioned earlier. This cut therefore should remove more events in data, but for real coincident IceTop-IceCube air showers these cases

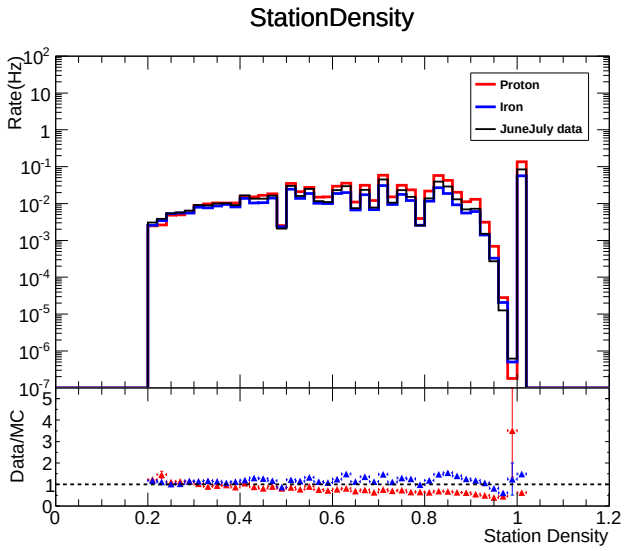

Figure 5.32: Station density distribution compared between two months of data (June and July 2010) and proton and iron simulations. The data/MC ratio is shown at the bottom.

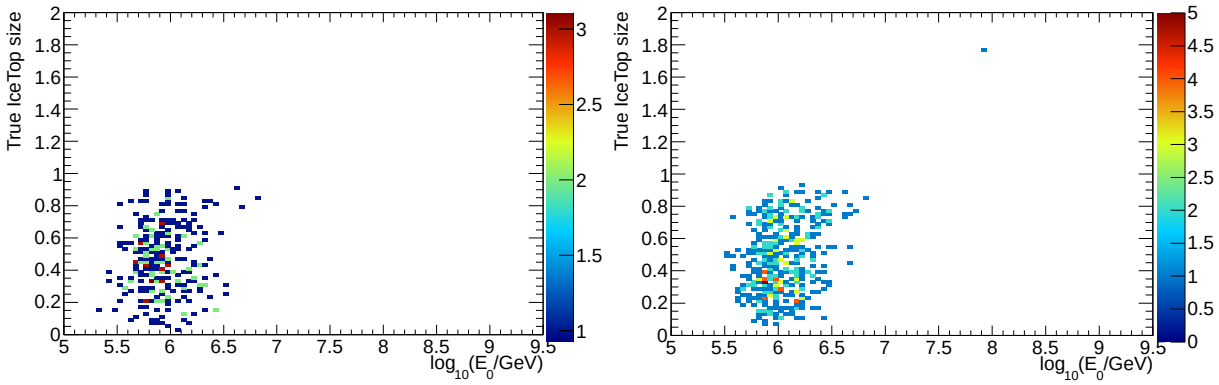

Figure 5.33: IceCube size distribution as a function of primary energy to illustrate the properties of events with a station density lower than 0.2 for proton (left) and iron (right) simulations.

are very rare.

5.4.2 IceCube reconstructions

The quality parameters from the segmented IceCube energy loss reconstruction are the reduced loglikihood or *rlogl* (the loglikelihood divided by the degrees of freedom) and the ratio of predicted charge from a forward folding of the resulting energy loss profile and the measured total charge in IceCube. The distributions for both quality parameters are shown in Fig. 5.34. Only a very few anomalously high rlogl values exist and are clear signatures of bad reconstructions. We therefore require the $\log_{10}$(rlogl) to be below 2. For a similar reason only events with $\log_{10}$(predicted total charge QTot/ measured total charge QTot) $>$ -0.03 are kept.

In Fig. 5.35 the primary energy dependence of this total charge ratio is plotted for both proton and iron simulations. It shows that the cut mainly removes a few low energy events. The large asymmetric tail is mainly present at low energies and decreases as a function of the energy. The reason for this behaviour is currently being investigated.

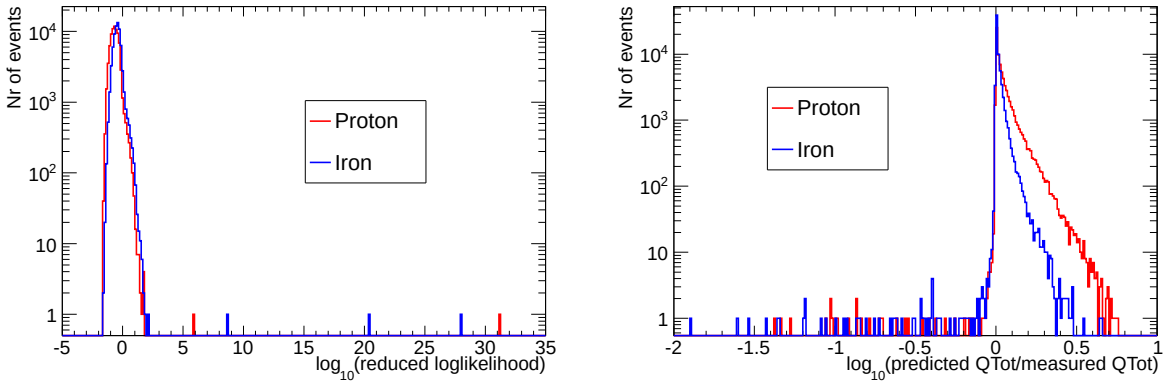

Figure 5.34: **Left**: Distribution of the reduced loglikelihood of the segmented energy loss reconstruction from Section 4.2.1 for proton (red) and iron (blue) simulations. **Right**: Distribution of the ratio of predicted total charge of the event from the segmented energy loss reconstruction over the total charge in the event for proton (red) and iron (blue) simulations.

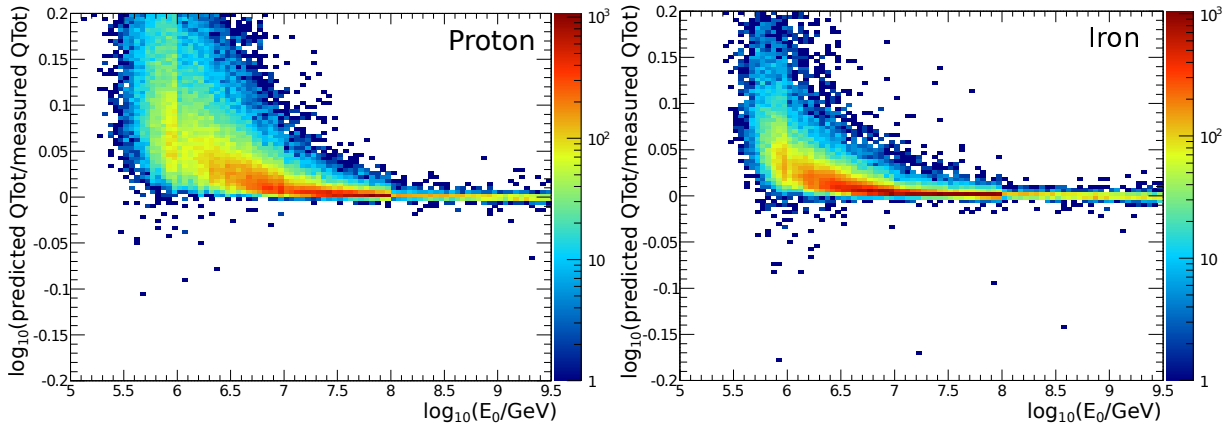

Figure 5.35: Primary energy dependence of the distribution from the right plot of Fig. 5.34 for proton (left) and iron (right) simulations.

The last step in IceCube reconstruction is the average energy loss fit to the unfolded energy loss profile. The unfolding can only reconstruct energies on track segments which give enough light to be seen by the IceCube DOMs. Many segments could have zero energies, certainly after the removal of tracksegments in the dust layer and outside the IceCube volume (see Chapter 4). Although the track segments with zero energies are also used in the fit, we require that at least three segments have a non-zero energy for a good fit quality. This is illustrated by Fig. 5.36. Bad reconstructions typically cause outliers in the correlation plot of reconstructed energy loss as a function of S_{125}. The red points show the events where the average energy loss fit found a solution. The events removed by the total charge ratio cut, are marked by the blue pluses. Many of those removed events were outliers which motivates the cut. The events removed with less than 3 non-zero cascades are tagged by the black crosses. In addition to the low-energy or barely contained events, almost all remaining outliers are removed, typical for bad reconstructions. The events which are removed by the rlogl cut are not visible on the plot because they have unrealistically high reconstructed energy losses.

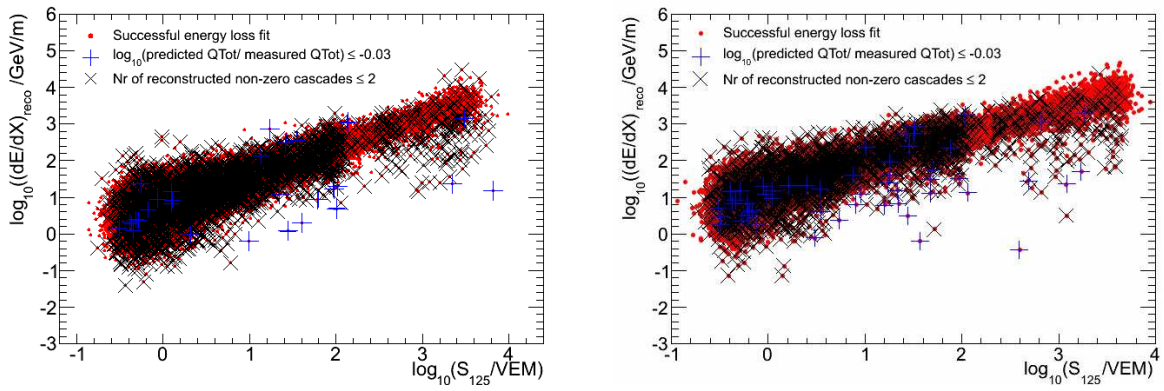

Figure 5.36: Effect of quality cuts on total charge ratio and minimum number of reconstructed cascades with non-zero energy in the $\mathrm{d}\,E/\,\mathrm{d}\,X - S_{125}$ plane for proton (left) and iron (right) simulation.

5.5 Data processing

Here I will give an overview of all hit cleaning procedures, cuts and reconstructions used for my analysis based on the physics discussed in this Chapter and the previous Chapter. The level 3 processing consists of the coincident event selection and IceTop reconstructions and cuts. The level 4 processing exists of extra IceCube pulse cleaning and the energy loss reconstruction procedure. The performance of the reconstruction and the comparisons of the most important distributions between data and MC are shown after all cuts at the end of this Section.

5.5.1 Level 3 processing

The level 3 processing (L3) starts with data that is processed with the standard level 1 and level 2 offline processing. None of the reconstructions performed during the standard level 2 processing will be used further. The standard IceTop pulse cleaning is also applied in the level 2 processing. From there the level 3 processing goes as follows in that order:

1. Only events that pass the prescale of the coincident online filters, IceTopSTA3_InIceSMT and IceTopSTA8_InIceSMT, are selected.

2. IceCube hit cleaning:

   (a) The early noise hits and noise HLC pairs are removed from the set of IceCube hits and the event is retriggered based on the cleaned hits. This results in unbiased trigger starting times.

   (b) Matching causal IceTop-IceCube trigger pairs are formed based on the retriggered triggers and the IceCube pulses are cleaned around the matching IceCube trigger if one is found.

3. Extra IceTop hit cleaning: Early/Late noise stations from multiple air showers that land on IceTop are cleaned with the *seeded RT algorithm*.

4. A minimum number of IceTop station hits of five is required after the IceTop hit cleaning from level 2 and a minimum number of IceCube DOM hits of eight is required after the coincident hit cleaning from level 3. This removes random coincidences where all pulses were cleaned.

5. Reconstruction-independent containment cuts:

   (a) The station with the largest total charge should not be on the boundary of the IceTop array.

(b) The largest charge in the event must be above 6 VEM.

(c) The charge of the neighbouring tank of the tank with the largest charge must be at least 4 VEM.

6. Reconstructions based on IceTop hits after the extra hit cleaning. Both first guess reconstruction were already performed at level two, but are repeated to prevent a bias from noise stations which are now cleaned:

   (a) The first guess core position is determined, based on the COG of the seven tanks with the largest pulse charges.

   (b) The first guess direction reconstruction relies on the planar shower front approximation.

   (c) The maximum loglikelihood procedure fits the core position, direction and LDF in three steps and accounts for the snow correction and saturated signals.

7. Quality cuts on the result of the reconstructions:

   (a) The IceTop station density should be above 0.2.

   (b) The LDF fit must have converged.

   (c) The slope of the LDF β is required to be between 1.4 and 9.5.

   (d) The reconstructed IceTop size needs to be below 1.0.

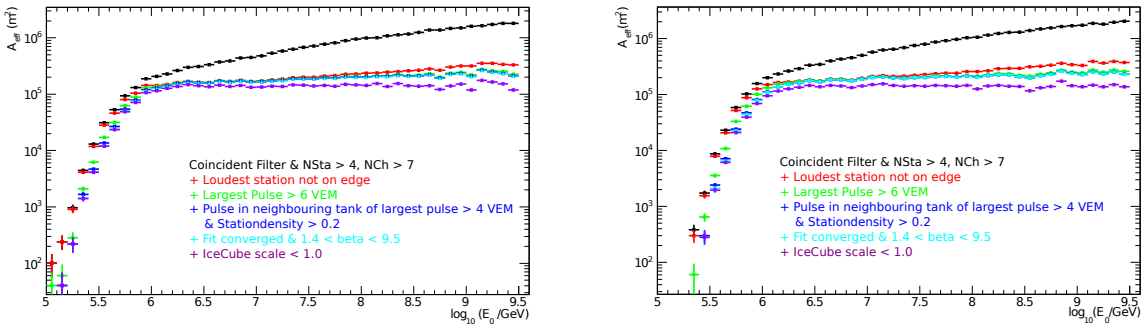

Figure 5.37: Effective area as function of primary energy for proton (left) and iron (right) after each cut performed at L3.

The effective area in Fig. 5.37 illustrates how many events survive each cut as function of true energy for both proton and iron simulations. The effective area is calculated here as the total number of events after each cut, divided by the number of events before any cut was performed and thus also includes the trigger efficiency. If this efficiency is multiplied with the area over which the events were simulated, we get the effective area. The cut that removes most events is the loudest station cut. The other containment cuts mainly remove events in the threshold region or at very high energies. The cuts performed at L3 remove the energy dependent slope, caused by the larger trigger efficiency at higher energies.

5.5.2 Level 4 processing

After the L3 processing of both data and MC simulations, I applied the following level 4 processing (L4):

1. Extra IceCube hit cleaning:

   (a) IceCube pulses that arrive earlier than the Cherenkov cone along the reconstructed muon bundle track, caused by multiple IceCube events, are cleaned by requiring a minimum time residual of -400 ns.

(b) IceCube DOMs further than 500 m from the reconstructed track only carry noise hits and slow down the energy loss reconstruction algorithm. Therefore they are removed.

(c) IceCube DOMs that carry a total charge of more than 30% of the total charge of the event, bias the energy loss reconstruction, are not well simulated and are discarded.

2. Again we check that the event has at least eight hit DOMs after the extra IceCube hit cleaning.

3. IceCube energy loss reconstruction:

   (a) The energies of cascades on 20 m long track segments at a slant depth between 1300 m and 2600 m are reconstructed by a Poisson-based maximum likelihood procedure seeded with the initial result from the unfolding.

   (b) The reconstructed energy are converted to energy losses per meter and track segments outside the IceCube volume or in the dust layer are removed.

   (c) The average energy loss profile is fitted to the reconstructed individual energy losses as a function of the slant depth. Two selection criteria, a standard one and a strong one, are used to select extreme stochastic energy losses and determine their properties.

4. Quality cuts on the result of the energy loss reconstructions:

   (a) An additional containment that removes the last few uncontained high energy events is performed by requiring a maximum reconstructed IceTop size of 0.96.

   (b) The maximum reduced loglikelihood value must be below 10^2.

   (c) The common logarithm of the ratio between the predicted total charge in the event, from a forward folding of the result, over the measured total charge must be higher than -0.03.

   (d) There must be at least three track segments with a non-zero energy loss.

   (e) The average energy loss must converge.

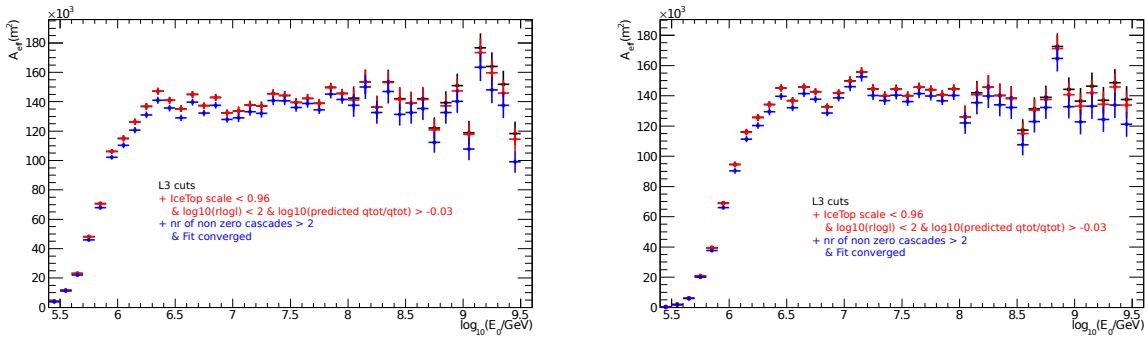

Figure 5.38: Effective area as function of primary energy for proton (left) and iron (right) after each cut performed at L4.

The effective area after a set of L4 quality cuts is shown in Fig. 5.38 for both proton and iron simulations. Except for the cut on the minimum number of cascade with an energy higher than zero, the quality only remove a very low number of events. Fig. 5.39 shows the final effective area for my analysis, compared between proton and iron simulations. Both are fitted separately with the sigmoid function $A_{\text{eff}} = \frac{a}{1+\exp(-b\log_{10}(E_0)+c)}$. To verify whether there is an energy dependence in the effective area a sigmoid function with a linear function in the numerator instead of a constant is fitted, illustrated by the dashed cyan line for iron. There is no gain in χ^2/ndf for a sigmoid fit which is not flat. For proton simulations the χ^2/ndf increases from 161/34 to

160/33, while for iron simulates it stays roughly the same (from 123/34 to 120/33). Therefore the effective area is flat in energy. The difference between the effective area of proton and iron showers is also very small (1.5%). If the threshold region is well understood, we can use the effective area to properly account for it. However, the threshold region is currently under investigation. From Fig. 5.38 I chose the energy threshold of my analysis to be 6.4 in $\log_{10}$ of energy, or 2.5 PeV. The effective area beyond the threshold if $1.36{\cdot}10^5 \mathrm{m}^2$.

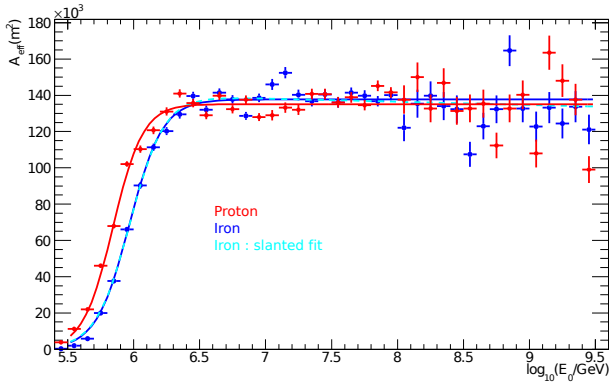

Figure 5.39: The final effective area as function of energy after all cuts for proton (red) and iron (blue). Both are fitted with a sigmoid function. A slanted sigmoid function fit is shown by the dashed cyan curve.

Event Selection	Number of remaining events (% of total – % of previous)				
	Data	Simulation (E^{-1})			
	June 2010 - May 12, 2011	Proton	Helium	Oxygen	Iron
Coincident filter	89277664 (100%-100%)	369949	386459	389346	392469
NSta ≥ 5 & NCh ≥ 8	21192725 (23.7%-23.7%)	270631	280474	281782	284525
Loudest station not on the border	16563705 (18.6%-78.2%)	105656	109860	108981	108471
Q1 > 6 VEM	14127326 (15.8%-85.2%)	97302	100262	98394	97145
Q1b > 4 VEM	12416858 (13.9%-87.9%)	93573	96123	93742	92189
Station density > 0.2	12148172 (13.6%-97.8%)	93240	95720	93276	91657
IceTop fit successful	11873732 (13.3%-97.7%)	92864	95298	92827	91171
$1.4 < \beta < 9.5$	11872282 (13.3%-99.99%)	92848	95278	92801	91144
IceCube size < 1.0	10259891 (11.5%-86.4%)	76747	76799	72800	69549
NCh ≥ 8 after hit cleaning	10225686 (11.5%-99.7%)	76572	76698	72753	69514
IceTop size < 0.96	10224077 (11.5%-99.98%)	76505	76635	72692	69452
$\log_{10}$(rlogl) < 2	10223667 (11.5%-99.996%)	76503	76629	72686	69448
$\log_{10}(\mathrm{QTot}_{\mathrm{predicted}}/\mathrm{QTot}_{\mathrm{measured}}) > -0.02$	10189418 (11.4%-99.7%)	76480	76604	72654	69405
Nr of reconstructed energy losses > 2	9722705 (10.9%-95.4%)	73611	73794	70133	67088
Average energy loss fit successful	9722705 (10.9%-100%)	73605	73791	70124	67074
$\log_{10}(E_0/\mathrm{GeV}) > 6.4$	1560138 (1.7%-16.0%)	47521	48255	48261	48030

Table 5.1: Number of events after each cut.

The angular resolution for proton and iron simulations as a function of the primary energy after all cuts is between 0.2° and 1.0° (see left plot of Fig. 5.40). The worse composition-dependent angular resolution is probably caused by the limited description of the shower front curvature with fixed curvature parameters. The core resolution is smaller than the tank spacing and is 6 - 12 m in the energy range between 6.4 and 9.5, used for this analysis.

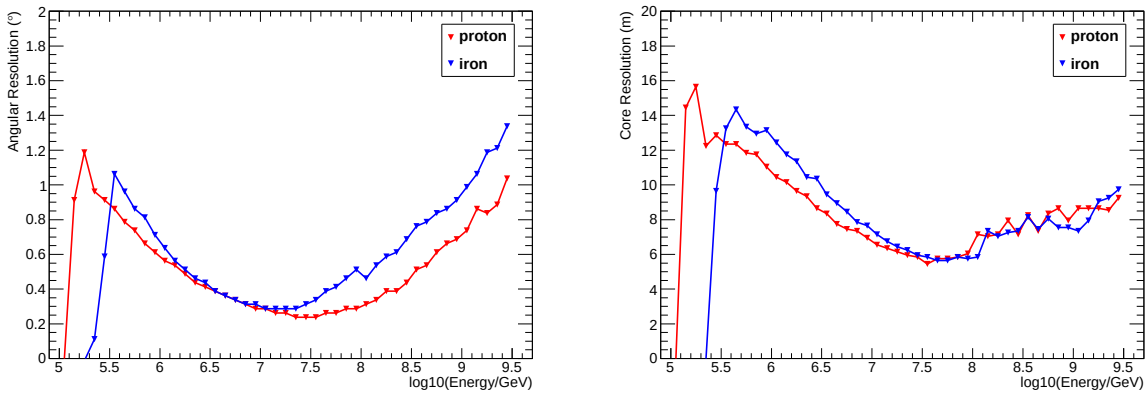

Figure 5.40: The angular resolution (left) and core resolution (right) after all cuts as function of primary energy for proton (red) and iron (blue) simulation.

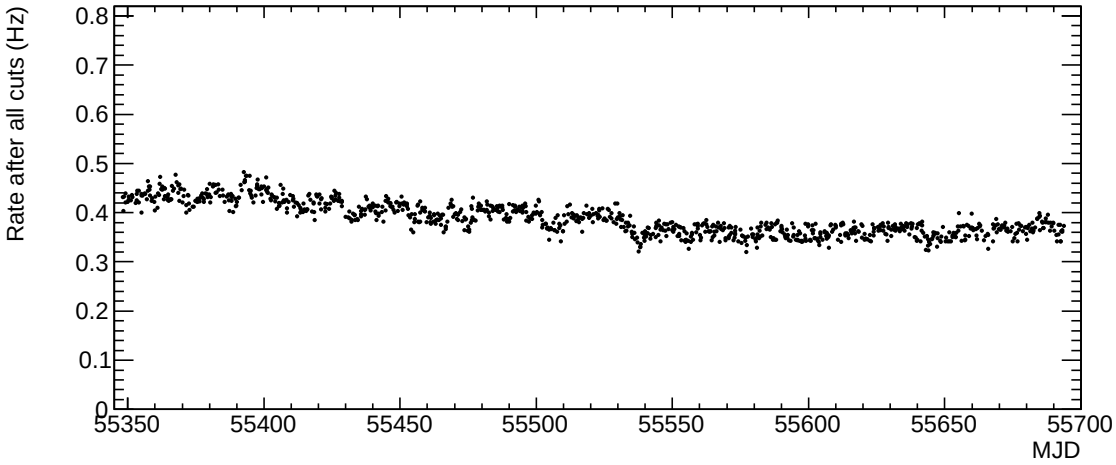

Figure 5.41: Rate variation after all cuts over the IT-73/IC-79 data taking period from June 1, 2010 to May 12, 2011 in Modified Julian Date (MJD).

In Fig. 5.41, the event rate of each run from June 1, 2010 to May 12, 2011 is plotted as a function of time represented by the Modified Julian Date (MJD). The rate is dominated by the low energy showers near the threshold. The local variation comes from daily surface pressure variations, because the rate of coincident events is still mainly determined by whether they trigger IceTop or not. Over a long time period the rate seems to gradually decline, for which the snow accumulation is the main culprit. This figure also demonstrates the stability of the detector and provides an important check for bad runs. A signature of bad runs are unexplained high or low rates. The good run selection I used for my analysis requires that both the IceTop detector and the IceCube detector were working properly and shows no outliers in Fig. 5.41.

5.5.3 Data/MC comparison

Before we can trust the simulation to give us the correct relation between the reconstructed variables and the primary energy and primary mass, we must verify whether the simulations agree with the data. Discrepancies otherwise result in wrong interpretations of the data and therefore in a wrong measurement. Here I will discuss only the most important variables that are used by the neural network analysis, described in the next

Chapter. A more detailed overview of low level, medium level and high level comparisons between data and simulations can be found in Appendix C.

The simulations are generated according to an E^{-1} spectrum, while the primary energy flux is expected to follow an E^{-3} spectrum beyond the knee at about 3 PeV. Data also consists of an unknown mixture of primary nuclei, while the simulations are done with pure proton, pure helium, pure oxygen and pure iron showers. For the comparison between data and simulation we therefore reweight the simulated energy spectrum to obtain the expected energy spectrum for proton and iron showers. This procedure is described in more detail in Appendix C. If we assume primary nuclei heavier than iron will not dominate the energy spectrum at some energies, then the data distribution should lie between between proton and iron. Deviations from that behaviour signal potential problems in the simulations.

The simulations are based on the July atmosphere in CORSIKA. Hence, the data chosen for the comparisons are from June and July 2010.

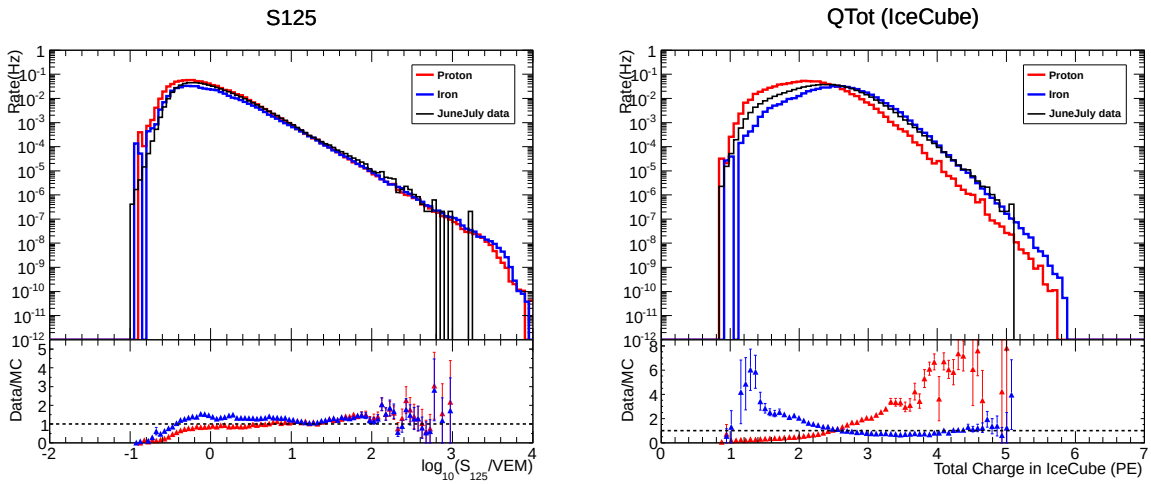

Figure 5.42: Data/MC comparison for the S_{125} distribution (left) and the distribution of the total charge observed in IceCube (right). The ratio between data and MC is plotted at the bottom.

The most important variable for primary energy reconstruction is the shower size S_{125}, because of the linear relation with the primary energy for a known primary. The data/MC comparison for the S_{125} in the left plot of Fig. 5.42 illustrates that the good agreement except for an unsimulated increase in rate between 1.4 and 2.4 in the common logarithm of S_{125}. This cannot be explained by reconstruction problems, different event topologies or multiple IceTop showers as those are all studied in detail and well accounted for. Therefore this must come from a primary flux that does not follow a smooth E^{-3} powerlaw.

The observed total charge in IceCube relates to the total energy deposit, which depends on the muon multiplicity. Thus, the total charge is a rough measure for the primary composition. The right plot of Fig. 5.42 demonstrates that the data distribution lies between the proton distribution and the iron distribution and therefore the total charge is well simulated. However, this variable , and other more dedicated energy loss variables, is very sensitive to the knowledge of the absolute light yield in the detector. In the systematics calculation this is discussed in more detail.

Figs.5.43 to 5.47 show the S_{125}-dependence of all composition sensitive variables under consideration for my analysis. The slope of the LDF, β, relates to the phase in the longitudinal shower development at which IceTop observed the event. The longitudinal shower development is different for proton and iron showers of the same primary energy. Fig. 5.43 demonstrates that proton and iron distributions behave differently , but that beyond $\log_{10}(S_{125})$ of 3 the simulated β's sharply increase, while the β from data is unbound by proton and iron. This is currently not understood and is the main argument why β is not used further in this analysis.

Also the energy dependence of the relative height of the selected stochastic peaks is not well simulated

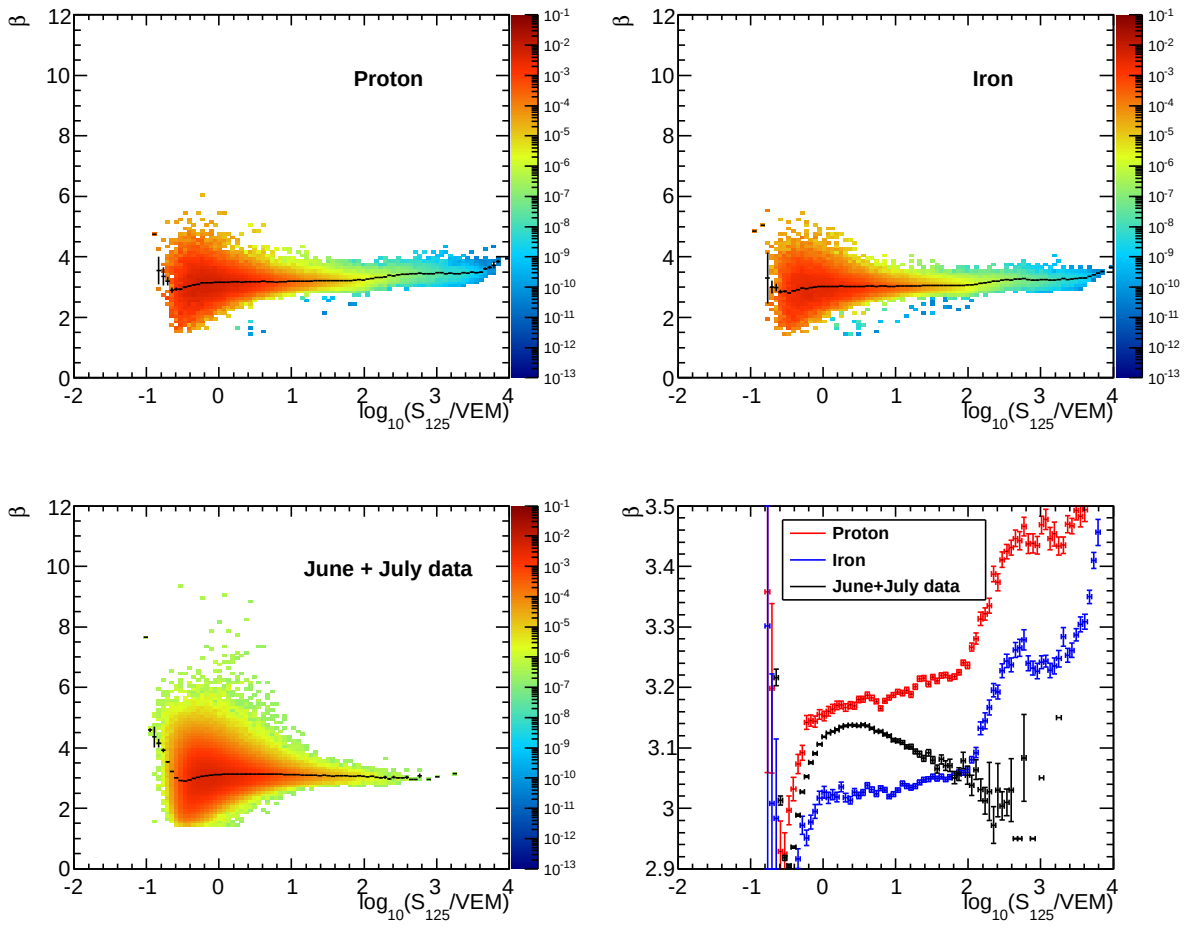

Figure 5.43: Distribution of β as a function of S_{125} for proton simulations (top left), iron simulations (top right), data (bottom left) and the mean of the distributions for each S_{125} bin (bottom right), with the error on the mean as error bar. The colour code is the event rate.

(see Fig. 5.44) beyond 1.6 in the common logarithm of S_{125} even though it is nicely bound by the well separated proton and iron distributions at lower energies.

The other three composition-sensitive variables under consideration, do exhibit clear agreement between data and MC, illustrated by Fig. 5.45 for the average energy loss and Figs. 5.46 and 5.47 for the number of selected stochastics with the standard and strong selection procedure.

Therefore only those last three variables are used in the composition analysis, described in the next Chapter.

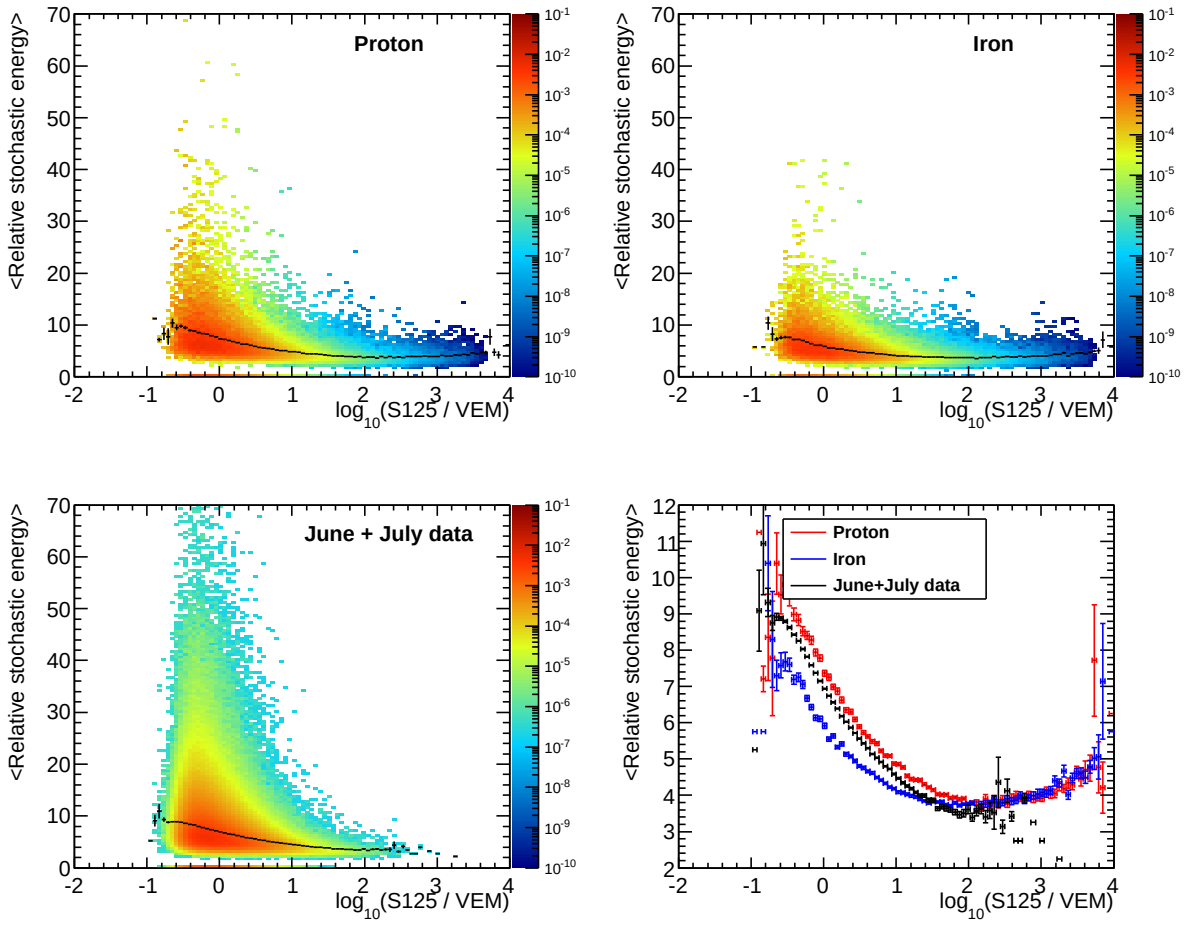

Figure 5.44: Distribution of the average ratio of the energy of the selected stochastics and the average energy loss as a function of S_{125} for proton simulations (top left), iron simulations (top right), data (bottom left) and the mean of the distributions for each S_{125} bin (bottom right), with the error on the mean as error bar. The colour code is the event rate.

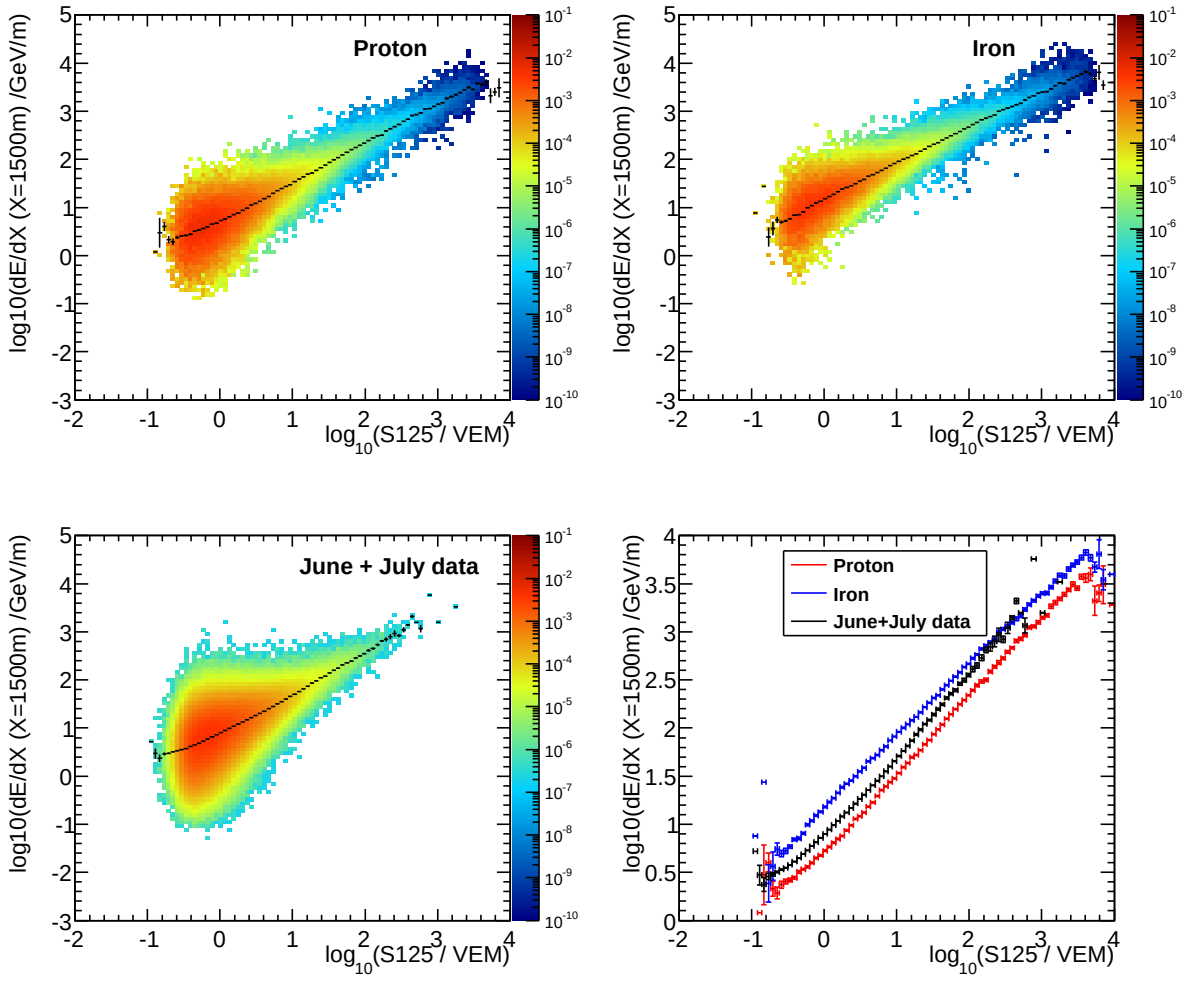

Figure 5.45: Distribution of the average energy loss as a function of S_{125} for proton simulations (top left), iron simulations (top right), data (bottom left) and the mean of the distributions for each S_{125} bin (bottom right), with the error on the mean as error bar. The colour code is the event rate.

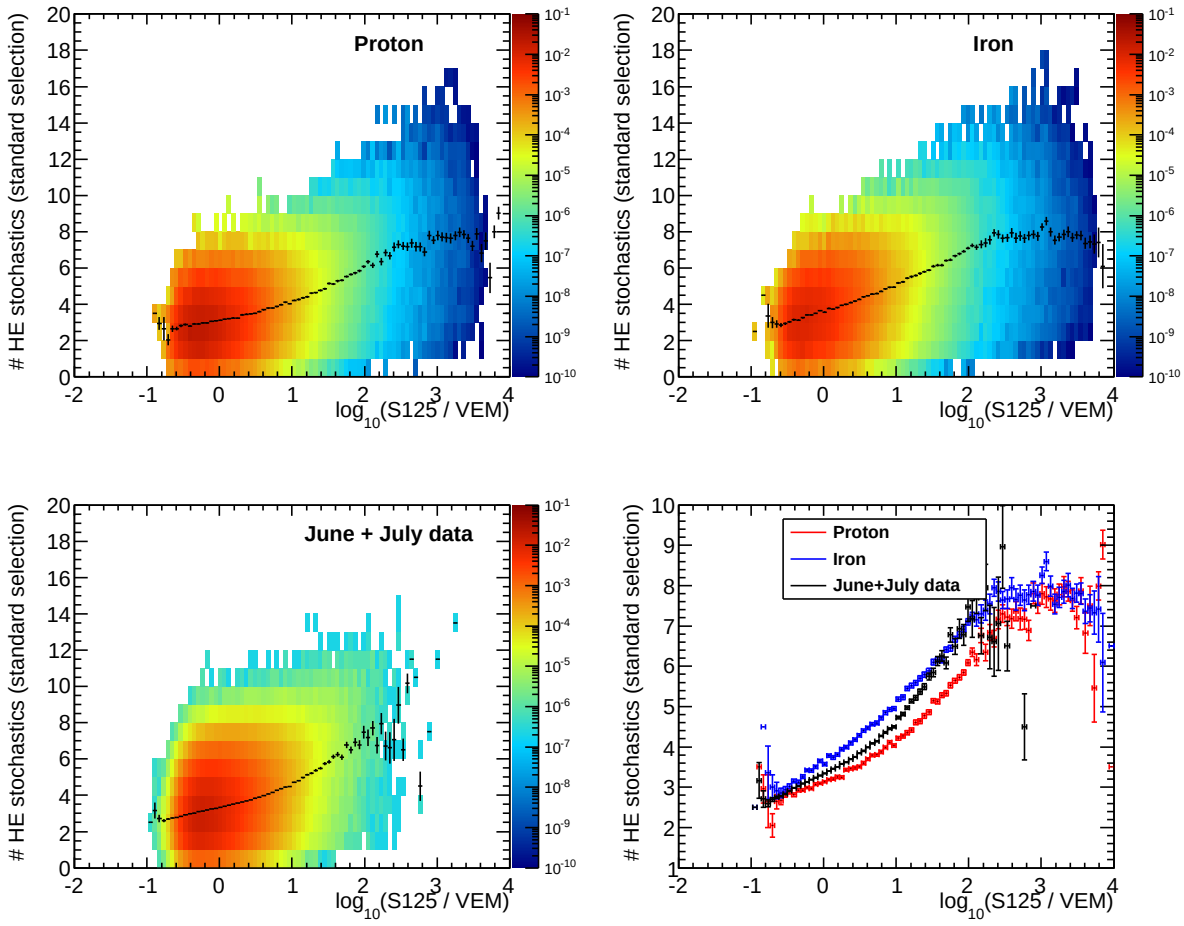

Figure 5.46: Distribution of the number of high energy stochastics selected by the standard selection as a function of S_{125} for proton simulations (top left), iron simulations (top right), data (bottom left) and the mean of the distributions for each S_{125} bin (bottom right), with the error on the mean as error bar. The colour code is the event rate.

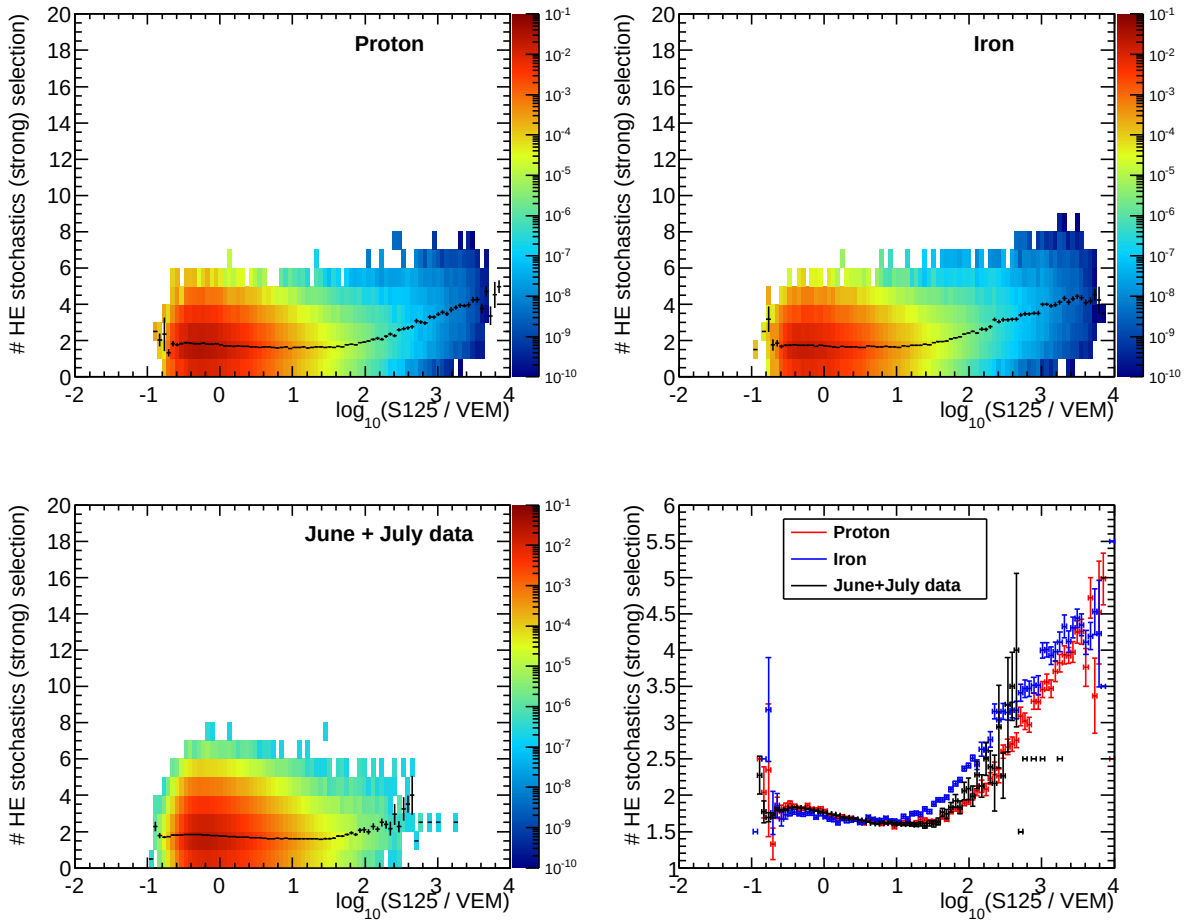

Figure 5.47: Distribution of the number of high energy stochastics selected by the strong selection as a function of S_{125} for proton simulations (top left), iron simulations (top right), data (bottom left) and the mean of the distributions for each S_{125} bin (bottom right), with the error on the mean as error bar. The colour code is the event rate.

Chapter 6

Analysis

My analysis/The analysis presented in this thesis aims to measure the differential primary cosmic ray flux or the cosmic ray energy distribution independent of any composition assumption. In addition I want to measure the average composition spectrum in the form of a mean log mass $\langle \log A \rangle$ as function of the primary energy. Because the average composition can be caused by many different combinations of individual mass groups, we will try to determine the individual energy spectra of four different mass groups.

To achieve this goal, we first need to determine the relation between the primary energy and primary mass dependence of a set of well chosen reconstructed variables. The variables acquired by IceTop reconstruction are the shower size S_{125} and the zenith angle θ. From the IceCube energy loss reconstruction we have the average energy loss at a slant depth of 1500 m, $\mathrm{d}\,E_\mu/\,\mathrm{d}\,X$ and the number of selected high energy stochastics from the standard and strong selection. Because these variables showed good data/MC agreement, demonstrated in the previous chapter, we can apply the energy and mass dependence known in simulation to data.

All five variables depend both on the primary energy and primary mass. To disentangle the energy and mass a neural network is used. After running the data through the network, trained on a fraction of the simulations, the primary energy can directly be extracted. On the reconstructed mass from the neural network, there is a large uncertainty. A method called template fitting, which uses the shapes of the mass distribution per reconstructed energy, is constructed to determine the individual contributions of each of the four simulated mass groups (proton, helium, oxygen and iron) and calculate the average composition in $\log A$.

6.1 Artificial Neural Network

The main properties of air showers that are used for the primary energy and composition measurement are the number of electrons N_e to which S_{125} is related, and the number of muons in IceCube N_μ to which the energy loss variables are sensitive. Fig. 6.1 demonstrates their relation with primary energy and primary mass. The left plot clearly shows a non-linear relation for the primary energy dependence on electron number for the different primary types (here proton, oxygen and iron). This means that for each primary type a different non-linear function is needed in the $N_\mu - N_e$ plane to translate N_e to primary energy. This also means that the lines that separate each set of points of the different types from each other, are different for the different primary energies. The right plot of Fig. 6.1 is the detector response analogue of the left plot. Here, the simulations used for my analysis range continuously between 10 TeV and 3.5 PeV and for clarity only proton and iron are shown. The same non-linearity is visible as in the left plot, illustrated by the contour lines in primary energy and the dashed lines to guide the eye, but is more prominent at low energies. The separation between proton and iron in this 2-type version, depends on the primary energy. Furthermore, the major advantage of a coincident analysis where different properties of the air shower are measured by different sub-detectors is clear.

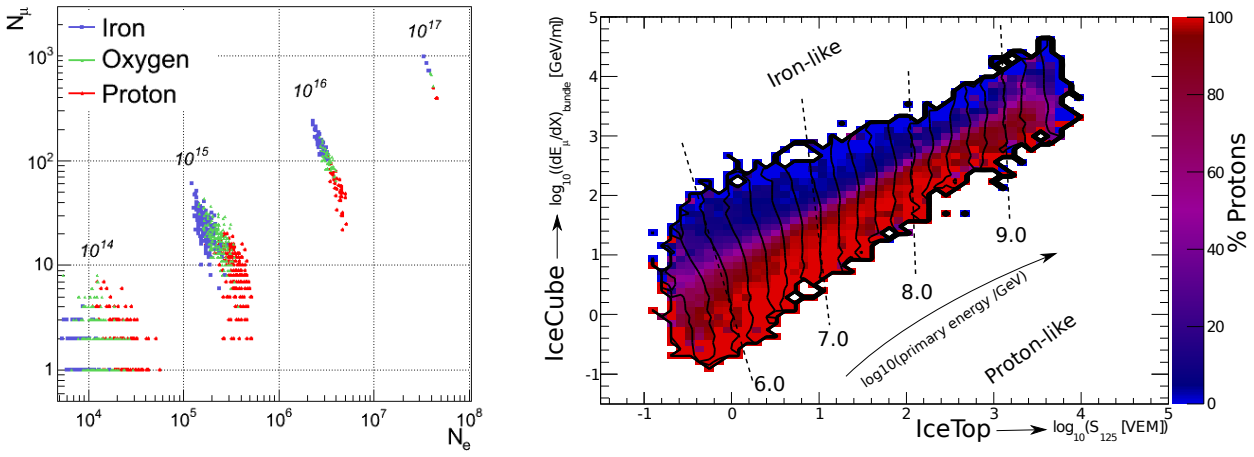

Figure 6.1: **Left**: Number of electrons as a function of the number of muons with energies above 500 GeV for simulated proton (red), oxygen (green) and iron (blue) air showers at fixed energies. **Right**: Average muon bundle energy loss, reconstructed in IceCube, as a function of the shower size S_{125}, reconstructed in IceTop, for proton and iron simulations. The contour lines show the boundary of the primary energy bins. The colour code describes the fraction of proton showers in each bin.

The reason for the non-linearity is that the rate of increase in N_e is larger for iron showers than for proton showers, because proton showers are approaching their shower maximum at the detector level (proton $X_{\max}$ is at the atmospheric depth of the detector, 692 g/cm^2, at about 100 PeV (see Fig. 2.3)). At higher energies, proton showers have not yet reached their shower maximum, which reduces the rate of increase in N_e relative to iron showers which are past their shower maximum. This creates the effect that the iron points in Fig. 6.1 have a larger increase in N_e than the proton points for higher energies.

At low energies, there is no distinction anymore between different primary types based on their muon multiplicity as expected from the Elbert formula (Fig. 1.25). The anti-correlation between muon multiplicity and electron multiplicity for a fixed cosmic ray energy is due to the conservation of energy. If more energy goes to the production of electrons, less energy can go to the muons.

In this analysis, five variables depend on primary energy and primary mass in a non-linear fashion. The analysis therefore exists in solving the set of five unknown non-linear equations in two variables, primary energy and primary mass. This mathematical problem is called multi-target regression. Because there is no analytical expression from theory that relates our input variables to primary mass and primary energy, the set of non-linear equations are determined from simulation. This is called *machine learning*.The software package TMVA [186] has a large variety of multi-variate algorithms. As can be seen from Fig. 6.2, only three methods can perform a multi-target regression. Based on the performance, robustness and speed of the algorithm (see Table 6 in [186]), the artificial neural network (NN) was chosen as analysis techique.

In [163, 16], the neural network technique (and template fitting procedure) is developed for the measurement of the cosmic ray composition of one month of IT-40/IC-40 data in the energy range between 1 PeV to 30 PeV. Here, I will build further on the experience gained during that analysis and extend the technique to more than two input variables, a larger primary energy range and larger scan of different network types for optimal performance. A major advantage is the availability of a larger set of simulations (see Chapter 3) which makes the neural network more robust.

MVA method	Classi-fication	Regress-ion	Multi-class/target classification	Multi-class/target regression	Treats event weights: positive	Treats event weights: negative	Variable ranking	Standalone response class	Help messages	Custom macros
Cut optimisation	•	○	○	○	•	○	○	○	•	○
Likelihood	•	○	○	○	•	•	•	•	•	•
PDE-RS	•	•	○	○	•	•	○	○	•	○
PDE-Foam	•	•	○	•	•	•	○	○	•	•
k-NN	•	•	○	•	•	•	○	○	•	○
H-Matrix	•	○	○	○	•	○	•	•	•	○
Fisher	•	○	○	○	•	○	•	•	•	○
LD	•	•	○	○	•	○	•	•	•	○
FDA	•	•	○	○	•	○	○	•	•	○
MLP	•	•	○	•	•	○	•	•	•	•
TMlpANN(*)	•	○	○	○	•	○	○	•	•	○
CFMlpANN	•	○	○	○	○	○	○	○	○	○
SVM	•	○	○	○	•	•	○	•	•	○
BDT	•	•	○	○	•	•	•	•	•	•
RuleFit	•	○	○	○	•	○	•	•	•	•

(*)Not a generic TMVA method – interface to ROOT class `TMultiLayerPerceptron`.

Figure 6.2: Properties of all multivariate analysis techniques implemented by the TMVA software package.

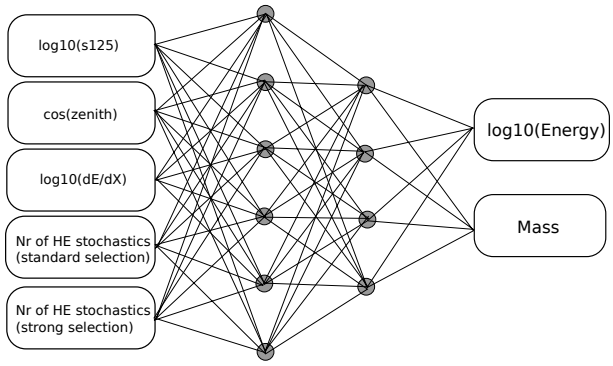

Figure 6.3: The neural network architecture of the best performing neural network. It maps five input variables onto two output variables using two hidden layers with respectively six and four neurons. It is therefore called a 5-6-4-2 network.

6.1.1 Method

An artificial neural network is basically a mapping from a space of input variables x_i onto a multi-dimensional space of output variables y_i. The simplest case of a neural network with one output variable y_0 is a so-called *single layer perceptron*:

$$y_0(\boldsymbol{x}) = \rho(\boldsymbol{x}) = \alpha \circ \kappa(\boldsymbol{x}) = \alpha(w_0 + \sum_{i=1}^{n} w_i x_i), \tag{6.1}$$

where n is the number of inputs. The *neuron response function* ρ maps the neuron inputs onto the neuron output. It exists first of a mapping of n input neurons onto the intermediate state of one neuron by the *synapse function* κ. Afterwards the result is mapped by the *neuron activation function* α onto the neuron output. This system can then be extended by adding one or more so-called hidden layers in between the *input layer* and the *output layer* to a *multi-layer perceptron* (MLP), illustrated by Fig. 6.3. That network architecture has five input nodes, two hidden layers of six and four neurons respectively and two output nodes. In an MLP, only direct connections between the neurons of one layer and the next layer are allowed.

For an MLP, Eq.6.1 is the formula for each neuron as a function of the connected input neurons, which

can be from the NN input or from the hidden layers [186, 187]. The main idea to use a neural network for finding the non-linear mapping between the five reconstructed input variables to primary energy and primary mass stems from the *Universal Approximation Theorem*. It states that any continuous, multivariate function can be approximated to any desired degree of accuracy by a single hidden-layer feed-forward[1] neural network employing sigmoid type activation functions [188, 189, 190]. This means that a failure of the function mapping is caused by a bad choice of weights and/or an inadequate number of hidden neurons.

For a set of data where both the input $\boldsymbol{x}$ and the output $\boldsymbol{y}$ are known, the weights w_i are fitted. This procedure is called training the network. For our purpose, simulations where we know the primary mass and energy are used. While the network is trained to one set of data, the fitted function could be so specific to the training data that it does not describe an independent sample. This overspecification of the network to the training data is called overtraining and should be prevented by monitoring an independent set of *test data*. At some point during the minimization the fit function will be less good for the test data than for the training. At that point, the training should be stopped.

Even though in principle, a very large set of neurons in one hidden layer should result in a network that describes the functional mapping, the training of such a large network is cpu intensive. Potentially a similar performance can be achieved by a smaller network with more hidden layers. This could also give a more robust network. The trick in a neural network analysis exists in finding the network architecture, that both fits the training and test data best, is most robust and does not require a too large processing time. The procedure for choosing the best network is explained below.

6.1.2 Procedure

The full L4 processed MC sample after all cuts is split in three parts. Half of the sample is used for the training and for testing the network (the *network sample*), . The other half (the *verification sample*) is used for making the template histograms to which data is fit, discussed in the next Section. The MC data used for the network, is again split in two. A little bit more than 50% of the network sample or 74357 events is used to train the network (the *training sample*). The remaining 67399 events (the *test sample*) serve to test the network and to select the network architecture and optimal activation function based on the network performance. The three MC samples are chosen in such a way that they contain an equal mixture of each of the four primary types (p, He, O and Fe) and cover the full energy range. The choice to keep 50% of the total MC sample as independent verification sample was also done in [16]. It guarantees that the template histograms will be unbiased and robust. The creation of an extra sample for the actual analysis is highly recommended by the TMVA developers [191].

The different resample area and the different number of generated showers in each decade of energy result in more events at low energy than at high energy. To make sure the NN training is not trained better to lower energies where more data are available, I used a weighted training. The weighted energy distribution is uniform in the common logarithm of the primary energy.

The input variables are $\log_{10}(S_{125}), \log_{10}(\mathrm{d}\,E/\,\mathrm{d}\,X), \cos\theta$, the number of selected stochastics with the standard selection and the number of stochastics with the strong selection. Four of them were discussed in Chapter 4. From [192, 170] we know that the relation between S_{125} and primary energy depends on the zenith angle. The output variables are $\log_{10}(E_0)$ and A. In contrast to the approach in [16], the network is trained to be able to fit the mass A instead of $\log A$ because ideally we want to measure the primary mass for each event, not its natural logarithm. Both the input variables and the output variables are linearly scaled to lie within $[-1, 1]$. This renders the minimization processes for finding the weights w_i more effective [186].

The error that the neural network fitting procedure tries to minimize by looking for best set of weight w_i

[1] Feed-forward neural networks means that the network works only in one direction, from input through the hidden layers to the input.

is the mean squared error (MSE):

$$MSE(\boldsymbol{x_1}, \boldsymbol{x_2}, ..., \boldsymbol{x_N}|\boldsymbol{w}) = \sum_{b=1}^{M}\sum_{a=1}^{N}\frac{1}{2}(y_{NN,ab} - \hat{y}_{ab})^2, \tag{6.2}$$

where $\boldsymbol{w}$ denotes the ensemble of adjustable weights and $\boldsymbol{x_i}$ are the N training events. The number of output neurons is M ($M = 2$ in my analysis). The desired value for output neuron b and event a is $\hat{y}_{ab}$ while the NN calculation gives $y_{NN,ab}$. The minimization algorithm utilized here is the BFGS algorithm (references in [186]). The other available minimization algorithm, called *back propagation*, was attempted for a few networks but exhibited a worse performance. Other TMVA users had a similar experience with a bad performance of back propagation for regression [193].

Because a large number of weights w_i need to be fit, a random and importance event sampling approach is followed. During the first 5000 of 10000 minimizer iterations (also called cycles or epochs), only a random selection of 60% of the training data is utilized. The probability for the same selection of events to be re-used for the next iteration decreases if the error of the test dataset decreases. This way the weights are reoptimized more for the worst fitting subset of the training sample. After the training converged on the random and importance sampled data, the training continues on the full training set. This sampling method speeds up the training for large samples and may also increase to robustness of the algorithm with respect to convergence to a local minimum [186]. To make the fitting procedure less vulnerable to a few outliers, the MSE error is only calculated for the mean 90% of the data.

Finally, the training ends when either the MSE error of the training converges or when 15 consecutive overtraining tests fail. If the MSE of the test data increases, then this signals overtraining and the overtraining test fails.

6.1.3 Selection Procedure

The neural network training procedure is performed with the settings from previous Section fixed. To find the best performing neural network two sigmoid type activation functions are tried, namely the sigmoid function $\alpha(x_i) = \frac{1}{1+e^{-x_i}}$ and the tanh function $\alpha(x_i) = \frac{e^{x_i}-e^{-x_i}}{e^{x}+e^{-x_i}}$. For the output nodes, however, a linear activation function is used based on the theory for function approximation by regression NNs [188, 189, 190]. The weighted sum is the synapse function κ employed for all networks, shown by Eq. 6.1. As mentionend earlier the largest unknown for neural networks is the network architecture. Because the training and testing of a particular network is relatively fast (15 minutes to a few hours), many networks are trained and tested in parallel on a cluster. Afterwards the best performing network out a large set of networks is selected.

Even though the five proposed input variables are not very correlated and depend on primary energy and primary mass, both 2-input networks ($\log_{10}(S_{125})$ and $\log_{10}(\mathrm{d}\,E/\,\mathrm{d}\,X)$), 3-input networks ($\cos\theta$ as extra input), 4-input networks (number of standard selected HE stochastics as extra input) and 5-input networks are attempted. Three groups of network structures are explored: one hidden layer, two hidden layers and three hidden layers. The number of neurons chosen is relative to the number of input neurons and for few hidden layers a larger number of neurons are tried. When more hidden layers are used, the relative number of neurons in each layer is not too high to prevent high computation times and too complex network architectures. This sums to a total of 207 networks for each of the two activation functions and for each number of inputs (about 1600 networks in total).

The goal is to find the network that can best reconstruct the primary energy over the whole energy range for all primaries and has a minimal energy resolution. The second criterium is that it can reconstruct the primary mass as accurate as possible over the whole energy range. As we will do a template fitting afterwards due to the large width of the distribution in the NN mass space (due to intrinsic fluctuations), this means the shapes of the four neural network mass output distribution per reconstructed energy (also called *template histograms*) templates should be as distinct as possible over the whole energy range.

The selection procedure I developed is the following:

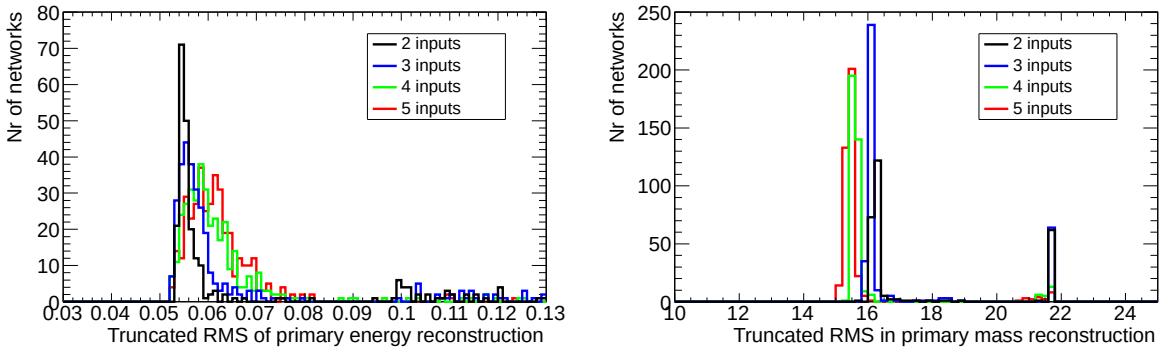

Figure 6.4: Distribution of the truncated RMS of the primary energy reconstruction (left) and primary mass reconstruction (right) for NNs with a different number of inputs.

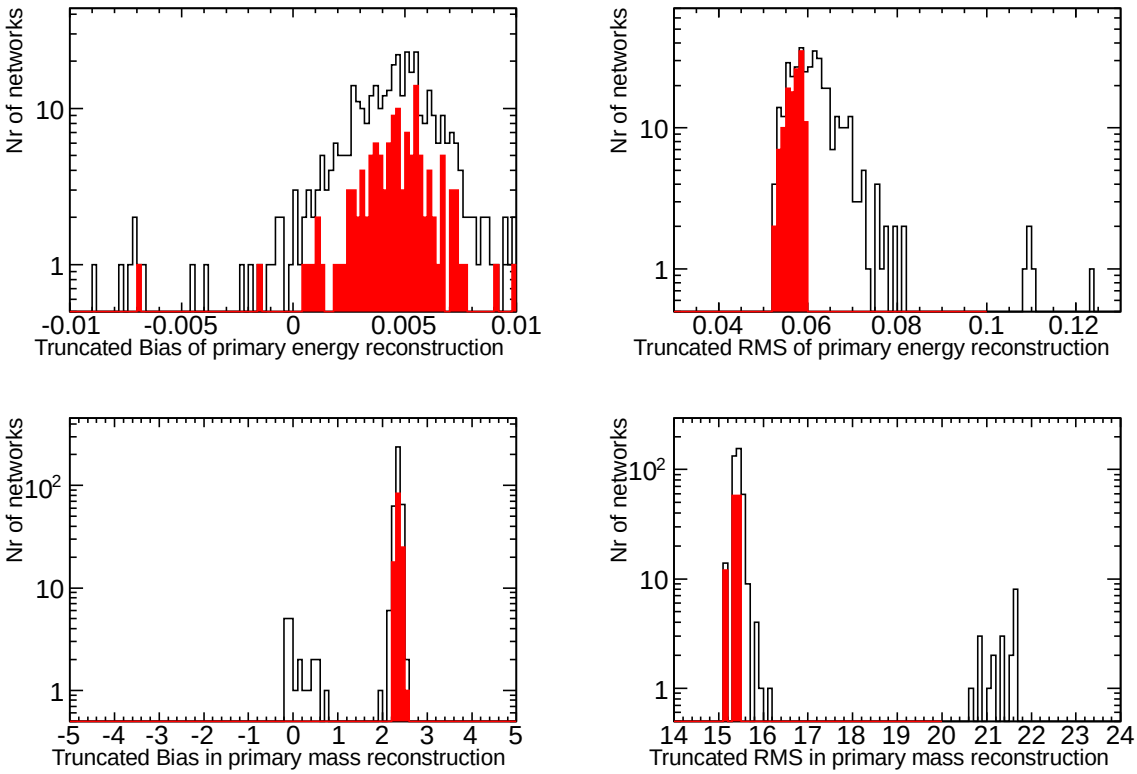

Figure 6.5: Distribution of truncated bias (left) and RMS (right) for both primary energy (top) and primary mass (bottom) reconstruction for 5-input networks before (black) and after the first cut (red).

1. A global selection based on the overall performance (integrated over all energies and primaries) performance for primary energy E_0 and mass A reconstruction. It is the global performance (see Eq.6.2 for MSE) that essentially is being minimized during the training of the NN. The first cut on the RMS calculated without the two sigma outliers, called truncated $\mathrm{RMS_T}$ greatly reduces the number of potentially good networks and is still a conservative cut. The reason for this cut is that we want the distributions for energy and mass reconstructions to be as narrow as possible to result in good energy resolutions and mass separations. The distribution of the truncated RMS for both energy and mass is shown in Fig. 6.4 and compared between the networks with a different number of inputs. There

are more networks with a smaller $\mathrm{RMS_T}(E_0)$ when there are less inputs in the network, but the mass reconstruction becomes worse. Therefore, for each group of networks a different cut is chosen. Only at the very end of the selection procedure a decision is made on the optimal number of inputs:

- 2-input NN: $\mathrm{RMS_T}(E_0) < 0.0555$ and $\mathrm{RMS_T}(A) < 16.35$: 122 networks remain.
- 3-input NN: $\mathrm{RMS_T}(E_0) < 0.0565$ and $\mathrm{RMS_T}(A) < 16.05$: 121 networks remain.
- 4-input NN: $\mathrm{RMS_T}(E_0) < 0.0585$ and $\mathrm{RMS_T}(A) < 15.65$: 127 networks remain.
- 5-input NN: $\mathrm{RMS_T}(E_0) < 0.0595$ and $\mathrm{RMS_T}(A) < 15.45$: 128 networks remain.

The effect of the cuts are illustrated in Fig. 6.5, where the distributions of truncated bias and RMS for both energy and mass reconstruction are shown for all 5-input network. The distributions for the selected networks are displayed in red.

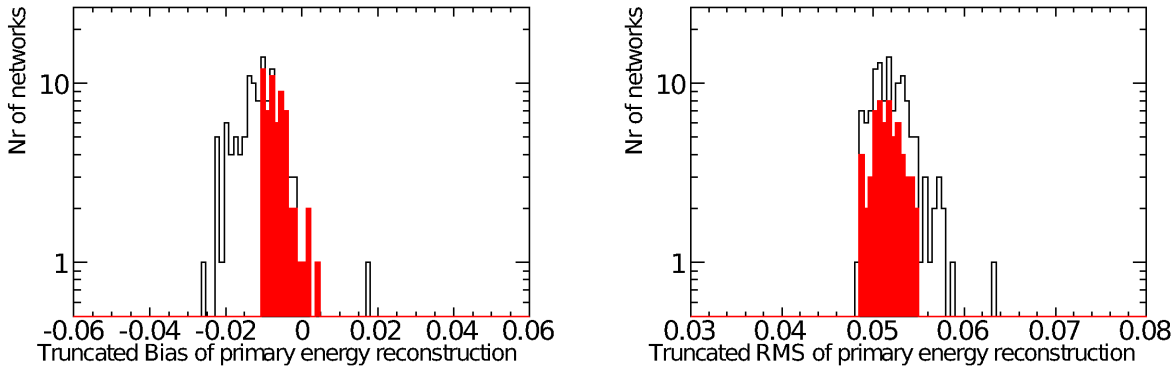

Figure 6.6: Distribution of the truncated bias (left) and RMS (right) for primary energy reconstruction, calculated in the energy range between 6.4 and 9.0 in $\log_{10}(E_0/\mathrm{GeV})$, for 5-input networks before (black) and after the second cut (red).

2. The overall behaviour of the NN could have been influenced by the energy region below the energy threshold of 6.4 in $\log_{10}(E_0/\mathrm{GeV})$ or beyond 1 EeV. There we do not expect a good performance because the analysis is not optimized for those energies. Therefore I require the truncated bias and resolution of the reconstructed energy in the relevant energy region from 6.4 to 9.0 to be small as second cut. For all networks I chose the cut: $\mathrm{RMS_T}(E_0) < 0.055$ and the absolute value of the truncated bias $(E_0) < 0.011$. The remaining networks are:

   - 2-input NN: 29 networks remain.
   - 3-input NN: 60 networks remain.
   - 4-input NN: 58 networks remain.
   - 5-input NN: 61 networks remain.

   On Fig. 6.6 this second cut is demonstrated for the 5-input networks by the red distribution in the truncated bias and RMS of the energy reconstruction.

3. The reconstructed mass has a large spread which is visible on Fig. 6.5. Hence, we cannot accurately reconstruct the mass of individual events. In the next Section, a method is discussed that fits the shapes of the neural network mass distributions for each type to the data. An important property of the NN is thus that the shape of the mass distributions for all four primary mass groups are very different from each other per reconstructed energy bin. Therefore, a manual inspection of the shapes of these so-called *template histograms* of the previously selected networks is performed. The networks

with the most distinct template histograms per energy bin over the whole energy range are selected. During the manual inspection of the template histograms, it became apparent that the high energy templates were most difficult to differentiate between the different types. Thus, a good performance of the template histograms at high energies formed an extra criterium for the selection of a particular network. Additional criteria that are employed to reduce the number of networks further are the energy resolution as a function of the primary energy, which should be as small as possible. The energy reconstruction is required to have a small bias which is as least energy dependent as possible. The resulting best performing networks are:

- Best 2-input NN: 2 - 5 - 2 - 4 - 2 network with a sigmoid neuron activation function.
- Best 3-input NN: 3 - 6 - 2 - 2 - 2 network with a sigmoid neuron activation function.
- Best 4-input NN: 4 - 7 - 6 - 3 - 2 network with a sigmoid neuron activation function, but this network would need a serious energy bias correction.
- Best 5-input NN: 5 - 6 - 4 - 2 network with a tanh neuron activation function and the 5 - 12 - 2 - 2 network with a sigmoid neuron function.

4. Occam's Razor : Choose the simplest NN structure that has comparable performance with other more complex networks.

The best overall performing network is the 5-input 5-6-4-2 network, because both the energy resolution and the bias as the NN mass distributions are over the whole energy range very good, which is discussed more in detail in the next section. In addition the NN architecture is quite simple.

6.1.4 Performance

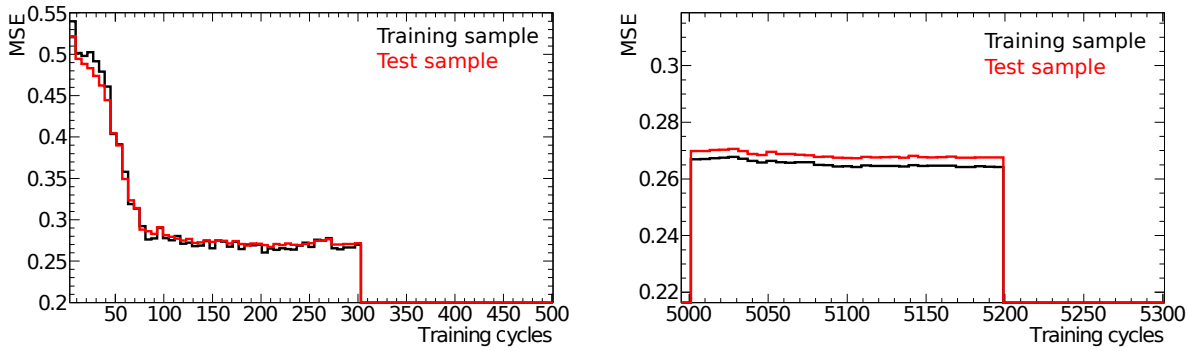

Figure 6.7: MSE minimization procedure of the 5-6-4-2 network for the training (black) and testing (red) sample. **Left**: The convergence of the random and importance sampled training data. **Right**: Convergence of the full training data.

The minimization process is demonstrated by Fig. 6.7 for the selected best performing neural network, a 5-input network with a 5-6-4-2 architecture and a tanh neuron activation function. In the random and importance sampling phase that utilizes 60% of the training sample, the minimization converges after 300 cycles. Using the weights from the sampling phase as an initial seed for the training phase with the full training data, the network converges fast after 200 iterations. The difference between the MSE of the training sample and test sample is small and does not start to increase again at the last cycles. Therefore is the network is not overtrained.

The energy resolution of the reconstructed NN energy for an primary energy spectrum with an E^{-3} power law behaviour, expected for the primary flux beyond the knee at 3 PeV, and above the threshold of this

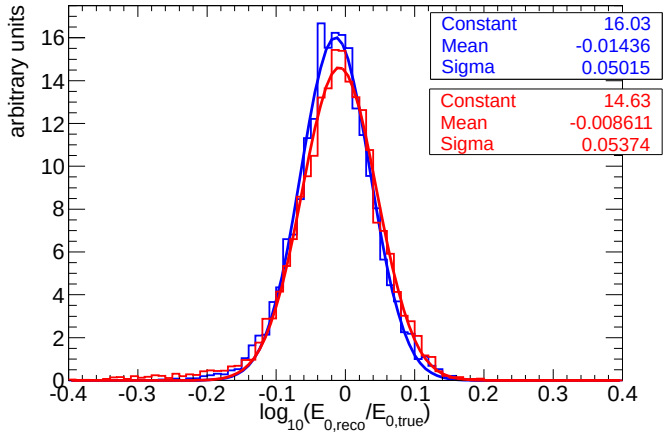

Figure 6.8: The common logarithm of the ratio between reconstructed NN energy and true energy to quantify the energy resolution and bias for proton (red) and iron (blue) simulations above a $\log_{10}(E_0/\mathrm{GeV})$ of 6.4. For this global resolution, both distributions are weighted to an E_0^{-3} spectrum.

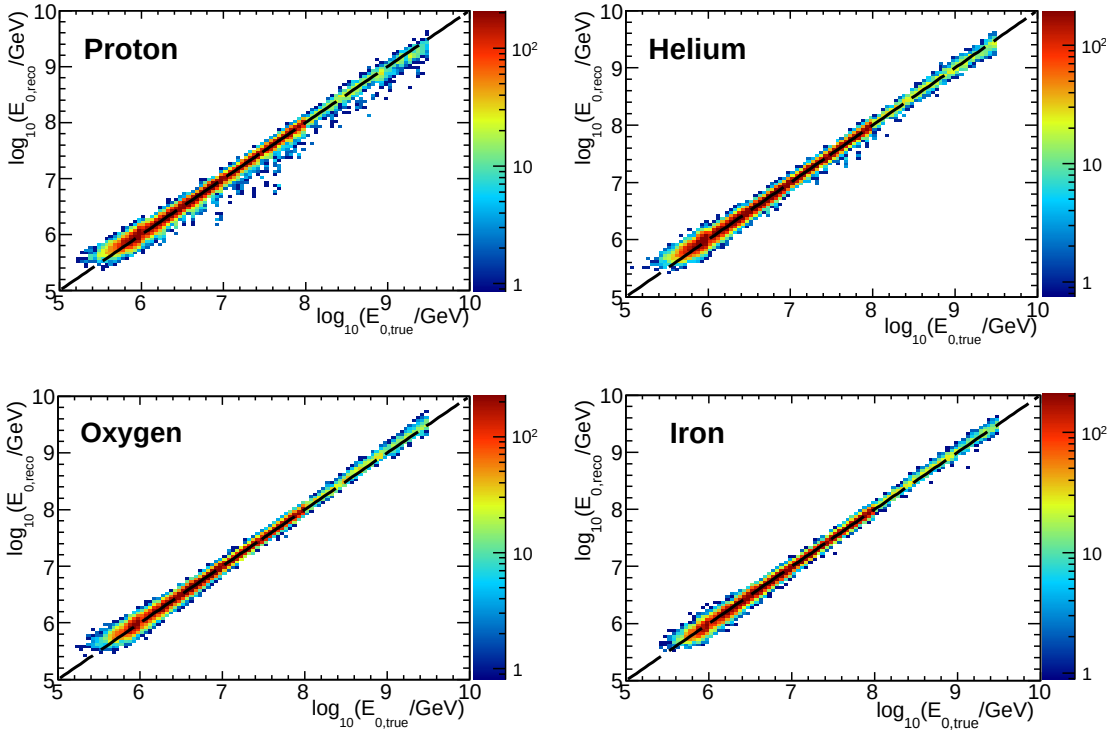

Figure 6.9: Energy reconstructed by the NN as a function of the true energy for proton simulations (top left), helium (top right), oxygen (bottom left) and iron (bottom right). The dashed line denotes where reconstructed and true energy are equal. The colour scale quantifies the number of simulated events.

analysis (6.4 in $\log_{10}(E_0/\mathrm{GeV})$) is shown in Fig. 6.8. The energy resolution is very good: 0.050 (11%) for iron showers and 0.053 (12%) for proton showers. The bias of the reconstructed energy is very small and the difference between the proton and iron energy reconstruction is 0.0057 on logarithmic scale (1.3%). The improvement over the global energy resolution from [16] (13% for proton events and 14% for iron events) is

due to the slightly higher energy threshold of this analysis. The difference between proton and iron bias is also much smaller than in the previous analysis (5.3% from Fig. 9(d) in [16]).

In Fig. 6.9 the reconstructed energy is plot as function of the true, simulated energy. It exhibits more details about the energy reconstruction over the whole primary energy range for each simulated primary type. For all primaries the points are centered around the dashed line where the true energy equals to the reconstructed energy. At low energy and less prominent at the highest energy the distributions becomes wider and gives a worse energy resolution.

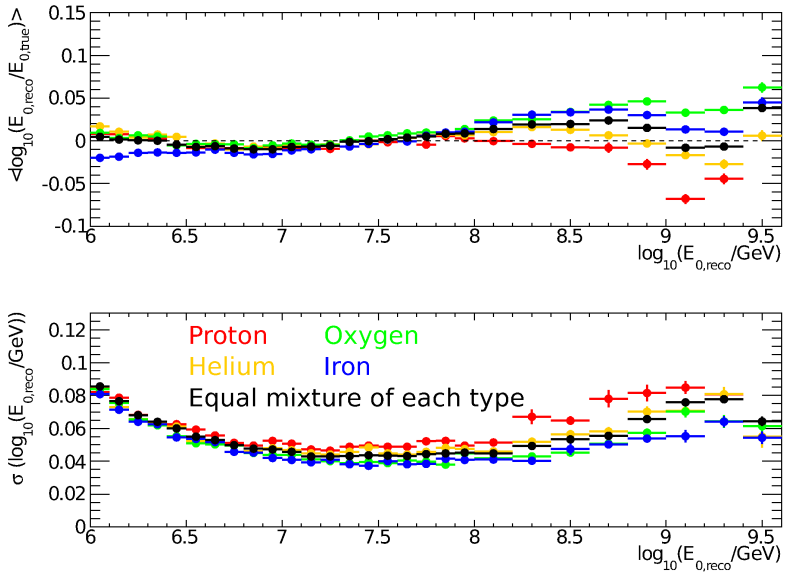

Figure 6.10: Energy reconstruction bias (top) and resolution (bottom) as a function of the reconstructed energy for the different primary types and for an equal mixture of each type.

The energy dependence for the NN energy bias and NN energy resolution of both proton and iron showers is shown on Fig. 6.10. The energy resolution (bottom plot) is between 9% (for iron showers at around 7.5 ($\sim$ 20 PeV) and 18% with the worst resolutions below my energy threshold and at the highest energies. Heavier primaries have a better energy resolution because of their lower intrinsic shower fluctuations. The increasing energy resolution beyond 8.0 (100 PeV) is partially be caused by the increasing angular resolution which creates an extra smearing in S_{125}. The energy bias, shown on the top plot of Fig. **??**, is much smaller than the energy resolution, which determines our binning choice for the energy spectrum, over the whole energy range. The differences between the energy bias of each primary specie is small up to a few hundred PeV. Because the IceCube variables become less sensitive to the primary mass, discussed below in more detail, the energy conversion becomes more mass dependent for higher energies. Motivated by the energy resolution, the energy bins chosen for the primary energy spectrum measurement are larger. Therefore the increasing differences in the bias between different primaries, stays small relative to the energy bin width and is not worrysome. Above 1 EeV the energy bias dependence on the primary type becomes too large and limits the energy range over which the analysis is optimal.

Hence, this neural network provides a high quality primary energy estimator. The energy resolution is comparable to the energy resolution obtained by the IT-73 analysis that only uses S_{125} and the zenith angle θ for the determination of the primary energy [170]. This means the primary energy is dominated by the IceTop variables and their fluctuations. The coincident event analysis presented here, however, results in an energy estimator which is to a high degree composition-independent in contrast to the IT-73 analysis. The reason is that extra composition-sensitive information measured by the IceCube, is used by the neural network to obtain the primary energy.

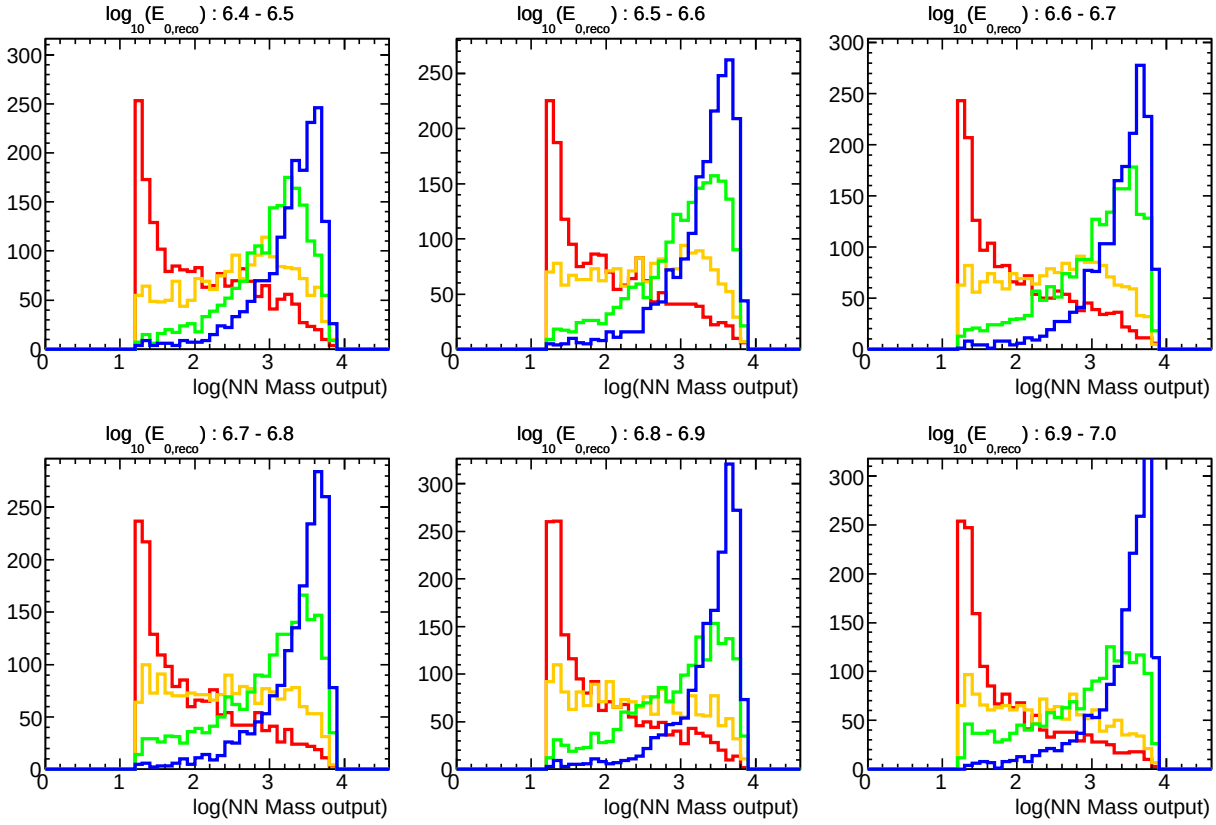

Figure 6.11: Distribution of the natural logarithm of the neural network mass output in the energy range between 6.4 and 7.0 in $\log_{10}(E_{0,\mathrm{reco}}/\mathrm{GeV})$. The y-axis represents the the number of simulated events for proton (red), helium (orange), oxygen (green) and iron (blue).

The performance of the selected NN for mass reconstruction is demonstrated by Figs. 6.11 to 6.14. They show the distributions of the natural logarithm of the reconstructed mass for the different primary types per reconstructed energy bin. As mentioned before, these do not peak strongly at the right masses and do not have a small spread. They do exhibit four distinct, very different shapes in each of the energy bins over the whole energy range. The template histograms are plotted in the natural logarithm because the four simulated types (proton, helium, oxygen and iron) are equidistant in logarithm space, but not in linear space. Thus, the template histograms are expected to be more distinct in logarithmic space. From 8.6 onwards it becomes a bit more difficult to separate between the different primary types, expected due to the worse energy loss resolution at high energies (see right plot of Fig. 4.23), but up to 9.0 (1 EeV) the templates histograms are still different. Above 1 EeV on the otherhand the overlap is too large. This determines the upper bound to where my analysis is sensitive. Fortunately, in a one square kilometer array the number of contained events above 1 EeV is very small, even over a few years. So the high end of the energy range of 1 EeV is both limited by the analysis and by the data statistics.

The different reconstructed energy bin width below 100 PeV and above 100 PeV are due to the lower simulation statistics above 100 PeV. This creates higher fluctuations and makes it more difficult to distinguish between the different types within the Poisson fluctuations on the number of simulated events.

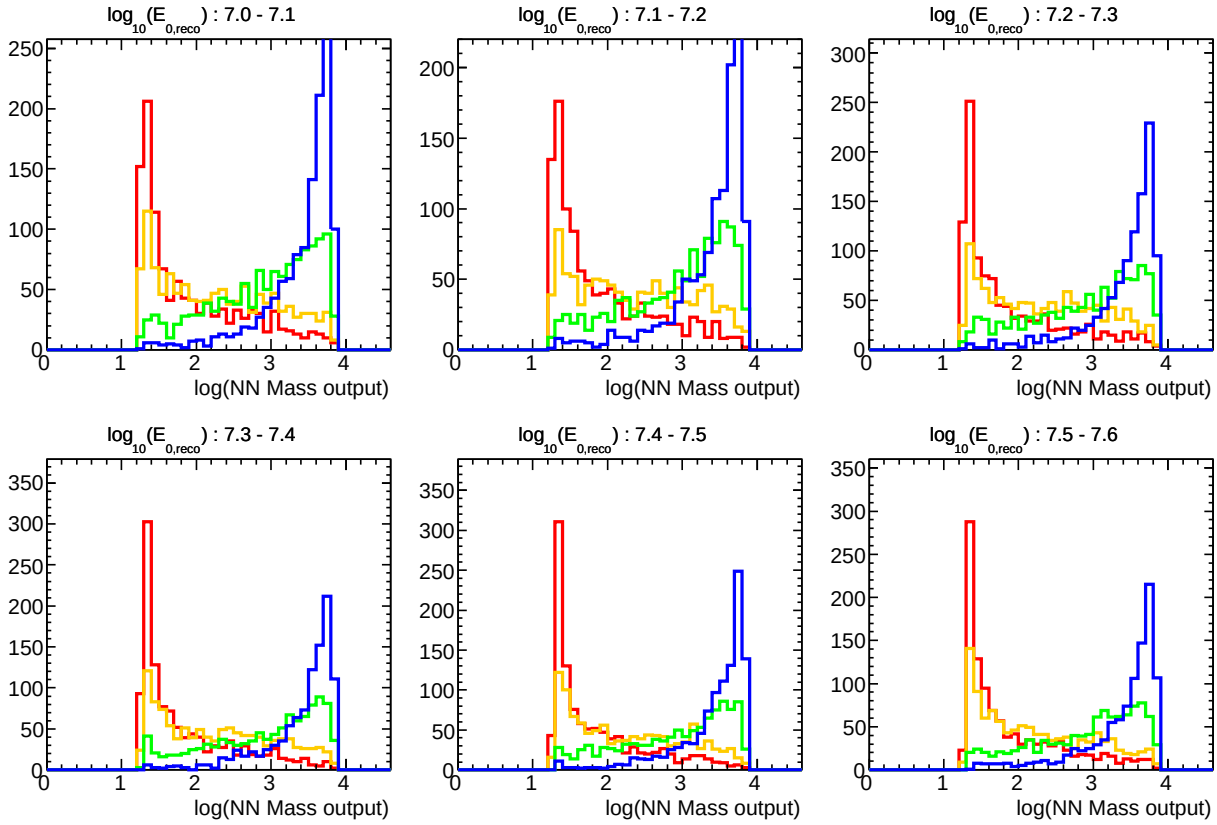

Figure 6.12: Distribution of the natural logarithm of the neural network mass output in the energy range between 7.0 and 7.6 in $\log_{10}(E_{0,\mathrm{reco}}/\mathrm{GeV})$. The y-axis represents the the number of simulated events for proton (red), helium (orange), oxygen (green) and iron (blue).

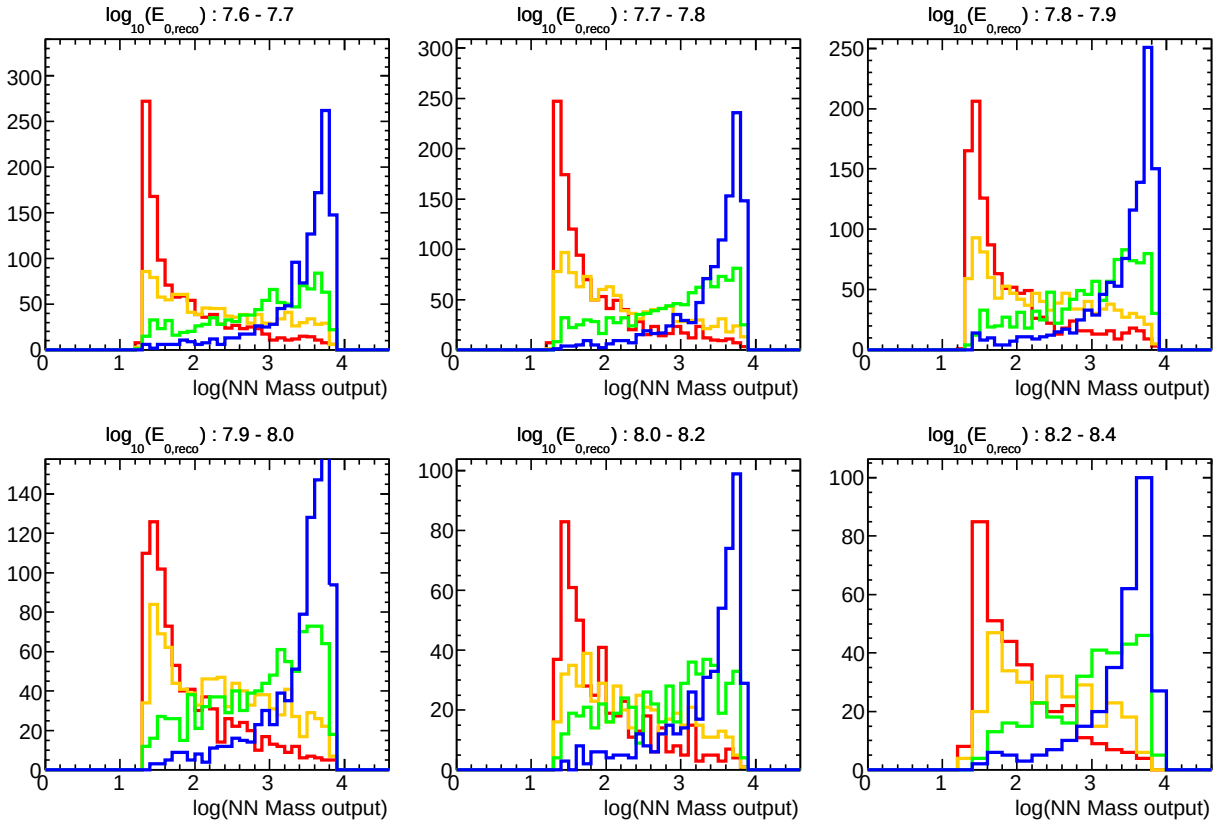

Figure 6.13: Distribution of the natural logarithm of the neural network mass output in the energy range between 7.6 and 8.4 in $\log_{10}(E_{0,\mathrm{reco}}/\mathrm{GeV})$. The y-axis represents the the number of simulated events for proton (red), helium (orange), oxygen (green) and iron (blue).

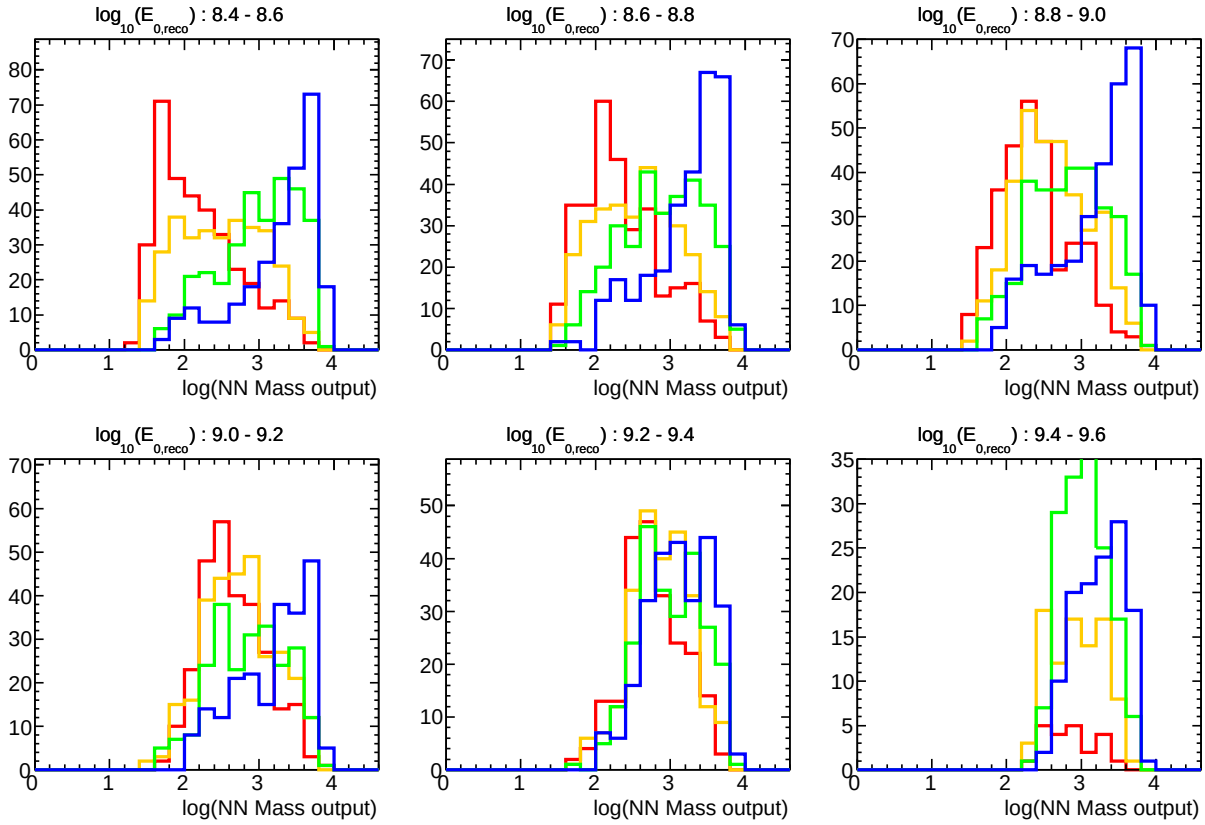

Figure 6.14: Distribution of the natural logarithm of the neural network mass output in the energy range between 8.4 and 9.4 in $\log_{10}(E_{0,\mathrm{reco}}/\mathrm{GeV})$. The y-axis represents the the number of simulated events for proton (red), helium (orange), oxygen (green) and iron (blue).

6.2 Template Fitting

The reconstructed mass from the neural network is not a good primary mass estimator because of the bias and the large spread of the mass distribution (see Figs. 6.11 to 6.14). The large spread is caused by the intrinsic shower fluctuations in the composition-sensitive observables which the neural network could not unfold. Here, an approach, called *template fitting* is used to deduce the individual contributions from the different mass groups based on the shape information of the mass distribution. This means the intrinsic shower fluctuations are exploited in the calculation of the average mass for a certain primary energy.

6.2.1 Method

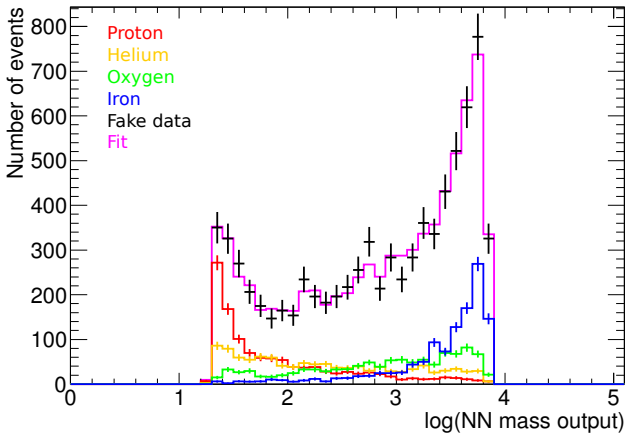

Figure 6.15: The template fitting method attempts to describe the data distribution (black) as a sum of the contributions from the four individual mass templates. Here the data distribution stems from a scrambled MC to test the method and is scaled by factor of 3.5 for clarity. The result of the best fit is shown in magenta.

In [163, 16], a χ^2-fitting method has been developed to fit the data distribution (shown in black in the example on Fig.6.15) as a weighted sum of the proton template, the helium template, the oxygen template and the iron template. The weights are constrained between 0 and 1 and an extra constraint that the weights must sum to one is imposed. This way and after normalizing the histograms, the weights are the fractions that a certain primary type contributes to the data distribution.

The data for a certain reconstructed energy bin is binned again in the NN $\log A$-space, and thus the number of events in a particular bin is often small. Therefore a binned maximum likelihood procedure using Poisson statistics is developed instead for this analysis. In addition to the Poisson fluctuations on the data in a particular bin, the number of events in the same bin for the MC template histograms is also not exact because of limited MC statistics. In [194], a new binned maximum likelihood technique is described which accounts both for the Poisson fluctuations on the data and for the Poisson fluctuations on the MC (the model we use to fit the data). The implementation of this algorithm I used is called *TFractionFitter* [195].

The maximum likelihood procedure has four free parameters called *event fractions* p_j, which only sum to one at the likelihood maximum but are unconstrained elsewhere [196]. The additional free parameters are the number of events in each bin of all four template histograms. These each come from a Poisson distribution. In principle, this creates a complex maximum likelihood space for a minimizer, but in the approach from [194] the event numbers from the template histograms can be calculated analytically. The approach works as following: the values p_j are changed iteratively by the minimizer to maximize the likelihood and during each iteration the event numbers of the MC template histograms that maximize the likelihood for that set of p_j are calculated analytically. The method is demonstrated by Fig.6.15. The fitting procedures scales the MC

template histograms up and down (fitting the p_j's) globally and changes locally the individual bin entries within the Poisson fluctuations until the likelihood is maximal. The result of the fit procedure, shown by the magenta histogram, describes the black data histogram quite well within the Poisson fluctuations on the data as intended.

There are two assumptions that are necessary to relie on the result of the fitting procedure. The first assumption is that the total number of event in each template is not too small so so that the Poisson uncertainty on the total can be neglected, which is explicitly assumed in [194] and would otherwise the method much more complex. The second assumption is that the number of events in each bin should be much smaller than the total number of events in each template to be able to apply Poisson statistics on the bin contents instead of multinomial statistics [195].

6.2.2 Procedure

The template histograms that model the contribution for each primary type in $\log A$-space from MC, are created from the verification sample. One of the properties of a good NN is the characteristic shape of the template histograms for the test set. After comparing the template histograms between the test dataset and the verification dataset, the network proved to be robust because of the good agreement. The simulations were generated according to an E^{-1} spectrum while the true underlying contribution from each of the template shapes should come from an $E^{-2.7}$ flux. The templates are therefore reweighted. After the reweighting, the weighted number of events is corrected in order to have the same number of events as the unweighted templates. A crucial part of the whole technique is to take care that the events in every bin follow Poissonian statistics.

My implementation of the binned maximum likelihood procedure allows for several optimizations that can improve the determination of the mean logarithm of the mass as a function of the reconstructed energy, the main objective of this analysis. First, the number of templates used to fit to the data range from two (p and Fe) to four (all simulated types). It is possible to combine the following templates for a 3-type fit: proton and helium, or helium and oxygen, or oxygen and iron, in addition to the remaining two pure templates. Secondly, the reconstructed energy binning in which each maximum likelihood fit is executed independently can be chosen between 0.1, 0.2 and 0.1 below 100 PeV and 0.2 above. The last choice that needs be made is the number of bins of the templates themselves. Both the number of fitted types as the number of bins for the template histograms, can be different in different energy ranges. The optimal settings are selected through application of the algorithm on known and unknown mixtures of primary masses. The so-called blind data challenge is explained below.

The method uses the MIGRAD algorithm from the Minuit package [173, 174] to minimize the negative binned loglikelihood. It starts from an equal mixture of all chosen types and an initial stepsize of 0.01. To be not affected by not well described tails, the fit is performed between 0 and 4.2 in $\log A$. Empty bins in that range can have a non-zero likelihood and are included. The fit parameters p_i are the event fractions (at the likelihood maximum) and are constrained between 10^{-6} and 1 for a stable fit performance. The flux of low energy showers is much higher than for higher energy showers and gives large numbers of events in each bin of the data histogram. This results in large likelihood values which often have difficulty obeying the standard convergence criterium. The convergence criterium is typically at 10^{-6}, while typical likelihood values for low energies get to $10^7 - 10^8$. Due to double precision the minimizer cannot find any improvement and fail to converge. If the minimizer fails, a new fit is performed with a reduced precision for the convergence iteratively until the fit converges.

From the fitted event fractions, the average mass is calculated:

$$< \log A >= p_H \log(A_H) + p_{He} \log(A_{He}) + p_O \log(A_O) + p_{Fe} \log(A_{Fe}), \tag{6.3}$$

for a 4-type approach.

6.2.3 Error Calculation

The minimizer calculates the fit parameters $\hat{p}_i$ at the loglikelihood maximum and their covariance matrix $\mathbf{V} = \mathrm{Cov}(\hat{p}_i, \hat{p}_j)$. To obtain the errors on the fitted fractions we need to propagate the covariance matrix $\mathbf{V}$ to the covariance matrix $\mathbf{U} = \mathrm{Cov}(p_i, p_j)$ on the event fractions [196]. This is because the fit parameters $\hat{p}_i$ can only be interpreted as event fractions at the likelihood maximum, where $\sum_i^4 \hat{p}_i = 1$. In the implementation in [195], the error is overestimated because away from the likelihood maximum the fit parameters are not constrained to 1. Therefore I follow the approach proposed in [196] to calculate the covariance matrix $\mathbf{U}$ and the real errors on the event fractions:

$$\mathbf{U} = \mathbf{A} \cdot \mathbf{V} \cdot \mathbf{A}^{\mathrm{T}}, \tag{6.4}$$

with $A_{ij} = \mathrm{d}\, p_i / \mathrm{d}\, \hat{p}_j$ at the likelihood maximum. Using Eq. 15 from [196], we get for matrix $\mathbf{A}$:

$$p_i = \frac{\hat{p}_i}{\sum_s \hat{p}_s} \qquad \text{where only at the LLH maximum: } \sum_s \hat{p}_s = 1 \tag{6.5}$$

$$\Rightarrow A_{ij} = \left.\frac{\delta_{ij} \cdot \sum_s \hat{p}_s - \hat{p}_j}{(\sum_s \hat{p}_s)^2}\right|_{\mathrm{LLHmax}} = \delta_{ij} - \hat{p_j} \tag{6.6}$$

$$\Rightarrow \mathbf{A} = \begin{pmatrix} 1-\hat{p}_0 & -\hat{p}_0 & -\hat{p}_0 & -\hat{p}_0 \\ -\hat{p}_1 & 1-\hat{p}_1 & -\hat{p}_1 & -\hat{p}_1 \\ -\hat{p}_2 & -\hat{p}_2 & 1-\hat{p}_2 & -\hat{p}_2 \\ -\hat{p}_3 & -\hat{p}_3 & -\hat{p}_3 & 1-\hat{p}_3 \end{pmatrix} \tag{6.7}$$

The square root of the diagonal elements of $\mathbf{U}$ yields the real error on the event fraction p_i.

The error on the $< \log A >$ is then calculated by further error propagation:

$$\mathbf{W} = \mathbf{B} \cdot \mathbf{U} \cdot \mathbf{B}^{\mathrm{T}} \quad \text{with } \mathbf{B}^{\mathrm{T}} = \begin{pmatrix} \log(1) \\ \log(4) \\ \log(16) \\ \log(56) \end{pmatrix}, \tag{6.8}$$

in the case of a 4-type fit. The variance on $< \log A >$ is then W_{00}.

6.2.4 Performance

The optimal settings for the template fitting are based on the performance for reconstructing the mean log mass for composition mixtures that exist out of one type or an equal contribution of three or four types. Because the template histograms are based on the verification MC sample, the hand-made composition mixtures were made from the NN training and testing sample.

The best performance is reached when 4 types are fit to the different composition mixtures over the whole energy range. The optimal energy binning is determined by the requirement that the total number of events in the template histograms must be large enough in order to neglect its Poisson fluctuations. Less MC is available beyond 100 PeV and therefore an energy binning of 0.1 in the common logarithm of the reconstructed energy is chosen below 100 PeV and 0.2 above. The binwidth of the template histograms depends both on the MC and data statistics as on the separation between the different template shapes. A binning of 0.1 is chosen below 100 PeV and 0.2 above in $\log(A)$.

To convince ourselves that the method really works and is unbiased, a large set of blind composition mixtures were prepared [197, 198]. These are then reconstructed based on the method and settings discussed above. The solution was then subsequently released after the reconstruction has been shown. Two of those blind data challenges are shown in Figs.6.16 and 6.17. In addition to a very good performance in the reconstruction of the average mass (bottom plots), the method also exhibits quite a good reconstruction of the individual elemental contributions. As expected from the NN energy resolution and bias and the template shapes, the performance beyond 1 EeV is not good anymore. The individual fitted fractions are in most

energy bins consistent with the true fractions except for some energy bins where some fraction of helium replaces a fraction of protons or where a fraction of oxygen replaces a fraction of iron. This behaviour is currently being investigated.

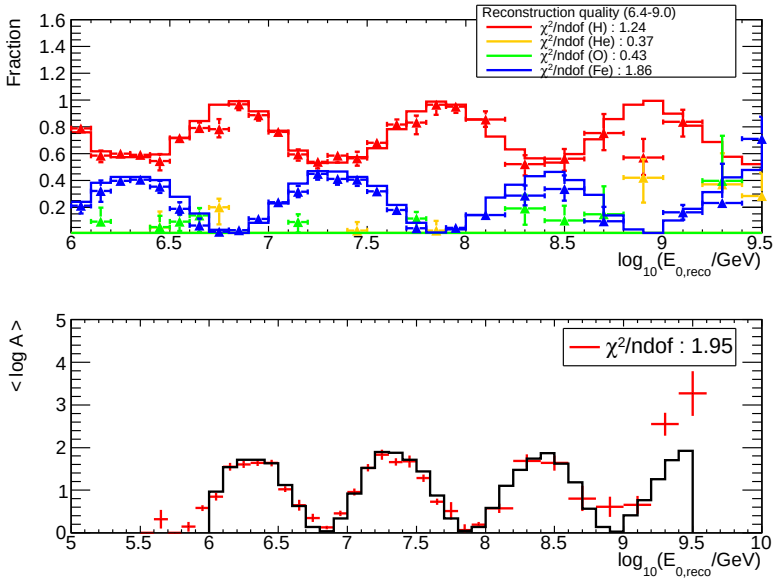

Figure 6.16: Example of a blind data challenge where a two composition mixture that changes alternatingly as function of the primary energy is reconstructed by the template fitting that uses four types as underlying MC model. **Top**: The histograms show the true fractions while the data points show the reconstructed fractions. **Bottom**: Mean log mass $< \log A >$ as function of primary energy compared between the true mass (black) and the reconstructed mass (red).

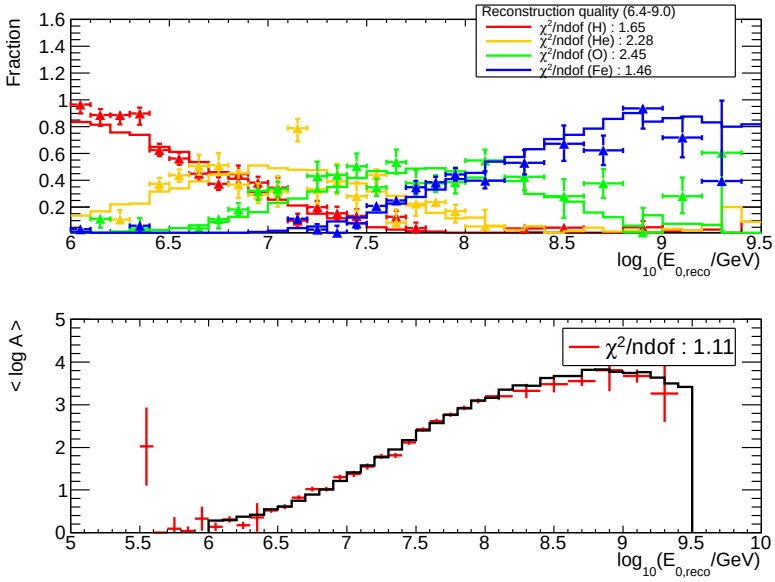

Figure 6.17: Example of a blind data challenge with a mixture of four types that each have different contributions as a function of the primary energy. **Top**: The histograms show the true fractions while the data points show the reconstructed fractions. **Bottom**: Mean log mass $< \log A >$ as function of primary energy compared between the true mass (black) and the reconstructed mass (red).

Chapter 7

Systematics

7.1 Hadronic Interaction Model

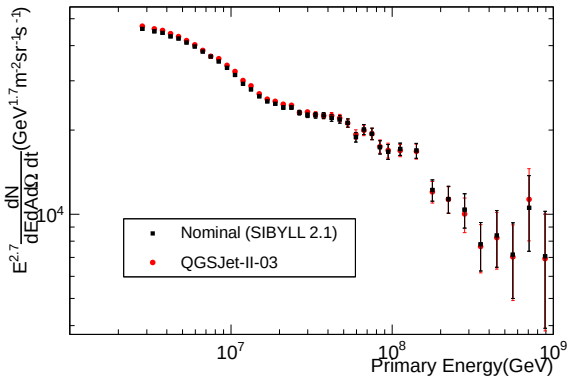

Figure 7.1: Differential cosmic ray flux, weighted to $E^{2.7}$, based on nominal SIBYLL 2.1 MC compared to QGSJet-II-03 as hadronic interaction model.

As there is no accelerator experiment on Earth that can measure the cross-section of proton and air nuclei at those energies, the MC is based on extrapolations from lower energy (using Feynman scaling). There are several models, of which the major ones are SYBILL, QGSJet-II-03 and EPOS, discussed more in detail in Chapter 3.

The Monte Carlo simulation from which we deduced the relation between the reconstructed variables that go into the Neural Network and the primary mass and energy is done with the hadronic interaction model SYBILL 2.1 above 80 TeV and FLUKA below 80 TeV. To determine the systematic uncertainty from our choice of hadronic interaction model, CORSIKA showers are simulated with QGSJet-II-03 as hadronic interaction model. Due to disk space limitations and cpu time limitations, we did not simulate EPOS.

QGSJet events over the whole energy range, from 100 TeV to 3.2 EeV, for all four primary types. Twenty percent of the simulation statistics used for the standard simulation are generated for the systematics calculations.

The systematic uncertainty on the energy spectrum is obtained by applying the neural network, trained on SYBILL simulations, on QGSJet simulations and using the bias in reconstructed energy as a function of the reconstructed energy as systematic uncertainty. The resulting energy spectrum is shown in Fig. 7.1 and compared to the energy spectrum based on SIBYLL 2.1. The uncertainty is very small because IceTop is located near the shower maximum of PeV-EeV showers where the hadronic interaction models are less uncertain. Additionally, the large uncertainty on the number of low energy muons does not affect the energy spectrum

that much because the IceTop shower size S_{125} is dominated by the energy deposition of electromagnetic particles.

The composition uncertainty is calculated by applying the neural network on the QGSJet simulations and using the templates from the QGSJet MC instead of the templates from the standard SIBYLL MC. Data is then being fit by the QGSJet templates instead. Although only one fifth of the statistics is available for the template histograms, the template fitting does take into account the larger Poisson fluctuations but larger statistical uncertainties are expected from the limited MC statistics.

7.2 Ice Model

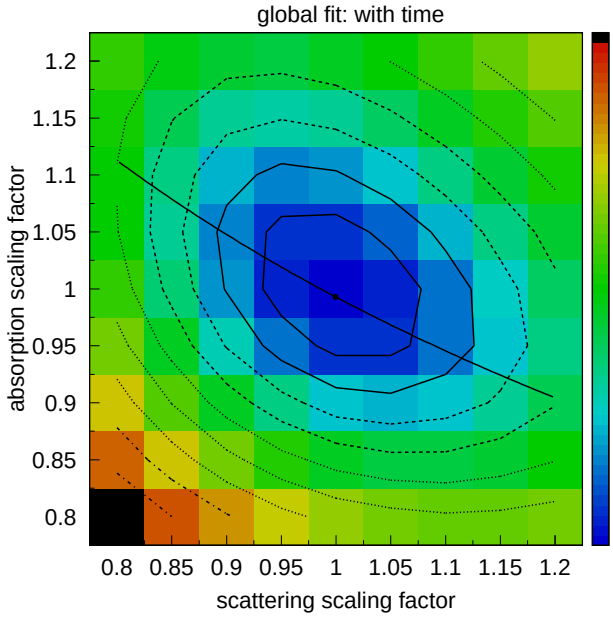

Figure 7.2: Likelihood map in the vicinity of the minimum for a fit including both charge and timing information from [115]. The contours are χ^2 contours.

The statistical uncertainties on the absorption and scattering coefficients are 5-7%, while the systematic uncertainties are in total 6.5%. The statistical uncertainties are uncorrelated between neighbouring depth bins, while the systematic uncertainties have depth dependent correlations. However, the grey band in Fig.2.12 shows the 10% error band if they are both added in quadrature [115].

Simulations use Photonics tables for calculating the expected number of photons according to a particular ice model. The only Photonics tables available for systematics simulations were those where both the absorption and scattering coefficient were scaled by 0.9 or 1.1. From the likelihood map on Fig. 7.2 it is clear the 1.1 scaling factor is slightly higher than a one sigma error, while the scaling factor of 0.9 for both absorption and scattering gives a larger overestimation of the systematic error.

The systematic uncertainties calculation for both the energy spectrum and the composition follows the same approach as for the hadronic interaction model. Fig. 7.3 illustrates that the uncertainty on the ice model only has a very small effect on the energy spectrum. The reconstructed energy based on the trained neural network is dominated by S_{125}. The information from IceCube is more used for making the energy estimator composition independent.

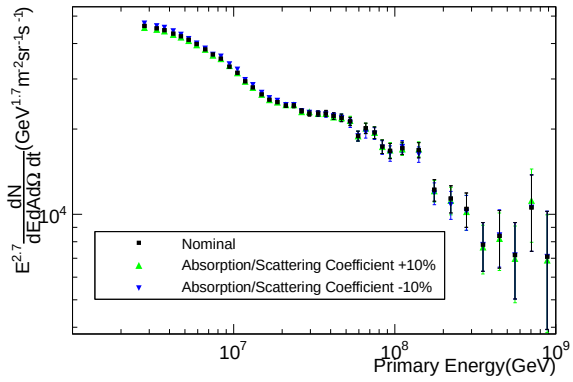

Figure 7.3: Differential cosmic ray flux, weighted to $E^{2.7}$, with an uncertainty of $\pm$10% on the absorption and scattering coefficient of the SPICE Mie Ice model.

7.3 DOM efficiency

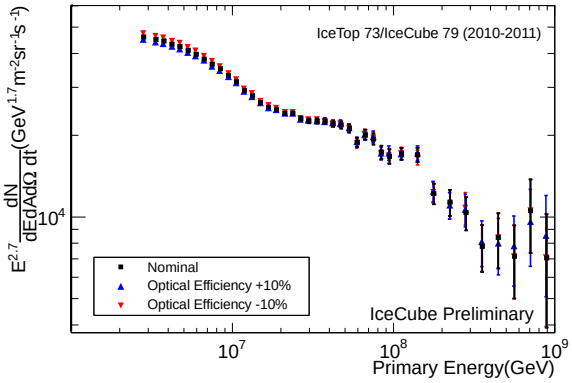

Figure 7.4: Differential cosmic ray flux, weighted to $E^{2.7}$, with an optical IceCube DOM efficiency uncertainty of $\pm$10%.

The DOM efficiency combines the quantum efficiency of the PMT and the transmission of photons through the glass and optical coupling gel. In the Photonics tables, also the angular acceptance of the DOM and a particular hole ice model[1] are included in the expected number of photon calculation. A recent analysis uses very low energy muons (median energy: 82 GeV), which produce a constant amount of Cherenkov light, at zenith angles between 45° and 70°. It shows that the DOM efficiency is 10% higher than what was assumed before [133]. This is already accounted for in the reconstruction (see Section 4.2.1). That analysis has an uncertainty of about 3%, but due to the lack of the current understanding between that analysis and other analyses the very conservative value of 10% on the DOM efficiency is used.

In Section 4.2.1, it is described how the DOM efficiency is included in the energy loss reconstruction. Therefore, to calculate the systematic uncertainties due to the DOM efficiency, the energy loss in data is reconstructed with $\pm$10% on the nominal value of 0.99. On Fig. 7.4, the optical efficiency uncertainty of $\pm$10% is plot. The optical efficiency only affects the IceCube variables, which are mainly sensitive to composition. Hence, the systematic uncertainty on the energy spectrum is small. At lower energy the uncertainty is slightly larger because there S_{125} alone is more sensitive to composition [170]. Therefore composition information

[1] Hole ice is the refrozen, filtered drill water around the strings.

from IceCube is needed for a better energy estimator independent of the composition. This is affected by the optical efficiency uncertainty and thus the systematic error is slightly larger.

Instead of separate uncertainties on the DOM efficiency and the IceModel, for the composition measurement a global effective light yield uncertainty, which might depend on the zenith angle, is necessary for the zenith angle range from 0° to 30°.

7.4 Snow correction uncertainty

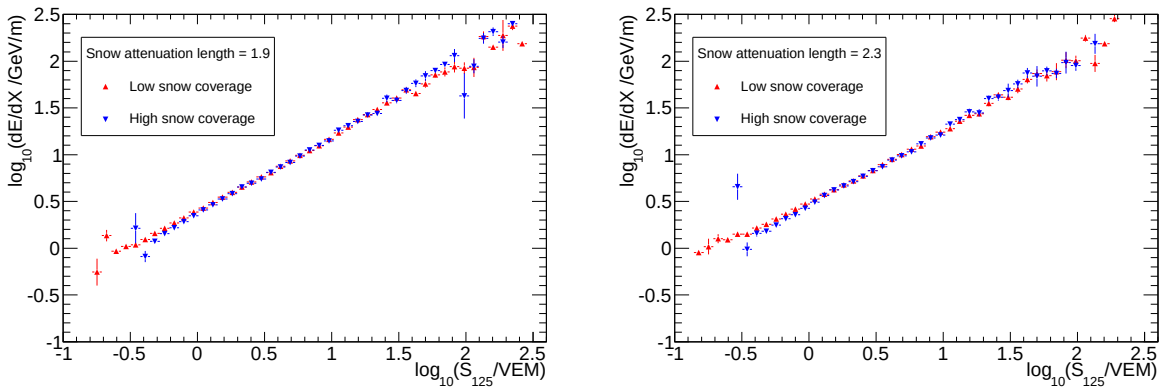

Figure 7.5: Reconstructed average energy loss as a function of S_{125} compared between the IceTop subarray with low snow coverage and the subarray with high snow coverage for events with a zenith angle between 0° and 15° (left) and for events with zenith angles above 15° (right).

The effective snow attenuation length λ is different for different zenith angle ranges. Coincident events with a zenith angle below 15° have an optimal snow correction with an attenuation length λ of 1.9 m (left plot of Fig. 7.5). Events with a larger zenith angle are better corrected with a λ of 2.3 m. The reason for that is currently unknown, because the zenith angle should have been accounted for in the snow correction (see Eq. 4.15). The variety in the snow density between snow accumulating on top of the tanks and compressed snow in the walls of the trenches, could contribute to that effect.

The effective attenuation lenght is a setting in the maximum likelihood reconstruction algorithm. Therefore the same approach as for the DOM efficiency is used to calculate the systematic uncertainty on the energy spectrum and on the composition.

On Fig. 7.6, the effect of the uncertainty on the snow attenuation length on the energy spectrum is shown. The uncertainty on the snow correction affects only S_{125}, which is the dominant variable for the energy reconstruction and creates a shift in the energy spectrum. The snow correction uncertainty is the largest systematic uncertainty on the differential flux in this analysis, because the energy estimator is by construction independent of any composition assumption, the largest uncertainty in the IT-73 analysis from [170].

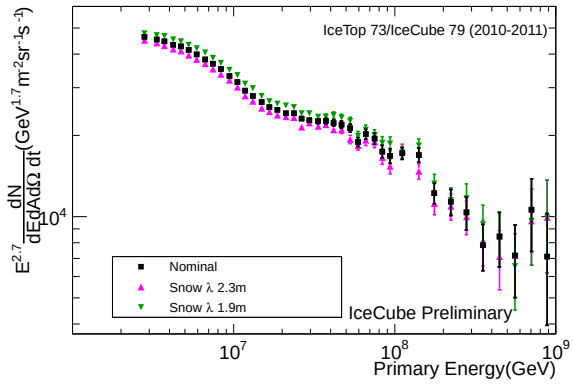

Figure 7.6: Differential cosmic ray flux, weighted to $E^{2.7}$, with an uncertainty of 0.2 m on the effective snow attenuation length.

7.5 Absolute energy scale

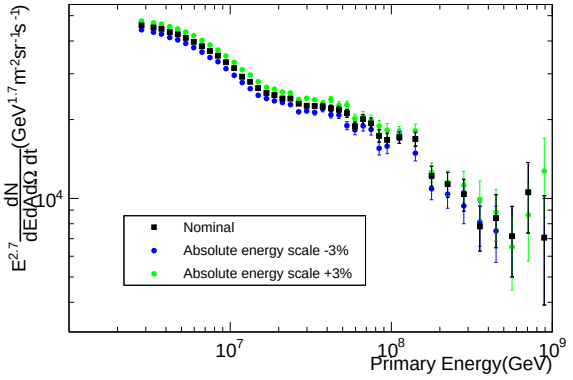

Figure 7.7: Differential cosmic ray flux, weighted to $E^{2.7}$, with an uncertainty of $\pm$3% on the VEM calibration of simulation.

In Section 3.2, it is described that the absolute calibration of the IceTop simulation is done by simulating the VEMCal procedure using low energy showers between 3 GeV and 10 TeV [165]. The systematic uncertainty on the absolute calibration of 3% gives us an uncertainty on the absolute energy scale for IceTop. This error is propagated as a shift in S_{125}. The effect of this uncertainty on the energy spectrum is demonstrated by Fig. 7.7. The uncertainty is of the same scale as the uncertainty on the snow correction and they both constitute the largest systematic uncertainties on the energy spectrum.

7.6 Photon propagation

The standard simulation for cosmic rays is based on lookup tables created by Photonics for the photon propagataion. It is well known that binning artefacts from incorrect interpolations are present [177]. The solution to that problem is direct photon propagation accelerated through parallel calculations on GPU's (Graphics Processing Units). For events which many muons, like high energy cosmic ray muon bundles, even with GPU's direct propagation is too slow. A method called hybrid simulation has been developed which directly propagates the Cherenkov photons from muons and uses spline fitted tables for the Cherenkov photons from

electromagnetic and hadronic cascades. However, currently there is no software support available to simulate this hybrid approach and the systematic uncertainty arising from the use of Photonics can not be calculated.

Chapter 8

Results

8.1 Energy Spectrum

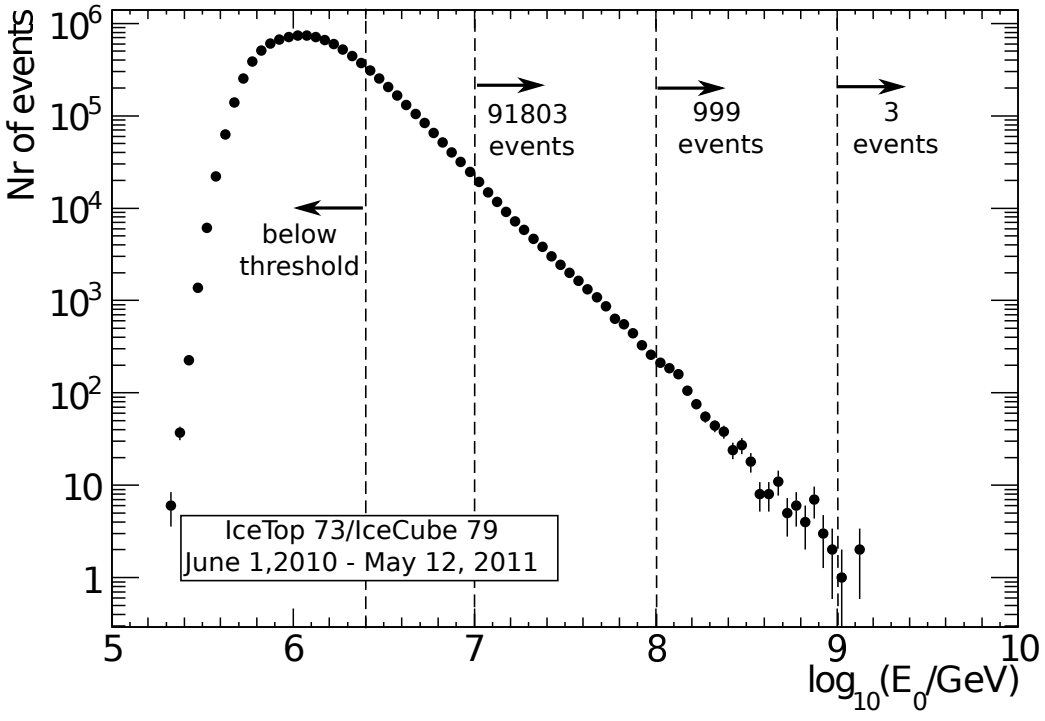

Figure 8.1: Raw energy spectrum based on data from June 1, 2010 to May 12, 2011 during the IT-73/IC-79 data taking period.

The regression approach through a neural network directly yields a composition-independent reconstructed primary energy for each event. The trained neural network calculates the energy by applying its non-linear function approximation on the input variables for that data event. The cosmic ray energy spectrum that is obtained in this way for the full IceTop 73/IceCube 79 dataset is shown in Fig. 8.1. The energy threshold of my analysis, determined by energy where the effective area become independent of the primary energy, is illustrated by the dashed line at 6.4 (2.5 PeV). In total 1560138 events are present for the composition measurement. This is 29% of the statistics for the IceTop-73 analysis as expected from the lower effective area, caused by the contained coincident IceTop-IceCube event requirement. Above 10 PeV, 91803 events survived

all cuts. Above 100 PeV, I have 999 events left in my sample, while 3 events with a reconstructed energy above 1 EeV are found.

To convert a distribution of event counts as function of the common logarithm of the reconstructed energy, $\mathrm{d}\,N/\,\mathrm{d}\log_{10}(E)$, to a differential flux $\mathrm{d}\,\Phi/\,\mathrm{d}\,E$, we need to account for the effective area A_{eff}, the solid angle weighted by the simulated zenith angle distribution Ω and the livetime t of the detector:

$$E\frac{\mathrm{d}\,\Phi}{\mathrm{d}\,E} = \frac{\mathrm{d}\,\Phi}{\mathrm{d}\log E} = \frac{1}{t\Omega A_{\mathrm{eff}}\log(10)}\frac{\mathrm{d}\,N}{\mathrm{d}\log_{10}(E)}. \tag{8.1}$$

Events with less than eight station hits were prescaled and are therefore weighted by the prescale factor of two. Based on the energy resolution we can achieve with this analysis (Fig. **??**), the energy bins below 6.5 and above 8.0 are 0.1 wide while the binwidth in the energy range between 6.5 and 8.0 is 0.05 in $\log_{10}$ space. Of course for the different energy bin widths are accounted for in the flux calculation.

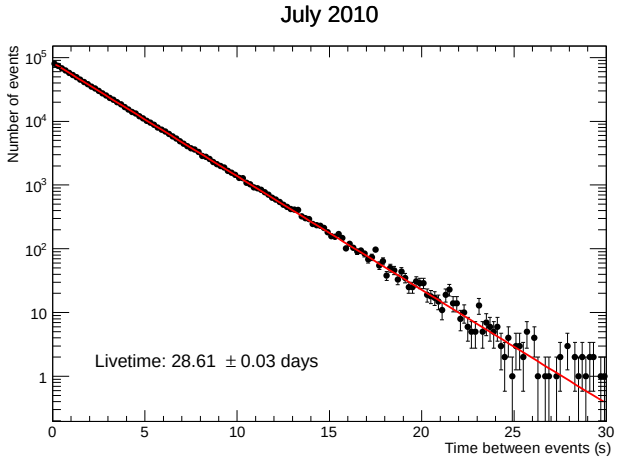

Figure 8.2: Example of the livetime calculation for data from July 2010, using the distribution of times between events to which an exponential function is fit. The error on the livetime comes from the uncertainty of the fit.

The livetime of the detector is the time during which the detector is stable and taking data. Because periods of unstability can exist during a run, which is typically eight hours long, we do not use the time difference Δt between the end time and the start time of the run for the livetime calculation. Instead an exponential function $N(\Delta t) = N_0 \cdot e^{-\Delta t/\tau}$ is fit to the distribution of time differences between events because they are Poisson distributed. The mean time difference between events is then the exponential decay constant τ. The livetime is obtained by multiplying the total number of events with their expected time difference τ. This approach is demonstrated for July 2010 data in Fig. 8.2 and ascertains that large gaps which do not follow the exponential distribution are not added to the total livetime. Those large gaps could come from periods during which the detector was unstable.

The livetime depends on the selected runs. Only runs where both IceCube and IceTop were in stable operation and which are longer than 10 minutes are selected. In total 1019 good runs were selected for this analysis (629 from 2010 and 390 from 2011). These result in a total livetime of 310.2 $\pm$ 0.4 days. The uncertainty on the livetime is 0.1% and will be neglected in the flux calculation.

The effective area from Fig. 5.38 is plot as a function of the true primary energy and illustrates that the cuts do not depend on energy and composition. For the differential flux, however, the effective area as a function of the reconstructed energy is required. This is shown in Fig. 8.3 both on linear and logarithmic scale. In the energy range between 6.2 and 6.9 the effective area is larger than at higher energies. This is not caused by a bias in the energy reconstruction which is very small but originates from a bin-to-bin migration of events with a steep power-law spectrum. The energy resolution at those energies is comparable to the

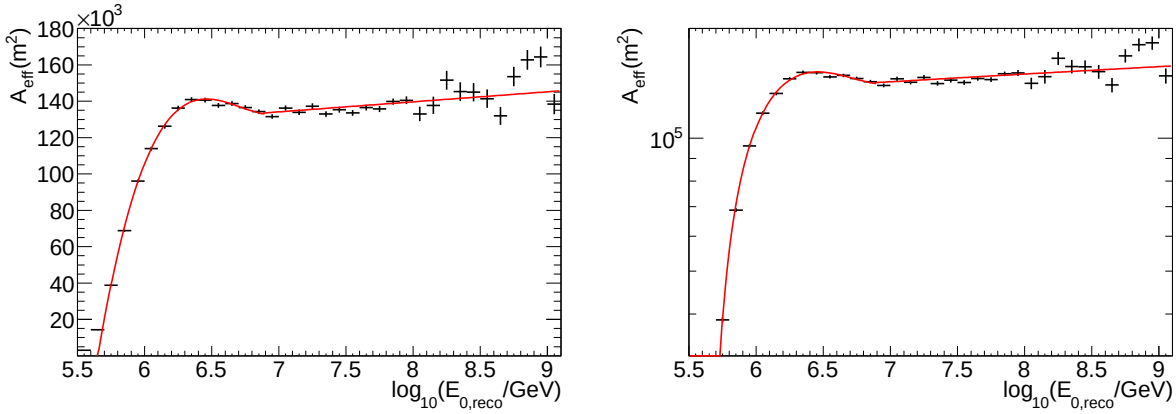

Figure 8.3: Effective area as a function of the reconstructed energy. The fit (in red) is a third degree polynomial between 5.5 and 6.9 and a line above 6.9.

binwidth, but due to the steep spectrum, more events are migrating to lower energies than to higher energies. Because the energy resolution is intrinsically composition-dependent and because the migration depends on the real energy spectrum, I assumed the same primary flux as the IT-73 analysis [170], namely the H4a model [67]. The effective area is then empirically fit by a third degree polynomial ($y = p_0 + p_1 x + p_2 x^2 + p_3 x^3$) between 5.7 and 6.9, and a line ($y = p_0 + p_1 x$) beyond 6.9. The fit parameters and χ^2 values of the fit are displayed in Table 8.1.

Energy Range (in $\log_{10}$(E/GeV))	p_0	p_1	p_2	p_3	χ^2/ndof
5.7 - 6.9	(-4.1619±0.0003)·10^7	(1.87241±0.00002)·10^7	(-2.7951±0.0001)·10^6	(1.3890±0.0001)·10^5	14/8
6.9 - 9.0	(9.49±0.05)·10^4	(5.43±0.06)·10^3	-	-	57/19

Table 8.1: Table of the fit parameters and χ^2 per degree of freedom for the two polynomial fits to the effective area.

The effective area and the simulated solid angle together give the detector aperture $\mathcal{A}$. The simulated solid angle Ω is the zenith angle distribution caused by the atmospheric attenuation integrated over the solid angle $\mathrm{d}\,\Omega$:

$$\mathcal{A} = A_{\text{eff}} \cdot \Omega \tag{8.2}$$

$$\Omega = \int \cos\theta \,\mathrm{d}\,\Omega = \iint \cos\theta \,\mathrm{d}\cos\theta \,\mathrm{d}\,\phi. \tag{8.3}$$

In order to get maximal statistics in simulation for coincident IceTop-IceCube events, the zenith angle ranges from 0 to 40°. The simulated solid angle is then 1.298 sr.

	3 PeV	30 PeV
VEM calibration	+3.9% -4.0%	+6.8% -4.6%
Snow correction	+3.6% -2.9%	+6.7% -1.8%
QGSJet-II-03	+2.1%	+2.6%
DOM efficiency	+2.7% - 2.3%	+1.2%
Ice Model	+2.1% -1.0%	+1.1%
Total	+6.6% -5.5%	+10.1% -4.9%

Table 8.2: Overview of the systematic uncertainties at two reconstructed energies.

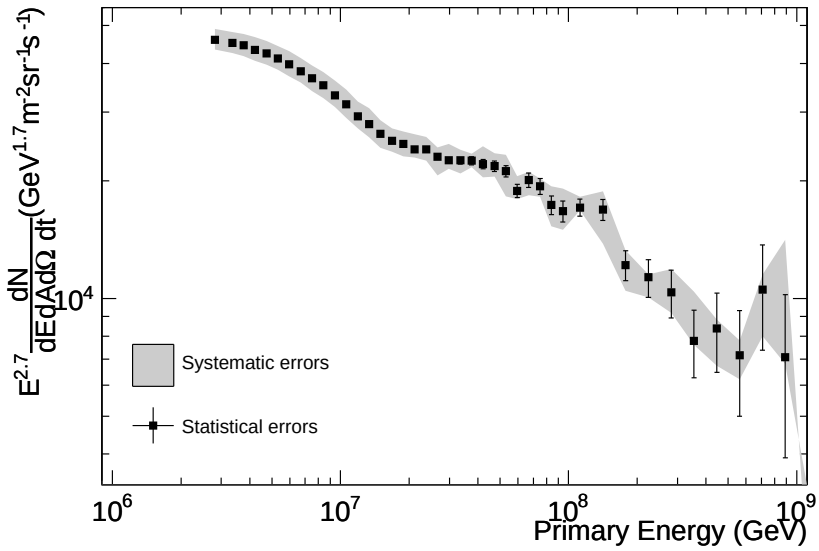

Figure 8.4: Differential cosmic ray flux, weighted to $E^{2.7}$, with all systematic uncertainties shown as grey band.

The resulting differential flux, weighted by $E^{2.7}$ for data is shown in Fig. 8.4. Table 8.2 gives an overview of the systematic uncertainties, described in more detail in Chapter 7, on the primary energy spectrum. Except for the DOM efficiency and the ice model, the systematic uncertainties are uncorrelated. Because the correlation between the uncertainty on the DOM efficiency and on the ice model is still being investigated, all systematic errors are added in quadrature to be conservative. The overall systematic error band is shown as a grey band in Fig. 8.4. At the highest statistical fluctuations also affect the systematic uncertainties. More statistics will therefore reduce the systematic error band. The total systematic uncertainties are in this analysis of course not dominated by the composition uncertainty but by the uncertainty on the effective snow attenuation length and on the absolute energy scale.

Fig. 8.5 compares the differential flux of two independent analyses, based on the same MC and the same data taking period. The IceTop-73 spectrum is based on the H4a composition assumption and has a $\pm$7% composition uncertainty, demonstrated by the grey band, while my spectrum did not assume any composition for the energy determination. All other systematic uncertainties that affect the spectrum are common between both analyses. Both results agree very well within the uncertainty over the whole energy range. The statistical uncertainties for the spectrum from this work are larger because the effective area is about a factor of three lower.

The knee of the cosmic ray energy spectrum is visible around 3-4 PeV as a change in the spectral index. After the knee, the spectrum is not a single powerlaw. At about 20 PeV the spectrum becomes significantly less steep. The spectrum steepens again from about 200 PeV. These spectral features are not caused by statistical or systematic (see Fig. 8.4) uncertainties and must therefore be related to the cosmic ray sources, acceleration and propagation mechanisms. Additional structure is visible in the spectrum, like the steep decrease in the flux after 150 PeV, visible in both analyses. However, more data is necessary to confirm whether the additional structure is significant or comes from statistal fluctuations.

In Fig. 8.6, the differential flux obtained by my analysis is compared to the most recent experimental results from the last six years. In addition, the H4a model and GST model, described in Section 1.1.5, are shown. It is clear that the IceTop results are the most accurate results up to date and are still consistent with the other experiments within error bars. While the IceTop 73 analysis has a factor of three more statistics, my coincident analysis has a smaller systematic uncertainty because no composition assumption is necessary by construction. The clear peak at 80 PeV from the GAMMA experiment is not consistent within error bars with

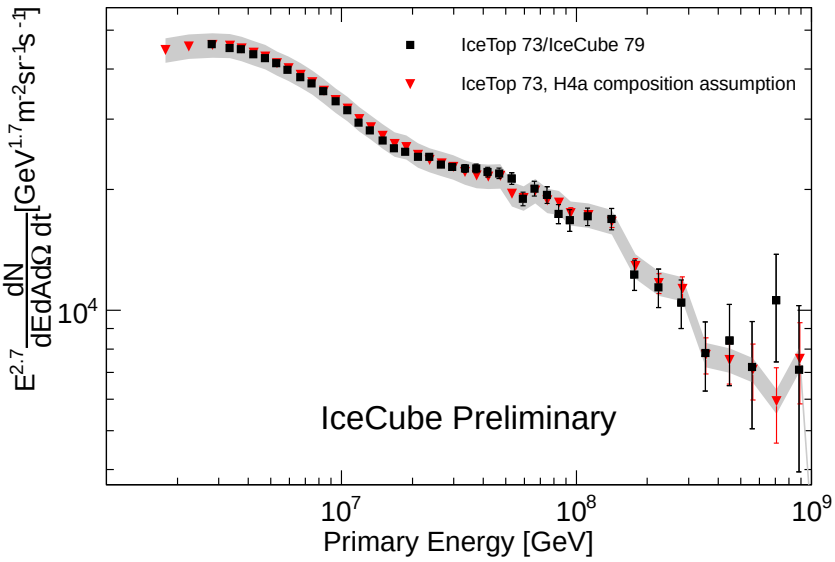

Figure 8.5: Differential cosmic ray flux, weighted to $E^{2.7}$, of the analysis presented here compared to the energy spectrum from [170] where the grey band shows the $\pm 7\%$ uncertainty on the composition assumption, not present in this analysis.

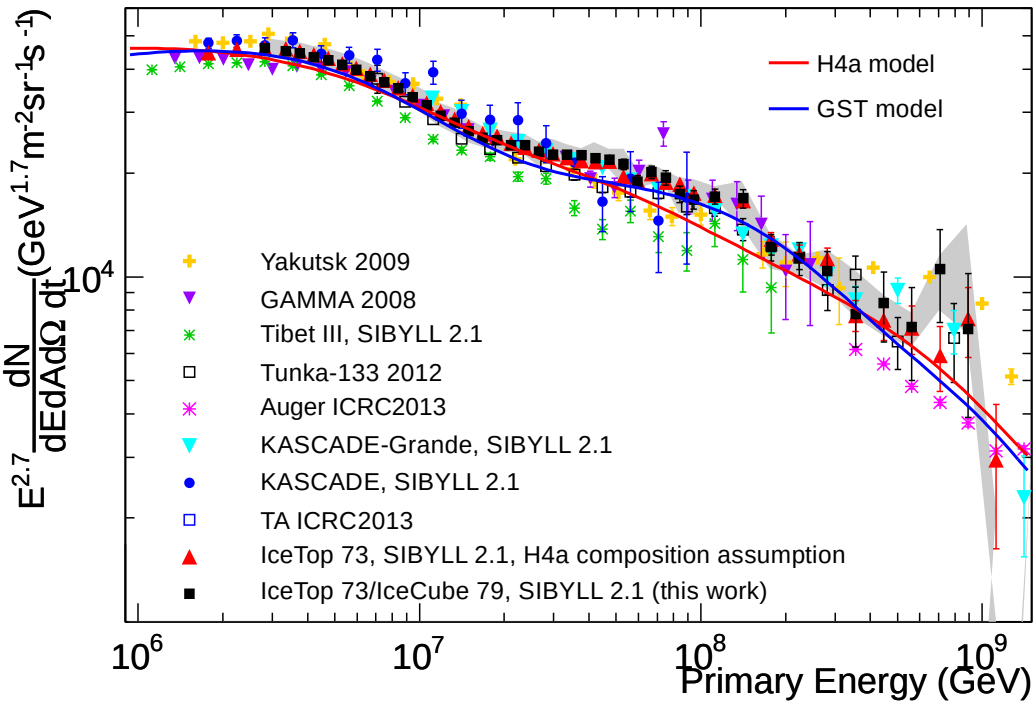

Figure 8.6: Comparison of the energy spectrum obtained in this thesis with the systematics as grey band, with the most recent experiments from the last 6 years. For the other experiments only the statistical uncertainties are shown. The H4a and GST are model fits discussed in Section 1.1.5.

the IceTop 73/ IceCube 79 result and is also not seen by any other experiment. The spectral flattening starting at 20 PeV is more clear in the IceTop results than in the other experiments. This flattening is not described by the H4a model, and is reasonably well described by the GST model although it should be stronger.

8.2 Composition Spectrum

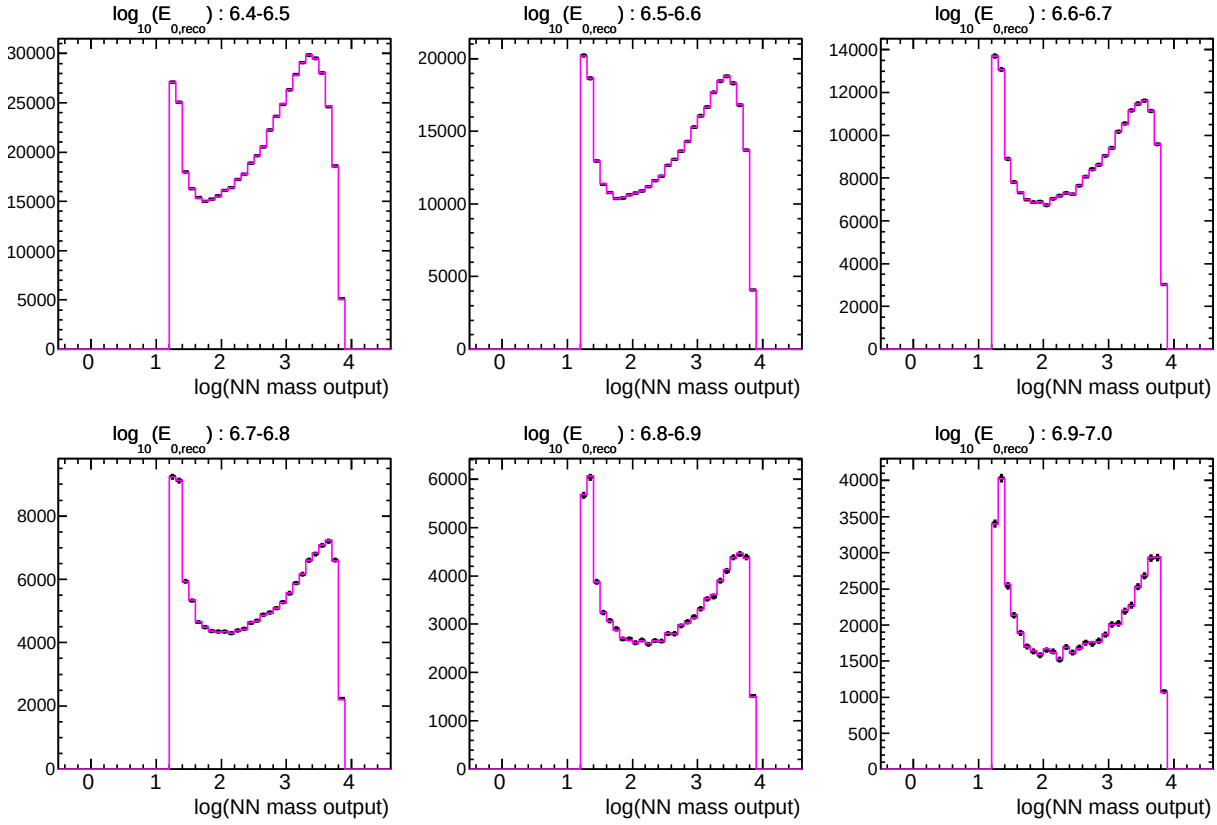

Figure 8.7: Result of the template fits (magenta) to the data distributions (black) in $\log$ (NN mass output) in the reconstructed energy between 6.4 and 7.0 in $\log_{10}(E_0/\mathrm{GeV})$. The y axis displays the number of events.

The template fitting procedure, described in Chapter 6, for reconstructed energy bins with at least 20 events yields the histograms from Fig. 8.7 to 8.10. No template fitting is performed when there are less than 20 events in order to keep the Poisson on the total number of events low enough as required by the method. The fit result, shown by the magenta histograms, describes the data distributions, represented by the black data points very well over the whole energy range. Although it appears that the fits in three highest energy bins are less good, but as over the rest of the energy range they are compatible with the data within the statistical uncertainties and yield good χ^2 values. The χ^2 per degree of freedom values ranges between 0.4 and 1.3 and is therefore also not unrealistically small.

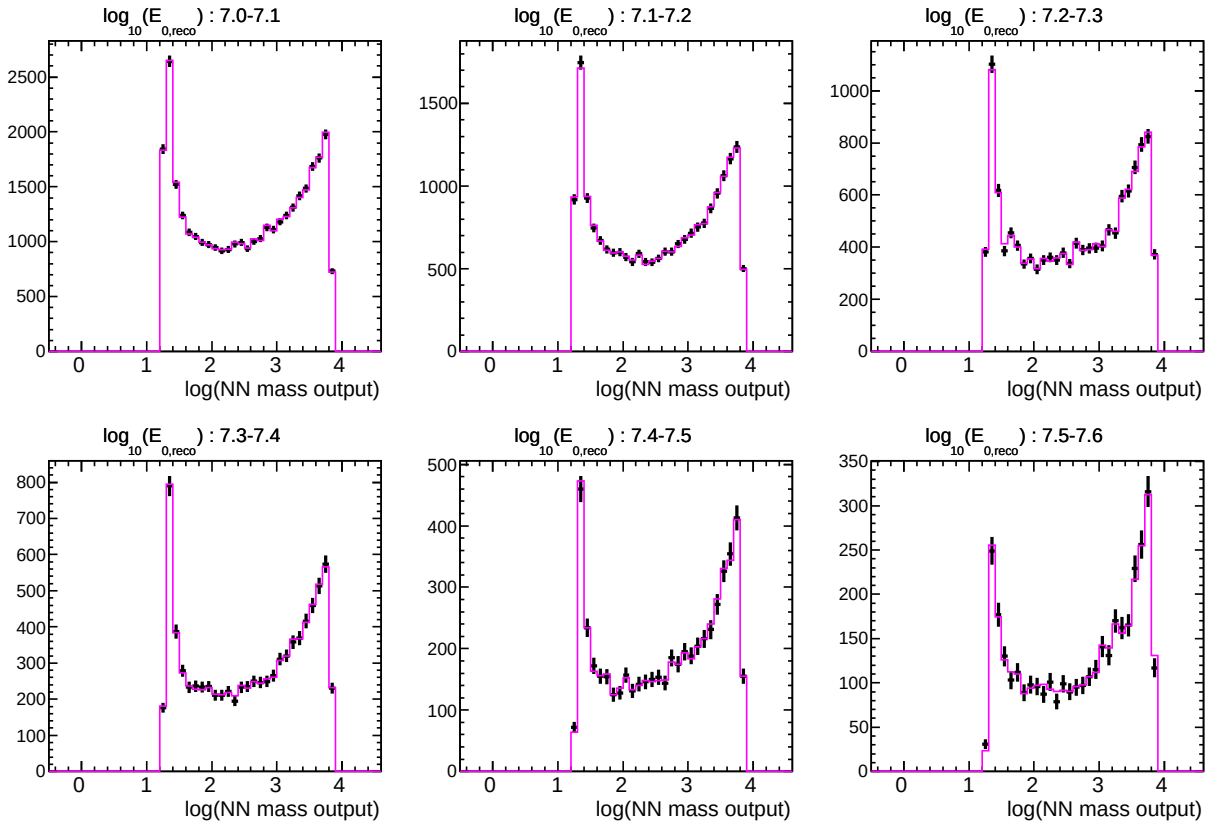

Figure 8.8: Result of the template fits (magenta) to the data distributions (black) in $\log$ (NN mass output) in the reconstructed energy between 7.0 and 7.6 in $\log_{10}(E_0/\mathrm{GeV})$. The y axis displays the number of events.

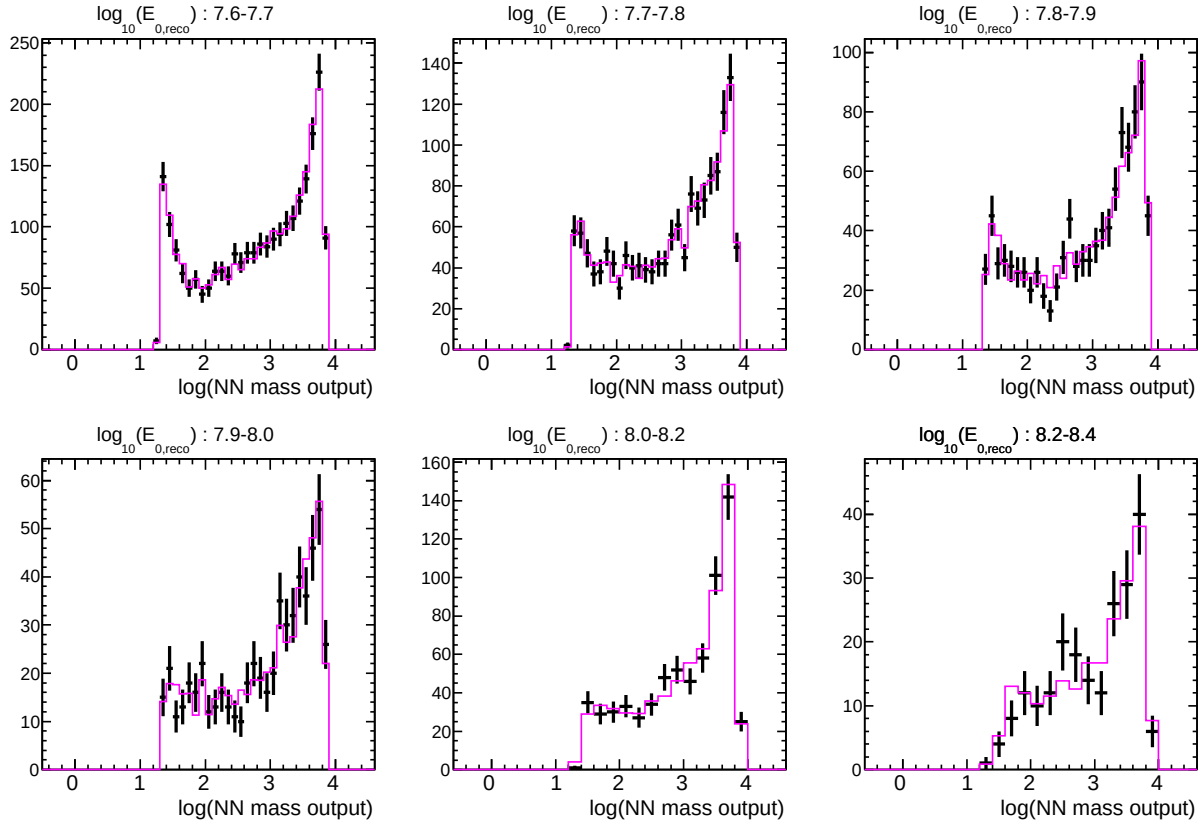

Figure 8.9: Result of the template fits (magenta) to the data distributions (black) in $\log$ (NN mass output) in the reconstructed energy between 7.6 and 8.4 in $\log_{10}(E_0/\mathrm{GeV})$. The y axis displays the number of events.

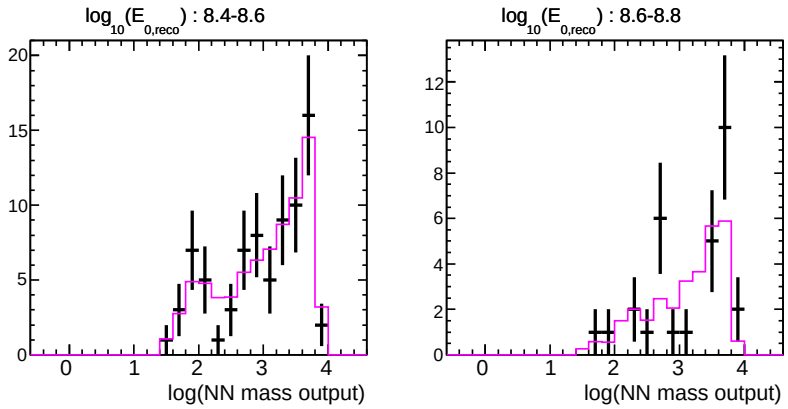

Figure 8.10: Result of the template fits (magenta) to the data distributions (black) in $\log$ (NN mass output) in the reconstructed energy between 8.4 and 8.8 in $\log_{10}(E_0/\mathrm{GeV})$. The y axis displays the number of events.

$\log_{10}(E_{0,reco}/GeV)$	Nr of events	p_H	p_{He}	p_O	p_{Fe}	χ^2/ndof
6.4 - 6.5	563702	$0.268^{+0}_{-0.030}$	$0.484^{+0.055}_{-0.067}$	$0.0191^{+0.055}_{-0}$	$0.229^{+0.022}_{-0}$	46/39
6.5 - 6.6	371350	$0.227^{+0.026}_{-0.028}$	$0.546^{+0.040}_{-0.142}$	$0.^{+0.137}_{-0}$	$0.227^{+0.014}_{-0.052}$	32/39
6.6 - 6.7	236908	$0.306^{+0.026}_{-0.026}$	$0.378^{+0.055}_{-0.053}$	$0.134^{+0.053}_{-0.057}$	$0.183^{+0.026}_{-0.024}$	13/39
6.7 - 6.8	148575	$0.351^{+0.035}_{-0.032}$	$0.269^{+0.070}_{-0.075}$	$0.234^{+0.074}_{-0.069}$	$0.146^{+0.028}_{-0.030}$	28/39
6.8 - 6.9	91303	$0.427^{+0.052}_{-0.054}$	$0.078^{+0.108}_{-0}$	$0.403^{+0.084}_{-0.084}$	$0.092^{+0.030}_{-0}$	52/39
6.9 - 7.0	56497	$0.287^{+0.024}_{-0.023}$	$0.280^{+0.048}_{-0.048}$	$0.272^{+0.045}_{-0.044}$	$0.161^{+0.017}_{-0.017}$	18/39
7.0 - 7.1	34113	$0.243^{+0.046}_{-0.046}$	$0.285^{+0.083}_{-0.082}$	$0.368^{+0.059}_{-0.058}$	$0.103^{+0.021}_{-0.022}$	33/39
7.1 - 7.2	20727	$0.297^{+0.042}_{-0.041}$	$0.214^{+0.091}_{-0.091}$	$0.357^{+0.081}_{-0.078}$	$0.133^{+0.028}_{-0.030}$	24/39
7.2 - 7.3	12960	$0.203^{+0.032}_{-0.030}$	$0.293^{+0.077}_{-0.081}$	$0.329^{+0.086}_{-0.081}$	$0.176^{+0.034}_{-0.034}$	23/39
7.3 - 7.4	8437	$0.246^{+0.038}_{-0.035}$	$0.063^{+0.081}_{-0}$	$0.638^{+0.102}_{-0.089}$	$0.054^{+0.040}_{-0.049}$	14/39
7.4 - 7.5	5437	$0.255^{+0.026}_{-0.042}$	$0.017^{+0.085}_{-0}$	$0.633^{+0.056}_{-0.076}$	$0.095^{+0.032}_{-0.031}$	14/39
7.5 - 7.6	3642	$0.082^{+0.069}_{-0.069}$	$0.354^{+0.117}_{-0.120}$	$0.287^{+0.087}_{-0.083}$	$0.276^{+0.039}_{-0.038}$	22/39
7.6 - 7.7	2407	$0.178^{+0.039}_{-0.041}$	$0.054^{+0.090}_{-0}$	$0.552^{+0.077}_{-0.078}$	$0.216^{+0.032}_{-0.033}$	15/39
7.7 - 7.8	1498	$0.151^{+0.0.022}_{-0.032}$	$0^{+0.065}_{-0}$	$0.711^{+0.056}_{-0.070}$	$0.137^{+0}_{-0.037}$	20/39
7.8 - 7.9	998	$0.069^{+0.119}_{-0}$	$0.242^{+0.173}_{-0}$	$0.407^{+0.222}_{-0.157}$	$0.282^{+0.068}_{-0.082}$	31/39
7.9 - 8.0	585	$0.130^{+0.034}_{-0.035}$	$0^{+0.057}_{-0}$	$0.610^{+0.080}_{-0}$	$0.260^{+0.057}_{-0.055}$	21/39
8.0 - 8.2	661	$0^{+0.067}_{-0}$	$0.149^{+0.113}_{-0}$	$0.313^{+0.229}_{-0.184}$	$0.537^{+0.095}_{-0.092}$	16.5/18
8.2 - 8.4	212	$0^{+0.029}_{-0}$	$0.295^{+0.140}_{-0.138}$	$0.346^{+0.260}_{-0.248}$	$0.359^{+0.148}_{-0.144}$	12/18
8.4 - 8.6	77	$0^{+0.194}_{-0}$	$0.322^{+0.112}_{-0}$	0^{+0}_{-0}	$0.678^{+0.151}_{-0.201}$	6.8/18
8.6 - 8.8	30	$0^{+0.24}_{-0}$	$0.184^{+0.149}_{-0}$	$0^{+0.427}_{-0}$	$0.816^{+0}_{-0.255}$	24/18

Table 8.3: Table of the fit parameters and χ^2 per degree of freedom for the template fitting to the data distributions over the whole energy range. The asymmetric errors are calculated based on the likelihood space, according to the MINOS algorithm [199].

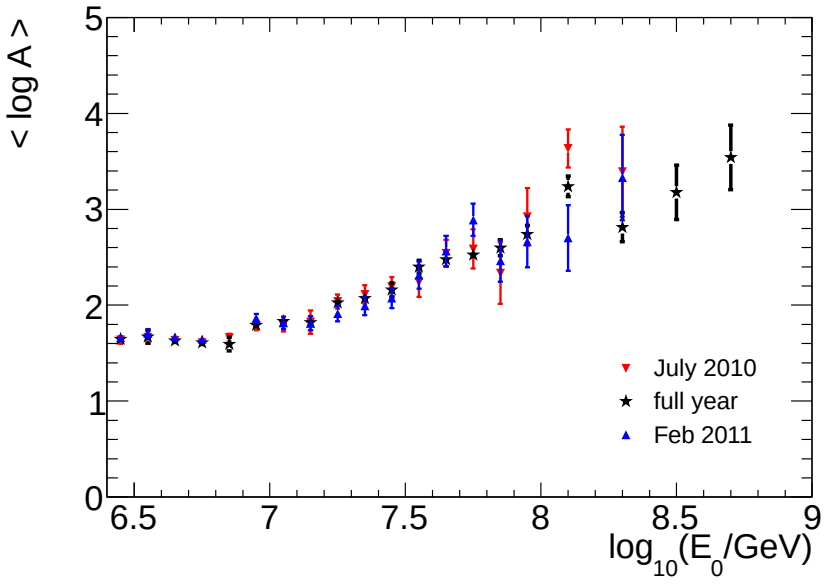

Figure 8.11: The composition spectrum or mean log mass as a function of the reconstructed primary energy, for data from the full IT-73/IC-79 data taking period (black), data from July 2010 (red) and Feb. 2011 (blue).

The mean logarithm of the mass $\langle \log A \rangle$, calculated from the fit parameters according to Eq. 6.3, for data from July 2010 (red), February 2011 (blue) and the full dataset from June 2010 to May 12, 2011 (black) is shown in Fig. 8.11. The two months with very different atmospheric temperature profiles (see Fig. 2.20) are compared with each other to verify whether the seasonal correction on the composition-dependent IceCube variables was successful. Within statistical uncertainties the $\langle \log A \rangle$ agree well over the whole energy range. This confirms that there is no systematic uncertainty on the composition from the seasonal atmospheric variation after the seasonal correction, as expected from Fig. 4.35. Both $\langle \log A \rangle$ spectra also agree well within statisical uncertainties with the $\langle \log A \rangle$ for the full year, which has smaller uncertainties.

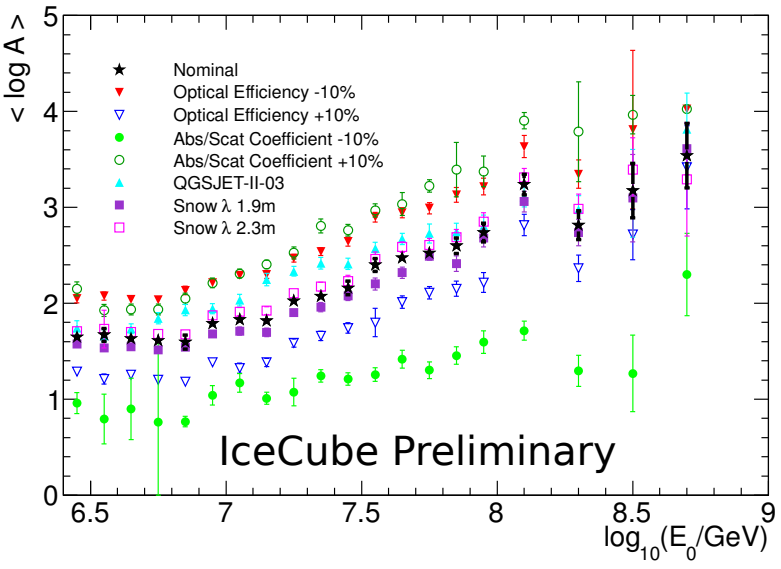

Figure 8.12: Mean log mass spectrum with systematic uncertainties included.

The composition spectrum with all systematic uncertainties included is shown on Fig. 8.12. The systematic uncertainties that only affect S_{125}, namely the uncertainty on the snow correction, are small. The systematic uncertainties that influence the absolute photon yield, which are the $\pm$10% uncertainty on the optical efficiency of the DOMs and the $\pm$10% uncertainty on the absorption and scattering coefficient from the SPICE-MIE ice model, on the other hand have a huge impact on composition measurement. The composition measurement is of course dominated by the knowledge of the energy loss detected by IceCube which is very sensitive to the knowledge on the absolute light yield. The hadronic interaction model uncertainty, represented here by QGSJet-II-03, changes both the electromagnetic and the muonic component of the shower and thus all NN input variables in a non-trivial way. Nonetheless, its systematic uncertainty is not large and most pronounced in the intermediate energy range.

The systematic uncertainties are all shown separately and not added in quadrature, because obviously the light yield systematics are highly correlated. An increase in the detected light yield can come from a decrease in the absorption coefficient or an increase in the optical efficiency of the DOM. Also, as discussed in Chapter 7, the largest systematic uncertainties are overestimated. Both the re-evaluation of the systematic uncertainties as the study on the correlation are ongoing. A correct evaluation and combination of these systematic uncertainties (mainly the light yield uncertainty) are crucial for the interpretation of the measurement.

All systematic uncertainties, except for the hadronic interaction model, do not change the energy dependence of the measurement but only the absolute scale. Two features are visible in this composition measurement and in most of the systematic uncertainties. The mean logarithm of the mass increases over the whole energy range and a clear decrease after 130 PeV is visible after which the cosmic ray composition is getting heavier again. This means that there is no sign yet from an extra-galactic component, which creates a lighter composition at the highest energies. Although the fitted templates from Fig. 8.10 are consistent with the data, statistics are low and more data is needed to be more certain about the composition at those energies. The decreasing composition at 130 PeV, visible in most systematics, and larger that the statistical errors is interesting and might be related to the decrease in the energy spectrum discussed earlier. If we look at the templates in the energy bin where the descreasing mass is observed, the bottom right plot of Fig. 8.9, we see that the heavy component is well described by the fit. Therefore a heavier average composition would not be consistent with the data.

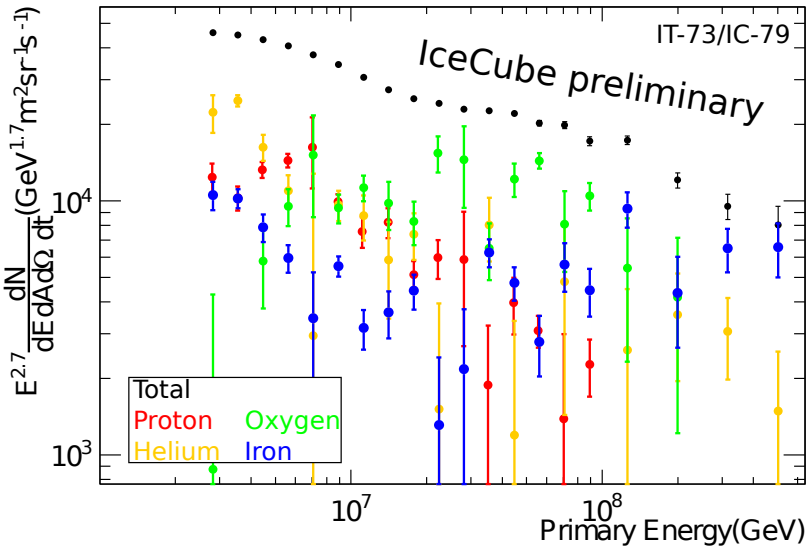

Figure 8.13: Differential cosmic ray flux weighted by $E^{2.7}$ for all primaries (black), proton (red), helium (orange), oxygen (green) and iron (blue).

Instead of calculating the average composition of data in a certain energy bin, we can study the individual contribution of the four components (proton, helium, oxygen and iron), used to fit the data neural network mass output distribution. In Section 6.2.4, the (blind) data challenges proved that the individual contributions of each type can describe unknown composition mixtures. From the individual fractions the individual energy spectra are calculated and their errors are propagated as well. The resulting differential proton flux, helium flux, oxygen flux and iron flux, weighted to $E^{2.7}$ are shown in Fig. 8.13 compared to the all-particle flux (black).

Several peaks are visible in each of the individual energy spectra. If the peak positions come from a source with a rigidity-dependent cutoff and are not random statistical fluctuations, they must be located at ZE_c, where Z is atomic number of the cosmic ray particle and E_c the cut-off energy for some source. The knee feature at 3.5 PeV is according to this measurement caused by a cut-off in the helium energy spectrum. This is consistent with previous experiments. For a source with a rigidity dependent cut-off, this implies there should be cut-off in the oxygen energy spectrum at 12-16 PeV, one in the silicon energy spectrum at 21-28 PeV and one in the iron energy spectrum at 39-52 PeV if we take the knee position at 3-4 PeV. Indeed, a cut-off in the oxygen spectrum from a peak at about 10 PeV is visible, but the cut-off is not as strong at the helium cut-off. Silicon is not simulated because of disk space limitations and from [163] we learned that it is very hard to separate silicon from iron. Silicon could however still be present and pronounced in data [200]. The natural logarithm of the silicon mass is right in between oxygen and iron. Therefore, in this analysis it can be seen as oxygen or iron. At 21-28 PeV, the energy where the silicon cut-off is expected, there is a clear peak in the oxygen spectrum with a sharp cut-off at 28 PeV. The silicon cut-off is thus interpreted as an oxygen cut-off which is not surprising. The last cut-off we expect from this source is slightly lower than 39 PeV, but still very close to where we expect it to be. It is very interesting to see that this measurements hints that four peaks in the individual energy spectra are at their rigidity-dependent cut-off energy from the source that creates the helium knee.

We can repeat this exercise to interpret the energy spectra as a series of rigidity-dependent cut-offs for a different cut-off energy. At about 7 PeV a peak with cut-off is seen in the proton energy spectrum. If this comes from a different source with a cut-off energy at E_c =7 PeV, the other peaks would be at 14 PeV (He), 56 PeV (O), 98 PeV (Si) and 182 PeV (Fe) if the cut-off energies for the second source also depend on their rigidity. At about 18 PeV there is a peak in the helium spectrum with a sharp cut-off. A very clear peak is visible at 56 PeV in the oxygen spectrum with a sharp cut-off and also at 90 Pev where the silicon cut-off is expected. Again silicon might have been interpreted by oxygen. In the iron energy spectrum there is a peak with a sharp cut-off at about 130 PeV. The energy binning beyond 100 PeV however is larger so this peak is also consistent with the expectation for a rigidity dependent cut-off from a second source. Five peaks in the reconstructed individual energy spectra seem to be consistent with a rigidity dependent cut-off source with at cricital energy at about 7 PeV.

At 15 PeV there is another peak with sharp cut-off in the proton energy spectrum. A third rigidity-dependent source would then give a helium peak at 30 PeV, which seems to be there. The expected oxygen peak at 120 PeV is not clearly visible due to the large energy bin and large uncertainty from low statistics and the same is true for an expected silicon peak at 210 PeV. The proton and helium peaks are consistent but more statistics and smaller energy bins are needed to see whether there really are oxygen and silicon peaks where it would be expected. A large, unexpected iron contribution is seen at 300-500 PeV, but the statistics is too limited to see hints of a cut-off at 390 PeV for iron.

The spectral change in the energy spectrum at roughly 20 PeV is according to this measurement started by the silicon peak from the first source, followed by the iron peak and the oxygen peak from the second source. The sharp decrease at 130 PeV in the energy spectrum is explained in this measurement by the sharp cut-off from iron from the second source, compensated by a helium component. This HE helium component might be consistent with the light ankle, seen recently by Kascade-Grande.

It should be stressed here that all the template histogram fits were done independently in each reconstructed energy bin and that no a priori information about the composition has been used.

Note that the two rigidity dependent cut-off sources that seem to be consistent with the measurement

presented in this thesis without any a priori knowledge, could come from different types of sources, eg. supernovae and hypernovae, or from reacceleration in the same source [200]. Of coure the interpretation of the spectrum here is only valid for the composition measurement with SYBILL as hadronic interaction and nominal values for the systematic uncertainties.

Chapter 9

Discussion and Summary

B.Peters noted in 1961 (see Section 1.1.5) that it is very hard to explain a featureless powerlaw for the cosmic ray energy spectrum. Since then many experiments have been performing cosmic ray energy spectrum measurements but only the last couple of years the first clear deviations from a single powerlaw have become apparent (CITE Fabian-Kascade-...).

Using events which are detected both by IceTop and IceCube I developed a neural network-based analysis based on the experience from [16]. Through improved and new reconstruction algorithms that are verified up to EeV energies and careful hit cleanings and event selections, a set of well reconstructed, contained events are selected. In addition to a much larger effective area compared to [16], data from the full year could be analyzed due to the seasonal correction on the IceCube variables that are sensitive to the muon multiplicity. Additionally, both the larger data set and the increased amount of high quality simulations increased the energy range of this analysis with respect to previous IceTop analyses. A neural network with five input variables and four types, yielded a good composition-independent primary energy estimator.

The energy spectrum obtained by this analysis shows a remarkable agreement with the IceTop-73 energy spectrum, but without composition uncertainty. They both see a clear deviation from a single powerlaw from about 20 PeV and again a strong spectral steepening at around 130 PeV. First hints of more substructure in the energy spectrum is visible thanks to the unprecendented accuracy and large statistics. However, more data is needed to verify whether these are statistical fluctuations or caused by physics. This analysis therefore provided an extra proof that the cosmic ray energy spectrum is not a simple powerlaw as B.Peters already suggested 52 years ago as very hard to believe. The largest systematic uncertainty on the energy spectrum is the uncertainty on the snow correction, which is currently being improved.

The template fitting method from [16] has been developed further in this analysis by using a binned maximum likelihood approach that also accounts for the Poisson fluctuations on the MC. The template histograms have distinct shapes over the whole energy range and are fit to the data distributions independently in each reconstructed energy bin. The method has been successfully tested with several blind data challenges. Although the composition spectrum shows an increasing mass over the whole energy range, and a local decrease at 130 PeV, the composition measurement is currently very much limited by the systematic uncertainties on the light yield. The determination of the correlated uncertainty on the effective light yield is crucial for the composition measurement and is still ongoing.

In addition to the mean composition in each energy bin, individual energy spectra for each primary type are determined. Those spectra show for the first time very interesting hints of three Peeters-cycle, three sources with a rigidity-dependent cut-off, but these have to be confirmed with more statistics. With more statistics in both data and simulations the individual energy spectra could be determined with the same accuracy as the total energy sepctrum. Also a correct evaluation of realistic systematic errors are necessary to verify the uncertainties on the individual energy spectra and the interpretation suggested here from the first hints.

Of course the analysis can easily be extended by adding more variables that do not correlate with the current NN input variables but also show good composition sensitivity. The resulting template histograms

should then be even more distinct and silicon can be added as fifth type. Still, a large amount of MC statistics are needed for better accuracy, certainly beyond 100 PeV. At those energies also a better energy resolution and more statistics are needed to be able to see more evidence of the cut-off spectra.

Appendix A

CORSIKA Steering File

CORSIKA showers were simulated in parallel on a computer cluster. Each job simulated only one shower with the steering file from below. The runnumber depends on the job number in a large set of parallel simulation jobs, while the seeds depend both on the dataset number and the job number. A dataset is mainly specified by an energy range, a primary particle type and a total number of showers.

```
RUNNR   {JOB_NR}+1                number of run
EVTNR   1                         number of first shower event
NSHOW   1                         number of showers to generate
PRMPAR  14 or 0402 or 1608 or 5626
                                  particle type of prim. particle
ESLOPE  -1.0                      slope of primary energy spectrum
ERANGE  {0.1 bins in the ERANGE
         that depends on the dataset
         and JOB_NR}
                                  energy range of primary particle (GeV)
THETAP  0. 40.                    range of zenith angle (degree)
PHIP    0. 360.                   range of azimuth angle (degree)
SEED    {depends on dataset
         and JOB_NR}     0   0    seed for 1. random number sequence (HAD)
SEED    "                0   0    seed for 2. random number sequence (EGS4)
OBSLEV  2834.e2                   observation level (in cm)
--> Safely above the highest tanks

ELMFLG  T   T                     em. interaction flags (NKG,EGS)
RADNKG  2.E5                      outer radius for NKG lat.dens.determ.
ARRANG  -119.                     rotation from CORSIKA to I3 coordinates
FIXHEI  0.  0                     first interaction height & target
FIXCHI  0.                        starting altitude (g/cm**2)
MAGNET  16.59 -52.79              magnetic field centr. (uT)
        --> averages over summer 2007
            (June 1 to Oct 31, 2007)
    from the NOAA Geomagnetic Online Calculator
HADFLG  0  1  0  1  0  2          flags hadr.interact.&fragmentation
SIBYLL  T  0                      model for high energy hadrons
SIBSIG  T                         hadronic cross sections
--> OR for Systematics : QGSJetII flags instead
ECUTS   .05 .05 .01 .002          energy cuts for particles (h/mu/e/gamma, GeV)
MUADDI  T                         additional info for muons
MUMULT  T                         muon multiple scattering angle
LONGI   T  20.  T  F              longit.distr. & step size & fit
MAXPRT  1                         max. number of printed events
ECTMAP  1.e4                      cut on gamma factor for printout
```

```
STEPFC  1.0                      mult. scattering step length fact.
DEBUG   F  6  F  1000000         debug flag and log.unit for out
DIRECT  .                        output directory
ATMOD   12                       atmospheric model
        --> July 1, 1997 ("July atmosphere" fitted with MSIS-90-E)
if thinned :
THIN    1.e-6  {E_MIN}*1.e-6  0  energy fraction below which thinning becomes
                                 active, weight limit, radial thinning
above 10^8.4 :
THIN    273./{E_MIN}  273.  0
THINH   10./1.e-6  1./({E_MIN}*1.e-6)
                                 hadronic thinning : ratio of EM and HAD thin
                                 level, ratio of EM weight limit and HAD.
EXIT                             terminates input
```

Appendix B

Muon bundle energy loss

The equation for the muon bundle energy loss [201] is :

$$\left(\frac{\mathrm{d}\,E_{\mu,B}}{\mathrm{d}\,X}\right)(X) := \left(\frac{\mathrm{d}\,E_{\mu}}{\mathrm{d}\,X}\right)_{\mathrm{bundle}}(X) = \int_{E_{\min}(X)}^{E_{\max}(X)} \frac{\mathrm{d}\,N_{\mu}(X)}{\mathrm{d}\,E_{\mu}(X)}(X)\frac{\mathrm{d}\,E_{\mu}}{\mathrm{d}\,X}(X)\,\mathrm{d}\,E_{\mu}(X), \tag{B.1}$$

where $\frac{\mathrm{d}\,N_{\mu}}{\mathrm{d}\,E_{\mu}}$ is the energy distribution of the muons at slant depth X and $\frac{\mathrm{d}\,E_{\mu}}{\mathrm{d}\,X}$ is the energy loss of a single muon. $E_{\min}$ is the minimum energy that a muon needs to get to slant depth X into the ice. $E_{\max}$ is the maximum energy a muon from a shower induced by particle A with energy E_0 can have. The muon multiplicity of air showers comes from the Elbert formula (Eq.1.48) where we approximate the high energy correction term $\left(1-\frac{AE_{\mu}}{E_0}\right)^{5.25}$ as one:

$$N_{\mu}(E_{\mu} > E_{\mu_{\mathrm{thr}}}) \sim \frac{\kappa A}{\cos\theta}\cdot\left(\frac{E_0}{A}\right)^{\gamma_{\mu}-1} E_{\mu}^{-\gamma_{\mu}}, \tag{B.2}$$

with γ_{μ} = 1.757, the muon spectral index and κ = 14.5 GeV, the muon energy distribution becomes:

$$\frac{\mathrm{d}\,N_{\mu}}{\mathrm{d}\,E_{\mu}} \sim \frac{\gamma_{\mu}\kappa A}{\cos\theta}\cdot\left(\frac{E_0}{A}\right)^{\gamma_{\mu}-1} E_{\mu}^{-\gamma_{\mu}-1}. \tag{B.3}$$

If this equation is integrated between $E_{\mu,\mathrm{thr}}$ and ∞, the Elbert formula reappears. The energy distribution of the muons at slant depth X is unknown, but from the Elbert formula the energy distribution at the surface is known so the integration needs to be changed from muon energy at X to their surface energies :

$$\left(\frac{\mathrm{d}\,E_{\mu}}{\mathrm{d}\,X}\right)_{\mathrm{bundle}}(X) = \int_{E_{\min}(X)}^{E_{\max}(X)} \frac{\mathrm{d}\,N_{\mu}(X)}{\mathrm{d}\,E_{\mu}(\mathrm{surf})}(X)\frac{\mathrm{d}\,E_{\mu}(\mathrm{surf})}{\mathrm{d}\,E_{\mu}(X)}(X)\frac{\mathrm{d}\,E_{\mu}}{\mathrm{d}\,X}(X)\,\mathrm{d}\,E_{\mu}(X) \tag{B.4}$$

$$= \int_{E_{\min}(\mathrm{surf})}^{E_{\max}(\mathrm{surf})} \frac{\mathrm{d}\,N_{\mu}(X)}{\mathrm{d}\,E_{\mu}(\mathrm{surf})}(X)\frac{\mathrm{d}\,E_{\mu}}{\mathrm{d}\,X}(X)\,\mathrm{d}\,E_{\mu}(\mathrm{surf}). \tag{B.5}$$

Now we only need to express the muon energy loss as a function of its energy at the surface. If we first solve the $\frac{\mathrm{d}\,E_{\mu}}{\mathrm{d}\,X}(X) = -a - bE_{\mu}(X)$ differential equation, we get $E_{\mu}(X) = \left(E_{\mu}(\mathrm{surf}) + \frac{a}{b}\right)e^{-bX} - \frac{a}{b}$. Using this expression in the energy loss formula gives the energy loss as a function of the energy at the surface :

$$\frac{\mathrm{d}\,E_{\mu}}{\mathrm{d}\,X} = -a - bE_{\mu}(X) \tag{B.6}$$

$$= -a - b\left[\left(E_{\mu}(\mathrm{surf}) + \frac{a}{b}\right)e^{-bX} - \frac{a}{b}\right] \tag{B.7}$$

$$= -b\left[\left(E_{\mu}(\mathrm{surf}) + \frac{a}{b}\right)e^{-bX}\right]. \tag{B.8}$$

Integrating over the muon energies at the surface, with an average energy loss behaviour $\frac{\mathrm{d}\,E_\mu}{\mathrm{d}\,X} = -b((E_\mu(\mathrm{surf}) + a/b)e^{-bX}$, $E_{\min} = a/b(e^{bX} - 1)$ and $E_{\max} = E_0/A$, the following fit function with E_0 and A as fit parameters is obtained :

$$\left(\frac{\mathrm{d}\,E_{\mu,B}}{\mathrm{d}\,X}\right)(X) = \left(\frac{\kappa A}{\cos\theta}\right) \cdot e^{-bX} \cdot \gamma_\mu \cdot \left(\frac{E_0}{A}\right)^{\gamma_\mu - 1} \cdot \left[\left(-\frac{E_0}{A}\right)^{-\gamma_\mu} \left(\frac{a}{\gamma_\mu} - \frac{b}{1-\gamma_\mu} \cdot \frac{E_0}{A}\right) + E_{\min}^{-\gamma_\mu} \left(\frac{a}{\gamma_\mu} - \frac{b}{1-\gamma_\mu} \cdot E_{\min}\right)\right], \tag{B.9}$$

Appendix C

Data-MC comparison

C.1 Weighting scheme

C.2 Low level

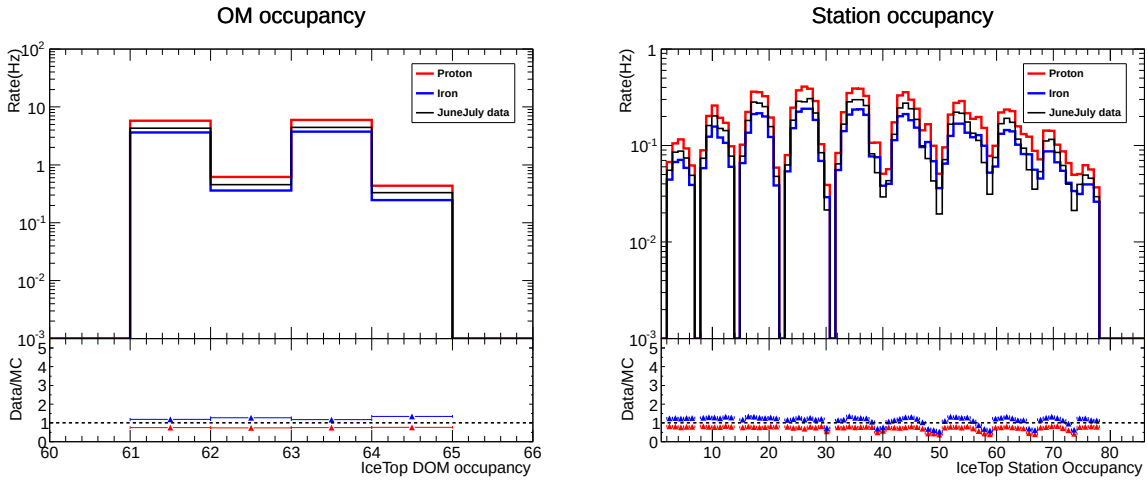

Figure C.1: **Left**: IceTop DOM occupancy. **Right**: IceTop station occupancy.

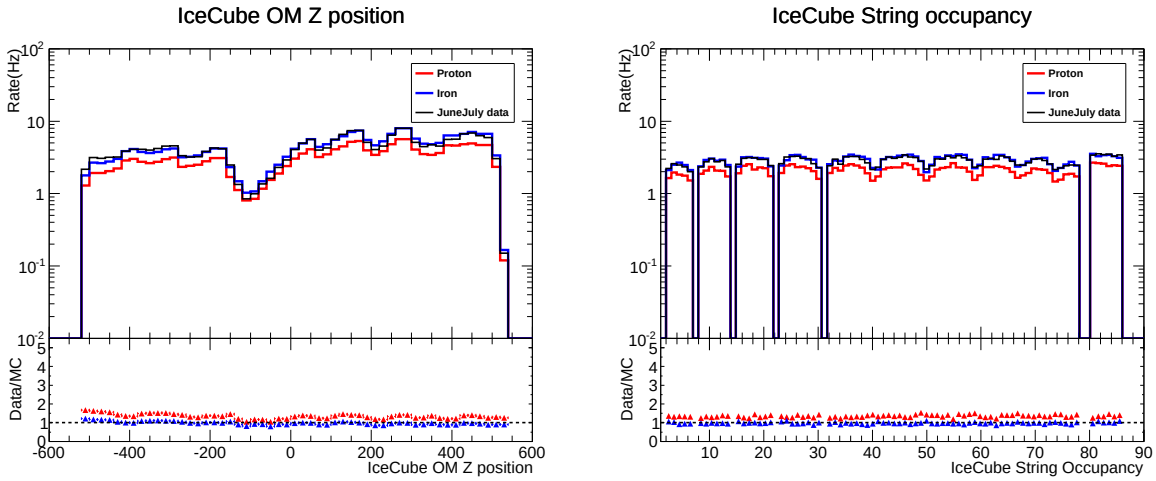

Figure C.2: **Left**: IceCube DOM occupancy plotted as a function of the depth of the DOMs. **Right**: IceCube string occupancy.

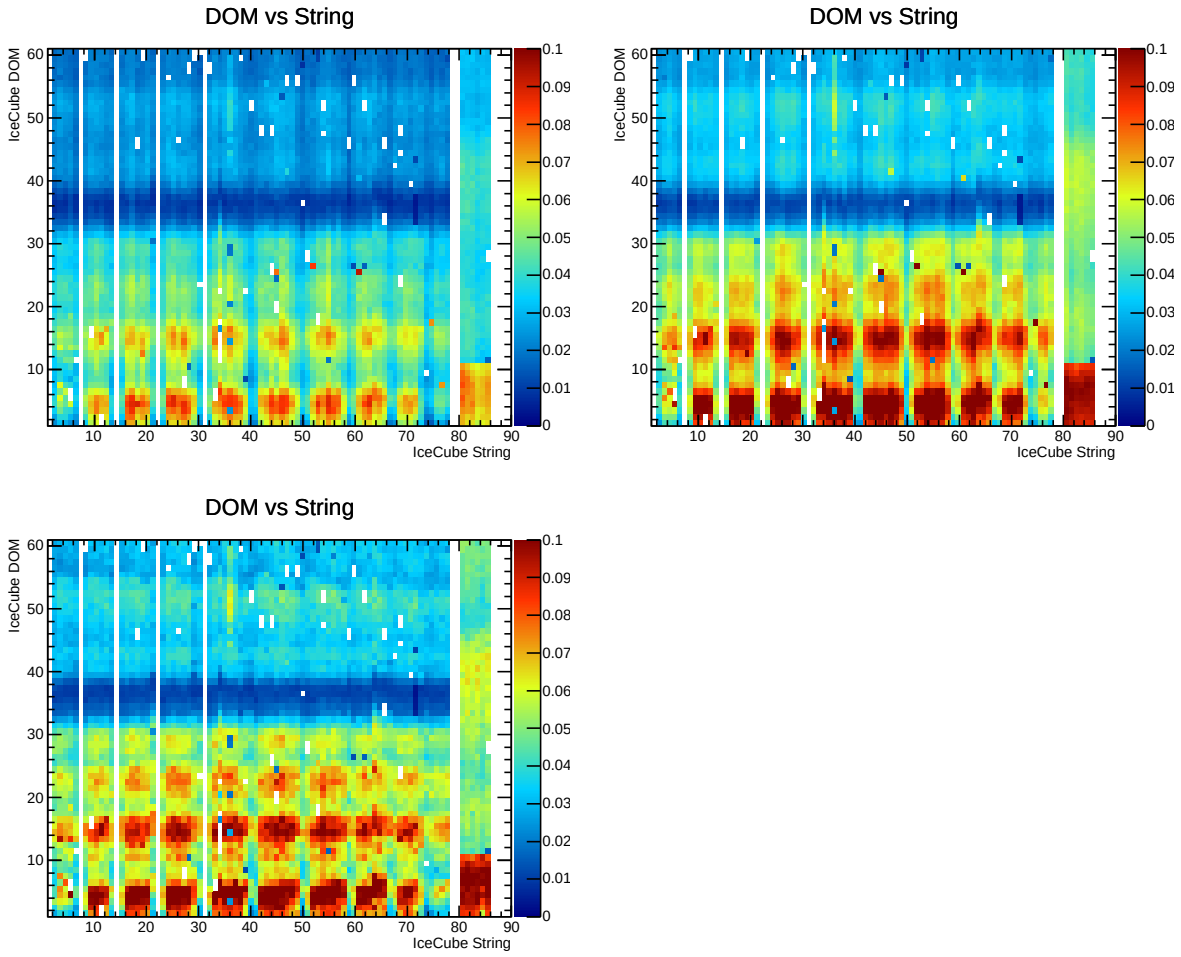

Figure C.3: Hit rate, shown by the colour code, for each individual IceCube DOM.

C.3 Medium level

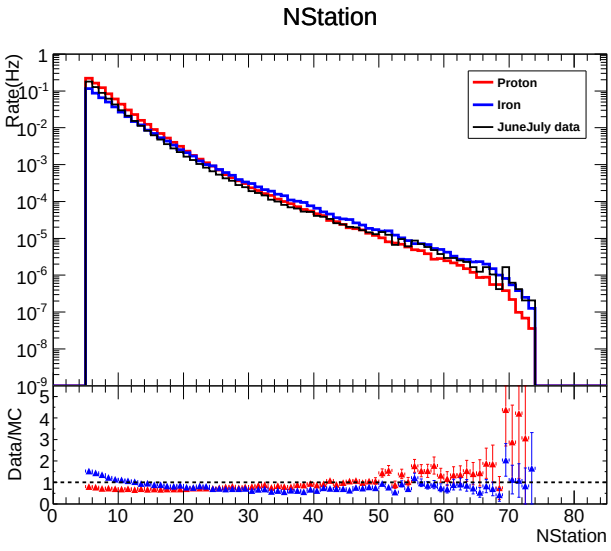

Figure C.4: Distribution of the number of IceTop station hits per event or *NStation* after the extra IceTop hit cleaning, explained in Section 5.3.2.

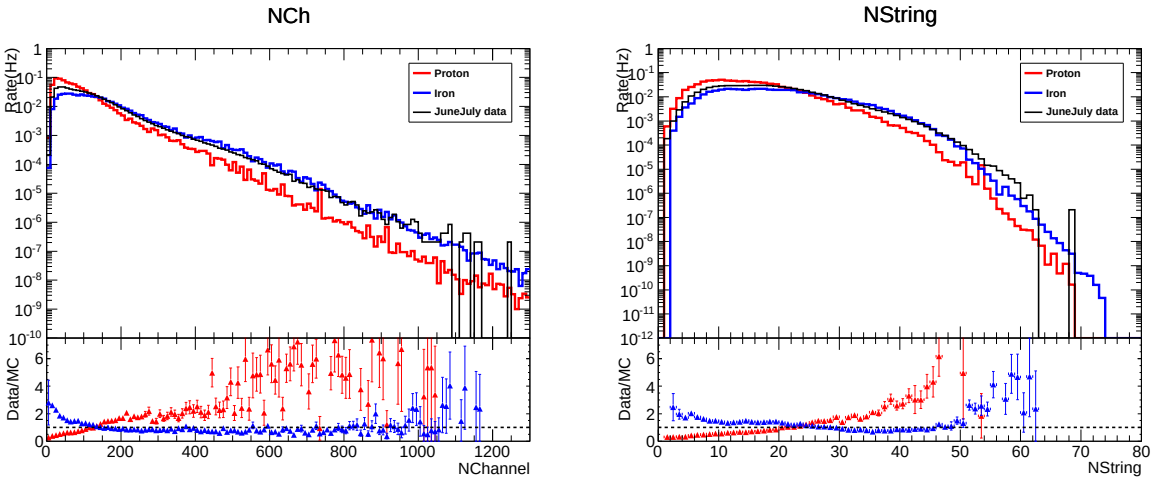

Figure C.5: **Left**: Distribution of the number of DOM hits per event, also called *NChannel*. **Right**: Distribution of the number of string hits within each event or *NString*.

C.4 High level

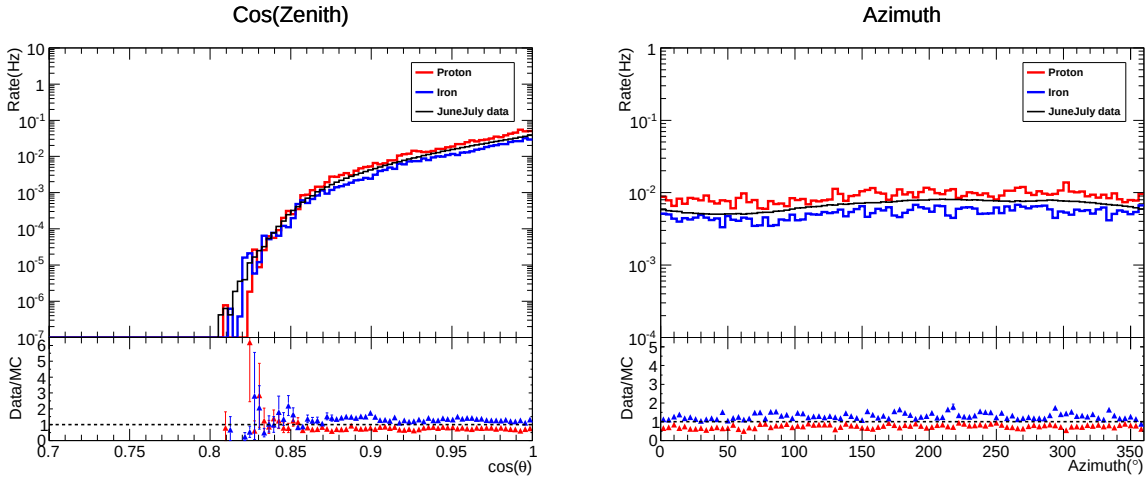

Figure C.6: The distribution of the cosine reconstructed of the reconstructed zenith angle (left) and the reconstructed azimuth angle (right).

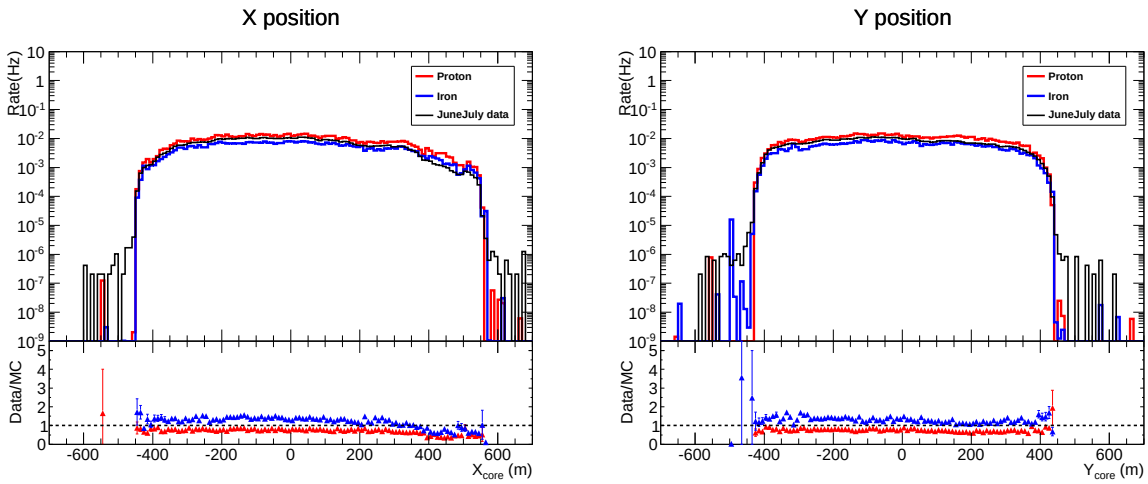

Figure C.7: The distribution of the x coordinate (left) and the y coordinate (right) of the reconstructed core position

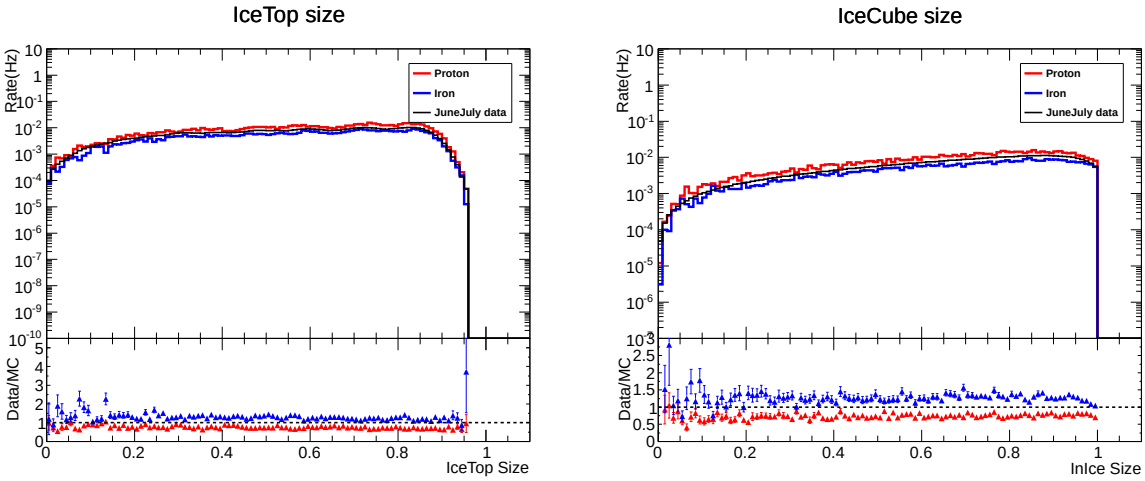

Figure C.8: **Left**: The IceTop size distribution. **Right**: The IceCube size distribution.

Acronyms

- **ADC**: Analog to Digital Converter.
- **AGN**: Active Galactic Nuclei.
- **AMRC**: Antarctic Meteorological Research Center.
- **ATWD**: Analog Transient Waveform Digitizer.
- **BR** : Branching ratio.
- **CMB**: Cosmic Microwave Background.
- **COG**: Center of Gravity.
- **DAC**: Digital to Analog Converter.
- **DC**: DeepCore.
- **DLP**: Double Logarithmic Parabola.
- **DOM**: Digital Optical Module.
- **FADC**: Fast Analog to Digital Converter.
- **FCU**: Freeze Control Unit.
- **FPGA**: Field Programmable Gate Array.
- **GRB**: Gamma Ray Burst.
- **GRT**: Gribov's Reggeon field theory.
- **HG**: High Gain.
- **HV**: High Voltage.
- **ICL**: IceCube Laboratory.
- **ISM**: Interstellar Matter.
- **LDF**: Lateral Distribution Function.
- **LED**: Light Emitting Diode.
- **LG**: Low Gain.
- **LHC**: Large Hadron Collider.
- **MB**: Main Board.

- **MC**: Monte Carlo.
- **MHD**: Magnetohydronamics.
- **MLP**: Multi-layer perceptron.
- **NLDSA**: Non-linear diffusive shock acceleration.
- **NN**: (Artificial) Neural Network.
- **NNLS**: Non-Negative Least Squares.
- **PE**: Photo-electron.
- **PMT**: Photomultiplier Tube.
- **QCD**: Quantum Chromodynamics.
- **RHIC**: Relativistic Heavy Ion Collider.
- **SNR**: Supernova remnant.
- **SPE**: Single Photo-electron.
- **VEM**: Vertical Equivalent Muon.

Nederlandse Samenvatting

De zoektocht naar de oorsprong van hoog-energetische kosmische straling is intussen al meer dan honderd jaar bezig. Door een nauwkeurige meting van het energiespectrum van deze kosmische deeltjes kunnen we afleiden hoe ze aan hun zulke energie geraken en welke mogelijke bronnen deze deeltjes kunnen veroorzaken. We kunnen immers geen gebruik maken van de de richting waar ze vandaag komen omdat de kosmische deeltjes geladen zijn en afgebogen in galactische magnetische velden.

Het energiespectrum tussen 1 TeV en 100 EeV kan beschreven worden door een machtswet. Er zijn echter twee verandering in de spectrale index van deze machtswet. Rond 3 PeV, ook "knie" genoemd, wordt het spectrum steiler en de spectrale index gaat van -2.7 naar -3.1. Rond 3 EeV, de "enkel" van het kosmische stralingsspectrum, wordt het energiespectrum terug minder steil en gaat de spectral index terug naar -2.7. De reden voor de knie ligt waarschijnlijk in een geleidelijke verandering van de bronnen van kosmische straling uit onze Melkweg, zoals restanten van supernovae, die geen voldoende energie meer kunnen geven aan de kosmische deeltjes, naar bronnen van buiten de Melkweg. Deze genereren minder kosmische straling, maar kunnen door andere versnellingsmechanismen de deeltjes een hogere energie geven. Het overgangsgebied tussen deze twee bronnen zou tussen de knie en de enkel liggen. Het is echter zeer eigenaardig en moeilijk te theoretisch te verklaren waarom er eigenlijk het spectrum een machtswet volgt tussen de knie en de enkel. De laatste jaren echter zijn de metingen nauwkeuriger geworden door betere detectoren en betere simulaties. Als gevolg hiervan hebben experimenten zoals IceTop en Kascade hints gezien dat het spectrum niet meer door n enkele machtswet kan beschreven worden tussen de knie en de enkel.

In deze thesis is er op basis van data van het IceCube Neutrino Observatorium een nieuwe, zeer nauwkeurige meting gedaan van het energiespectrum en daarbij ook van de samenstelling van de kosmische straling in in het energiebereik tussen 2.5 PeV en 1 EeV. Het IceCube Neutrino Observatorium is daar zeer geschikt voor omdat het twee detectorcomponenten bezit, IceTop en IceCube, die verschillende eigenschappen van de deeltjeslawines veroorzaakt door hoog-energetische kosmische straling in de atmosfeer kunnen bestuderen.

Voor de data die in deze thesis gebruikt zijn, van 1 juni 2010 tot 11 mei 2011, bestond IceTop uit 73 stations, die elk gevormd worden door 2 ijs Cherenkov tanks. IceTop detecteert voornamelijk de electromagnetische component van de deeltjeslawines en is dus vooral geschikt om de energie van het primaire kosmische deeltje te bepalen. IceCube bestond uit 79 IceCube kabels waaraan 60 detector modules bevestigd zijn tussen 1450 en 2450 m diepte. Nadat de deeltjeslawines doorheen IceTop gegaan zijn, worden de electromagnetische deeltjes, electronen en fotonen, gestopt in de sneeuw en in het ijs. De bundels van muonen met zeer hoge energie ($>$ 300 GeV) geraken tot diep in het ijs waar de IceCube detectormodules zijn. Doordat ze zulke hoge energie hebben genereren ze Cherenkov licht dat opgepikt wordt door deze detectormodules en daar omgezet worden naar electronische signalen. Het detectie principe voor de IceTop ijstanks is volledig analoog.

In mijn analyse zijn de signalen in IceTop van deeltjeslawines die zowel door IceTop als door IceCube gezien worden gebruikt om de richting en positie van de kern van de deeltjeslawine op het Zuidpoolopper-vlak te reconstrueren. Vervolgens wordt verdeling van de signaalsterkte als functie van de afstand tot de kernpositie gefit door een maximum likelihood procedure, die ook een betere richting en kernpositie bepaalt. De S_{125}-parameter, of gefitte signaalsterkte op 125 m van de kernpositie van de deeltjeslawine, is een zeer goede schatter voor de energie van het primair kosmische deeltje. Maar hij is ook afhankelijk van het type kosmisch deeltje.

De signalen gedetecteerd door IceCube worden gedeconvolueerd door een reconstructie die hier beschreven is, naar een profiel van energieverlies per segment van het gereconstrueerde spoor (dat een verlenging is van de gereconstrueerde richting van het kosmisch deeltje). Aan de variatie van het reconstructueerde energie als functie van de afgelegde weg in de detector, is een gemiddeld energieverlies gefit, die gerelateerd is aan het aantal muonen in de muonenbundel en dus ook aan het type kosmisch deeltje. Als extra informatie gebruik ik hoe stochastich het energieverlies verloop is door te tellen hoeveel gereconstrueerde energieverliezen per segment er veel hoger zijn dan het gemiddelde. Dit is ook gerelateerd aan het aantal muonen in de muonenbundle van een deeltjeslawine.

Om ervoor te zorgen dat deze reconstructies goede resultaten geven, hou ik enkel de deeltjeslawines bij die een kernpositie hebben die binnenin de grenzen van de IceTop array ligt en die ook doorheen het IceCube detectorvolume gaan. Daarbij heb ik ook extra aandacht besteed om deeltjeslawines die lijken alsof ze zowel door IceTop als IceCube gaan, maar eigenlijk afkomstig zijn van twee onafhankelijke kosmische deeltjes uit de analyse te verwijderen. Als er tijdens een standaard IceTop-IceCube deeltjeslawine andere muonen of andere sporen in de detector zijn, of andere deeltjeslawines IceTop stations raken, worden enkel deze zorgvuldig verwijderd.

Na de reconstructie en selectie van goede gebeurtenissen, wordt een neuraal network getraind dat de het niet-lineaire ongekende functioneel verband tussen de variabelen die ik gereconstrueerd heb en die gevoelig zijn aan het type deeltje en afhankelijk zijn van hun energie, bepaalt. Eens dit ongekend functioneel verband bepaald is op basis van simulaties, kan ik hetzelfde functioneel toepassen op data waar de primaire deeltjesenergie en zijn type niet gekend zijn.

Het energiespectrum wordt dan bepaald na acceptantiecorrectie en op basis van de gereconstrueerde energie van mijn neuraal netwerk. Voor de bepaling van de gemiddelde massa of nog beter van het energiespectrum van 4 deeltjestypes die gesimuleerd waren (proton, helium, zuurstof en ijzer), is er nog een extra stap nodig omdat een nauwkeurige massabepaling met het neuraal netwerk niet mogelijk is. Ik gebruik echter de vorm van de 4 distributies in gerecostrueerde massa voor de 4 types per gereconstrueerde energiebin en fit een gewogen som van deze 4 distributies aan de data distributie. Op deze manier kan ik de individuele bijdrage van elk van de 4 distributies bepalen en een gemiddelde massa berekenen per energiebin.

Het energiespectrum dat uit mijn analyse komt is volledig consistent met het energiespectrum dat bepaald werd door een onafhankelijke analyse op basis van deeltjelawines die IceTop raken en niet door IceCube moeten gaan. Het grote voordeel van mijn resultaat echter is, dat ook al heb ik factor 3 minder statistiek, er geen veronderstelling nodig was voor de samenstelling van de kosmische straling terwijl dat bij de andere analyse een $\pm 7\%$ onzekerheid veroorzaakt. In beide spectra zien we de knie op ongeveer 3.5 PeV, een duidelijk verandering van de spectrale index van de machtswet vanaf 20 PeV vervolgt door een duidelijk steiler spectrum vanaf 130 PeV. De afwijking van n enkele machtswet tussen de knie en de enkel is zeer significant en kan niet verklaard worden door de statistische of systematische onzekerheden. Er is meer structuur zichtbaar in het energiespectrum, maar meer data is nodig om te weten of deze statistische fluctuaties zijn of komt van een fysisch proces.

De meting van de gemiddelde massa wordt gedomineerd door grote systematische fouten, maar deze zijn duidelijk gecorreleerd en overschat. De kwalitatieve trend is echter zichtbaar in bijna alle systematische onzekerheden, namelijk dat de gemiddelde samenstelling van kosmische straling zwaarder wordt tot ongeveer 130 PeV, waarna de samenstelling terug lichter wordt en voor de hoogste energieën bij 300-500 PeV terug verzwaart. De statistiek bij deze twee laatste datapunten is echter klein en meer data is nodig om met meer zekerheid te weten wat de massa is.

Tot slot, heb ik ook de energiespectra van de 4 individuele types bepaald. Hoewel meer data nodig is en een grondige, correcte evaluatie van de systematische onzekerheid nodig is, zijn er hints zichtbaar dat deze spectra consistent zouden met 2 tot 3 bronnen van kosmiche straling die een rigiditeitsafhankelijke cutoff energie hebben.

Bibliography

[1] VF Hess Society. Schloss Pöllau, Austria.

[2] J. Elster and H. Geitel, "Versuche an Becquerelstrahlen.," *Annalen der Physik und Chemie* **302** (1898) 735–740.

[3] F. Linke, "Luftelektrische Messungen bei zwölf Ballonfahrten.," in *Abhandlungen d. Knigl. Ges. d. Wissensch. zu Göttingen (NF)*, vol. 3, pp. 1–90. 1904.

[4] M. Walter, "100 Years of Cosmic Rays." `http://www-zeuthen.desy.de/exps/2012_VictorHess/booklet/broschuere_hess_conference_web.pdf`, 2012.

[5] V. Hess, "Über Beobachtungen der durchdringenden Strahlung bei sieben Freiballonfahrten.," *Z.Phys.* **XIII** (1912) 1084–1091.

[6] M.H.Israel *et al.*, "Isotopic Composition of Cosmic Rays: Results from the Cosmic Ray Isotope Spectrometer on the ACE Spacecraft," *Nucl.Phys.A* **758** (2005) 201c–208c.

[7] K.Lodders, "Solar System abundances and condensation temperatures of the elements," *Ap.J.* **591** (2003) 1220–1247.

[8] K.Greisen, "End of the Cosmic-Ray Spectrum?," *Phys.Rev.Lett.* **16** (1966) 748–750.

[9] G.T.Zatsepin and V.A.Kuz'min, "Upper Limit of the Spectrum of Cosmic Rays," *J. Exp. Theor. Phys. Lett.* **4** (1966) 78–80.

[10] G. Kulikov and G. Khristiansen, "On the Size Spectrum of Extensive Air Showers," *Soviet Physics, JETP* **35** (1959) 441–444.

[11] J.Linsley, "Volcano Ranch Evidence on Cosmic Ray Energy Spectrum, a Preliminary Re-evaluation," in *Proc., 13th ICRC*, vol. 5, pp. 3207–3211, Denver, Colorado. 1973.

[12] **Pierre Auger** Collaboration, J.Abrahams *et al.*, "Properties and performance of the prototype instrument for the Pierre Auger Observatory," *Nucl.Inst.Meth.* **A523** (2004) 50–95.

[13] **Telescope Array** Collaboration, T. Nonaka *et al.*, "The present status of the Telescope Array experiment," *Nucl. Phys. B (Proc. Suppl.)* **190** (2009) 26–31.

[14] **Telescope Array** Collaboration, H. Tokuno *et al.*, "On Site Calibration for New Fluorescence Detectors of the Telescope Array Experiment," *Nucl.Inst.Meth.* **A601** (2009) 364–371.

[15] **Pierre Auger and Telescope Array and Yakutsk** Collaboration, B. Dawson *et al.*, "The energy spectrum of cosmic rays at the highest energies," *EPJ Web of Conferences* **53** (2013) 01005.

[16] **IceCube** Collaboration, R. Abbasi *et al.*, "Cosmic ray composition and energy spectrum from 130 PeV using the 40-string configuration of IceTop and IceCube," *Astropart.Phys.* **42** 15–32.

[17] http://www.nasa.gov/home/hqnews/2008/may/HQ_08126_Chandra_Supernova.html.

[18] W.Baade and F.Zwicky, "On Super-Novae," *Proc.Nat.Acad.Sci.* **20** (5) (1934) 254–259.

[19] W.Baade and F.Zwicky, "Cosmic Rays from Super-Novae," *Proc.Nat.Acad.Sci.* **20** (5) (1934) 259–263.

[20] R. A. Freedman and W. J. KaufmannIII, *Universe*. Freeman, 2005.

[21] X-ray: NASA/CXC/ASU/J.Hester et al.; Optical: NASA/ESA/ASU/J.Hester & A.Loll; Infrared: NASA/JPL-Caltech/Univ. Minn./R.Gehrz.

[22] X-ray: NASA/CXC/SAO, Infrared: NASA/JPL-Caltech; Optical: MPIA, Calar Alto, O.Krause et al.

[23] X-ray: NASA/CXC/SAO/D.Patnaude, Optical: DSS.

[24] X-ray: NASA/CXC/SAO; Optical: NASA/STScI; Infrared: NASA/JPL-Caltech/Steward/O.Krause et al.

[25] X-ray (NASA/CXC/NCSU/S.Reynolds et al.); Radio (NSF/NRAO/VLA/Cambridge/D.Green et al.); Infrared (2MASS/UMass/IPAC-Caltech/NASA/NSF/CfA/E.Bressert).

[26] X-ray: NASA/CXC/PSU/S.Park & D.Burrows.; Optical: NASA/STScI/CfA/P.Challis.

[27] E. Fermi, "On the Origin of the Cosmic Radiation," *Phys.Rev.* **75** (8) (1949) 1169–1174.

[28] W. J. M. Rankine, "On the thermodynamic theory of waves of finite longitudinal disturbances," *Phil. Trans. R. Soc. Lond.* **160** (1870) 277–288.

[29] H. Hugoniot, "Mémoire sur la propagation des mouvements dans les corps et spécialement dans les gaz parfaits (première partie)," *Journal de l'École Polytechnique* **57** (1887) 3–97.

[30] H. Hugoniot, "Mémoire sur la propagation des mouvements dans les corps et spécialement dans les gaz parfaits (deuxième partie)," *Journal de l'École Polytechnique* **58** (1887) 1–125.

[31] A. Hillas, "Can diffusive shock acceleration in supernova remnants account for high-energy galactic cosmic rays?," *J.Phys.G:Nucl.Part.Phys.* **31** (2005) 95–131.

[32] T. K. Gaisser, *Cosmic Rays and Particle Physics*. Cambridge University Press, 1990.

[33] L. D. Landau and E. M. Lifshitz, *Fluid Mechanics*. Pergamon Press, Oxford, 1982. p. 315-331.

[34] P.O.Lagage and C.J.Cesarsky, "The maximum energy of cosmic rays accelerated by supernova shocks," *Astron.Astrophys.* **125** (1983) 249–257.

[35] T. Bell, "Theory of diffuse shock acceleration." http://homepages.dias.ie/~cappa/work_shop/Tony_Bell.pdf.

[36] P.Blasi, "Cosmic rays : Fermi acceleration and its observational implications." Fermi symposium : http://fermi.gsfc.nasa.gov/science/mtgs/symposia/2011/program/session12/Blasi_FermiSymp_r.pdf, 2011.

[37] J. Giacalone and J. R. Jokipii, "Magnetic Field Amplification by Shocks in Turbulent Fluids," *Ap.J.* **663** (2007) L41–L44.

[38] A.R.Bell and S.G.Lucek, "Cosmic ray acceleration to very high energy through the non-linear amplification by cosmic rays of the seed magnetic field," *Mon.Not.R.Astron.Soc.* **321** (2001) 433–438.

[39] A.R.Bell, "Turbulent amplification of magnetic field and diffusive shock acceleration of cosmic rays," *Mon.Not.R.Astron.Soc.* **353** (2004) 550–558.

[40] V.L.Ginzburg and S.I.Syrovatskii, *The Origin of Cosmic Rays*. Pergamon Press, Oxford, 1964.

[41] T. Stanev, *High Energy Cosmic Rays*. Springer-Praxis, 2004.

[42] A.W.Strong, I.V.Moskalenko, and V.S.Ptuskin, "Cosmic ray propagation and interactions in the galaxy," *Ann.Rev.Nucl.Particle Sci.* **57** (2007) 285–327.

[43] V.S.Ptuskin, "Propagation of galactic cosmic rays," *Astropart.Phys.* **39-40** (2012) 44–51.

[44] A. M. Kolmogorov, "The local structure of turbulence in incompressible viscous fluids at very large Reynolds numbers," *Dokl. Akad. Nauk. SSSR* **30** (1941) 299–303. Reprinted in *Proc. R. Soc. London* **A434**, 9-13 (1991).

[45] A. M. Kolmogorov, "Dissipation of energy in isotropic turbulence," *Dokl. Akad. Nauk. SSSR* **32** (1941) 19–21.

[46] J.Holder, "TeV gamma-ray astronomy: A summary," *Astropart.Phys.* **39-40** (2012) 61–75.

[47] **Fermi-LAT** Collaboration, M.Ackermann *et al.*, "Detection of the Characteristic Pion-Decay Signature in Supernova Remnants," *Science* **339** (2013) 807–810.

[48] **VERITAS** Collaboration, V. A. Acciari *et al.*, "Discovery of TeV Gamma-ray emission from Tycho's Supernova Remnant," *Ap.J.* **730** (2) (2011) L20–L25.

[49] **VERITAS** Collaboration, E.Aliu *et al.*, "Discovery of TeV Gamma-ray Emission Toward Supernova Remnant SNR G78.2+2.1," *Ap.J.* **770** (2) (2013) 93–99.

[50] A. Hillas, "The Origin of Ultra-High Energy Cosmic Rays," *Ann.Rev.Astron.Astrophys.* **22** (1984) 425–444.

[51] K.Kotera and A.V.Olinto, "The Astrophysics of Ultrahigh Energy Cosmic Rays," *Ann.Rev.Astron.Astrophys.* **49** (2011) 119–153.

[52] J.R.Hörandel, "Models of the knee in the energy spectrum of cosmic rays," *Astropart.Phys.* **21** (2004) 241–265.

[53] J.R.Hörandel, "Overview on direct and indirect measurements of cosmic rays," *Int.J.Mod.Phys.A* **20** (29) (2005) 6753–6764.

[54] B.Peters, "Primary Cosmic Radiation and Extensive Air Showers," *Il Nuovo Cimento* **XXII** (4) (1961) 800–819.

[55] K.Kampert and M.Unger, "Measurements of the Cosmic Ray Composition with Air Shower Experiments," *Astropart.Phys.* **35** (2012) 660–678.

[56] P. Blasi and E. Amato, "Diffusive propagation of cosmic rays from supernova remnants in the Galaxy. I: spectrum and chemical composition," *JCAP* **01** (2012) 010.

[57] A. Erlykin and A. Wolfendale, "The Knee in the Cosmic Ray Energy Spectrum," in *Proc. 31^{st} ICRC*, Lodz, Poland. 2009.

[58] M. Shibata, Y. Katayose, J. Huang, and D. Chen, "Chemical Composition and Maximum Energy of Galactic Cosmic Rays," *Ap.J.* **716** (2010) 1076–1083.

[59] V.Ptuskin, V.Zirakashvili, and E.Seo, "Spectrum of Galactic Cosmic Rays Accelerated in Supernova Remnants," *Ap.J.* **718** (2010) 31–36.

[60] R. Aloisio, V. Berezinsky, and A. Gazizov, "Ultra high energy cosmic rays: The disappointing model," *Astropart.Phys.* **34** (2011) 620–626.

[61] R.Aloisio, V. Berezinsky, and A.Gazizov, "Transition from galactic to extragalactic cosmic rays," *Astropart.Phys.* **39-40** (2012) 129–143.

[62] R. Liu and X. Wang, "Energy Spectrum and Chemical Composition of Ultrahigh Energy Cosmic Rays from Semi-Relativistic Hypernovae," *Ap.J.* **746** (1) (2012) 40–46.

[63] J.R.Hörandel, "On the knee in the energy spectrum of cosmic rays," *Astropart.Phys.* **19** (2003) 193–220.

[64] V.S.Berezinsky, S.I.Grigorieva, and B.I.Hnatyk, "Extragalactic UHE proton spectrum and prediction for iron-nuclei flux at 10^8-10^9 GeV," *Astropart.Phys.* **21** (2004) 617–625.

[65] J.Blümer., R.Engel, and J.R.Hörandel, "Cosmic Rays from the Knee to the Highest Energies," *Progr.Part.Nucl.Phys.* **63** (2009) 293–338.

[66] C. Donato and G. Medina-Tanco, "Experimental contraints on the astrophysical interpretation of the cosmic ray Galactic-extragalactic transition region," *Astropart.Phys.* **32** (2009) 253–268.

[67] T.K.Gaisser, "Spectrum of cosmic-ray nucleons, kaon production, and the atmospheric muon charge ratio," *Astropart.Phys.* **35** (2012) 801–806.

[68] T.K.Gaisser, T.Stanev, and S. Tilav, "Cosmic Ray Energy Spectrum from Measurements of Air Showers," *Front.Phys.* (April 2013) , `arXiv:1303.3565v1 [astro-ph.HE]`.

[69] L.G.Sveshnikova, E.E.Korosteleva, L.A.Kumichev, V.A.Prosin, V.S.Ptuskin, and O.N.Strelnikova, "Nearby sources in the transition region between Galactic and Extragalactic cosmic rays," *J.Phys.: Conf.Series* **409** (2013) 012062.

[70] K.Kampert and A.Watson, "Extensive air showers and ultra high-energy cosmic rays: a historical review," *Eur.Phys.J. H* **37** (2012) 359–412.

[71] B.Rossi, "Über die Eigenschaften der durchdringenden Korpuskularstrahlung im Meereseniveau," *Z.Phys.* **82** (1934) 151.

[72] E.Regener and G.Pfotzer, "Vertical intensity of cosmic rays by threefold coincidences in the stratosphere," *Nature* **136** (1935) 718–719.

[73] K.Schmeiser and W.Bothe, "Die harten Ultrastrahlschauer," *Ann. Phys.* **424** (1938) 161–177.

[74] W.Kolhörster, I.Matthes, and E.Weber, "Gekoppelte Höhenstrahlen," *Naturwissenschaften* **26** (1938) 576.

[75] B.Rossi, "Misura sulla distribuzione angolare di intensia della radiazione penetrante all' Asmara," *Supplemento a la Ricerca Scientifica* **1** (1934) 579.

[76] P.Auger, P.Ehrenfest, R.Maze, J.Daudin, Robley, and A.Fréon, "Extensive Cosmic-Ray Showers," *Rev.Mod.Phys.* **11** (1939) 288–291.

[77] W.B.Fretter in *Proc. Echo Lake Cosmic Ray Symposium*. 1949.

[78] K.Greisen, "Cosmic ray showers," *Ann.Rev.Nucl.Sci.* **10** (1960) 63–108.

[79] R.Engel, D.Heck, and T.Pierog, "Extensive Air Showers and Hadronic Interactions at High Energy," *Annu.Rev.Nucl.Part.Sci.* **61** (2011) 467–489.

[80] W.Heitler, *Quantum Theory of Radiation*. Oxford: Oxford Univ. Press. 2nd ed., 1944.

[81] J.F.Carlson and J.R.Oppenheimer, "On multiplicative showers," *Phys.Rev.* **51** (1937) 220–231.

[82] J.Matthews, "A Heitler model of extensive air showers," *Astropart.Phys.* **22** (2005) 387–397.

[83] J.W.Elbert, "Multiple muons produced by cosmic ray interactions," in *Proc., DUMAND Summer Workshop*, vol. 2, pp. 101–119, La Jolla, CA. 1978.

[84] T.K.Gaisser and T.Stanev, "Muon bundles in underground detectors," *Nucl.Instrum.Meth.* **A235** (1985) 183–192.

[85] C.Forti *et al.*, "Simulation of atmospheric cascades and deep-underground muons," *Phys.Rev. D* **42** (11) (1990) 3668–3689.

[86] P.Lipari, "TeV muons in hadronic showers," *Astropart.Phys.* **1** (1993) 399–415.

[87] M.Boezio and E.Mocchiutti, "Chemical composition of galactic cosmic rays with space experiments," *Astropart.Phys.* **39-40** (2012) 95–108.

[88] E.S.Seo, "Direct measurements of cosmic rays using balloon borne experiments," *Astropart.Phys.* **39-40** (2012) 67–87.

[89] P.Grieder, *Extensive Air Showers*. Springer-Verlag, 2010.

[90] **IceCube** Collaboration, R. Abbasi *et al.*, "IceTop: The surface component of IceCube," *Nucl.Instrum.Meth.* **A700** (2013) 188–220.

[91] M.A.Lawrence, R.J.O.Reid, and A.A.Watson, "The Cosmic ray energy spectrum above 4×10^{17}eV as measured by the Haverah Park array," *J.Phys.* **G17** (1991) 733–757.

[92] **IceCube** Collaboration, A. H. Ismail *et al.*, "Low Energy Air Showers With IceTop," in *Proc. 33^{rd} ICRC*, Rio De Janeiro, Brazil. 2013.

[93] **AMANDA** Collaboration, E. Andres *et al.*, "The AMANDA neutrino telescope: principle of operation and first results," *Astropart.Phys.* **13** (2000) 1–20.

[94] **AMANDA** Collaboration, R. Wischnewski *et al.*, "Performance of the AMANDA-II Detector," in *Proc. 27^{th} ICRC*, pp. 1105–1108, Hamburg, Germany. 2001.

[95] **AMANDA** Collaboration, S. W. Barwick *et al.*, "Potential of AMANDA-II in HE Neutrino Astrophysics," in *Proc. 27^{th} ICRC*, pp. 1101–1104, Hamburg, Germany. 2001.

[96] D. M. Lowder, T. Miller, P. B. Price, A. Westphal, S. W. Barwick, F. Halzen, and R. Morse, "Observation of muons using the polar ice cap as a Cerenkov detector," *Nature* **353** (1991) 331–333.

[97] **IceCube** Collaboration, A. Achterberg *et al.*, "First Year Performance of the IceCube Neutrino Telescope," *Astropart.Phys.* **26** (2006) 155–173.

[98] **IceCube** Collaboration, J. Ahrens *et al.*, "IceCube Preliminary Design Document," *Rev 1.24* (Oct.11, 2001). `http://www.icecube.wisc.edu/science/publications/pdd/pdd.pdf`.

[99] **IceCube** Collaboration, R. Abbasi *et al.*, "The Design and Performance of IceCube DeepCore," *Astropart.Phys.* **35** (2012) 615–624.

[100] P. A. Cherenkov, "Vidimoe svechenie chistykh zhidkostei pod deistviem γ-radiatsii ("visible glow of pure liquids under γ-irradiation")," *Dokl.Akad.Nauk. SSSR* **2** (8) (1934) 451.

[101] P. A. Cherenkov, "Visible radiation produced by electrons moving in a medium with velocities exceeding that of light," *Phys.Rev.* **52** (1937) 378–379.

[102] I. M. Frank and I. E. Tamm, "Kogerentnoe izluchenie bystrogo elektrona v srede ("the coherent radiation of a fast electron in a medium")," *Dokl. Akad. Nauk SSSR* **14** (1937) 107.

[103] J. V. Jelley, *Cherenkov radiation and its applications*. Pergamon Press, NY, 1958.

[104] P. B. Price and K. Woschnagg, "Role of group velocity and phase velocity in high-energy neutrino observatories," *Astropart.Phys.* **15** (2001) 97–100.

[105] **Particle Data Group** Collaboration, J. Beringer *et al.*, "Review of particle physics (passage of particles through matter)," *Phys.Rev.D* **86** (2012) 010001.

[106] C. Wiebusch, *The Detection of Faint Light in Deep Underwater Neutrino Telescopes*. PhD thesis, RTWH Aachen, 1995.

[107] **AMANDA** Collaboration, M. Kowalski, "On the cherenkov light emission of hadronic and electro-magnetic cascades," *AMANDA Internal Report* **20020803** (2002) .

[108] **IceCube** Collaboration, L. Radel, "Simulation Studies of the Cherenkov Light Yield from Relativistic Particles in High-Energy Neutrino Telescopes with Geant4," *IceCube Internal Report* **201210001** (2012) .

[109] D. Chirkin and W. Rhode, "Propagating Leptons Through Matter with Muon Monte Carlo (MMC)," (2004) , `arXiv:0407075v2 [hep-ph]`.

[110] D. E. Groom, N. V. Mokhov, and S. I. Striganov, "Muon Stopping Power and Range Tables 10 MeV – 100 TeV," *Atomic Data and Nuclear Data Tables* **78** (2) (2001) 183–356.

[111] P. Miočinović, *Muon energy reconstruction in the Antarctic Muon And Neutrino Detector Array (AMANDA)*. PhD thesis, University of California, Berkeley, 2001.

[112] P. B. Price *et al.*, "Temperature Prole for Glacial Ice at the South Pole: Implications for Life in a Nearby Subglacial Lake," *Proc.Natl.Acad.Sci.* **99** (12) (2002) 7844–7847.

[113] **AMANDA** Collaboration, M. Ackermann *et al.*, "Optical Properties of Deep Glacial Ice at the South Pole," *J.Geophys.Res.* **111** (2006) D13203.

[114] P. B. Price, K. Woschnagg, and D. Chirkin, "Age vs depth of glacial ice at South Pole," *Geophys.Res.Letters* **27** (14) (2000) 2129–2132.

[115] **IceCube** Collaboration, M. G. Aartsen *et al.*, "Measurement of South Pole ice transparency with the IceCube LED calibration system," *Nucl.Instrum.Meth.* **A711** (2013) 73–89.

[116] R. C. Bay *et al.*, "South Pole paleowind from automated synthesis of ice core records," *J.Geophys.Res.* **115** (2010) D14126.

[117] R. C. Bay. `http://icecube.berkeley.edu/~bay/dustmap/`.

[118] **IceCube** Collaboration, D. Chirkin *et al.*, "Evidence of optical anisotropy of the South Pole Ice," in *Proc.33rd ICRC*, Rio De Janeiro, Brazil. 2013.

[119] `http://amrc.ssec.wisc.edu/`.

[120] "Meteorology Department, Amundsen-Scott South Pole Station, Antarctica." `http://amrc.ssec.wisc.edu/usap/southpole/met-handout.pdf`.

[121] **IceCube** Collaboration, T. Waldenmaier and T. Feusels, "Snow Density Measurements at the IceTop Site," *IceCube Internal Report* **201111003** (2011) 1–5.

[122] S. D. Ridder, "Influence of South Pole atmosphere on cosmic rays observed by IceCube," Master's thesis, Universiteit Gent, 2011-2012.

[123] L. Dorman, *Cosmic Rays in the Earths Atmosphere and Underground*. Springer Verlag, 2004.

[124] T. R. Parish and D. H. Bromwich, "On the forcing of seasonal changes in surface pressure over Antarctica," *J.Geophys.Res.* **102** (D12) (1997) 13785–13792.

[125] **IceCube** Collaboration, S. Tilav *et al.*, "Atmospheric variations as observed by IceCube," in *Proc. 31st ICRC*, Lodz, Poland. 2009. `arXiv:1001.0776 [astro-ph.HE]`.

[126] P. Barrett *et al.*, "Interpretation of cosmic-ray measurements far underground," *Rev.Mod.Phys.* **24** (3) (1952) 133–178.

[127] **IceCube** Collaboration, P. Desiati *et al.*, "Seasonal variation of atmospheric neutrinos in IceCube," in *Proc. 33rd ICRC*, Rio De Janeiro, Brazil. 2013.

[128] **IceCube** Collaboration, R. Abbasi *et al.*, "The IceCube Data Acquisition System: Signal Capture, Digitization, and Timestamping," *Nucl.Instrum.Meth.* **A601** (2009) 294–316.

[129] **IceCube** Collaboration, R. Abbasi *et al.*, "Calibration and Characterization of the IceCube Photomultiplier Tube," *Nucl.Instrum.Meth.* **A618** (1-3) (2010) 139–152.

[130] K. Hanson. Private communication.

[131] `https://www.spacecomm.nasa.gov/spacecomm/programs/tdrss/default.cfm`.

[132] E. Blaufuss. Private communication.

[133] **IceCube** Collaboration, M. G. Aartsen *et al.*, "Energy Reconstruction Methods and Performance in the IceCube Neutrino Detector," *To Be Published* (2013) .

[134] C. L. Lawson and R. J. Hanson, *Solving least squares problems*. Prentice-Hall, Englewood Cliffs, NJ, 1974.

[135] D. Heck, J. Knapp, J. N. Capdevielle, G. Schatz, and T. Thouw, "CORSIKA: A Monte Carlo Code to Simulate Extensive Air Showers," *FZKA 6019* (1998) . `http://www-ik.fzk.de/~heck/publications`.

[136] A. E. Hedin, "Extension of the MSIS thermosphere model into the middle and the lower atmosphere," *J.Geophys.Res.* **96** (1991) 1159–1172.

[137] **Pierre Auger** Collaboration, P. Abreu *et al.*, "Measurement of the Proton-Air Cross Section at $\sqrt{s} = 57$ TeV with the Pierre Auger Observatory," *Phys.Rev.Lett.* **109** (2012) 062002.

[138] M. Harrison, S. Peggs, and T. Roser, "The RHIC Accelerator," *Ann.Rev.Nucl.Part.Sci.* **52** (2002) 452.

[139] M. Harrison, T. Ludlam, and S. Ozaki, "RHIC Project Overview," *Nucl.Instrum.Meth.* **A499** (2-3) (2003) 235.

[140] **ALICE** Collaboration, K. Aamodt *et al.*, "The ALICE experiment at the CERN LHC," *Journal of Instrum.* **3** (8) (2008) S08002.

[141] S. Ostapchenko, "Nonlinear screening effects in high energy hadronic interactions," *Phys.Rev.D* **74** (2006) 014026.

[142] S. Ostapchenko, "QGSJET-II: Towards reliable description of very high energy hadronic interactions," *Nucl.Phys.Proc.Suppl.* **151** (2006) 143–146.

[143] S. Ostapchenko, "Status of QGSJET," *AIP Conference Proceeding* **928** (2007) 118–125.

[144] K. Werner, F.-M. Liu, and T. Pierog, "Parton ladder splitting and the rapidity dependence of transverse momentum spectra in deuteron-gold collisions at the BNL Relativistic Heavy Ion Collider," *Phys.Rev.C* **74** (2006) 044902.

[145] T. Pierog and K. Werner, "EPOS Model and Ultra High Energy Cosmic Rays," *Nucl.Phys.Proc.Suppl.* **196** (2009) 102–105.

[146] J. Engel, T. K. Gaisser, T. Stanev, and P. Lipari, "Nucleus-nucleus collisions and interpretation of cosmic-ray cascades," *Phys. Rev. D* **46** (1992) 5013–5025.

[147] R. S. Fletcher, T. K. Gaisser, P. Lipari, and T. Stanev, "SIBYLL: An Event generator for simulation of high-energy cosmic ray cascades," *Phys. Rev. D* **50** (1994) 5710–5731.

[148] E. Ahn, R. Engel, T. Gaisser, P. Lipari, and T. Stanev, "Cosmic ray interaction event generator SIBYLL 2.1," *Phys. Rev. D* **80** (2009) 094003.

[149] V. N. Gribov, "A Reggeon Diagram Technique," *Sov.Phys., JETP* **26** (2) (1968) 414–423.

[150] A. B. Kaidalov and K. A. Ter-Martirosian, "Hadron multiple production at high energies in the quark-gluon string model," *Sov.J.Nucl.Phys.* **39** (1984) 979–986.

[151] A. B. Kaidalov, "Soft interactions of hadrons in QCD," *Surv.High Energy Phys.* **13** (1999) 265–330.

[152] S. Ostapchenko, "Studies of Very High Energy Cosmic Rays: Status, Puzzles, and the Impact of LHC Data," *Progr.Theor.Phys.Suppl.* **193** (2012) 204–211.

[153] T. Pierog, I. Karpenko, J. M. Katzy, E. Yatsenko, and K. Werner, "EPOS LHC : test of collective hadronization with LHC data," `arXiv:1306.0121 [hep-ph]`.

[154] R. J. Glauber and G. Matthiae, "High-energy scattering of protons by nuclei," *Nucl.Phys.B* **21** (1970) 135–157.

[155] K. G. Boreskov and A. B. Kaidalov, "Nucleus-nucleus scattering in the Glauber approach," *Sov.J.Nucl.Phys.* **48** (1988) 367–374.

[156] G. Battistoni *et al.*, "The FLUKA code: Description and benchmarking," *AIP Conference Proceeding* **896** (2007) 31–49.

[157] A. Ferrari, P. R. Sala, A. Fasso', and J. Ranft, "FLUKA: a multi-particle transport code," *CERN-2005-10* (2005) . INFN/TC_05/11, SLAC-R-773.

[158] W. R. Nelson, H. Hirayama, and D. W. O. Rogers *Technical Report* **SLAC 265** (1985) . Stanford Linear Accelerator Center, `http://www.slac.stanford.edu/pubs/slacreports/slac-r-265.hmtl`.

[159] A. M. Hillas, "Shower simulation: lessons from MOCCA," *Nucl.Phys.B (Proc.Suppl.)* **52B** (1997) 29–42.

[160] D. Heck and J. Knapp, "Upgrade of the Monte Carlo Code CORSIKA to Simulate Extensive Air Showers with Energies $> 10^{20}$ eV," *FZKA 6097* (1998) . `http://www-ik.fzk.de/~heck/publications`.

[161] **IceCube** Collaboration, J. Madsen and A. Tamburro, "Simulating UHE cosmic-ray showers in IceTop," *IceCube Internal Report* **200911001** (2009) .

[162] **Pierre Auger** Collaboration, M. Kobal, "A thinning method using weight limitation for air-shower simulations," *Astropart.Phys.* **15** (2001) 259–273.

[163] K. Andeen, *First Measurements of Cosmic Ray Composition from 1-50 PeV using New Techniques on Coincident Data from the IceCube Neutrino Observatory*. PhD thesis, University of Wisconsin-Madison, 2011.

[164] **GEANT4** Collaboration, S. Agostinelli *et al.*, "GEANT4 - a simulation toolkit," *Nucl.Instrum.Meth.* **A506** (2003) 250–303.

[165] **IceCube** Collaboration, A. V. Overloop *et al.*, "Simulation of icetop vem calibration and the dependency on the snow layer," in *Proc. 32^{nd} ICRC*, Beijing, China. 2011.

[166] **IceCube** Collaboration, D. Chirkin, "dcorsika update," *IceCube Internal Report* . `http://icecube.wisc.edu/~dima/work/BKP/DCS/REPORT8/paper.pdf`.

[167] J. Lundberg *et al.*, "Light Tracking Through Ice and Water - Scattering and Absorption in Heterogeneous Media with PHOTONICS," *Nucl.Instrum.Meth.* **A581** (2007) 619–631.

[168] **IceCube** Collaboration, F. Kislat, S. Klepser, and A. V. Overloop, "A Lateral Distribution Function and Fluctuation Parametrisation for IceTop," *IceCube Internal Report* **200702001** (2007) .

[169] **IceCube** Collaboration, J. Gonzalez *et al.*, "Inclined Cosmic Ray Air Showers in IceCube," in *Proc. 33^{rd} ICRC*, Rio De Janeiro, Brazil. 2013.

[170] **IceCube** Collaboration, M. G. Aartsen *et al.*, "Measurement of the cosmic ray energy spectrum with IceTop-73," *Phys.Rev.D* **88** (2013) 042004.

[171] **IceCube** Collaboration, K. Rawlins *et al.*, "The Effect of Snow Accumulation on Signals in IceTop," in *Proc. 33^{rd} ICRC*, Rio De Janeiro. 2013.

[172] J. A. Nelder and R. Mead, "A simplex method for function minimization," *Comput. J.* **7** (1965) 308–313.

[173] F. James and M. Roos, "Minuit: A System for Function Minimization and Analysis of the Parameter Errors and Correlations," *Comp.Phys.Commun.* **10** (1975) 343–367.

[174] F. James, "MINUIT : Function Minimization and Error Analysis, Reference Manual ," *CERN Program Library Long Writeup* **D506** (2000) . `http://wwwasdoc.web.cern.ch/wwwasdoc/minuit/minmain.html`.

[175] **AMANDA** Collaboration, J. Ahrens *et al.*, "Muon Track Reconstruction and Data Selection Techniques in AMANDA," *Nucl.Instrum.Meth.* **A524** (2004) 169–194.

[176] X. Bai, D. Chirkin, T. Gaisser, T. Stanev, and D. Seckel, "Muon bundle energy loss in deep underground detector," in *Proc. 31^{st} ICRC*, Lodz, Poland. 2009.

[177] N. Whitehorn, J. van Santen, and S. Lafebre, "Penalized splines for smooth representation of high-dimensional Monte Carlo datasets," *Comp.Phys.Comm.* **184** (9) (2013) 2214–2220.

[178] **IceCube** Collaboration, S. Grullon, D. Boersma, and G. Hill, "Photonics-based Log-Likelihood Reconstruction in IceCube," *IceCube Internal Report* **200807001** (2008) 1–50.

[179] **IceCube** Collaboration, S. Grullon, D. Boersma, G. Hill, K. Hoshina, and K. Mase, "Reconstruction of high energy muon events in IceCube using waveforms," in *Proc. 30^{th} ICRC*, Mérida, Mexico. 2007.

[180] **IceCube** Collaboration, R. Abbasi *et al.*, "A Search for a Diffuse Flux of Astrophysical Muon Neutrinos with the IceCube 40-String Detector," *Phys.Rev.D* **84** (2011) 082001.

[181] **IceCube** Collaboration, R. Abbasi *et al.*, "An improved method for measuring muon energy using the truncated mean of dE/dx," *Nucl.Instrum.Meth.* **A703** (2012) 190–198.

[182] E. V. D. Broucke, "Chemische samenstelling van kosmische straling bestudeerd via het energieverlies in Antarctisch ijs," Master's thesis, Universiteit Gent, 2010-2011.

[183] **IceCube** Collaboration, S. D. Ridder, T. Feusels, *et al.*, "Seasonal variation of the muon multiplicity in cosmic rays at South Pole," in *Proc. 33^{rd} ICRC*, Rio De Janeiro, Brazil. 2013.

[184] `http://aqua.nasa.gov/`.

[185] T. Karg. Private communication.

[186] A. Hoecker, P. Speckmayer, J. Stelzer, J. Therhaag, E. von Toerne, H. Voss, *et al.*, "TMVA - Toolkit for Multivariate Data Analysis," *PoS ACAT* **040** (2007) , `arXiv:physics/0703039 [physics]`.

[187] C. M. Bishop, *Neural Networks for Pattern Recognition*. Oxford University Press, 1996.

[188] G. Cybenko, "Approximation by Superpositions of a Sigmoidal Function," *Math.Control Signal Systems* **2** (4) (1989) 303–314.

[189] K. Hornik, M. Stinchcombe, and H. White, "Multilayer Feedforward Networks are Universal Approximators," *Neural Networks* **2** (5) (1989) 359–366.

[190] K. Funahashi, "On the approximate realization of continuous mappings by neural networks," *Neural Networks* **2** (3) (1989) 183–192.

[191] J. Therhaag and H. Voss. `http://sourceforge.net/p/tmva/mailman/message/30001095/`.

[192] **IceCube** Collaboration, R. Abbasi *et al.*, "All-particle cosmic ray energy spectrum measured with 26 IceTop stations," *Astropart.Phys.* **44** (2013) 40–58.

[193] P. Speckmayer. `http://sourceforge.net/p/tmva/mailman/message/30260450/`.

[194] R. Barlow and C. Beeston, "Fitting using finite Monte Carlo samples," *Comp. Phys. Comm.* **77** (1993) 219–228.

[195] `http://root.cern.ch/root/html534/TFractionFitter.html`.

[196] A. Nappi, "A pitfall in the use of extended likelihood for fitting fractions of pure samples in mixed samples," *Comp. Phys. Comm.* **180** (2009) 269–275.

[197] K. Rawlins. Private communication.

[198] S. D. Ridder. Private communication.

[199] W. T. Eadiea, D. Drijard, F. James, M. Roos, and B. Sadoulet., *Statistical Methods in Experimental Physics*. . North-Holland, 1971.

[200] S. Tilav. Private communication.

[201] **IceCube** Collaboration, T. Feusels, J. Eisch, and C. Xu, "Reconstruction of IceCube coincident events and study of composition-sensitive observables using both the surface and deep detector," in *Proc. 31st ICRC*, Lodz, Poland. 2009. `arXiv:0912.4668 [astro-ph.HE]`.

List of Tables

List of Figures